Quantum Transport and Non-Unitary Gauge Invariance in Graphene-Based Electronic Systems

Wolf-Rüdiger Hannes

Dissertation
submitted for the degree of
Doctor of Philosophy
to the Institute of Photonics and Quantum Sciences
at Heriot-Watt University, Edinburgh

April 2013

Abstract

Quantum transport is studied in electronic two-terminal devices with mono- and few-layer graphene samples described by the low-energy effective theories. Using the scattering approach, the full counting statistics of the transmission distribution, including conductance and noise, are analyzed in the ballistic regime. For undoped few-layer graphene the transport properties are reduced to those of uncoupled monolayers, which manifests a non-unitary gauge invariance owing to the chiral symmetry. Gauge transformations are also used to analyze the effect of external magnetic fields and to facilitate the conformal mapping between the rectangular and Corbino disk sample geometries. The gate-voltage dependence of the ballistic transport properties is studied in a simplistic model and a self-consistent model taking into account the partial doping of the sample by the metallic electrodes. The long-range contact potential is shown to cause strong electron-hole asymmetries in the conductance and noise. Disordered graphene samples are investigated by means of a recently developed approach based on the assumption of non-overlapping impurities. The magnetoconductance of graphene with scalar impurities shows a transition from the diffusive transport regime at weak magnetic fields to the quantum Hall regime, and a transition at stronger magnetic fields to an effectively ballistic regime.

Acknowledgements

Here I would like to take the opportunity to thank everybody who has contributed to this dissertation in one way or another.

First and foremost, I would like to thank Dr Misha Titov, who has been a very kind and patient supervisor at all times. Without his guidance this work could certainly not have been created. Our discussions were often exciting and he understood it well to keep me motivated. He gave me the required support without solving the problems on his own, and set up the next goals without demanding too much of me. I would also like to thank him for allowing me to visit many interesting schools, conferences, as well as experimental and theoretical groups studying graphene and topological insulators at the university of Würzburg. Through Misha I have also had the pleasure to get acquainted with other nice people, who stayed in his house at the same time as I did. Among these I would like to particularly mention Prof Prem B. Bisht, who shared a lot of research experiences with me.

Next I would like to express my gratitude to Prof Mats Jonson for supporting and motivating me with his sense of humor. I am also grateful for his collaboration in the project on contact effects discussed in chapter 6, where his experience and complementary views on the subject have been extremely valuable.

Many thanks go to my fellow student Sebastian Gattenlöhner, without whom my university life would have been far less exciting. The discussions with him were always interesting, and the journeys to schools and conferences with him very enjoyable. Furthermore, I would like to thank him for the collaboration in the project on magnetotransport in disordered graphene (chapter 8).

Belonging to a community of nice fellow students and postdocs has greatly enhanced my life at the university. The exchange of ideas and experiences in research and other matters were invaluable. I would like to especially thank Jean-Christoph Denis, Matthew Edmonds, Peter & Natalia McDonald, Sebastian Gattenlöhner, Stefan Schumacher, and Frank Zimmer (titles omitted) for the entertaining and motivating discussions. Mastering my studies would also have been difficult if I had not shared an office with friendly colleagues, who created a wonderful atmosphere. My deepest thanks go to Ashleigh Barron, Rose Mary, Peter Kremer, Sebastian Gattenlöhner, and Richard Carter.

I am grateful to Prof Ian Galbraith for his motivation and for assisting me in many matters. I would also like to thank every academic staff of the institute, who assisted me in one way or another, and who contributed in organizing seminars and other events.

Among the other people I got to know at the university, I am particularly grateful to Steve King and the entire Heriot-Watt orchestra. Being part of this orchestra

was fantastic and has provided lots of motivation for my studies.

The financial support from the Scottish Universities Physics Alliance (SUPA) is gratefully acknowledged. I am also thankful for the opportunity to attend graduate school courses offered by SUPA.

Finally, I would like to thank my mother Heike and my sisters Ulrike and Sigrun for all the support that I received from them. Without this support I would not have been able to live and study abroad for several years. It was very nice to have been welcomed at home many times.

Contents

1 Introduction **1**

2 Graphene and Quantum Hall Effect Basics **11**

2.1 Electronic Properties of Monolayer Graphene 11

2.1.1 Crystal structure and tight-binding model 11

2.1.2 2D massless Dirac equation in graphene 15

2.1.3 Berry phase, chirality, and Klein tunneling 17

2.1.4 Plane wave eigenstates, velocity operator, and current density 18

2.1.5 Magnetic field and Landau quantization 19

2.2 Electronic Properties of Bilayer and Multilayer Graphene 21

2.2.1 Bilayer graphene 22

2.2.2 Multilayer graphene 25

2.3 (Half-) Integer Quantum Hall Effect and Quantum Hall Phase Transition 27

2.3.1 Unconventional quantum Hall effect 27

2.3.2 Quantum Hall phase transition 28

3 Scattering Theory, Full Counting Statistics, and Green's Function Formalism **31**

3.1 Introduction 31

3.2 Scattering Matrix and Transfer Matrix 32

3.3 Transport Properties in Zero-Bias Limit 35

3.4 Full Counting Statistics 36

3.4.1 Full counting statistics in general terms 36

3.4.2 Application to mesoscopic transport 38

3.5 Application to Two-Terminal Graphene Device 39

3.5.1 Model of two-terminal graphene device 40

3.5.2 Wave function matching in graphene 43

3.5.3 Transfer matrix method 45

3.5.4 Relation between evolution matrix and transfer matrix . . . 46

3.5.5 Ballistic transport properties of monolayer graphene 47

3.6 Fischer-Lee Relation and Kubo Formula 51

3.7 Matrix Green's Function Formalism 54

4 Ballistic Transport in Chiral Symmetric Few-Layer Graphene **57**

4.1 Model 58

4.2 Method 60

4.3 Transport in Undoped Few-layer Graphene 61

4.4 Gate-voltage Dependence of Transport Properties 64
4.5 Summary and Discussion 69

5 Generalized Transformations for Graphene Devices in Rectangular and Corbino Geometry 71
5.1 Bare Green's Function in Rectangular Geometry 72
5.2 Eigenstates and Bare Green's Function in Isotropic Potential 75
5.2.1 Green's functions in Corbino geometry 76
5.3 Conformal Mapping Transformation 78
5.4 Non-Unitary Gauge Transformation of Vector Potential 80
5.4.1 Rectangular geometry 80
5.4.2 Corbino geometry 81
5.5 Applications of the Conformal Mapping 82
5.5.1 Kubo formula in Corbino geometry 82
5.5.2 Ballistic conductance of Corbino device 83
5.6 Green's Functions in Real Space 85
5.6.1 Rectangular setup with large aspect ratio 86
5.6.2 Corbino geometry with small central lead 87
5.7 Matrix Green's Function and Transmission Distribution 88
5.7.1 Conformal mapping 89
5.7.2 Matrix Green's function without source field transformations 89
5.7.3 Transmission distribution of short and wide rectangular device 91
5.8 Transformations of the Counting Field 92
5.8.1 Transformation in Keldysh space 92
5.8.2 Zero-energy transformations 93
5.8.3 Summary 96

6 Contact Potential and Effect on Ballistic Transport Properties 97
6.1 Introduction 97
6.2 Charge and Potential Profiles 100
6.2.1 Model 100
6.2.2 Self-consistent Hartree approximation 103
6.2.3 Thomas-Fermi approximation 104
6.2.4 Self-consistent solutions 104
6.3 Transport Properties 106
6.4 Conclusions 110

7 Unfolded Scattering Approach for Point-like Impurities 111
7.1 Solution of the Dyson Equation 111
7.2 T-Matrix of Scalar Impurities in Undoped Graphene 114
7.3 Impurity Correction to the Cumulant Generating Function 116

8 Magnetoconductance of Undoped Graphene with Point-like Impurities **117**
8.1 Transformation of Full Green's Function 118
8.2 Full Counting Statistics of Charge Transport 120
8.2.1 Disorder correction through unfolded scattering approach . . 121
8.2.2 Transport properties for scalar impurities in a magnetic field 122
8.3 Conductance and LDoS of a Sample with One and Two Impurities . 124
8.3.1 Single scalar impurity 126
8.3.2 Two scalar impurities 129
8.4 Conductivity for Many Scalar Impurities in Magnetic Field 130
8.4.1 Overview of results 131
8.4.2 Interpretation of the Quantum Hall regime 133
8.4.3 Interpretation of the level condensation regime 136
8.5 Summary and Discussion 138

9 Summary **141**

List of References **145**

Chapter 1 – Introduction

Hexagonal layers of carbon atoms are the building blocks of graphite and as such have been studied already more than 60 years ago. Since the layer spacing of 3.37Å in graphite is large compared with the carbon-carbon distance of 1.42Å within a layer, a starting approximation for the electronic properties of graphite can be obtained from the tight-binding model of a single layer, which was studied by Wallace [1] in 1947 in the nearest-neighbour hopping approximation. He calculated the unusual π-band structure, where the conduction band and the valence band touch each other at the six corners of the hexagonal Brillouin zone, so that the Fermi surface of undoped layers is point-like. In a single layer the dispersion of low-energy excitations is linear instead of parabolic as in usual metals. Later McClure [2] and Slonczewski and Weiss [3] developed a more rigorous tight-binding model of graphite, and thereby also laid the foundation for the low-energy effective theory of a single layer. In 1984 DiVincenzo and Mele [4] and Semenoff [5] identified the low-energy excitations as massless Dirac fermions. In this description the electrons have a pseudospin corresponding to the sublattice degree of freedom, and an effective speed of light given by the Fermi velocity of $\sim 10^6$m/s [6].

Since then it was clear that single layers of crystalline carbon provide a condensed-matter realization of 2+1-dimensional quantum electrodynamics (QED), which attracted a lot of theoretical interest. However, the attempts to directly investigate the electronic properties of single layers were not successful at this time. This is somewhat surprising, as single layers of carbon had been observed already in 1962 by chemist Boehm and coworkers using reduction of graphite oxide [7]. Boehm also introduced the name 'graphene' for single layers in 1994 [8]. In the 1980s and 1990s the single layers were discussed mainly in the context of graphite intercalation compounds, in which the carbon layers are separated by layers of intervening atoms or molecules [9]. The newly discovered carbon allotropes, namely fullerenes and carbon nanotubes, which can be viewed as derivatives of graphene, also attracted a lot of interest. As a consequence, graphene became one of the best studied materials in the world.

The experimental breakthrough happened in 2004, when Novoselov and coworkers [10] succeeded to isolate few-layer graphite films by means of micromechanical cleavage of graphite, a method which became known as the 'Scotch-tape' method. This study is considered groundbreaking, because the atomic films were electrically contacted and the electric field effect was demonstrated. The electric field effect in single graphene layers was demonstrated shortly afterwards by the same group in Manchester [10]. In 2005 transport experiments proved that theoretical expectations are correct as Dirac fermions in graphene really exist [11, 6]. The discovery

of the anomalous integer quantum Hall effect in the same studies further boosted the tremendous interest in this new material, which was expected to hold many more surprises in the field of quantum transport, due to its unusual band structure. As a consequence, strong efforts in the condensed-matter community have been undertaken since 2005 to better understand the electronic properties of this new material. Although the 'Scotch-tape' method did not seem to be feasible for electronic applications, it was sufficient to carry out fundamental research on the material properties. Other production techniques, in particular epitaxial growth of graphene on silicon carbide, were developed simultaneously with first successful experiments in 2004 [12].

The tremendous interest in graphene is also driven by its huge potential for device applications which are not feasible in silicon-based electronics. In view of electronic applications, graphene has several key advantages over conventional two-dimensional electron gases (2DEGs) in semiconductor systems such as heterostructures, quantum wells, and inversion layers. The electric field effect, allowing the control of the carrier density by an applied gate voltage, is one important feature of this material, resulting from its atomic thickness. Since graphene does not need to be sandwiched between other materials, the entire sample area can be accessible for measurements or manipulations e.g. through scanning tunneling tips. It is also easily possible to pattern mesoscopic structures using nanolithography (standard or STM). Another key feature of graphene is its extraordinarily high crystal quality, which results in extremely high mobilities of charge carriers even in graphene on SiO_2 substrates. However, due to its atomic thickness, graphene is essentially unprotected from the environment [13]. Thus higher mobilities are achieved in freely suspended samples, with values above 200 000 cm^2/Vs [14, 15], and in graphene sandwiched between two hexagonal boron-nitride crystals, where values 500 000 cm^2/Vs have been reported [16]. The corresponding mean free paths of electrons are in the micron range, and therefore the ballistic transport regime can be approached in graphene devices [15, 14]. However, in most transport experiments electron scattering at some sort of disorder plays an important role. The presence of impurities can even be desired in graphene due to a large potential of chemical functionalization.

Before turning to disorder, which strongly complicates the theory of electronic transport in graphene, I mention some of the remarkable electronic properties of ideal graphene, making this material so distinct from other 2D semiconductor systems. In charge-neutral graphene the Fermi energy lies exactly at the degeneracy points of conduction and valence band, known as the Dirac points. Since the density of states (DoS) at this energy vanishes, graphene should be considered as a semimetal with zero band overlap. A characteristic of graphene is the interconnection between electron and hole states, which are both described by the same

two-dimensional (2D) Dirac equation. This is analogous to the charge-conjugation symmetry in QED [17] and leads to properties which were previously known only in high-energy physics. Examples are the chiral nature of the 2D quasiparticles and their non-zero Berry phase [18]. Due to these exotic properties, quantum transport in graphene is very distinct from that in other 2DEGs. For instance, Dirac fermions do not show any backscattering at potential barriers [19], which is known as the phenomenon of Klein tunneling in graphene [17, 20]. Another consequence of the Berry phase π of quasiparticles is a topological singularity at the Dirac point [21], where the DoS vanishes linearly.

This topological singularity is at the origin of various zero-mode anomalies [22], some of which are discussed in the following. Despite the vanishing DoS at the energy of the Dirac points, the ballistic conductivity has a finite minimum as a function of carrier density. It is thus neither zero as in a band gap of an ordinary semiconductor nor infinite as for a disorder-free metal at finite carrier density. Moreover, the minimal conductivity is predicted to assume the universal value $4e^2/\pi h$ in the limit of a large sample aspect ratio of width over length. This result was obtained from the scattering approach to quantum transport in refs. [23, 24] and agrees with the result obtained from linear response theory for an infinite graphene sheet by taking the limit of zero disorder [25, 26]. The finite conductivity is facilitated by purely evanescent modes with wavefunctions decaying across the sample, so that quasiparticles tunnel from one contact to an opposite contact. Another quantum anomaly at the Dirac point is the Landau level [27], which is located at this energy independently of the magnetic field strength. This results in an unusual integer quantum Hall effect, where the Hall conductivity is quantized in half-integer multiples of the conductance quantum [11, 6].

Some experiments in the near-ballistic regime confirmed the theoretical value $4e^2/\pi h$ of the minimal conductivity [28, 29, 14, 30], but the topic is controversial. For example, the conductivity could have been underestimated, if the contact resistance had played a role [31] in these two-probe measurements. In general, the minimal value of the conductivity of graphene has been the subject of a lot of controversial studies. This is known as the problem of the missing pi, because the typical minimal conductivity observed at the supposed charge-neutrality point in gated graphene devices is approximately $4e^2/h$ instead of the theoretically predicted value $4e^2/\pi h$. It was pointed out recently [32] that a reason for the discrepancy may be an inappropriate limiting procedure in the calculation of the dc conductivity. Other possible reasons are the presence of short-range scatterers creating midgap states and thereby enhancing the conductivity [33, 34], contact-induced charge inhomogeneity in two-probe measurements [31], or the presence of electron-hole puddles near the charge-neutrality point, which have been studied theoretically by means of a random resistor network model [35].

In this work I study the ballistic transport properties of a variety of clean graphene devices, thereby concentrating on their dependence on externally applied gate voltage and magnetic field and on the number of layers in a few-layer graphene stack. After this part I analyze the transport in undoped graphene with certain types of disorder. Disorder generally plays an important role in the experimentally observed gate voltage dependence of the conductivity. Typically the conductivity is approximately linearly dependent on the carrier concentration n, which is a strong deviation from the dependence $\sim n^{1/2}$ expected for a clean graphene sample. The origin is the presence of disorder limiting the mobility of charge carriers. However, despite the large number of transport experiments carried out with graphene in the last decade, and intensive theoretical studies on disordered graphene (see, for example, refs. [36, 37, 38, 39, 26, 40] and references therein), it is not yet fully understood which type of disorder is limiting the mobility of charge carriers in various graphene devices. One reason for the complexity of the disorder problem is simply the 2D lattice structure of monolayer samples, which gives rise to a variety of defects with characteristic effects on the charge transport. In the following I will briefly discuss the most important types of disorder.

As mentioned above, graphene exhibits an extraordinarily high crystal quality. However, since monolayer graphene is a strictly 2D crystal, it is extremely flexible and prone to out-of-plane deformations. In fact, so-called ripples, microscopic corrugations of the graphene sheet, are an inherent feature of graphene. Ripples occur not only due to substrate roughness but also in freely suspended graphene, where the out-of-plane deformations are of the order of 1nm [41] and can create a long-range scattering potential [42]. Furthermore, ripples can create random strain fields, which is another type of long-range disorder. Ripples are generally much weaker in bilayer graphene.

Another common source of disorder are charged impurities, which, for instance, can be trapped between the graphene sheet and the substrate. These have been considered for some time as the dominant source of electron scattering in graphene. Their effect on charge carrier transport has been studied theoretically e.g. in refs. [36, 43, 40]. The long-range Coulomb fields of charged impurities are certainly important in weakly doped graphene, which has very low screening capabilities. These impurities are also made responsible for the often observed electron-hole puddles [44] at the charge neutrality point. In recent years charged impurities are not considered anymore the limiting mechanism for carrier mobility, but the topic remains controversial (see ref. [45]).

So far I discussed disorder which is smooth on the scale of the lattice constant. However, defects on the scale of the lattice constant may play an important role in graphene transport. Such defects can occur in the honeycomb lattice itself or as external impurities. For example, short-range potentials may be created by

charged impurities very close to the graphene sheet. Examples for defects localized at a single lattice site are strongly bound adsorbates or vacancies (missing carbon atoms at lattice sites), which create so-called midgap states [46], i.e. a peak in the density of states at the Dirac energy, where the density of states vanishes in clean graphene. The effect of such impurities has been studied theoretically in refs. [26, 39, 47, 48, 49, 50, 51] and is now considered as a major source of electron scattering in graphene [45]. Neutral impurities (ad-atoms), which do not create midgap states, give rise to short-range scattering only and are not considered very relevant in typical devices. At higher temperatures phonon scattering may be an important contribution.

Another interesting and not yet fully understood topic is the effect of quantum interference on the electronic transport through weakly doped graphene with some amount of disorder. In principle one would expect quantum interference to be a dominant feature since the Fermi wavelength at the Dirac point diverges and is thus much larger than the electron mean free path [52]. However, even though the experimentally observed minimal conductivity is of the order of the conductance quantum only, it shows a surprisingly weak dependence on temperature in a large range from 300K down to $\sim$ 1K [53]. In particular, no metal-insulator transition due to Anderson localization has been observed for a long time. Only recently Anderson localization was probably observed in double-layer graphene heterostructure, where a control layer is used to screen out the electron-hole puddles in the studied layer [52]. Another interesting feature is that the weak localization correction may be positive or negative depending on the interaction range of impurity potentials. For long-range impurities the suppression of backscattering due to the Berry phase π leads to weak antilocalization [54]. On the other hand, weak localization may result from inter-valley scattering, which is due to the trigonal warping of the band structure (next-nearest neighbour hopping) or the presence of defects on the scale of the lattice constant [38].

The graphene-based electronic systems studied in this work consist of graphene monolayers or naturally stacked few-layers, which may be viewed as extremely thin films of graphite. These materials are referred to as bilayer and multilayer graphene and constitute a whole family of 2DEG systems with chiral charge carriers. Their individual electronic properties are strongly dependent on the stacking order which leads to a whole set of behaviours [55]. A notable example is the integer quantum Hall effect, which manifests itself in many different forms, and was observed so far in bilayer graphene [56]. Bilayer and few-layer graphenes have also a large potential for new electronic applications. As in monolayers, the low-energy excitations belong to one of two Dirac cones in the band structure. This so-called valley degree of freedom may be used for applications in an analogous way as the real electron spin in spintronics [34]. A device for generating a valley polarized current in the

bulk of bilayer graphene has been proposed recently [57]. A feature lacking in monolayer graphene but present in bilayer graphene is the opening of a gap between the valence and conduction band upon applying an external electric field [58]. This gate-induced insulating state has been confirmed experimentally [59] and makes bilayer graphene a suitable candidate for building field-effect transistors and similar electronic devices.

In this work the graphene samples are generally described in the effective-mass continuum approximation and the electronic transport is studied as a single-electron problem, so that many-body effects are disregarded. Electron-electron interactions are either neglected or included in the mean field approximation. The most suitable approach for this transport regime is the scattering approach due to Landauer and Büttiker [60, 61]. This approach is used throughout this work and complemented by supplementary methods such as the transfer matrix method in the study of clean samples and the unfolded scattering approach [48, 50] in the study of disordered samples. Although I make extensive use of Green's functions, I do not employ the linear response theory (however, a Kubo formula derived from the Landauer approach is used) or the so-called non-equilibrium Green's function approach. The study of clean samples includes both phase-coherent and incoherent ballistic transport. In general I consider the limit of zero temperature and bias voltage.

The studied two-terminal device geometries are rectangular samples with periodic boundary conditions, also referred to as the cylinder geometry, and the Corbino disk geometry, in which the current flows radially from an inner to an outer lead. Examples of varied parameters are the externally induced charge density, the external magnetic field, and the number of layers. It turns out that in charge-neutral graphene both the external magnetic field as well as the inter-layer coupling can be treated by means of non-unitary gauge transformations. This is a consequence of the chiral symmetry, which exists at the band center in the half-filled graphene lattice. This discrete symmetry is not exactly fulfilled in more sophisticated models and might be difficult to preserve in a typical electronic transport device (due to the metallic contacts). However, exploring the consequences of this symmetry provides much insight into the electronic behaviour of intrinsic graphene. In more detail, for undoped samples I derive the following gauge invariances and mappings relying on the chiral symmetry:

(i) In a clean mono- or multi-layer sample, an arbitrary spatially dependent magnetic field can be mapped to a magnetic flux piercing the cylinder (or the central lead in the Corbino geometry). This flux induces a change of boundary conditions in the transverse direction (so that the quantized transverse momentum is shifted). A gauge invariance exists for a short and wide sample (large aspect ratio), since in this case the momentum shift is irrelevant. The corresponding transformation has been first employed in ref. [62] for a monolayer sample with simply connected

boundaries.

(ii) The same transformation is useful in the case of an undoped monolayer sample with point-like impurities. In this case the T-matrices of the impurities are affected so that their scattering properties change. However, if the impurities preserve the chiral symmetry, then they are unaffected, which leads to another gauge invariance.

(iii) The interlayer hopping (in a clean multilayer), which may be spatially dependent, can be gauged away in the same way as the magnetic field. Thus any multilayer can be mapped to independent monolayers with various magnetic fluxes piercing the cylinders. This means that a short and wide multilayer sample has just the same universal transport characteristics as the same number of isolated monolayers in parallel, corresponding to the pseudodiffusive transport regime. So far this was known for bilayer graphene [63], but the origin of the universality was not yet fully understood.

(iv) A conformal transformation is employed to map the rectangular geometry to the Corbino geometry. This transformation is also useful for a sample with point-like disorder as long as the sample is undoped. Such a transformation has been first employed in the study of ballistic transport in ref. [64].

Other parts of this thesis are concerned with graphene systems without chiral symmetry. The gate voltage dependence, which is generally an important feature, is evaluated for clean multilayer samples in the absence of magnetic field. I show that the transport properties are non-universal, reflecting the various stacking types of multilayers and the corresponding band structures. The chiral symmetry may also be broken by the boundary conditions at the sample-lead interfaces. In particular, it is absent for weakly doped graphene leads, in which case the transport properties become electron-hole asymmetric. This asymmetry is shown to be strongly enhanced if a realistic contact potential is used, which decays into the sample due to the weak screening in graphene. Magnetotransport through a sample with scalar impurities of finite scattering length, which violate the chiral symmetry, makes the final part of this thesis as described in more detail below.

This thesis is structured as follows.

In **chapter 2** I derive the elementary electronic properties of graphene. Starting from the nearest-neighbour tight binding model, I derive the low-energy effective theory, in which the quasiparticles are described by the 2D massless Dirac equation. The resulting properties such as Berry phase π and chirality are briefly discussed. The corresponding effective theory is derived for bilayer and few-layer graphene. The Landau quantization and quantum Hall effect in monolayer and bilayer graphene are briefly discussed. I also discuss the quantum Hall phase transition, which occurs when the external magnetic field (or gate voltage) is changed such that the Hall conductivity changes from one quantized value to the next. This

is a delocalization transition in a disordered system.

Chapter 3 (along with chapter 7) provides the theoretical methods used to calculate transport properties in this work. It starts with a short review of the Landauer-Büttiker scattering approach to electronic transport in mesoscopic systems. This approach provides the framework for all transport studies in this thesis. All transport properties, such as conductance, noise, and higher moments, are related to the transmission eigenvalues of the scattering device. I also introduce the transfer matrix method, which is a practical alternative to the derivation of scattering amplitudes by means of mode matching. Another section of this chapter deals with the full counting statistics of charge transport, which allows to encode all moments of the transmission distribution in a single so-called cumulant generating function. Then I go on to apply the approach to a two-terminal graphene device, thereby providing a conceptual basis for the transport studies in the subsequent chapters. Using the model of heavily doped graphene leads, the known ballistic transport properties of a rectangular monolayer sample are derived. The remainder of the chapter still relies on the scattering approach, but translates it into the language of Green's functions. Retarded and advanced Green's functions are far more easily calculated for a disordered sample than the transfer matrix. By deriving graphene versions of the Fisher-Lee relations known from conventional semiconductors, I write any moment of the transmission distribution in terms of Green's functions. The conductance formula is equivalent to the Kubo formula known from linear response theory. Another useful tool provided in this chapter is the multi-component Green's function, which allows one to express the cumulant generating function of the transmission distribution in terms of Green's functions as well.

The ballistic transport properties of chiral symmetric few-layer graphenes are studied by means of a transfer matrix approach in **chapter 4**. For undoped systems I use a non-unitary gauge transformation to show the equivalence of transport with that in uncoupled monolayers as discussed above. This includes the presence of arbitrary magnetic and strain fields. I then proceed with transport calculations for doped few-layer stacks, in which the stacking configuration is shown to be crucial for the transport properties, which also feature prominent Fabry-Perot like oscillations in the coherent transport regime. An averaging over theses oscillations is performed by treating the device as two contacts in series, and treating the phase accumulated by quasiparticles in the sample as random. I further show that a mapping of Bernal-stacked multilayers to effective bilayers (and one monolayer for odd number of layers) derived by Koshino and Ando [65] is applicable within the model of heavily doped leads.

Several generalized transformations, which lay the foundation for the transport calculations in disordered graphene, are discussed for a clean undoped graphene

sample in **chapter 5**. The first one is the conformal transformation between the rectangular and the Corbino geometry, which was mentioned above. I also derive explicit expressions for the gauge transformation accounting for the presence of a constant magnetic field, both in the rectangular and the Corbino geometry. The conformal mapping and the gauge transformation for the vector potential are used to evaluate the Green's functions, the Kubo formula, and the ballistic conductance in the Corbino geometry with constant magnetic field. The chapter is concluded with a decomposition of the multi-component Green's function in the external counting field. This is achieved by means of generalized transformations, which show that in undoped graphene with periodic boundary conditions the counting field, which conventionally acts at the sample-lead interfaces, may be equivalently introduced as a flux through the cylinder (in the rectangular geometry) or through the central lead (in the Corbino geometry). This is another manifestation of the chiral symmetry in intrinsic graphene, and will prove extremely valuable in the evaluation of the transport properties of graphene with point-like impurities, even if the disorder breaks the chiral symmetry.

In **chapter 6** I refine the simplistic model of a two-terminal graphene device, in an attempt to explain the electron-hole asymmetric features that are typically observed in measurements in the ultra-ballistic transport regime. Instead of modeling the leads as heavily doped graphene with abrupt potential steps at the interfaces with the sample, I develop a more realistic model taking into account the charge transfer at the interfaces in a self-consistent manner. Potential profiles are calculated numerically using two methods, namely the self-consistent Hartree approximation and the Thomas-Fermi approximation. Due to the weak screening in graphene, the potential penetrates deeply into the sample, which results in an asymmetric gate voltage dependence of conductance and noise. The same mechanism explains the strongly enhanced Fabry-Perot oscillations observed experimentally on one side of the conductance minimum.

A recently developed method to study electronic transport in a sample with short-range scatterers is discussed in **chapter 7**. This so-called unfolded scattering approach is non-perturbative in the impurity potential and becomes particularly handy in the case of non-overlapping point-like impurities, i.e. in the limit of s-wave scattering. The approach may be used to calculate the retarded and advanced Green's functions and evaluate the Kubo formula, or to directly evaluate the impurity correction to the full counting statistics. The impurities enter only through their positions and their T-matrices, describing their individual scattering properties in an infinite system. I briefly discuss the case of scalar impurity, which are described by a scalar potential in the 2D Dirac equation, and for which the T-matrix is simply proportional to the impurity scattering length.

Using the unfolded scattering approach along with the transformations devel-

oped in chapter 5, I address in **chapter 8** the full counting statistics of an undoped graphene sample with point-like impurities in the presence of a perpendicular magnetic field. In particular, the conductance is studied for scalar impurities. I start with the case of one and two impurities, where the conductance is typically enhanced due to impurity-assisted tunneling. A better interpretation of the results is facilitated by evaluating the local density of states. Then I turn to the case of many randomly placed impurities, where the conductivity, averaged over many configurations, has an interesting dependence on the magnetic field strength. From the regime of negligible field strength, I discuss a crossover to the quantum Hall regime. In this regime the longitudinal conductivity crucially depends on the distribution of the impurity scattering lengths, which determines whether the energy of the Dirac point lies at a quantum Hall phase transition or in the quantum Hall plateau region. In particular, if all impurities have a positive scattering length, they shift the quantum Hall phase transition away from the Dirac point - note that the $n = 0$ Landau level is generally located at the Dirac point in a clean sample. On the other hand, if the mean value of impurity scattering lengths is chosen to be zero, one can study the longitudinal conductivity exactly at the quantum Hall phase transition. In the past two decades numerical studies for a variety of systems have substantiated that this conductivity value, averaged over impurity configurations, is universal and of the order of 0.6 times the conductance quantum. It is possible that by gathering more numerical data, this conductivity value can be confirmed in the present model of graphene with scalar impurities. As briefly mentioned above, I reveal another crossover at higher field strength, where the conductivity and all higher moments of charge transfer return to their ballistic values without any fluctuations, hence they are unaffected by the impurities. This strong-field regime is explained by the level condensation of the $n = 0$ Landau level at the energy of the Dirac point. Finally, I discuss the possible extensions of the project, and compare the results with other disorder types studied recently be means of the same approach.

I conclude the thesis in **chapter 9** by summarizing the main results and pointing out possible future research directions.

Chapter 2 – Graphene and Quantum Hall Effect Basics

This chapter contains a brief review of the elementary electronic properties of graphene. In section 2.1 I discuss and solve the nearest neighbour tight-binding model of monolayer graphene, following refs. [66, 20, 67]. The peculiar band structure features a point-like Fermi surface at the charge neutrality point. I further review the low-energy effective theory in which the quasiparticles are massless and obey a Dirac-like equation analogous to the one known from quantum electrodynamics. From this description many peculiar properties follow, such as a non-zero Berry's phase, chirality, and, in the presence of an external magnetic field, an unusual Landau level spectrum, which leads to a distinctive half-integer quantum Hall effect. Most of the basic physics of graphene has been known for decades. Due to the strong experimental efforts in recent years, many of the peculiar properties of the Dirac fermions in graphene have been confirmed experimentally.

The low-energy effective theory of graphene will be used exclusively in this dissertation. This theory can be extended to graphene stacks, in which the electronic motion is still genuinely 2D. Multilayer graphene occurs in many variations due to the manifold stacking configurations. The effective theory and the band structure of bilayer and few-layer graphene with staggered stacking configurations are discussed in section 2.2. In the simplistic tight-binding model the multilayers are gapless semiconductors just as monolayer graphene.

In section 2.3 the unconventional (half-) integer quantum Hall effect occurring in monolayer and bilayer graphene is reviewed. I also discuss the quantum Hall phase transition, which takes place in any 2D electron gas at strong magnetic field strength, when the quantized Hall conductivity jumps from one value to the next as the field strength or the gate voltage is varied. This phase transition is described as a delocalization transition in a disordered system. The predictions for the critical behaviour of the conductivity components are summarized.

2.1 Electronic Properties of Monolayer Graphene

2.1.1 Crystal structure and tight-binding model

In graphene the carbon atoms are arranged on a 2D honeycomb lattice as shown in figure 2.1 (a). Covalent σ-bonds between the neighbouring atoms, separated by $a_0 \approx 1.42$Å, result from the sp^2 hybridization between one $2s$-orbital and the $2p_x$- and $2p_y$-orbitals. These bonds are responsible for the extraordinary robustness of graphene. Each atom has one remaining $2p_z$-orbital which is centered on the atom and oriented perpendicular to the molecular plane. The hybridization of these orbitals leads to a π-band with strong tight-binding character. Since each $2p_z$-orbital

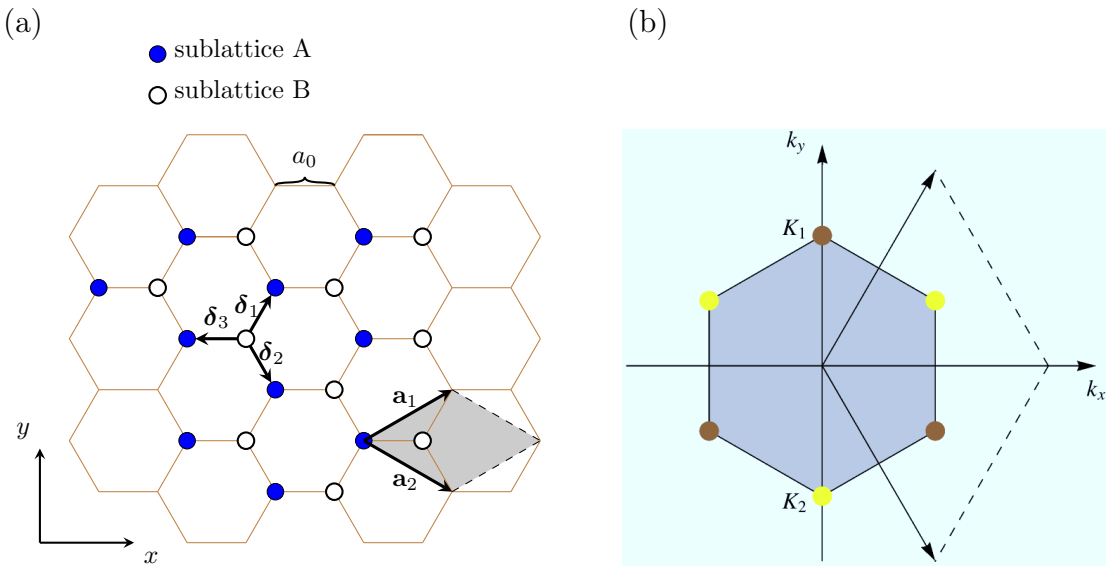

Figure 2.1: (a) Lattice structure of graphene. Indicated are the nearest-neigbhour distance and vectors, and the lattice vectors. (b) Brillouin zone in reciprocal space showing the two inequivalent corner points and the reciprocal lattice vectors.

contains one electron, the π-band is exactly half filled and determines the electronic properties of graphene. In the nearest-neighbour tight-binding approximation the electronic transport is due to the hopping of π-electrons from the $2p_z$-orbital of a carbon atom to one of its three neighbouring atoms.

The hexagonal lattice is a superposition of two triangular sublattices, labeled A and B in figure 2.1 (a). This means that the unit cell of the Bravais lattice is triangular and contains two atoms. Each atom of sublattice A has three nearest neighbours belonging to sublattice B, and vice versa. The length of the unit cell vectors is $a = \sqrt{3}a_0$. In the simplest model, valid for low energies, only nearest-neighbour hopping is considered, and the tight-binding Hamiltonian takes the form

$$\hat{H} = -t \sum_{\sigma} \sum_{<i,j>} \hat{a}^{\dagger}_{i\sigma} \hat{b}_{j\sigma} + \text{h.c.}, \tag{2.1}$$

where here and in the following h.c. stands for Hermitian conjugate. The operator $\hat{a}^{\dagger}_{i\sigma}$ creates an electron with spin σ on lattice point i belonging to sublattice A ($\hat{b}^{\dagger}_{j\sigma}$ is defined equivalently). $< i, j >$ denote nearest neighbour site indices. As the spin index is conserved, it is emitted in the following.

The bilinear Hamiltonian $\hat{H}$ from equation (2.1) can be easily solved exactly. I define the lattice vectors as shown in figure 2.1 (a),

$$\mathbf{a}_1 = \frac{a}{2} \begin{pmatrix} \sqrt{3} \\ 1 \end{pmatrix}, \quad \mathbf{a}_2 = \frac{a}{2} \begin{pmatrix} \sqrt{3} \\ -1 \end{pmatrix}. \tag{2.2}$$

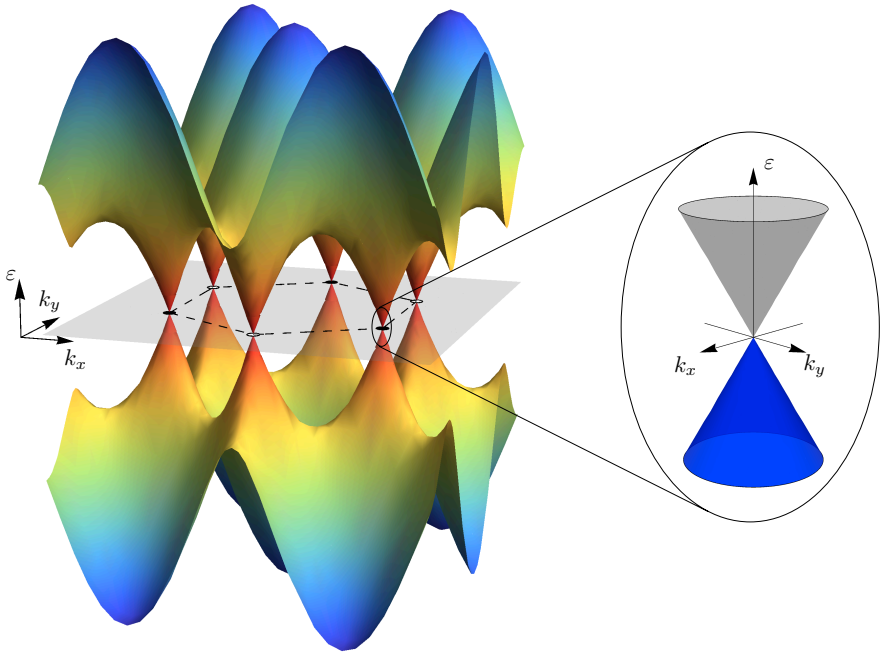

Figure 2.2: Electronic band structure [equation (2.8)] of graphene in nearest-neighbour tight-binding approximation. The dashed line shows the first Brillouin zone. The zoom shows a single Dirac cone with the Fermi energy at the Dirac point as for undoped graphene.

The three nearest-neigbhour vectors are given by

$$\boldsymbol{\delta}_1 = \frac{a}{2}\begin{pmatrix} 1/\sqrt{3} \\ 1 \end{pmatrix}, \quad \boldsymbol{\delta}_2 = \frac{a}{2}\begin{pmatrix} 1/\sqrt{3} \\ -1 \end{pmatrix}, \quad \boldsymbol{\delta}_3 = \frac{a}{2}\begin{pmatrix} -2/\sqrt{3} \\ 0 \end{pmatrix}, \tag{2.3}$$

and can be used to write the Hamiltonian (2.1) as

$$\hat{H} = -t \sum_{\boldsymbol{R}} \sum_{\alpha=1}^{3} \hat{a}^\dagger_{\boldsymbol{R}+\boldsymbol{\delta}_\alpha} \hat{b}_{\boldsymbol{R}} + \text{h.c.} \tag{2.4}$$

By Fourier transforming the operators,

$$\hat{a}_{\boldsymbol{R}} = \frac{1}{\sqrt{N}} \sum_{\boldsymbol{k}} e^{-i\boldsymbol{k}\boldsymbol{R}} \hat{a}_{\boldsymbol{k}} \tag{2.5a}$$

$$\hat{b}_{\boldsymbol{R}} = \frac{1}{\sqrt{N}} \sum_{\boldsymbol{k}'} e^{-i\boldsymbol{k}'\boldsymbol{R}} \hat{b}_{\boldsymbol{k}'}, \tag{2.5b}$$

and using $\frac{1}{N}\sum_{\boldsymbol{R}} e^{i(\boldsymbol{k}-\boldsymbol{k}')\boldsymbol{R}} = \delta_{\boldsymbol{k},\boldsymbol{k}'}$, one finds

$$\hat{H} = -t \sum_{\alpha=1}^{3} \sum_{\boldsymbol{k}} e^{i\boldsymbol{k}\boldsymbol{\delta}_\alpha} \hat{a}^\dagger_{\boldsymbol{k}} \hat{b}_{\boldsymbol{k}} + \text{h.c.} \tag{2.6}$$

Using vectors in sublattice space, this can be rewritten as [68]

$$\hat{H} = \sum_{\boldsymbol{k}} \hat{\Psi}_{\boldsymbol{k}}^{\dagger} \hat{\mathcal{H}}_{\boldsymbol{k}} \hat{\Psi}_{\boldsymbol{k}}, \quad \hat{\Psi}_{\boldsymbol{k}} = \begin{pmatrix} \hat{a}_{\boldsymbol{k}} \\ \hat{b}_{\boldsymbol{k}} \end{pmatrix}, \quad \hat{\mathcal{H}}_{\boldsymbol{k}} = \begin{pmatrix} 0 & -ts_{\boldsymbol{k}} \\ -ts_{\boldsymbol{k}}^{*} & 0 \end{pmatrix}, \quad s_{\boldsymbol{k}} = \sum_{\alpha=1}^{3} e^{i\boldsymbol{k}\boldsymbol{\delta}_{\alpha}}. \tag{2.7}$$

The eigenvalues of $\mathcal{H}_{\boldsymbol{k}}$ are given by

$$\varepsilon_1(\boldsymbol{k}) = \pm t|s_{\boldsymbol{k}}| = \pm t\sqrt{3 + 2\cos(ak_y) + 4\cos\left(\frac{\sqrt{3}}{2}ak_x\right)\cos\left(\frac{1}{2}ak_y\right)}, \tag{2.8}$$

where the positive and negative solution correspond to the conduction band and the valence band, respectively. This dispersion relation is shown in figure 2.2. The two bands touch each other at zero energy at the six corner points, called Dirac points or K points, of the Brillouin zone, which is also shown in figure 2.1 (b). Since in neutral graphene the π-band is half-filled, the Fermi energy lies exactly at the energy $\varepsilon_{\boldsymbol{K}} = 0$ of the Dirac points. There are exactly two inequivalent K points which I choose at wave vectors

$$\boldsymbol{K}_1 = \frac{4\pi}{3a}\begin{pmatrix} 0 \\ 1 \end{pmatrix}, \quad \boldsymbol{K}_2 = \frac{4\pi}{3a}\begin{pmatrix} 0 \\ -1 \end{pmatrix}, \tag{2.9}$$

and to which all other Dirac points are related by reciprocal lattice vectors. Expanding $\varepsilon_1(\boldsymbol{k})$ around one of the K points one obtains the conical dispersion

$$\varepsilon \approx \pm\hbar v_{\mathrm{F}} |\boldsymbol{\kappa}|, \quad v_{\mathrm{F}} = \frac{\sqrt{3}ta}{2\hbar}, \quad \boldsymbol{\kappa} \equiv \boldsymbol{k} - \boldsymbol{K}, \qquad \text{for } |\varepsilon| \ll t. \tag{2.10}$$

This dispersion relation means that the low-energy quasiparticles move with an energy-independent group velocity $\partial\varepsilon/\hbar\partial\boldsymbol{\kappa} = v_{\mathrm{F}}$ in the same way as massless relativistic particles. From the hopping energy $t \approx 2.7\mathrm{eV}$ the Fermi velocity follows as $v_{\mathrm{F}} \lesssim 10^6\mathrm{m/s}$, which is about 300 times smaller than the speed of light. Therefore genuine relativistic effects in graphene are negligible as expected for a condensed-matter system. Nevertheless, the conical dispersion leads to the emergence of many analogous effects known from relativistic quantum mechanics, because the low-energy excitations are in fact governed by a 2D massless Dirac equation as described in the next section.

Including next-nearest neighbour hopping leads to a trigonal warping of the band-structure (2.10), meaning that the group velocity becomes direction dependent with a threefold symmetry. However, the Fermi energy in undoped graphene remains located exactly at the Dirac points. Further deviations from the ideal dispersion (2.10) are caused by spin-orbit interaction [66]. Since carbon is a light element, the intrinsic spin-orbit interaction in graphene is negligibly small [69]. However, extrinsic spin-orbit interactions, created by an external field (Rashba effect) [69] or by a curvature of the graphene sheet [70], e.g. due to rippling, can

induce a gap in the spectrum by generating a mass-term.

2.1.2 2D massless Dirac equation in graphene

The derivation of the massless Dirac equation in graphene is based on the continuum limit of the nearest-neighbour tight-binding approximation and is due to DiVincenzo and Mele [4] and Semenoff [5]. Here I also follow unpublished notes by S. Gattenlöhner.

For small excitation energies only momenta close to one of the Dirac points are contributing to the electronic transport. Instead of the full Fourier transforms (2.5) of the electron operators I can take an approximation around the two K points:

$$\hat{a}_{\boldsymbol{R}} \approx e^{-i\boldsymbol{K}_1\boldsymbol{R}}\hat{a}_{1,\boldsymbol{R}} + e^{-i\boldsymbol{K}_2\boldsymbol{R}}\hat{a}_{2,\boldsymbol{R}}, \tag{2.11a}$$

$$\hat{b}_{\boldsymbol{R}} \approx e^{-i\boldsymbol{K}_1\boldsymbol{R}}\hat{b}_{1,\boldsymbol{R}} + e^{-i\boldsymbol{K}_2\boldsymbol{R}}\hat{b}_{2,\boldsymbol{R}}, \tag{2.11b}$$

where the operators $\hat{a}_{i,\boldsymbol{R}}, \hat{b}_{i,\boldsymbol{R}}$ vary slowly over the unit cell. Substitution into the tight-binding Hamiltonian (2.4) gives

$$\begin{aligned}\hat{H} = -t \sum_{\boldsymbol{R}} \sum_{\alpha=1}^{3} \big(& e^{i\boldsymbol{K}_1\boldsymbol{\delta}_\alpha} a^\dagger_{1,\boldsymbol{R}+\boldsymbol{\delta}_\alpha} b_{1,\boldsymbol{R}} + e^{i\boldsymbol{K}_2\boldsymbol{\delta}_\alpha} a^\dagger_{2,\boldsymbol{R}+\boldsymbol{\delta}_\alpha} b_{2,\boldsymbol{R}} + \\ & e^{i\boldsymbol{K}_1\boldsymbol{\delta}_\alpha} \underbrace{e^{i(\boldsymbol{K}_1-\boldsymbol{K}_2)\boldsymbol{R}} a^\dagger_{1,\boldsymbol{R}+\boldsymbol{\delta}_\alpha} b_{2,\boldsymbol{R}}}_{(*)} + e^{i\boldsymbol{K}_2\boldsymbol{\delta}_\alpha} \underbrace{e^{-i(\boldsymbol{K}_1-\boldsymbol{K}_2)\boldsymbol{R}} a^\dagger_{2,\boldsymbol{R}+\boldsymbol{\delta}_\alpha} b_{1,\boldsymbol{R}}}_{(*)} \big) + \text{h.c.}\end{aligned} \tag{2.12}$$

The mixed-valley terms contain short-wavelength Fourier components [marked by (*)] of the product of slowly varying electron operators and can be neglected. In this approximation the excitations at the different K points (valleys) become separated so that their dynamics is independent.

The crucial step is to perform the continuum limit $\frac{1}{a}\lim_{a\to 0}\ldots$ in equation (2.12) by taking the slowly varying operators continuously dependent on the coordinate and expanding these operators in linear order in $\boldsymbol{\delta}$,

$$\hat{a}_{l,\boldsymbol{R}+\boldsymbol{\delta}_\alpha} \to \hat{a}_l(\boldsymbol{R}+\boldsymbol{\delta}_\alpha) \approx \hat{a}_l(\boldsymbol{R}) + \boldsymbol{\delta}_\alpha\, \boldsymbol{\nabla}_{\boldsymbol{r}} \hat{a}_l(\boldsymbol{r})|_{\boldsymbol{r}=\boldsymbol{R}}\,. \tag{2.13}$$

This approximation is called the gradient expansion. The Hamiltonian now takes the form

$$\hat{H} = -t \int \mathrm{d}^2 r \sum_{\alpha=1}^{3} \Big(e^{i\boldsymbol{K}_1\boldsymbol{\delta}_\alpha} \boldsymbol{\delta}_\alpha \boldsymbol{\nabla}_{\boldsymbol{r}} a_1^\dagger(\boldsymbol{r}) b_1(\boldsymbol{r}) + e^{i\boldsymbol{K}_2\boldsymbol{\delta}_\alpha} \boldsymbol{\delta}_\alpha \boldsymbol{\nabla}_{\boldsymbol{r}} a_2^\dagger(\boldsymbol{r}) b_2(\boldsymbol{r}) \Big) + \text{h.c.}, \tag{2.14}$$

where I have used the relation $\sum_{\alpha=1}^{3} e^{\pm i\boldsymbol{K}_l\boldsymbol{\delta}_\alpha} = 0$. Integration by parts and plugging

in the vectors $\boldsymbol{K}_1, \boldsymbol{K}_2, \boldsymbol{\delta}_\alpha$ yields

$$\hat{H} = -i\hbar v_{\mathrm{F}} \int \mathrm{d}^2 r \left[\left(\hat{a}_1^\dagger(\boldsymbol{r}), \hat{b}_1^\dagger(\boldsymbol{r}) \right) \begin{pmatrix} 0 & -i\partial_x - \partial_y \\ i\partial_x - \partial_y & 0 \end{pmatrix} \begin{pmatrix} \hat{a}_1(\boldsymbol{r}) \\ \hat{b}_1(\boldsymbol{r}) \end{pmatrix} + \left(\hat{a}_2^\dagger(\boldsymbol{r}), \hat{b}_2^\dagger(\boldsymbol{r}) \right) \begin{pmatrix} 0 & -i\partial_x + \partial_y \\ i\partial_x + \partial_y & 0 \end{pmatrix} \begin{pmatrix} \hat{a}_2(\boldsymbol{r}) \\ \hat{b}_2(\boldsymbol{r}) \end{pmatrix} \right]. \tag{2.15}$$

Finally, by rotating the basis the Hamiltonian can be brought into the valley-symmetric representation

$$\hat{H} = \int \mathrm{d}^2 r \; \hat{\Psi}^\dagger(\boldsymbol{r}) \hat{\mathcal{H}} \hat{\Psi}(\boldsymbol{r}), \qquad \hat{\mathcal{H}} = -i\hbar v_{\mathrm{F}} \; \tau_0 \otimes (\boldsymbol{\sigma} \cdot \boldsymbol{\nabla}) = v_{\mathrm{F}} \; \tau_0 \otimes (\boldsymbol{\sigma} \cdot \hat{\boldsymbol{p}}), \tag{2.16}$$

where $\hat{\Psi}(\boldsymbol{r}) = \left(\hat{\Psi}_1(\boldsymbol{r}), \hat{\Psi}_2(\boldsymbol{r}) \right)^T$ and

$$\hat{\Psi}_1(\boldsymbol{r}) = \begin{pmatrix} \hat{a}_1(\boldsymbol{r}) \\ -i\hat{b}_1(\boldsymbol{r}) \end{pmatrix}, \quad \hat{\Psi}_2(\boldsymbol{r}) = \begin{pmatrix} -i\hat{b}_2(\boldsymbol{r}) \\ \hat{a}_2(\boldsymbol{r}) \end{pmatrix}. \tag{2.17}$$

Here I have introduced the two-component vector $\boldsymbol{\sigma} = (\sigma_x, \sigma_y)$ of Pauli matrices acting in sublattice space. Throughout this work the Pauli matrices are defined in the standard form

$$\sigma_x = \begin{pmatrix} 0 & 1 \\ 1 & 0 \end{pmatrix}, \quad \sigma_y = \begin{pmatrix} 0 & -i \\ i & 0 \end{pmatrix}, \quad \sigma_z = \begin{pmatrix} 1 & 0 \\ 0 & -1 \end{pmatrix}. \tag{2.18}$$

The corresponding matrices in valley space are denoted by τ_x, τ_y, τ_z, and complemented by the unit matrix τ_0.

According to equation (2.16) the envelope wave-function of low-energy excitations close to one of the K points is a two-component spinor (hats on spinors are emitted in the following) satisfying the 2D massless Dirac-Weyl equation

$$\hat{\mathcal{H}} \Psi(\boldsymbol{r}) = \varepsilon \Psi(\boldsymbol{r}), \qquad \hat{\mathcal{H}} = v_{\mathrm{F}} \boldsymbol{\sigma} \cdot \boldsymbol{p} = -i v_{\mathrm{F}} \boldsymbol{\sigma} \cdot \boldsymbol{\nabla}. \tag{2.19}$$

In this work I will refer to this equation simply as the Dirac equation. The spectrum of the low-energy effective Hamiltonian $\hat{\mathcal{H}}$ is given by the conical dispersion

$$\varepsilon = \pm v_{\mathrm{F}} |\boldsymbol{p}| = \pm \hbar v_{\mathrm{F}} \, |\boldsymbol{\kappa}|, \tag{2.20}$$

which agrees with the linear expansion (2.10) of the spectrum of the exact Hamiltonian.

The two spinor components of the eigenstates Ψ are related to the guiding wave function amplitudes on the two sublattices according to equation (2.17). We will see below that the spinor structure, which corresponds to the sublattice degree of

freedom, can be interpreted as a pseudospin $\frac{1}{2}$. An external electrostatic potential, that is smooth on the scale of the lattice constant, can be treated as a scalar potential in the sublattice space.

Another formal pseudospin is related with the valley degree of freedom. The two valleys are related by the time reversal operation.[1] If no disorder is present on the scale of the lattice constant, which causes inter-valley scattering, then the two valleys can be treated independently, as long as edges can be neglected. Physical observables can then be obtained from the single-valley Hamiltonian $\hat{\mathcal{H}}$ and the valley degree of freedom only causes an extra two-fold degeneracy in addition to the real spin degeneracy. A microscopic lattice termination generally lifts the valley degeneracy due to the valley-dependent boundary conditions to the Dirac equation [73].

The symmetry between the electron- and hole-like bands of the Hamiltonian $\hat{\mathcal{H}}$ in equation (2.19) is a consequence of the chiral symmetry

$$\sigma_z \hat{\mathcal{H}} \sigma_z = -\hat{\mathcal{H}}. \tag{2.21}$$

In particular, corresponding to every particle-like eigenstate Ψ with positive energy ε, there is a hole-like eigenstate $\sigma_z\Psi$ with negative energy $-\varepsilon$. This symmetry is also a property of the tight-binding Hamiltonian (2.1) and reflects the fact that each two nearest neighbours belong to different sublattices. It is thus broken if next-nearest neighbour hopping is included. However, the symmetry is generally fulfilled approximately in the vicinity of the Dirac points. Furthermore, including next-nearest neighbour hopping does not shift the location of the Fermi energy away from the Dirac points.

2.1.3 Berry phase, chirality, and Klein tunneling

Before calculating the eigenstates explicitly, I can further characterize these states directly from the Dirac equation (2.19). First, it is easy to see that a rotation of the coordinate system by an angle ϕ transforms the spinor as $\Psi \to \exp(i\sigma_z\phi/2)\Psi$. This means that upon a rotation by 2π the phase of the eigenstate changes by π, which is indeed the characteristic Berry phase of spinors. In this work I generally use the term pseudospin for this spin-$\frac{1}{2}$ degree of freedom in the sublattice space. It was shown recently that the pseudospin in graphene is associated with a real angular momentum [74].

Another important property of the single-valley spinor is its well-defined chiral-

[1] The fact that there are *two* touching points in the Brillouin zone is a consequence of the fermion doubling theorem [71, 72, 68].

ity: The Hamiltonian $\hat{\mathcal{H}}$ is just proportional to the helicity operator

$$\hat{h} = \frac{1}{2}\boldsymbol{\sigma} \cdot \frac{\hat{\boldsymbol{p}}}{|\boldsymbol{p}|}, \tag{2.22}$$

which projects the pseudospin onto the momentum direction. Therefore the energy eigenstates are also eigenstates of the helicity operator with eigenvalues $\pm\frac{1}{2}$, depending on the band index. The pseudospin direction is thus uniquely determined by the direction of momentum, a property known as chirality. In valley 1 the pseudospin is parallel (antiparallel) to the momentum for electrons in the conduction band (valence band). The chirality in valley 2 is opposite due to the reversed definition of sublattice components in equation (2.17).

In the absence of any short-range potential, the pseudospin is conserved and inter-valley scattering is absent. These properties lead to the so-called Klein tunneling in graphene, which was discussed already in the 1990's [19]. A plane wave normally incident on a potential barrier cannot be backscattered, since this process would involve a flip of the pseudospin. Even if the Fermi energy inside the barrier region lies in a different band, a normally incident electron is perfectly transmitted [17].

2.1.4 Plane wave eigenstates, velocity operator, and current density

The eigenstates $\Psi(\boldsymbol{r})$ of the Dirac Hamiltonian in equation (2.19) are plane waves in the form [67]

$$\Psi(\boldsymbol{r}) = e^{i\boldsymbol{\kappa}\boldsymbol{r}} \begin{pmatrix} u \\ v \end{pmatrix} = \langle \boldsymbol{r}|\Psi\rangle, \tag{2.23}$$

where $\boldsymbol{\kappa} = (\kappa_x, \kappa_y)$ is the wave vector and the components of the spinor are the wave function amplitudes on the two sublattices corresponding to the basis chosen above. The kinetic energy is $\varepsilon = \alpha\hbar v_{\mathrm{F}}\sqrt{\kappa_x^2 + \kappa_y^2}$ where $\alpha = \pm 1$ is the band index. The propagating solutions at $\varepsilon \neq 0$ are found as

$$\Psi(\boldsymbol{r}) = Ce^{i\boldsymbol{\kappa}\boldsymbol{r}} \begin{pmatrix} 1 \\ \alpha e^{i\phi} \end{pmatrix} = \langle \boldsymbol{r}|\boldsymbol{\kappa}, \alpha\rangle, \tag{2.24}$$

where $C = 1/\sqrt{2\mathcal{A}}$ is a normalization factor ($\mathcal{A}$ is the system size) and $\phi = \arctan(\kappa_y/\kappa_x)$ is the angle between the wave vector $\boldsymbol{\kappa}$ and the x-axis. It should be noted that apart from plane wave eigenstates, there are also radial wave eigenstates. Furthermore, in a finite sample with open boundary conditions there are also evanescent states. These decaying states will be discussed in section 3.5.2.

The velocity operator is obtained from the Heisenberg equation of motion as [67]

$$\hat{\boldsymbol{v}} \equiv \frac{d\hat{\boldsymbol{r}}}{dt} = \frac{1}{i\hbar}[\hat{\boldsymbol{r}}, \hat{\mathcal{H}}] = v_{\mathrm{F}}\hat{\boldsymbol{\sigma}}. \tag{2.25}$$

This operator does not commute with $\hat{\mathcal{H}}$, hence the velocity is not conserved, which leads to the phenomenon of Zitterbewegung [75]. The expectation value for the velocity of a plane wave $|\boldsymbol{\kappa}, \alpha\rangle$ is found as

$$\boldsymbol{v} \equiv \langle \boldsymbol{\kappa}, \alpha | \hat{\boldsymbol{v}} | \boldsymbol{\kappa}, \alpha \rangle = \alpha v_{\mathrm{F}} \frac{\boldsymbol{\kappa}}{\kappa}. \tag{2.26}$$

The velocity is parallel to the wave vector, but it is opposite to the wave vector for electrons in the valence band ($\alpha = -1$).

The probability current density can be defined as

$$\boldsymbol{j} = \Psi^{\dagger} v_{\mathrm{F}} \hat{\boldsymbol{\sigma}} \Psi, \tag{2.27}$$

and the corresponding charge current density is obtained by multiplying with the electron charge $-e$. Probability current conservation, $\boldsymbol{\nabla} \boldsymbol{j} = 0$, follows directly from the Dirac equation (2.19). For an eigenstate of the velocity operator the current density $\boldsymbol{j}(\boldsymbol{r}, t)$ is the product of the probability density $|\Psi(\boldsymbol{r}, t)|^2$ and the velocity. The average velocity and the average probability current are related as

$$\langle \Psi | \hat{\boldsymbol{v}} | \Psi \rangle = \int d^2 r \; \boldsymbol{j}. \tag{2.28}$$

2.1.5 Magnetic field and Landau quantization

In this section I consider a perpendicular magnetic field, generated by the 2D vector potential $\boldsymbol{A}(\boldsymbol{r})$ as $\boldsymbol{B} = B \boldsymbol{e}_z = \partial_x A_y(\boldsymbol{r}) - \partial_y A_x(\boldsymbol{r})$. Due to the gauge freedom this vector potential is determined up to a term $\boldsymbol{\nabla} \lambda(\boldsymbol{r})$, i.e. the gradient of an arbitrary scalar field $\lambda(\boldsymbol{r})$. Since I use the continuum approximation to describe the electronic motion in the graphene plane, I can describe the coupling of the orbital momentum to the magnetic field by the substitution [76]

$$\mathcal{H}(\boldsymbol{p}) \to \mathcal{H}(\boldsymbol{p} + e\boldsymbol{A}) \equiv \mathcal{H}^B(\boldsymbol{p}, \boldsymbol{r}). \tag{2.29}$$

This is known as the method of minimal coupling. Note that the momentum $\boldsymbol{p}$ in $\mathcal{H}^B$ is gauge-dependent and no longer a conserved quantity. Instead, the momentum $\boldsymbol{\Pi} = \boldsymbol{p} + e\boldsymbol{A}$ is gauge-invariant and proportional to the electron velocity $\boldsymbol{v}$. The minimal substitution (2.29) requires that the magnetic length

$$\ell_B = \sqrt{\frac{\hbar}{e|B|}} \tag{2.30}$$

remains much larger than the lattice constant a. This condition is fulfilled in graphene up to very high field strengths.

An external magnetic field couples both to the spin and the orbital momentum

of an electron. The latter effect leads to the Landau quantization, while the first effect causes the splitting of each Landau level into two spin branches separated by the Zeeman energy $g\mu_B|B|$, where g is the g-factor and μ_B is the Bohr magneton. However, even for large magnetic fields, the Zeeman gap in graphene is relatively small. Therefore I will neglect any effect arising from the spin degree of freedom.

Applying the minimal substitution (2.29) to the single valley Hamiltonian in equation (2.19) gives

$$\mathcal{H}^B = v_{\mathrm{F}}\boldsymbol{\Pi}\cdot\boldsymbol{\sigma}. \tag{2.31}$$

The eigenvalue problem can be solved by introducing ladder operators (here $B > 0$)

$$\hat{a} = \frac{\ell_B}{\sqrt{2}\hbar}(\Pi_x - i\Pi_y), \tag{2.32}$$

$$\hat{a}^\dagger = \frac{\ell_B}{\sqrt{2}\hbar}(\Pi_x + i\Pi_y), \tag{2.33}$$

in analogy to the quantum-mechanical problem of a one-dimensional harmonic oscillator. In terms of these operators, the Hamiltonian (2.31) reads

$$\mathcal{H} = \hbar\omega_c \begin{pmatrix} 0 & \hat{a} \\ \hat{a}^\dagger & 0 \end{pmatrix}, \tag{2.34}$$

For $B < 0$ the definitions of the ladder operators $\hat{a}$ and $\hat{a}^\dagger$ are interchanged, which ensures the commutation relation $[\hat{a}, \hat{a}^\dagger] = 1$, and the Hamiltonian takes the transpose form of equation (2.34).

The cyclotron frequency is determined by the Fermi velocity as

$$\omega_c = \sqrt{2}\frac{v_{\mathrm{F}}}{\ell_B}, \tag{2.35}$$

which is in contrast to the non-relativistic case, where the cyclotron frequency depends on the mass of the particles. As a consequence, ω_c scales like $\sqrt{|B|}$ as opposed to the linear field dependence in the non-relativistic case.

The spectrum of the Dirac Hamiltonian in the presence of magnetic field is found as [77]

$$\varepsilon_{\alpha,n} = \alpha\hbar\omega_c\sqrt{n}, \qquad \text{for } n \geq 1, \tag{2.36}$$

where $\alpha = \pm$ is again the band index and n is the Landau level index. In addition there is a single $n = 0$ - Landau level at $\varepsilon = 0$, which in neutral graphene is exactly half-filled. Note that each level has a four-fold degeneracy due to spin and valley degrees of freedom. The lowest Landau levels are plotted as a function of the magnetic field in figure 2.3. The unequal spacing together with the existence of a Landau level at the charge neutrality point makes the Landau level structure very different from the non-relativistic case. This leads to an unconventional quantum

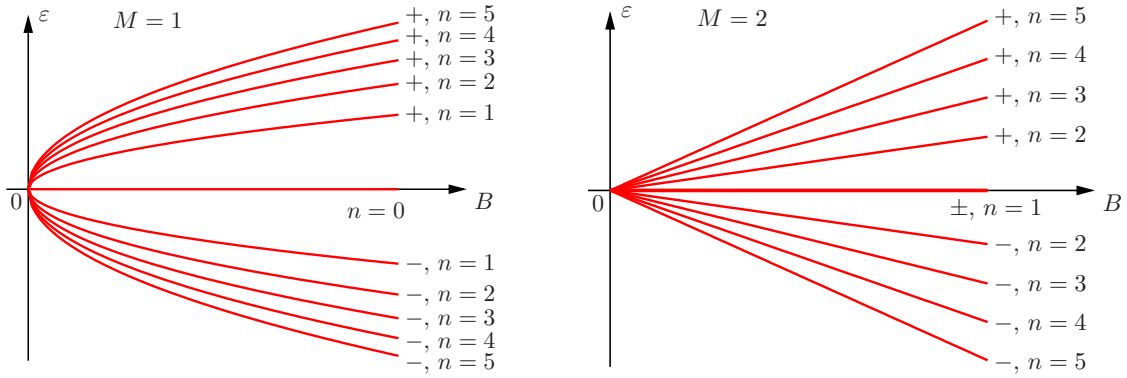

Figure 2.3: The Landau level structure of a graphene monolayer (left panel, $M = 1$) and bilayer (right panel, $M = 2$) as a function of magnetic field B. The gapped branches are labeled by band index $\alpha = \pm$ and Landau level index n.

Hall effect, which is discussed in section 2.3.1.

2.2 Electronic Properties of Bilayer and Multilayer Graphene

Since graphene originates from graphite, stacks of several graphene layers are also naturally stable. In such stacks the graphene layers are separated by 3.3 Å and hold together by van-der-Waals like interactions. The layers are coupled electronically due to the hopping terms between π-electrons in different layers. However, the electronic motion is frozen in the direction perpendicular to the layers and therefore remains genuinely 2D. This fact justifies the name multilayer graphene.[2] Distinct surface effects start to appear from about 5 layers [78], so that the 2D description should not be applied to much thicker stacks.

The tight-binding model for monolayer graphene can be extended to stacks of graphene layers. Bulk graphite corresponds to an infinite number of layers and is phenomenologically described by the Slonczewski-Weiss-McClure model [2, 3] which has seven parameters. This is the most general tight-binding model consistent with the crystal symmetry. In this work I will describe few-layer graphene by the most simple tight-binding model, which only includes a single interlayer hopping term. In general, the importance of other hopping terms such as next-nearest layer hopping increases with the number of layers. Using a more sophisticated tight-binding approach [79] the electronic structure can be studied in the transition from graphene to graphite. Tight-binding parameters of few-layer graphene have also been derived from first principles [80]. The stability of the dispersion and of the Fermi points has been studied based on density-functional theory in refs. [81, 82] and by means of topological arguments in ref. [83].

A characteristic feature of multilayer graphene, that strongly influences its electronic properties, is the stacking configuration. I consider the natural stacking

[2]The term multilayer graphene is sometimes also used in the literature for electronically decoupled graphene sheets.

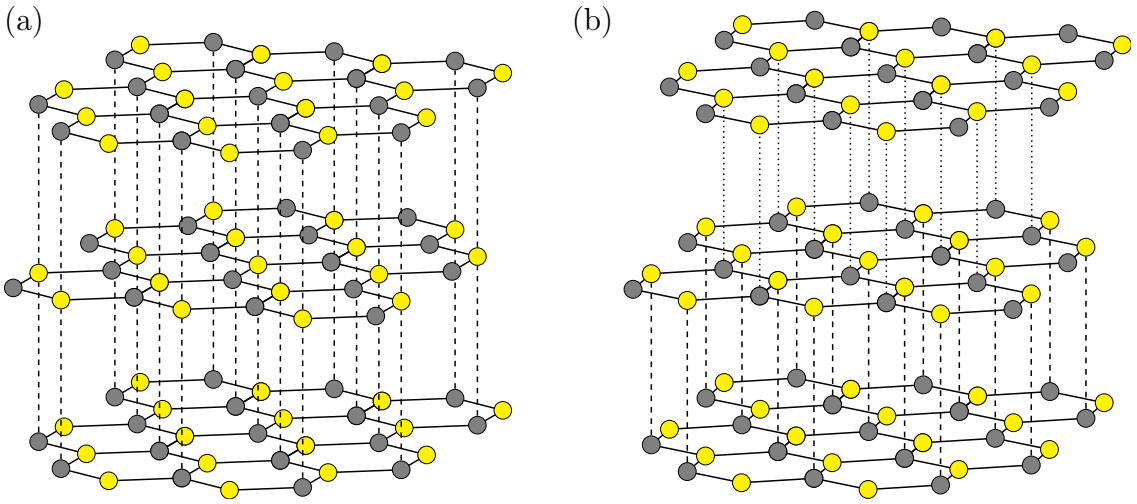

Figure 2.4: The lattice structure of trilayer graphene. (a) AB-stacking. (b) ABC-stacking.

configurations, in which each two neighbouring layers (labeled 1 and 2) are displaced such that the atoms of one sublattice in layer 1 sit on top of one sublattice in layer 2, while the atoms of the other sublattice sit on top of the centers of the hexagonal cells of layer 2. This displacement allows for three inequivalent positions labeled by A,B, and C. Thus bilayer graphene has a stacking configuration AB, while trilayer graphene exists in two distinct configurations ABA and ABC as shown in figure 2.4. The two regular configurations ABA... and ABC... are known as Bernal stacking and rhombohedral stacking, respectively. The stacking in graphite is of the Bernal type, but stacking faults are common and regions with ABC stacking have been observed. In this work I exclude the hexagonal stacking type AA, which is energetically unfavourable [84], and any other stacking faults such as rotated layers.

In the following I extend the tight-binding model of monolayer graphene first to bilayer and then to few-layer graphene. The band structures will be discussed for the regular stacking types Bernal and rhombohedral.

2.2.1 Bilayer graphene

By contrast to monolayer graphene, in bilayer graphene the two sublattices in each layer become inequivalent due to the different couplings to the neighbouring layer. As shown in figure 2.5, the unit cell of the Bravais lattice still remains triangular, with 4 atoms per unit cell, and the reciprocal lattice corresponds to the hexagonal Brillouin zone of a monolayer shown in figure 2.1 (b).

The tight-binding Hamiltonian of bilayer graphene contains intra-layer and inter-layer hopping terms. In the simplest model one can treat both types in a nearest-neighbour approximation, so that the Hamiltonian consists of two copies of the monolayer nearest-neighbour tight-binding Hamiltonian (2.4), and an inter-layer

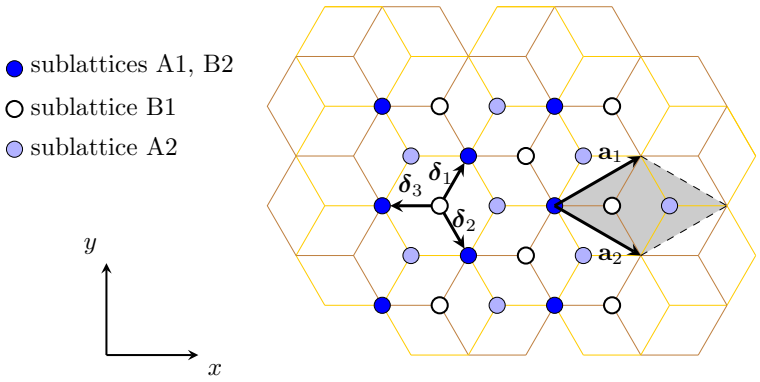

Figure 2.5: The lattice structure of bilayer graphene. Indicated are the intra-layer nearest-neighbour vectors and the lattice vectors.

hopping term accounting for the coupling of the two sublattices sitting on top of each other. The inter-layer hopping integral $t_\perp \approx 0.3$eV is about 10 times smaller than the intralayer coupling constant t. Writing the layer index as a superscript (for example, $\hat{a}^{(1)\dagger}_{\boldsymbol{R}}$ is defined as the operator $\hat{a}^\dagger_{\boldsymbol{R}}$ acting in layer 1), the Hamiltonian reads

$$\hat{H} = -t \sum_{\boldsymbol{R}} \sum_{\alpha=1}^{3} \left(\hat{a}^{(1)\dagger}_{\boldsymbol{R}} \, \hat{b}^{(1)}_{\boldsymbol{R}-\boldsymbol{\delta}_\alpha} + \hat{a}^{(2)\dagger}_{\boldsymbol{R}+\boldsymbol{\delta}_\alpha} \hat{b}^{(2)}_{\boldsymbol{R}} + \text{h.c.} \right) - t_\perp \sum_{\boldsymbol{R}} \left(\hat{a}^{(1)\dagger}_{\boldsymbol{R}} \, \hat{b}^{(2)}_{\boldsymbol{R}} + \text{h.c.} \right). \tag{2.37}$$

The spectrum of $\hat{H}$ is obtained by Fourier transforming the operators into momentum space, and consists of four bands with the dispersion

$$\varepsilon_2(\boldsymbol{k}) = \pm \sqrt{\varepsilon_1^2(\boldsymbol{k}) + \frac{t_\perp^2}{4}} \pm \frac{t_\perp}{2}, \tag{2.38}$$

where ε_1 is the monolayer dispersion (2.8). An electron-like and a hole-like band touch each other at the same K points (2.9) as for monolayer graphene. The quasiparticles belonging to these ungapped branches are located on the sublattices B1 and A2, which form a projected hexagonal lattice. The hopping between these sites takes place via the directly coupled sublattices A1 and B2 only, since other inter-layer hopping terms are neglected. On these directly coupled sublattices the inter-layer coupling forms 'dimer' states [85] leading to one more electron- and hole-like band shifted by $t_\perp$ and $-t_\perp$, respectively.

The dispersion of all bands is parabolic near the K points, but for $\varepsilon \gg t_\perp$ the dispersion of all bands becomes that of the monolayer dispersion $\varepsilon_1(\boldsymbol{k})$ shifted by $\pm t_\perp/2$. The Fermi energy of charge-neutral bilayer graphene still coincides with the degeneracy point at $\varepsilon = 0$.

The continuum approximation can be carried out within each layer in the same way as for a monolayer. The effective Hamiltonian, valid for quasiparticles with

long-wavelength, is given by

$$\hat{H} = \int \mathrm{d}^2 r \sum_{l=1}^{2} \hat{\Psi}_l^\dagger(\boldsymbol{r}) \hat{\mathcal{H}}_l \hat{\Psi}_l(\boldsymbol{r}), \tag{2.39}$$

where l labels the valleys and the single-valley Hamiltonians and the corresponding basis states are given by

$$\hat{\mathcal{H}}_1 \equiv \begin{pmatrix} -i\hbar v_\mathrm{F} \boldsymbol{\sigma}\boldsymbol{\nabla} & \begin{matrix} 0 & -it_\perp \\ 0 & 0 \end{matrix} \\ \begin{matrix} 0 & 0 \\ it_\perp & 0 \end{matrix} & -i\hbar v_\mathrm{F} \boldsymbol{\sigma}\boldsymbol{\nabla} \end{pmatrix}, \quad \hat{\Psi}_1(\boldsymbol{r}) \equiv \begin{pmatrix} \hat{a}_1^{(1)}(\boldsymbol{r}) \\ -i\hat{b}_1^{(1)}(\boldsymbol{r}) \\ \hat{a}_1^{(2)}(\boldsymbol{r}) \\ -i\hat{b}_1^{(2)}(\boldsymbol{r}) \end{pmatrix}, \tag{2.40}$$

$$\hat{\mathcal{H}}_2 \equiv \begin{pmatrix} -i\hbar v_\mathrm{F} \boldsymbol{\sigma}\boldsymbol{\nabla} & \begin{matrix} 0 & 0 \\ -it_\perp & 0 \end{matrix} \\ \begin{matrix} 0 & it_\perp \\ 0 & 0 \end{matrix} & -i\hbar v_\mathrm{F} \boldsymbol{\sigma}\boldsymbol{\nabla} \end{pmatrix}, \quad \hat{\Psi}_2(\boldsymbol{r}) \equiv \begin{pmatrix} -i\hat{b}_2^{(1)}(\boldsymbol{r}) \\ \hat{a}_2^{(1)}(\boldsymbol{r}) \\ -i\hat{b}_2^{(2)}(\boldsymbol{r}) \\ \hat{a}_2^{(2)}(\boldsymbol{r}) \end{pmatrix}. \tag{2.41}$$

The spectrum is found as

$$\varepsilon(\boldsymbol{\kappa}) = \pm\sqrt{(\hbar v_\mathrm{F}\boldsymbol{\kappa})^2 + \frac{t_\perp^2}{4}} \pm \frac{t_\perp}{2}. \tag{2.42}$$

The two electron- (hole-) like branches are parabolic around the minimum (maximum), i.e. for $\hbar v_\mathrm{F}\kappa \ll t_\perp$, and linear for larger values of κ. The parabolic regime in the vicinity of the K points is given by

$$\varepsilon(\boldsymbol{\kappa}) \approx \pm\left(\frac{(\hbar v_\mathrm{F}\boldsymbol{\kappa})^2}{t_\perp} + \frac{t_\perp}{2}\right) \pm \frac{t_\perp}{2}, \qquad \text{for } \hbar v_\mathrm{F}\kappa \ll t_\perp. \tag{2.43}$$

Therefore the effective mass of the long-wavelength quasiparticles is $m^* \approx t_\perp/2v_\mathrm{F}^2$.

The gapped branches of the spectrum (2.42) are not relevant for the electronic motion in the low-energy regime $|\varepsilon| \ll t_\perp$, where the dispersion is parabolic. An effective two-band Hamiltonian can be derived, describing the ungapped branches only [85]. This is most easily achieved by a unitary transformation to diagonalize the Hamiltonian, and rotating back using the same transformation in the limit $\kappa \to 0$. In the resulting Hamiltonian matrix the dynamics of all branches is separated so that the high-energy branches can be removed. Alternatively the low-energy effective model can be derived from degenerate second-order perturbation theory [86, 87]. The effective 2×2-dimensional Hamiltonian in second order in κ is given by

$$\hat{H}_\mathrm{eff} = \int \mathrm{d}^2 r \sum_{l=1}^{2} \Psi_{l,\mathrm{eff}}^\dagger(\boldsymbol{r}) \hat{\mathcal{H}}_\mathrm{eff} \Psi_{l,\mathrm{eff}}(\boldsymbol{r}), \tag{2.44}$$

where the single-valley Hamiltonian matrix and the basis states are given by

$$\hat{\mathcal{H}}_{\text{eff}} = \frac{(\hbar v_{\text{F}})^2}{t_\perp} \begin{pmatrix} 0 & (\partial_x - i\partial_y)^2 \\ (\partial_x + i\partial_y)^2 & 0 \end{pmatrix}, \tag{2.45}$$

$$\Psi_{1,\text{eff}}(\boldsymbol{r}) = \begin{pmatrix} \hat{a}_1^{(2)}(\boldsymbol{r}) \\ \hat{b}_1^{(1)}(\boldsymbol{r}) \end{pmatrix}, \quad \Psi_{2,\text{eff}}(\boldsymbol{r}) = \begin{pmatrix} \hat{b}_2^{(1)}(\boldsymbol{r}) \\ \hat{a}_2^{(2)}(\boldsymbol{r}) \end{pmatrix}. \tag{2.46}$$

In this description the low-energy and long-wavelength quasiparticles are chiral and feature a Berry phase 2π. As for monolayer graphene, the helicity eigenvalue depends on the band index due to the charge conjugation symmetry. However, the Berry phase 2π means that the quasiparticles resemble a chirality associated with spin 1. The Klein tunneling described for monolayer graphene manifests itself in just the opposite way in bilayer graphene, where normally incident states are perfectly reflected from a potential barrier, in which the Fermi energy lies in the other band than outside, or even from a single $p-n$ junction [17]. These findings are restricted to the parabolic regime of the ungapped branches of the spectrum, $|\varepsilon| \ll t_\perp$.

The Landau-level spectrum in this low-energy regime is also very distinct from monolayer graphene [85],

$$\varepsilon_{\alpha,n} = \pm\hbar\omega_c\sqrt{n(n-1)}, \qquad \text{for } n \geq 2, \tag{2.47}$$

where $\omega_c = \hbar/m^*\ell_B^2$ is the cyclotron frequency. As seen in figure 2.3, these levels are almost equidistantly spaced. In addition there is a two-fold (eight-fold including valley and spin) degenerate zero-energy Landau level with a relatively large energy distance to the neighbouring $n = 2$ -levels.

2.2.2 Multilayer graphene

The extension of the effective-mass approximation to more than two layers is straightforward. As before I restrict myself to the minimal model which takes into account only nearest neighbour hopping within and between the layers. The Brillouin zone remains 2D and hexagonal as shown in figure 2.1 (b), despite the finite thickness of the crystal. The Hamiltonian describing excitations in the vicinity of one of the K points can be written as a sum of intralayer and interlayer terms,

$$\hat{\mathcal{H}} = \hat{\mathcal{H}}_0 + \hat{\mathcal{H}}_\perp, \tag{2.48}$$

where $\hat{\mathcal{H}}_0 = \mathbb{1}_M \otimes (-i\hbar v_{\text{F}}\boldsymbol{\sigma}\boldsymbol{\nabla})$ (for simplicity I consider a single valley), and M is the number of layers. The interlayer term depends on the stacking order of the

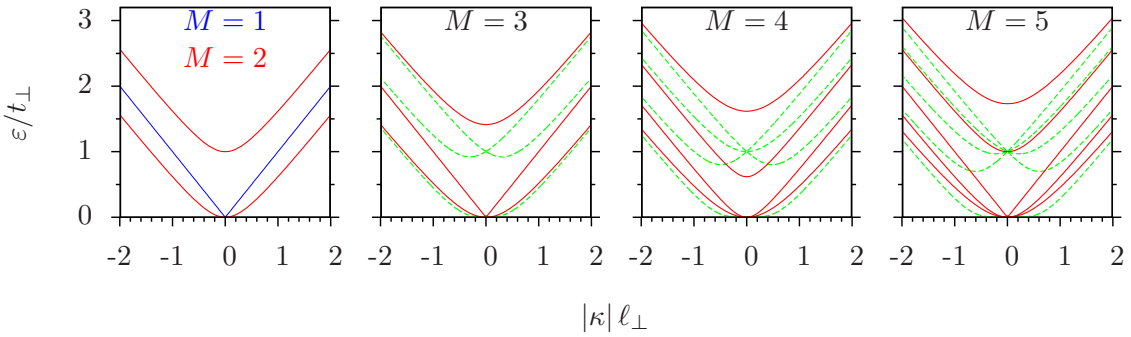

Figure 2.6: The band structures of multilayer graphene with ABA (red solid lines) and ABC (green dashed lines) stacking order. The left panel shows that of monolayer and bilayer graphene. All spectra are symmetric with respect to $\varepsilon = 0$.

layers, but can be written in the general form

$$\hat{\mathcal{H}}_\perp = t_\perp \begin{pmatrix} 0 & \sigma_{(1)} & 0 & 0 & \dots \\ \sigma_{(1)}^\dagger & 0 & \sigma_{(2)} & 0 & \dots \\ 0 & \sigma_{(2)}^\dagger & 0 & \sigma_{(3)} & \dots \\ 0 & 0 & \sigma_{(3)}^\dagger & 0 & \dots \\ \dots & \dots & \dots & \dots & \dots \end{pmatrix}, \tag{2.49}$$

where in one valley $\sigma_{(m)} = (i\sigma_-)^{(\dagger)} = \pm i\sigma_x + \sigma_y$, depending on the orientation of the adjacent layers, and the corresponding matrices in the other valley are $\sigma_{(m)}^{\mathrm{T}}$. In the case of Bernal stacking one has $\sigma_{(2m)} = -i\sigma_+$, $\sigma_{(2m+1)} = i\sigma_-$, while rhombohedral stacking yields $\sigma_{(m)} = -i\sigma_+$ for any m. Stacking faults are described by irregular sequences of σ matrices.

An external perpendicular magnetic field leaves the interlayer coupling unchanged, hence its effect can be included into the low-energy effective theory of multilayer graphene by the minimal substitution (2.29).

The dispersion relation $\varepsilon(\kappa)$ of the multilayer Hamiltonian in the effective mass approximation follows from the spectral equation

$$\hat{\mathcal{H}}\Psi = \varepsilon\Psi, \tag{2.50}$$

by performing the Fourier transformation $\Psi \to e^{i\boldsymbol{\kappa r}}\psi$. The number of positive (negative) energy branches is given by the number of layers. Since the Hamiltonian $\hat{\mathcal{H}}$ in equation (2.48) has the chiral symmetry (2.21), its spectrum is symmetric with respect to the band center at $\varepsilon = 0$. In the following I discuss the spectra of the two regular stacking types, shown in figure 2.6.

The most simple case is the Bernal stacking, where the Hamiltonian can be mapped to a system of uncoupled bilayer-like systems plus one additional monolayer if M is odd [65]. This mapping is exact and can be derived by means of a matrix decomposition of the Hamiltonian. The $[M/2]$ uncoupled bilayer systems have

effective interlayer hopping constants

$$t_\perp^* = 2\beta_m t_\perp, \quad \beta_m = \cos\left(\frac{m\pi}{M+1}\right), \qquad m = 1, \dots [M/2]. \tag{2.51}$$

As a consequence, the spectrum is given by [88],

$$\frac{\varepsilon_m}{t_\perp} = \beta_m \pm \sqrt{\left(\frac{\hbar v_\mathrm{F}}{t_\perp}\kappa\right)^2 + \beta_m^2}, \qquad m = 1, \dots M. \tag{2.52}$$

Thus, for $m = [(M+1)/2]$ monolayer-like bands exist for this stacking order.

The case of rhombohedral stacking is more complicated and the full spectrum is not known exactly. The numerical solutions for the spectra are shown in figure 2.6 as well. For $|\varepsilon| \gg t_\perp$ the dispersion of all bands is linear and independent of the stacking type, so that they follow from equation (2.52). Furthermore, there is only one electron-like and one hole-like ungapped branch, so that one can derive a low-energy effective Hamiltonian in the same way as for bilayer graphene. The effective Hamiltonian of M-layer graphene in the rhombohedral stacking order has the form [85, 83]

$$\hat{\mathcal{H}}_\mathrm{eff} = t_\perp \left(\frac{\hbar v_\mathrm{F}}{t_\perp}\right)^M \tau_0 \otimes \begin{pmatrix} 0 & (\partial_x - i\partial_y)^M \\ (\partial_x + i\partial_y)^M & 0 \end{pmatrix}. \tag{2.53}$$

The dispersion follows as

$$\frac{\varepsilon_m}{t_\perp} \approx \pm \left(\frac{\hbar v_\mathrm{F}}{t_\perp}\kappa\right)^M, \qquad \varepsilon \ll t_\perp. \tag{2.54}$$

This shows that the low-energy long-wavelength excitations are chiral with a Berry phase $M\pi$ [85]. We will see in chapter 4 that the chirality of the charge carriers, which exists for any of the considered stacking configurations, has important consequences on the charge transport in such few-layers.

2.3 (Half-) Integer Quantum Hall Effect and Quantum Hall Phase Transition

2.3.1 Unconventional quantum Hall effect

The Landau level structure (2.36) of a monolayer leads to an unconventional quantum Hall (QH) effect in graphene, the observation of which provided one of the first experimental confirmations of the Dirac-like behaviour of the quasiparticles [11, 6]. Due to the half-filled Landau level at the Dirac point the Hall conductivity σ_{xy} is quantized in half-integer multiples of e^2/h (per spin and valley) [27, 26]. The lowest plateaus (at filling factors $\pm\frac{1}{2}$) can be observed even at room temperature at

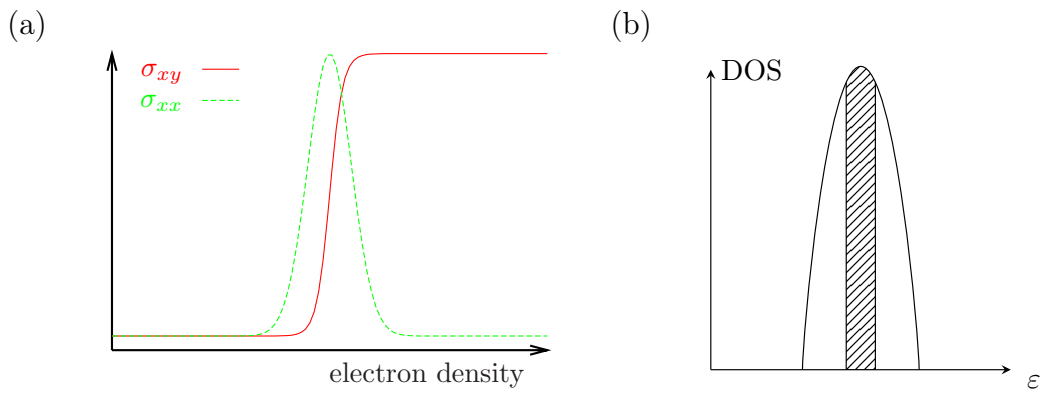

Figure 2.7: (a) Schematic behaviour of σ_{xx} and σ_{xy} at the QH transition. (b) DoS of a disorder-broadened Landau level. In the shaded region at the band center the localization length exceeds the sample size so that states are extended throughout the sample.

very strong magnetic field [89]. This is mainly a consequence of the relatively large spacing of the lowest Landau levels [55]. On the other hand, at low temperatures the lowest plateaus appear for magnetic field strengths well below 1T due to the different energy scale, equation (2.35), of Dirac fermions in a magnetic field.

The QH effect takes a different form in bilayer graphene with the Landau level structure (2.47). Here the Hall conductivity is quantized in integer multiples of e^2/h (per spin and valley), but there is no plateau at $\sigma_{xy} = 0$ due to the Landau level at $\varepsilon = 0$. This peculiar Hall quantization has been observed experimentally [56].

2.3.2 Quantum Hall phase transition

Here I provide a theoretical background on the QH phase transition occurring in a 2D electron gas in a strong magnetic field. This background is required to interpret the results in chapter 8 on magnetotransport in disordered graphene. As in the entire thesis, I restrict myself to the single-electron description neglecting interactions, which is sufficient for a basic understanding of this transition. In this section I follow the articles by Chalker [90] and by Kramer *et al.* [91].

Figure 2.7 (a) schematically shows the behaviour of the two components of the conductivity tensor at the QH phase transition. In order to observe such a transition, a certain amount of disorder is necessary, which lifts the macroscopic degeneracy of and broadens each Landau level. Let us assume that the magnetic field is strong enough, so that the broadening is small compared to the spacing of Landau levels. Thus each Landau level turns into a Landau band as shown in figure 2.7 (b). The states in the tail of the band are localized and do not participate in current flow, while the states in the center are extended throughout the sample. This distinction may be understood from the so-called percolation model, which I do not want to describe in further detail. The picture of the QH phase transition is as follows: For quantized values of the filling factor ν, all states available at the

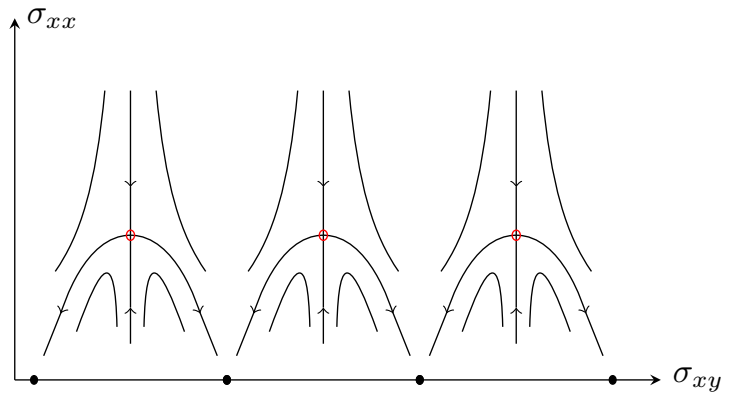

Figure 2.8: Scaling flow diagram for the (half-)integer QH effect. The solid circles are the stable fixed points at the QH plateaus with (half-)integer σ_{xy}. The red circles are the unstable fixed points at the QH transition. (Adapted from [90].)

Fermi energy are localized. Thus the longitudinal conductivity σ_{xx} vanishes and σ_{xy} assumes a quantized plateau value (half-integer in graphene) independent of the carrier density. As the electron density is increased, the Fermi energy moves into a region of extended states. Consequently the Hall conductivity σ_{xy} rises by the conductance quantum (times degeneracies) to the next plateau value, and σ_{xx} is non-zero due to dissipative transport. The peaks of σ_{xx} may be viewed as Shubnikov - de Haas oscillations, which also occur for weaker magnetic fields. At low temperatures the transition region is small compared to the plateau region. The width of the transition reflects the width of the energy region, in which extended states exist.

The QH phase transition is a delocalization transition in a disordered system and has been discussed in the framework of scaling theory. The concept of scaling theory was developed in an acclaimed paper by Abrahams, Anderson, Licciardello, and Ramakrishnan [92]. In the absence of magnetic field the longitudinal conductivity σ_{xx} serves as a scaling parameter (coupling constant). Pruisken and collaborators used field-theoretic methods to study the QH effect and identified σ_{xy} as a second coupling constant in the QH regime [93, 94]. A scaling flow diagram in the $\sigma_{xx} - \sigma_{xy}$ plane was first suggested by Khmel'nitskii, which is illustrated in figure 2.8. This diagram shows how σ_{xx} and σ_{xy} change as the length scales are increased at fixed filling factor. In graphene, the stable fixed points are located at $\sigma_{xx} = 0$ and $\sigma_{xy} = n + 1/2$, with n integer. These points correspond to the QH plateaus, and almost all flow lines end on one of such points. A discrete set of flow lines, however, ends at unstable fixed points, with $\sigma_{xx} > 0$ and $\sigma_{xy} = n$. These points correspond to the QH phase transitions. The renormalization group flow of σ_{xx} and σ_{xy} has been developed for graphene with long-range (not valley-mixing) and short-range (valley-mixing) impurities in ref. [95].

In addition to the scaling theory, the QH phase transition may be interpreted as a quantum critical point, which leads to further predictions. One expects that

the correlation length for this transition, which in the single-particle description is the localization length at the Fermi energy, diverges with a critical exponent as the critical point is approached. All numerical studies for a wide variety of models have confirmed that the critical exponent is universal, hence the QH effect may be viewed as a genuine universal quantum phase transition. The same critical exponent governs the singularities of the components of the conductivity tensor, which in the vicinity of the critical point are scaling functions. This leads to predictions, e.g. for the temperature-dependent width of the Shubnikov-de Haas peaks of σ_{xx} as a function of magnetic field [94].

Based on the percolation picture of the QH phase transition, generic models have been developed to describe the electronic properties of a 2D electron gas in the presence of a random potential and a strong perpendicular magnetic field. The best studied one is the random network model by Chalker and Coddington [96]. Such models not only allow to prove the existence of a delocalization transition, but also allow further predictions on the critical behaviour by means of numerical methods. These predictions by means of models not including any microscopic details of the 2D electron gas are only possible because of the universality of the critical behaviour.

In fact, the numerical models have provided evidence that at the unstable fixed points of the QH transition the conductivity σ_{xx} itself acquires an approximately universal value in the critical regime. In particular, the critical conductivity is found to be in the range from 0.5 to 0.6 [97, 98, 99]. In chapter 8 I am trying to approach the critical regime at the QH transition of the zero-energy Landau level using a more realistic model describing undoped graphene with isolated scalar impurities. The obtained data for the conductivity at large system scales seems to be in agreement with the range given above.

Chapter 3 – Scattering Theory, Full Counting Statistics, and Green's Function Formalism

3.1 Introduction

In electronic devices of macroscopic dimensions the quantum nature of charge carriers is usually irrelevant. By contrast, in mesoscopic devices various inelastic processes as well as dephasing can be neglected. This implies that electronic transport has to be considered as a quantum mechanical problem. On the other hand mesoscopic systems are large compared to atomic distances, hence fluctuations on microscopic length scales are usually irrelevant, and effective instead of microscopic Hamiltonians can be employed. This regime of quantum transport is suitable for a description by the scattering approach, which was pioneered by Landauer [60] and Büttiker [61]. The intuitively appealing approach provides a complete picture of electron transport at low frequencies, temperatures, and bias voltages, under conditions such that electron-electron interactions are negligible in the transport dynamics [100]. Under theses assumptions the scattering approach is equivalent with more complicated approaches such as the non-equilibrium Green's function formalism. It should be emphasized that the physical assumptions of the scattering approach may not be met in all mesoscopic systems of interest [101].

In this approach the conductor is modeled as an elastic scattering region, which is connected by ideal leads to an arbitrary number of electron reservoirs serving as sources and drains for the conduction electrons. The current through a given lead, measured at the interface to the electron reservoir, is determined by the occupation of the incoming and the outgoing scattering states, which are assumed to be completely independent in the asymptotic region far from the sample [102]. The longitudinal (along the leads) and the transverse motion of charge carriers in the asymptotic region of the leads are separable, and the transverse motion is quantized due to the finite width of the leads. This assumption allows one to define transverse scattering channels. Sub-channels may exist due to other degrees of freedom, such as spin or valley in graphene.

The concept of the scattering approach is introduced for a two-terminal device in section 3.2. Electronic transport properties are obtained from scattering amplitudes of single-particle wave functions describing electrons incident in the leads. This means that any dynamic effects due to electron-electron interactions are neglected, and these interactions are treated in a mean-field approximation. Another assumption of the scattering approach is the absence of inelastic scattering processes, which means that the energy of an electron is a conserved quantity. Thus the scattering matrix depends only on a single energy.

As described in section 3.3, the transport properties of the non-interacting system can be written in terms of the transmission properties of the quasiparticles at the Fermi energy. In this work I generally consider the limit of zero bias voltage and zero temperature. This corresponds to the regime of linear response, in which the non-equilibrium transport properties are effectively obtained from equilibrium properties. Any transport property in this regime becomes a linear statistic on the transmission eigenvalues, which means that they do not contain any product of different transmission eigenvalues [100].

A full description of electronic transport includes not only conductance and noise, but also the higher moments of charge transfer. In section 3.4 I introduce the concept of the full counting statistics, which facilitates the characterization of the whole transmission distribution of charge transfer by means of a cumulant generating function, which is expressed in terms of the scattering amplitudes.

In section 3.5 I apply the scattering approach to a two-terminal monolayer graphene device in the rectangular sample geometry. Using the model of heavily doped graphene leads I carry out the wavefunction matching to calculate the conductance and the noise, which have been first studied in refs. [24, 23].

Section 3.6 deals with the Green's function formalism, which is more suitable for calculating the transport properties of a disordered conductor. The scattering amplitudes are expressed as projections of the Green's functions onto the scattering states in the leads. Such a relation between scattering amplitudes and Green's functions has been first derived by Fisher and Lee [103] for non-relativistic electrons and is thus known as a Fisher-Lee relation. By means of these relations any transmission moment can be expressed in terms of Green's functions. In fact, the formula for the conductance is equivalent with the Kubo formula known from linear response theory.

In section 3.7 the full counting statistics of the transmission distribution is also reformulated by introducing Nazarov's multi-component Green's function which depends on an external counting field [104]. This formalism facilitates the expression of the cumulant generating function in terms of Green's functions without the use of the scattering amplitudes.

3.2 Scattering Matrix and Transfer Matrix

I consider a two-terminal transport device, which is modeled by the scattering approach as shown in figure 3.1. Here $\mu_{L,R}$ and $T_{L,R}$ are the chemical potential and the temperature in the left and right reservoir, respectively. The bias voltage corresponds to the difference $V = \mu_L - \mu_R$. The transport takes place along the x direction.

In this section I follow ref. [100]. The electrons in the leads at certain energy are plane waves traveling in longitudinal direction. Thus their wavefunction separates

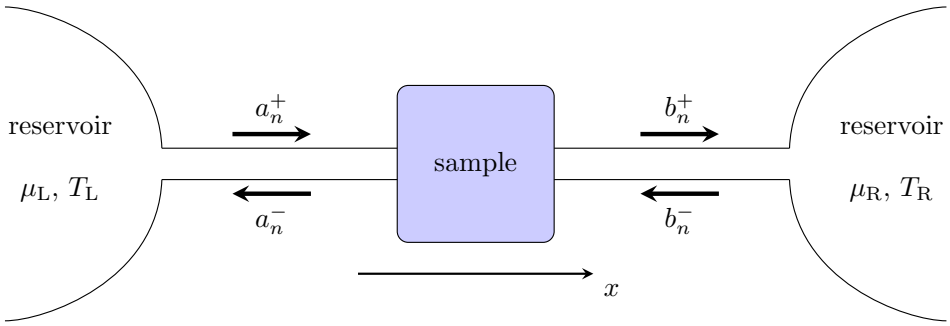

Figure 3.1: Model of the conductor as a scattering region between ideal leads, which are attached to electron reservoirs.

into longitudinal and transversal parts as

$$|\psi_m^\pm\rangle = e^{\pm ik_m x}|\phi_m^\pm\rangle, \tag{3.1}$$

where the mode index m labels the scattering channels, defined by real longitudinal wave number k_m and a set of functions of transverse coordinates $|\phi_m^\pm\rangle$, where the index $+(-)$ labels right (left) -moving electrons. The states are normalized such that they carry unit current,

$$\langle\psi_m^\pm|\hat{v}_x|\psi_m^\pm\rangle = \pm 1. \tag{3.2}$$

Here $\hat{v}_x$ is the velocity operator in x direction.

Expressed in the basis of the scattering modes (3.1), incident and outgoing waves are described by sets of coefficients

$$c^{\mathrm{in}} = (a_1^+, a_2^+, \ldots, a_N^+, b_1^-, b_2^-, \ldots, b_N^-)^T, \tag{3.3}$$

$$c^{\mathrm{out}} = (a_1^-, a_2^-, \ldots, a_N^-, b_1^+, b_2^+, \ldots, b_N^+)^T, \tag{3.4}$$

respectively. Here N is the number of channels, which is assumed to be identical in the left and right lead. In principle this number can be infinite, but usually only a finite number of channels is relevant for the transport. The scattering matrix S, relating these two vectors by

$$c^{\mathrm{out}} = Sc^{\mathrm{in}}, \tag{3.5}$$

has the block structure

$$S = \begin{pmatrix} r & t' \\ t & r' \end{pmatrix}. \tag{3.6}$$

It follows from current conservation that S is unitary, $SS^\dagger = 1$. This means that the four matrices $tt^\dagger, t't'^\dagger, 1-rr^\dagger$, and $1-r'r'^\dagger$ have the same set of eigenvalues $T_1, T_2, \ldots$, which are real numbers between 0 and 1 and called transmission eigenvalues.

The scattering matrix completely describes the transport properties of the scat-

tering region. An equivalent description is provided by the transfer matrix, which relates states in the left lead to states in the right lead. In analogy to equations (3.3) the occupations of these states are written in vectors

$$c^{\mathrm{L}} = (a_1^+, a_2^+, \ldots, a_N^+, a_1^-, a_2^-, \ldots, a_N^-)^T, \tag{3.7a}$$

$$c^{\mathrm{R}} = (b_1^+, b_2^+, \ldots, b_N^+, b_1^-, b_2^-, \ldots, b_N^-)^T, \tag{3.7b}$$

for the left and right lead, respectively. The two vectors are related by the transfer matrix $\mathcal{M}$,

$$c^{\mathrm{R}} = \mathcal{M}\, c^{\mathrm{L}}. \tag{3.8}$$

The advantage of the transfer matrix $\mathcal{M}$ is its multiplicativity property. In a series of samples connected by ideal leads, the total transfer matrix is the product of individual transfer matrices. Another advantage specific to graphene is that the transfer matrix can be related to the evolution operator as we will see below.

From the block structure (3.6) of S and its unitarity, it follows that $\mathcal{M}$ has the block structure

$$\mathcal{M} = \begin{pmatrix} t^{\dagger\,-1} & r't'^{-1} \\ -t'^{-1}r & t'^{-1} \end{pmatrix}. \tag{3.9}$$

The unitarity of the scattering matrix translates into the symplectic property

$$\mathcal{M}^\dagger \Sigma \mathcal{M} = \Sigma, \tag{3.10}$$

where Σ is a diagonal matrix with $\Sigma_{nn} = 1$ for $1 \le n \le N$ and $\Sigma_{nn} = -1$ for $N+1 \le n \le 2N$. As a consequence, the matrix product $\mathcal{M}\mathcal{M}^\dagger$ and its inverse $(\mathcal{M}\mathcal{M}^\dagger)^{-1} = \Sigma\mathcal{M}\mathcal{M}^\dagger\Sigma$ have the same set of eigenvalues. Therefore these $2N$ eigenvalues come in inverse pairs and I can express them as $\exp(\pm 2\xi_n)$, where $\xi_n \ge 0$ and $n = 1, 2, \ldots, N$.

By writing the scattering matrix and the transfer matrix in polar decompositions, one can prove the following relation between the transfer and transmission matrices [100],

$$\frac{\mathcal{M}\mathcal{M}^\dagger}{(1 + \mathcal{M}\mathcal{M}^\dagger)^2} = \frac{1}{4}\begin{pmatrix} tt^\dagger & 0 \\ 0 & t't'^\dagger \end{pmatrix}, \tag{3.11}$$

which is called Pichard formula [105, 100]. The transmission eigenvalues T_n are thus related to the eigenvalues $\exp(\pm 2\xi_n)$ of $\mathcal{M}\mathcal{M}^\dagger$ as

$$T_n = \frac{1}{\cosh^2 \xi_n}, \quad n = 1, 2, \ldots, N. \tag{3.12}$$

In the next section I will express the two most basic transport properties, conductance and noise, in terms of the transmission eigenvalues.

3.3 Transport Properties in Zero-Bias Limit

The scattering approach is a non-equilibrium theory, because an imbalance between the chemical potentials in different reservoirs is required in order to define an electric current. However, the potential difference V between the reservoirs must be sufficiently small, so that the single-particle picture of electron transport remains valid. If we further assume that this potential difference V, which is usually generated by a bias voltage, goes to zero, and assume the limit of zero temperature, then the current is linearly proportional to the bias voltage. In this regime of linear response the formulas for conductance and noise become particularly simple, as they are linear statistics on the transmission eigenvalues. Here I follow ref. [100] and omit the explicit derivation of the intuitively comprehensible formulas from the scattering approach, referring the reader to ref. [102]. Parts of this and the following section are adapted from ref. [106].

First, let us look at the most basic transport property, the two-probe conductance. In the linear response regime it is defined as

$$\mathrm{G} = \lim_{V \to 0} \frac{\bar{I}}{V}, \tag{3.13}$$

where $\bar{I}$ is the time-averaged electrical current through the sample. The two-probe conductance can be expressed through the famous Landauer formula as the sum of the transmission eigenvalues,

$$\mathrm{G} = \mathrm{g}_0 \sum_{n=1}^{N} T_n = \mathrm{g}_0 \,\mathrm{Tr}(t^\dagger t), \quad \mathrm{g}_0 \equiv e^2/h, \tag{3.14}$$

where g_0 is the conductance quantum. In later chapters I will sometimes absorb an integer factor into g_0 accounting for the degeneracies excluded from the channel space (e.g. a 2-fold spin degeneracy in the case of spin-independent transport).

Since I consider the limit of zero temperature, only the transmission eigenvalues exactly at the Fermi energy are relevant for the transport. However, even at zero temperature the current through the sample fluctuates in time due to the discreteness of the electron charge. The next higher moment of charge transfer after the conductance is the shot noise. In the zero-frequency limit it is given by the auto-correlator

$$\mathrm{P} = 2 \int_0^\infty dt \; \overline{\delta I(t + t_0) \delta I(t_0)}, \tag{3.15}$$

where $\delta I(t) = I(t) - \bar{I}$ is the time-dependent current fluctuation, and the overline denotes the average over the initial time t_0. Applying the scattering approach, this transport property can also be expressed in terms of transmission eigenvalues. The

result is [61]

$$\mathrm{P} = \mathrm{P}_0 \sum_{n=1}^{N} T_n(1-T_n), \quad \mathrm{P}_0 \equiv eV\mathrm{g}_0. \tag{3.16}$$

The strongest contribution is from half-open channels, $T_n = 1/2$. If all channels are in the tunneling limit $T_n \ll 1$, one gets

$$\mathrm{P} = e\bar{I} \equiv \mathrm{P}_{\mathrm{Poisson}}. \tag{3.17}$$

This result was already derived in 1918 by W. Schottky [107], who assumed that the transmission of electrons is a Poissonian process. His assumption is indeed correct in the tunneling limit, where the transmission of charge carriers occurs so rarely that such events become uncorrelated.

For any conductor, which is not in the tunneling regime, the shot noise (3.16) is suppressed below the Poissonian value. The source of this correlation is the Pauli principle, according to which no two electrons can share an incoming or outgoing channel. By contrast to the conductance, the shot noise thus contains genuine quantum effects which cannot be explained in classical terms.

The noise is usually quantified by means of the Fano factor, defined as the ratio between the noise and $\mathrm{P}_{\mathrm{Poisson}}$, and expressed in terms of transmission amplitudes as

$$\mathrm{F} = \frac{P}{P_{\mathrm{Poisson}}} = \frac{\sum_{n=1}^{N} T_n(1-T_n)}{\sum_{n=1}^{N} T_n} = \frac{\mathrm{Tr}[t^\dagger t(1-t^\dagger t)]}{\mathrm{Tr}(t^\dagger t)}. \tag{3.18}$$

In order to characterize the whole transmission distribution rather than individual transmission moments, the concept of the full counting statistics is introduced in the next section.

3.4 Full Counting Statistics

The transport properties of a given setup are characterized by conductance, noise, and higher moments of charge transfer. By introducing counting fields the whole characteristics of the distribution can be encoded in a single generating function. This is the idea of the full counting statistics of mesoscopic transport which was developed by Levitov [108]. The concept is introduced in general terms in section 3.4.1 and applied to mesoscopic transport in section 3.4.2.

3.4.1 Full counting statistics in general terms

Let $p(n)$ be a normalized probability distribution function of the number n of a given event, e.g. the number of electrons which are transferred to a particular terminal in a given electronic structure during a fixed detection time (in this case n can be positive or negative). In order to characterize the statistics of the distribution $p(n)$, it is convenient to accumulate these probabilities $p(n)$ in a generating function, the

so-called characteristic distribution function,

$$Z(\chi) = \langle e^{n\chi} \rangle = \sum_n e^{n\chi} p(n), \tag{3.19}$$

where the variable χ is called the counting field. From the normalization of the function $p(n)$ it follows that $Z(0) = 1$. The general moments $\langle n^k \rangle = \sum_n n^k p_n$, which characterize the distribution $p(n)$, are the coefficients of the series expansion of $Z(\chi)$,

$$Z(\chi) = \sum_k \frac{\chi^k}{k!} \langle n^k \rangle, \quad \langle n^k \rangle = \frac{\partial^k}{\partial \chi^k} Z(\chi) \bigg|_{\chi=0}. \tag{3.20}$$

The cumulant generating function (CGF) is given by the logarithm of $Z(\chi)$ and defines the cumulants as the coefficients of its series expansion,

$$\ln Z(\chi) = \sum_{k=1}^{\infty} \frac{\chi^k}{k\,!} m_k, \quad m_k = \frac{\partial^k}{\partial \chi^k} \ln Z(\chi) \bigg|_{\chi=0}. \tag{3.21}$$

The first and the second cumulant are equal to the mean and the variance, $m_1 = \langle n \rangle$, $m_2 = \langle \delta n^2 \rangle$ with $\delta n \equiv n - \langle n \rangle$. The third cumulant is given by $m_3 = \langle \delta n^3 \rangle$ and characterizes the asymmetry of the probability distribution. The higher cumulants are further characteristics of the distribution, while the relations between the cumulants and the correlators are generally more complicated than for the lowest orders.

As an example, let us consider a Poisson process, which describes independent events occurring with constant probability during a given period of time. It was discussed in Sec. 3.3 that the charge transport in the tunneling regime can be described by such a process. The Poisson distribution reads ($n \geq 0$)

$$p(n) = \frac{e^{-\bar{n}}\, \bar{n}^n}{n!}, \tag{3.22}$$

where $\bar{n}$ is the average number. The generating function (3.19) is found as $Z(\chi) = \exp\left((e^{i\chi} - 1)\bar{n}\right)$. The second moment is given by $\bar{n}(1 + \bar{n})$, corresponding to a mean-square deviation $\langle (n - \langle n \rangle)^2 \rangle = \langle n \rangle$. By expanding $\ln Z$ in χ one finds that all cumulants are identical: $m_k = \bar{n}$.

The concept of the counting field can be generalized to an arbitrary number of different processes counted simultaneously. The statistics is then described by a multivariate distribution $p(n_1, \ldots, n_K) \equiv p(\{n\})$, and one can introduce counting fields for each number, $\chi = (\chi_1, \ldots, \chi_K)$. Statistically independent processes factorize in the distribution, e.g. $p(n_1, \ldots, n_K) = p(n_1) \cdot p(n_2, \ldots, n_K)$, and the same applies to the generating function: $Z(\chi) = Z_1(\chi_1) \cdot Z_{\{2,\ldots K\}}(\chi_2, \ldots, \chi_K)$.

3.4.2 Application to mesoscopic transport

The concept of the cumulant generating function can be applied to the problem of electronic transport in the framework of the scattering approach. I start from the same assumptions as above. In particular, different energies and different spin degrees of freedom are assumed to be statistically independent, so that the generating function $Z(\chi)$ factorizes into the according processes. For a single energy and one spin projection, the full counting statistics simplifies drastically due to the Fermi-Dirac statistics of electrons. If we count electrons in individual channels, the distribution function is multivariate. The characteristic function for such a distribution is given by [108]

$$Z(\chi) = \sum_{i_1,\ldots,i_k,j_1,\ldots,j_k} e^{i(\chi_{j_1}+\ldots+\chi_{j_k}-\chi_{i_1}-\ldots-\chi_{i_k})} P_{i_1,\ldots,i_k|j_1,\ldots,j_k}, \tag{3.23}$$

where the sum is over all different multi-particle scattering processes. These processes involve $k \leq m$ particles which are emitted from k different channels $i_1, \ldots, i_k$, and scattered to k different channels $j_1, \ldots, j_k$. The probability $P_{i_1,\ldots,i_k|j_1,\ldots,j_k}$ for such a process depends on the scattering matrix S and on the energy-dependent occupation $f_i(\varepsilon)$ of the incoming channels in the following way,

$$P_{i_1,\ldots,i_k|j_1,\ldots,j_k} = |S^{i_1,\ldots,i_k}_{j_1,\ldots,j_k}|^2 \prod_{i\neq i_\alpha} (1 - f_i(\varepsilon)) \prod_{i=i_\alpha} f_i(\varepsilon). \tag{3.24}$$

Here $S^{i_1,\ldots,i_k}_{j_1,\ldots,j_k}$ is a minor of the scattering matrix S, with rows $j_1, \ldots, j_k$ and columns $i_1, \ldots, i_k$. This corresponds to an antisymmetrized product of k single particle amplitudes, which arises due to the indistinguishability of possible particle paths associated with the particular scattering process. The other factors in equation (3.24) describe the probability that the incoming channels $i_1, \ldots, i_k$ are filled while all other channels are empty.

In this work I consider only transport in two-terminal devices in the limit of zero temperature. At the relevant energy only incoming channels in the left lead are filled, while all other (incoming and outgoing) channels are empty. Furthermore, since I am only interested in the total number of electrons transmitted in all channels, I can use a single counting field χ_L (χ_R) for all channels in the left (right) lead. This means that only a single counting field $\chi \equiv \chi_R - \chi_L$ for the number of transmitted electrons is required. The characteristic distribution function can be written as the following determinant [108],

$$Z(\chi) = \det\left[1 - tt^\dagger + e^\chi\, tt^\dagger\right], \tag{3.25}$$

where I used $rr^\dagger = 1 - tt^\dagger$. The corresponding cumulant generating function is

$$\mathcal{F}(\chi) = \ln\det\left[1 - tt^\dagger + e^\chi\, tt^\dagger\right]. \tag{3.26}$$

Any moment of the transmission distribution is obtained from the derivatives of $\mathcal{F}(\chi)$ with respect to χ. The conductance (3.14) and the Fano factor (3.18) are obtained from the first and second derivatives as

$$\mathrm{G} = \mathrm{g}_0 \lim_{\chi\to 0} \frac{\partial\mathcal{F}}{\partial\chi}, \quad \mathrm{F} = \frac{\mathrm{g}_0}{\mathrm{G}} \lim_{\chi\to 0} \frac{\partial^2\mathcal{F}}{\partial\chi^2}. \tag{3.27}$$

I can rewrite the cumulant generating function (3.26) in terms of the transfer matrix using the Pichard relation (3.11), with the following result

$$\mathcal{F}(\chi) = \frac{1}{2}\ln\det\left[\left(1 - \mathcal{M}\mathcal{M}^\dagger\right)^2 + 4e^\chi\, \mathcal{M}\mathcal{M}^\dagger\right]. \tag{3.28}$$

I will use this approach in the study of the full counting statistics of multilayer graphene in chapter 4.

3.5 Application to Two-Terminal Graphene Device

The scattering approach provides the framework for the transport studies throughout this thesis. After the rather general description I now apply it to a clean rectangular graphene sample in a two-terminal geometry. This provides a conceptual basis for the various models in the subsequent chapters. The scattering approach will be complemented by Green's functions in the study of disordered systems. Using this approach I generally assume that electron-electron interactions can be treated in a mean field approximation. This means that any resistivity or relaxation due to such interactions must be negligible.

The transport calculations in this thesis are restricted to two-terminal devices. In subsection 3.5.1 I introduce the model of the rectangular sample geometry, which will be employed in similar forms throughout this work. In subsection 3.5.2 I discuss the method of wave-function matching, which is the most basic technique for calculating the scattering amplitudes. A similar method is provided by the transfer matrix as discussed in subsection 3.5.3. The spinor structure of charge carriers in graphene leads to a relation between the transfer matrix and the evolution matrix, which describes the propagation in the sample. This relation makes the calculation of scattering amplitudes from the transfer matrix method very convenient and is presented in subsection 3.5.4. Finally, the ballistic transport properties of a monolayer graphene sample are derived in section 3.5.5.

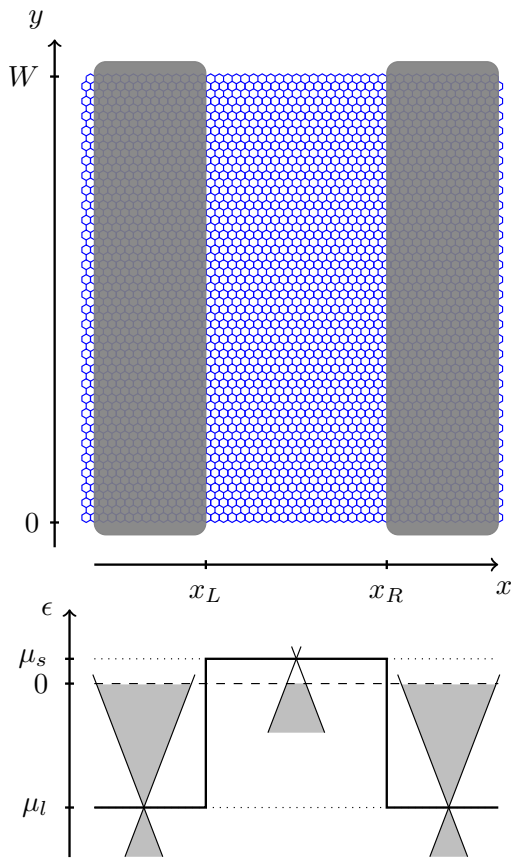

Figure 3.2: Upper panel: Schematics of a rectangular graphene transport device in two-terminal geometry. Lower panel: The corresponding scalar potential model, equation (3.29), in which the sample and lead regions are described by the Dirac Hamiltonian with different doping.

3.5.1 Model of two-terminal graphene device

The charge density in graphene can be controlled by means of the electric field effect. In a typical device the graphene sheet is placed on top of a dielectric substrate, which is usually made of a 300nm thick layer of silicon dioxide. The graphene sheet forms a plane capacitor with the back gate, and the charge density is adjusted by the gate voltage V_{g}. Since the substrate is a source of disorder in the graphene sample, high-mobility devices are often made by freely suspending graphene between the electrical contacts. In such devices the inducible charge density is more limited due to the fragility of the graphene sheet. By using additional top gates one can further induce electrostatic potential steps in the graphene sheet. In the case of multilayer graphene a global top gate in addition to the back gate is useful for inducing a charge without creating a potential difference between the graphene layers.

The two-terminal rectangular geometry considered in the following is shown schematically in figure 3.2. The graphene sheet is contacted at $x < x_L$ and $x > x_R$ by metallic electrodes which act as source and drain for conduction electrons. The isolated section corresponds to the scattering region of length $L = x_R - x_L$, while the contacted regions define the leads. Although the leads connect the sample

with the reservoirs, it is not necessary to model the reservoirs explicitly. Instead the chemical potential in a reservoir determines the occupation of the incoming scattering modes in the corresponding lead far away from the sample. The openness of the system is therefore effectively replaced by the scattering boundary conditions in the asymptotic regions of the leads. Furthermore, I consider the limit of zero bias voltage and zero temperature, so that transport takes place in an infinitesimally small energy range around the Fermi energy.

The leads are assumed to be ideal, which means that they are perfectly conducting and support an infinitely large number of scattering states. Nevertheless there remains some freedom in how the electron propagation is modeled in the ideal leads. The leads consist of a graphene sheet, the electronic properties of which may be strongly altered by the absorption onto the metal. For instance, the leads are modeled as a quantum wire described by the non-relativistic Schrödinger equation in ref. [23] and as strongly doped graphene in ref. [24]. However, it turns out that the various models result in the same ballistic transport properties of weakly doped samples. This is due to the fact that in weakly doped graphene samples only scattering modes with transverse momentum close to the Dirac points contribute to the transport [109]. The conductivity of undoped graphene is of the order of the conductance quantum and thus comparable to that of a metallic sample in the diffusive regime. Therefore the transport through weakly doped graphene is largely independent of the particular model of the contacts. This allows for the definition of effective models [109], for example as graphene with an infinitely strong decoherence term [110]. At energies far away from the Dirac point the transport properties are dependent on the model of the leads [111, 112].

In this work I exclusively employ the most widely used model in which the leads are described by graphene with a large chemical potential due to the charge transfer from the metal surface. The resistance of the metal-graphene interfaces will be generally neglected. I assume that the low-energy effective Hamiltonian applies to the entire system so that the propagation is governed by

$$(-i\hbar v_{\mathrm{F}}\boldsymbol{\sigma}\boldsymbol{\nabla} + \mu(x))\Psi = \varepsilon\Psi, \qquad \mu(x) = \begin{cases} \mu_s, & \text{for } x_L < x < x_R, \\ \mu_l, & \text{for } x < x_L,\ x > x_R. \end{cases} \tag{3.29}$$

The wavelength of free Dirac quasiparticles at energy ε is thus determined by $|\varepsilon - \mu_s| = hv_{\mathrm{F}}/\lambda$ in the sample and by $|\varepsilon - \mu_l| = hv_{\mathrm{F}}/\lambda_{\mathrm{F}}$ in the leads. This model will be used for the most part of the transport studies in this thesis.

In equation (3.29) I have assumed that the interfaces between the sample and the leads are abrupt on the scale of the sample length L, but smooth on the scale of the lattice constant. Furthermore, if one considers a finite energy ε, then the extension of the transitional regions at the interfaces must also be small in comparison with the wavelength λ of quasiparticles in the sample, in order for the model to be

accurate [62]. The oversimple assumption of abrupt sample-lead interfaces will be exchanged in chapter 6 by a self-consistent contact potential, which turns out to be long-range decaying into the sample due to a weak screening. In this more realistic model the doping strength in the leads does have an effect on the transport properties. Finally, I emphasize that although an abrupt interface model implicitly assumes infinitely strong electron-electron interactions, I completely neglect any dynamic effects of interactions in the transport problem.

In the evaluation of the transport properties I will mostly assume that the width W is much larger than the length L, so that the choice of boundary conditions in the transverse y direction is unimportant. For definiteness I consider periodic boundary conditions in y direction, hence the transverse momentum q is quantized as $q_n = 2\pi n/W$ with integer n. This model is of course applicable to any aspect ratio W/L if one bears in mind that the sample has the topology of a cylinder.

In parts of this section I include a constant magnetic field $\boldsymbol{B} = \boldsymbol{\nabla} \times \boldsymbol{A}$ via the minimal coupling (2.29). In this case the Dirac equation in the sample becomes

$$(-i\hbar v_{\mathrm{F}} \boldsymbol{\sigma} \boldsymbol{\nabla} + e\boldsymbol{\sigma} \boldsymbol{A})\Psi = (\varepsilon - \mu_s)\Psi, \tag{3.30}$$

where $e > 0$ is the elementary charge, which is taken positive. In a short and wide sample, $W \gg L$, the vector potential $\boldsymbol{A}$ has the standard gauge freedom, so that it is defined up to an arbitrary gradient function. However, for arbitrary aspect ratio W/L there are restrictions due to the boundary conditions in the y-direction. Periodic boundary conditions in y impose that

$$\int_0^W A_y(x)dy = \Phi_c(x), \tag{3.31}$$

where $\Phi_c(x)$ is the magnetic flux piercing the cylinder in x-direction. Such a flux has an observable effect on the transport properties for $W \lesssim L$. This will be discussed in more detail in chapter 5.

In order to preserve the translational invariance of the system in the y direction I use the Landau gauge

$$\boldsymbol{A}(\boldsymbol{r}) = B \begin{pmatrix} 0 \\ x - \bar{x} \end{pmatrix}, \tag{3.32}$$

where $\bar{x}$ is the position at which the magnetic flux piercing the cylinder equals zero. This position may be within the leads. However, in this work I generally consider the case where the magnetic field in the leads can be neglected, which requires a sufficiently large doping so that $(e/h)|B|L\lambda_{\mathrm{F}} \ll 1$.

3.5.2 Wave function matching in graphene

By employing the scattering approach I assume that the time during which electrons relax phase or energy due to interactions is much larger than the time needed to traverse the scattering region. Under this assumption all transport properties are determined by single-particle scattering amplitudes as described in section 3.3. The transmission and reflection amplitudes are combined in the scattering matrix S [cf. equation (3.6)], which is unitary due to current conservation. The scattering amplitudes from a particular incoming channel are determined (up to an irrelevant phase factor) by the global solution to the Schrödinger equation for a given incoming scattering state. This solution is called the *scattering wave function*, as it describes the scattering of an incoming scattering state in a particular channel. Since the Dirac equation (3.29) describing the entire system is a linear differential equation, the 'boundary' condition at the sample-lead interfaces is the continuity of the wave function, while there are no restrictions on the spatial derivative as in the non-relativistic case.

In the two-terminal setup the scattering wave function due to a left-incident state in channel n can be written as

$$\Psi_{n,L} = \Psi_{n,+} + \sum_m r_{mn}\Psi_{m,-}, \qquad \text{left lead,} \tag{3.33a}$$

$$\Psi_{n,R} = \sum_m t_{mn}\Psi_{m,+}, \qquad \text{right lead,} \tag{3.33b}$$

with matrices of reflection and transmission amplitudes r and t, respectively. The scattering amplitudes r' and t' for right-incident states are defined analogously. Since the scattering region is extended in x, I need to match the scattering wave function with the general solution in the scattering region.

Before doing so, let us first discuss the scattering states in the leads. In monolayer graphene there is just one right-moving and one left-moving scattering spinor for each value of the transverse momentum, hence the channel index corresponds to the transverse momentum quantum number. In the model (3.29) the scattering spinors in the leads obey the Dirac equation

$$v_\mathrm{F}\,\boldsymbol{\sigma}\boldsymbol{p}\,\Psi = [\varepsilon - \mu_l]\Psi, \tag{3.34}$$

where μ_l is the energy shift of the Dirac point with respect to the Fermi energy at $\varepsilon = 0$. In the following I set $\hbar v_\mathrm{F} = 1$ for simplicity. The spectrum is given by $\varepsilon = \mu_l \pm \sqrt{k^2 + q^2}$, where k and q are longitudinal and transverse components of the momentum. The transverse momentum is restricted to $|q| \leq |\varepsilon - \mu_l|$ so that the momentum is always real. As stated above the transverse momentum q is quantized due to the finite width W of the leads. Scattering states corresponding to right (+)-

and left $(-)$-moving charges are found as

$$\Psi_{q,\pm} = \frac{1}{\sqrt{z_q + z_q^*}} e^{iqy \pm ikx} \begin{pmatrix} 1 \\ \pm z_q^{\pm 1} \end{pmatrix}, \qquad z_q = \frac{k + iq}{\varepsilon - \mu_l}, \tag{3.35}$$

where the sign of k corresponds to the band index $\alpha = \mathrm{sign}(\varepsilon - \mu_l)$,

$$k = \alpha \sqrt{(\varepsilon - \mu_l)^2 - q^2}. \tag{3.36}$$

The number z_q lies on the unit circle in the complex plane, so that $z_q^* = 1/z_q$, and is related to the angle of incidence ϕ as $z_q = \alpha e^{\alpha i \phi}$. For approximately normally incident states with $|q| \ll |k|$ one may approximate $z_q = 1$. The states (3.35) are normalized to the unit current,

$$v_{x,\pm} = \Psi_\pm^\dagger \sigma_x \Psi_\pm = \pm 1, \tag{3.37}$$

where I have used the velocity operator $\hat{v}_x = \sigma_x$.

Having determined the scattering states in the leads, I now consider the propagation in the rectangular sample, which is described by the equation (3.30). Note that the solutions are not required explicitly, if one makes use of the evolution operator discussed in subsection 3.5.3. For absent magnetic field the propagating solutions in the sample are given by [cf. equation (2.24)]

$$\Psi_q(\boldsymbol{r}) = C e^{ikx + iqy} \begin{pmatrix} \varepsilon - \mu_s \\ k + iq \end{pmatrix}, \tag{3.38}$$

where $k = \pm\sqrt{(\varepsilon - \mu_s)^2 - q^2}$ and the normalization factor C is determined by the boundary conditions following from the wave-function matching. For $q^2 > (\varepsilon - \mu_s)^2$ evanescent solutions exist, which for $\varepsilon - \mu_s \neq 0$ can be written as

$$\Psi_q(\boldsymbol{r}) = C e^{iqy} e^{-\kappa x} \begin{pmatrix} 1 \\ i\,\mathrm{sgn}(\varepsilon - \mu_s) \sqrt{\frac{q+\kappa}{q-\kappa}} \end{pmatrix}, \tag{3.39}$$

where $\kappa = \pm\sqrt{q^2 - (\varepsilon - \mu_s)^2}$. A special case is the Dirac point energy $\varepsilon - \mu_s = 0$, where the two differential equations of the system (3.30) decouple and the solutions on the two sublattices become independent. Each of the two solutions with $\kappa = \pm|q|$ is completely localized on one of the two sublattices, so that the general solution is

$$\Psi_q(\boldsymbol{r}) = C e^{iqy} e^{\sigma_z q x} \begin{pmatrix} a \\ b \end{pmatrix}, \tag{3.40}$$

where the coefficients a and b are again determined by matching the states with the scattering states (3.35) in the leads.

In the presence of a magnetic field, eigenstates in the sample exist only at the energies of the Landau levels. The solution at the zero energy Landau level, $\varepsilon - \mu_s = 0$, is given by [76]

$$\Psi_q(\boldsymbol{r}) = \exp\left[\mathrm{sgn}(B)\sigma_z \frac{1}{2}\left(\frac{x - \bar{x} - x_0}{\ell_B}\right)^2 + iqy\right]\begin{pmatrix} a \\ b \end{pmatrix}, \tag{3.41}$$

where the position x_0 is related to the transverse momentum as $x_0 = -\hbar q/eB$. The magnetic length is given by equation (2.30), $\ell_B = \sqrt{\hbar/e|B|}$. The solution (3.41) is localized in the form of a Gaussian on one sublattice. The wave function on the other sublattice is exponentially increasing towards the leads. This unlocalized component is only allowed since the sample is finite and the magnetic field is neglected in the strongly doped leads, $|\mu_l| \gg ev_\mathrm{F}|B|L$.

3.5.3 Transfer matrix method

This subsection applies not only to monolayer but also to multilayer graphene if described by the single-valley Dirac-like Hamiltonian (2.48).

The wave-function matching procedure can be carried out in various manners. In order to avoid the additional coefficients of the general solution in the sample I can make use of the evolution matrix, which relates the wave functions at the two interfaces,

$$\Psi|_{x=x_R} = \mathcal{T}\Psi|_{x=x_L}, \qquad \mathcal{T} \equiv \mathcal{T}(x_R, x_L). \tag{3.42}$$

Here the evolution operator $\mathcal{T}(x, x')$ yields a solution Ψ to the Dirac equation (3.30) in the form

$$\Psi(x) = \mathcal{T}(x, x')\Psi(x'). \tag{3.43}$$

The operator itself as a function of its first argument is a solution to the Schrödinger equation with the initial condition $\mathcal{T}(x, x) = 1$. In the case of the single-valley Dirac Hamiltonian its evolution has the multiplication form

$$\frac{d\mathcal{T}}{dx} = \mathcal{A}\mathcal{T}, \tag{3.44}$$

which leads to the multiplicativity property

$$\mathcal{T}(x_2, x_0) = \mathcal{T}(x_2, x_1)\mathcal{T}(x_1, x_0). \tag{3.45}$$

Current conservation is reflected by the property

$$\mathcal{T}^\dagger(x, x')\hat{v}_x\mathcal{T}(x, x') = \hat{v}_x. \tag{3.46}$$

It is often convenient to consider the evolution matrix in transverse momentum space, which relates the wave-function Fourier components in the left and the right

lead as

$$\Psi_q(x_R) = \sum_{q'} \mathcal{T}_{q,q'} \Psi_{q'}(x_L). \tag{3.47}$$

The scattering amplitudes are found by substituting the scattering wave functions at the interfaces. In the case of monolayer graphene scattering channels are defined by the transverse momentum q, so that for left-incident scattering wave functions (3.33) equation (3.47) takes the form

$$\left[\sum_{q'} t_{qq'} \Psi_{q',+}\right]_{x=x_R} = \sum_{q'} \mathcal{T}_{q,q'} \left[\Psi_{q',+} + \sum_{q''} r_{q''q'} \Psi_{q'',-}\right]_{x=x_L}. \tag{3.48}$$

In the case of y-independent scattering the evolution matrix becomes diagonal in transverse momentum space, $\mathcal{T}_{q,q'} = \mathcal{T}_q \delta_{q,q'}$, which implies that the transport is quasi-one-dimensional, $t_{q,q'} = t_q \delta_{q,q'}$.

By solving equation (3.48) for the transmission amplitudes $t_{qq'}$ one may derive the transmission eigenvalues, which are the eigenvalues of $tt^\dagger$ and which determine the transport properties. A more direct approach to the transmission eigenvalues is discussed in the following subsection.

3.5.4 Relation between evolution matrix and transfer matrix

So far I have used the wave-function matching to obtain the transmission amplitudes as the elements of the scattering matrix. An equivalent description of the scattering region is provided by the transfer matrix $\mathcal{M}$ [cf. equation (3.8)]. Transmission eigenvalues can be obtained from the matrix $\mathcal{M}\mathcal{M}^\dagger$ via the Pichard relation (3.11).

One of the peculiar properties of the single-valley Dirac Hamiltonian is the direct relation between the spinor structure and the direction of momentum. This implies a simple relation between the transfer matrix $\mathcal{M}$ and the evolution matrix $\mathcal{T}$ introduced in the previous subsection [33]. In order to account for the multilayer case (N layers), I assume that for each value of the transverse momentum q there are N right-moving and N left-moving scattering states,

$$\Psi_\pm^{(n)} = e^{iqy \pm ikx} \psi_\pm^{(n)}, \quad n = 1, \ldots, N. \tag{3.49}$$

Here $\psi_\pm^{(n)}$ is a $2N$-spinor. I can arrange these spinors in a square matrix P with the columns

$$P_{\bullet n} = \begin{cases} \psi_+^{(n)}, & \text{for } 1 \le n \le N, \\ \psi_-^{(n-N)}, & \text{for } N+1 \le n \le 2N. \end{cases} \tag{3.50}$$

The matrix P is not generally unitary but it is generally invertible. Applying the matrix P^{-1} to a superposition of scattering states with transverse momentum q in the left (right) lead, one obtains the vector c^L (c^R) of scattering amplitudes,

cf. equation (3.7). Since the vectors c^L and c^R are related by the transfer matrix (3.8), while the original states are related by the evolution matrix (3.42), the two matrices are related as

$$\mathcal{T} = P\mathcal{M}P^{-1}. \tag{3.51}$$

Note that for y-dependent scattering $\mathcal{T}$ and $\mathcal{M}$ have a non-trivial structure in transverse momentum space, and the matrix P corresponds to the diagonal matrix of P-matrices in transverse momentum space.

As an example I consider monolayer graphene with the scattering states (3.35). The inverted matrix P is

$$P^{-1} = \frac{1}{\sqrt{z_q + z_q^*}} \begin{pmatrix} z_q^* & 1 \\ z_q & -1 \end{pmatrix}, \tag{3.52}$$

which transforms the scattering states into

$$P^{-1}\Psi_+ = e^{iqy+ikx} \begin{pmatrix} 1 \\ 0 \end{pmatrix}, \tag{3.53a}$$

$$P^{-1}\Psi_- = e^{iqy-ikx} \begin{pmatrix} 0 \\ 1 \end{pmatrix}. \tag{3.53b}$$

The sublattice space is thus transformed into the incoming/outgoing channel space for each particular value of the transverse momentum q.

For normally incident electrons ($q = 0$) one may approximate $z_q = 1$ so that the matrix P becomes unitary, $P = P^{-1} = \mathcal{L} \equiv (\sigma_x + \sigma_z)/\sqrt{2}$. Since the scattering states are normalized to the current, this statement holds generally, because normally incident states are generally eigenstates of the current operator. This fact may be exploited in the limit of strongly doped leads ($\mu_l \gg \max\{hv/L, \mu_s\}$), where the only scattering states relevant for transport are those with negligible transverse momentum in the leads (compared with their longitudinal momentum component). In this case the transmission eigenvalues may be obtained directly from the eigenvalues of $\mathcal{T}\mathcal{T}^\dagger$.

3.5.5 Ballistic transport properties of monolayer graphene

The basic results of this section have been first obtained in ref. [24]. For the application of the transfer matrix technique in graphene see also refs. [113, 33, 114]. Analytical results for the case of a short and wide monolayer sample have been obtained in ref. [62].

In order to solve the transport problem I consider the evolution operator $\mathcal{T}$, which is determined by

$$\partial_x \mathcal{T} = [\sigma_z(q - A_y) + i\sigma_x(\varepsilon - \mu_s)]\,\mathcal{T}, \tag{3.54}$$

where I used the Landau gauge (3.32). Since the transverse momentum q is conserved, the evolution operator in momentum space is given by $\mathcal{T}_{q,q'} = \mathcal{T}_q \delta_{qq'}$, where the evolution operator $\mathcal{T}_q$ fulfills the equation

$$\partial_x \mathcal{T}_q(x, x') = \mathcal{A}(x)\mathcal{T}_q(x, x'), \qquad \mathcal{A}(x) = \sigma_z(q - A_y) + i\sigma_x(\varepsilon - \mu_s), \tag{3.55}$$

with the initial condition $\mathcal{T}_q(x, x) = 1$. The solution to this equation is difficult to obtain away from the Dirac point ($\varepsilon \neq \mu_s$) in the presence of a magnetic field ($B \neq 0$), since in this case the matrix $\mathcal{A}(x)$ is non-commutative with itself at different positions. Therefore, the general solution to this equation has to be written formally as an x-ordered matrix exponent.[1] Due to the conservation of transverse momentum, the transmission matrix is also diagonal, $t_{qq'} = \delta_{qq'} t_q$. Substitution of the scattering states (3.35) into the wave-function matching approach (3.48) gives

$$t_q = (1 + z_q^2) \left[\begin{pmatrix} 1 & z_q \end{pmatrix} \mathcal{T}_q \begin{pmatrix} 1 \\ z_q \end{pmatrix} \right]^{-1}, \tag{3.56}$$

where an irrelevant phase factor has been absorbed in the definition of t_q. In the limit of strongly doped leads the scattering spinors are independent of q so that $z_q = 1$.

In the following I set the doping μ_s to zero, since it only causes an energy shift in the evolution operator $\mathcal{T}_q$, and hence, in the transmission eigenvalues (for strongly doped leads, $|\mu_l| \gg |\mu_s|$). In the absence of any potential the solution to equation (3.55) is given by the matrix exponent

$$\mathcal{T}_q \equiv \mathcal{T}_q(x_R, x_L) = \exp\left\{(\sigma_z q + i\sigma_x \varepsilon)L\right\}, \tag{3.57}$$

where $L = x_R - x_L$. The transmission probability through the rectangular setup with strongly doped leads is found as

$$T_q = \left[\cos^2(kL) + \frac{\varepsilon^2}{k^2} \sin^2(kL) \right]^{-1}, \tag{3.58}$$

where $k = \sqrt{\varepsilon^2 - q^2}$ is the longitudinal wave number. The transmission probability (3.58) is shown in figure 3.3. Due to the absence of backscattering discussed in section 2.1.3, normally incident states are fully transmitted, $T_0 = 1$. For non-zero angles of incidence a single interface between the lead and the sample is generally opaque. However, due to quantum interference certain modes for $q \neq 0$ also feature a perfect transmission through the entire system. These Fabry-Perot oscillations occur as I consider completely coherent transport between the two interfaces.

[1] This is in analogy to the time-ordered matrix exponent that occurs in the evolution operator of an out-of-equilibrium many body system.

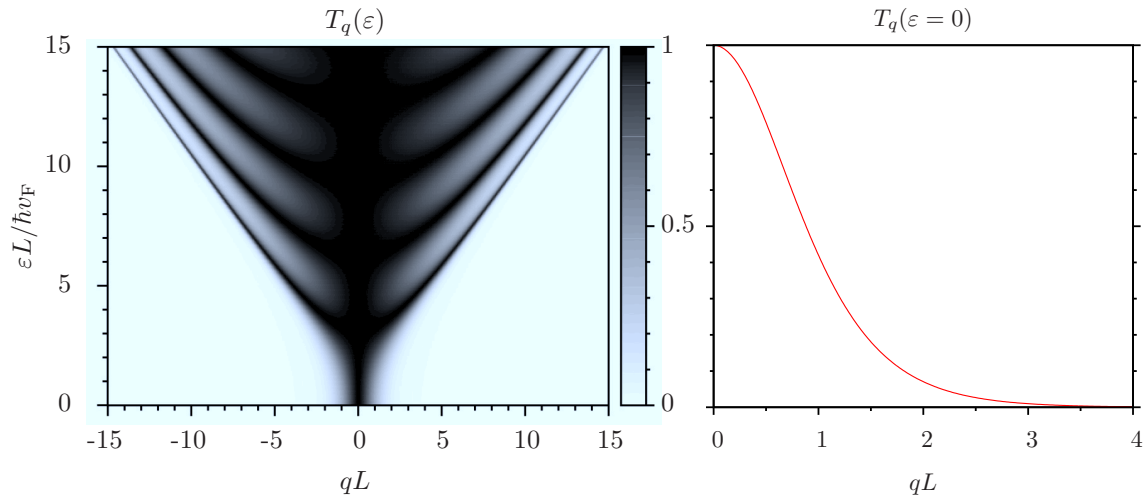

Figure 3.3: Left panel: Transmission T_q trough a clean monolayer sample as a function of transverse momentum q and energy ε (equations (3.58) and (3.59)). Right panel: T_q as a function of q at energy $\varepsilon = 0$ (equation (3.61)). Note that T_q is symmetric in q and ε with respect to $q = 0$ and $\varepsilon = 0$.

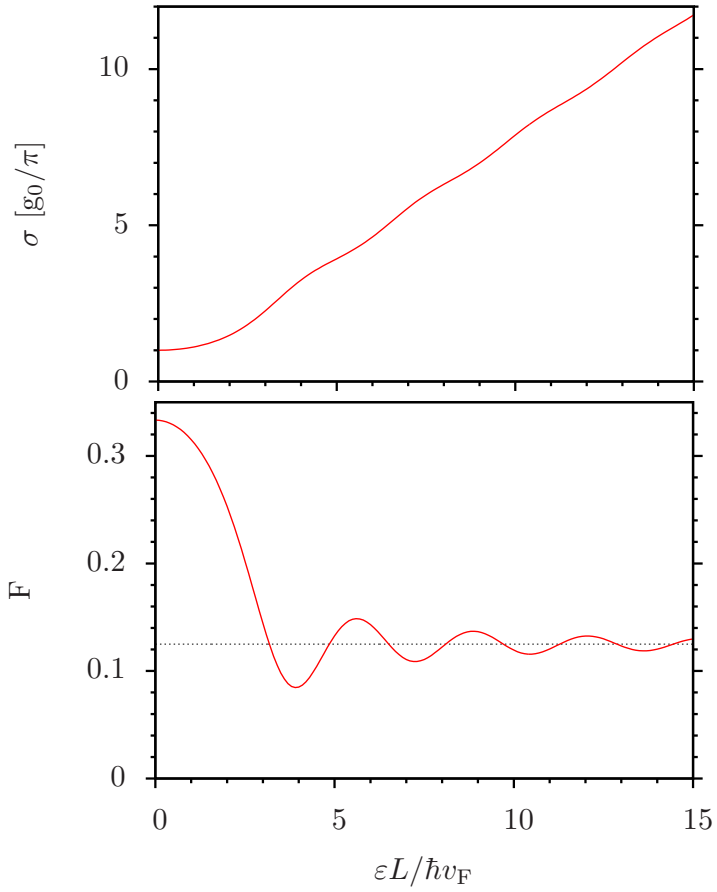

Figure 3.4: Conductivity σ (upper panel) and Fano factor F (lower panel) of a clean rectangular monolayer sample with $W \gg L$ as a function of energy ε. The dotted line corresponds to $F = 1/8$.

For $|q| > |\varepsilon|$ the transport is facilitated by evanescent modes and equation (3.58) can be written as

$$T_q = \frac{2\kappa^2}{\kappa^2 - \varepsilon^2 + q^2 \cosh(2\kappa L)}, \tag{3.59}$$

where $\kappa = \sqrt{q^2 - \varepsilon^2}$. Evanescent modes play a significant role only near the Dirac point, $|\varepsilon| < \hbar v_{\mathrm{F}}/L$, where the number of propagating modes is small.

The conductance G and the Fano factor F are obtained from equations (3.14) and (3.18), respectively. The trace corresponds to the sum over the quantized values of the transverse momentum, which can be replaced by an integration if the junction is short and wide, $W \gg L$. In this case the conductance and Fano factor read

$$\mathrm{G} = \frac{4e^2}{h}\frac{W}{2\pi}\int dq\; T_q, \qquad \mathrm{F} = 1 - \frac{\int dq\; T_q^2}{\int dq\; T_q}, \qquad \text{for } W \gg L, \tag{3.60}$$

where the factor 4 accounts for the (each two-fold) spin- and valley-degeneracies. The conductivity $\sigma = \mathrm{G}L/W$ and the Fano factor obtained by carrying out the integrations numerically are plotted in figure 3.4. For high energies the transport properties become linear in energy (reflecting the linear dispersion relation) with small oscillating corrections due to quantum interference. The high-energy asymptotics of the averaged conductance and Fano factor are given by $\mathrm{G} = (e^2/h)W|\varepsilon|$ and $\mathrm{F} = 1/8$. (These asymptotics are derived in section 4.4.) These results are based on the assumption that the sample-lead interfaces are sharp on the scale of the Fermi wavelength λ, which is inversely proportional to the energy. In the other case, where the interfaces become adiabatically smooth in the high-energy limit, the Fano factor goes to zero [62].

Particularly interesting results are obtained at the energy of the Dirac point, $\varepsilon = 0$. At this energy the evolution matrix is diagonal in the sublattice space, $\mathcal{T} = \exp(qL\sigma_z)$, because the dynamics on each sublattice are independent of each other. The transmission eigenvalues are found as

$$T_q = \frac{1}{\cosh^2(qL)}. \tag{3.61}$$

The transport is facilitated entirely by evanescent modes. This is in strong contrast to conventional semiconductors, where evanescent modes in the band gap exist but do not conduct.

A striking feature of graphene is that the transport properties obtained from equation (3.61) become universal in the limit of large aspect ratio, $W/L \gg 1$. In particular, the conductivity and the Fano factor are given by

$$\sigma = \frac{4e^2}{\pi h}, \qquad \mathrm{F} = \frac{1}{3}, \qquad \text{for } W \gg L. \tag{3.62}$$

The conductance $\mathrm{G} = W\sigma/L$ therefore obeys Ohm's law since it is inversely pro-

portional to the sample length [111]. The Fano factor should be compared with that of a clean metallic system, for which it is zero since the shot noise is absent. The same value $F = 1/3$ is found in a diffusive metallic wire [100]. In fact, this correspondence with diffusive transport holds for the full counting statistics at the Dirac point as discussed in the following chapter. The transport properties (3.62) have been confirmed in experiments with submicron graphene flakes in the short and wide rectangular sample geometry [28, 115, 29, 116].

At the energy of the Dirac point, $\varepsilon = 0$, it is straightforward to take into account a constant magnetic field B. In the case of strongly doped leads it causes a shift of the transverse momentum q by $B(\bar{x} - L/2)$, so that the transmission eigenvalues become

$$T_q = \frac{1}{\cosh^2[qL - BL(\bar{x} - L/2)]}. \tag{3.63}$$

Here I again assumed that the leads are strongly doped. For a short and wide sample, $W \gg L$, the magnetic field is thus not observable in the transport properties at the Dirac point. This statement can be generalized to an arbitrary spatially varying magnetic field as discussed in chapter 4.

3.6 Fischer-Lee Relation and Kubo Formula

The scattering approach provides a complete picture of coherent non-interacting electron transport. It is particularly simple in quasi-one-dimensional systems where transmission amplitudes are easily calculated within the transfer matrix approach. However, calculating the transfer matrix of a disordered or arbitrarily shaped conductor is a complicated task. On the other hand, disorder can be easily incorporated in the Green's functions of the conductor. Green's functions can be viewed as generalized scattering matrices and provide the response at any point caused by an excitation at any other point [117]. Although the two concepts are equivalent for non-interacting transport, the use of Green's functions is much more practical in disordered systems.

Green's functions are often employed in the linear response theory developed by Kubo, which is yet another method to relate transport properties to equilibrium properties [117]. The scattering approach is based on the assumption of a sufficiently small bias voltage, so that the single-electron picture of electron transport remains valid. By contrast, the linear response theory uses the fluctuation-dissipation theorem to relate the equilibrium noise with the conductivity in linear response. The typical regime for employing the Kubo formula is electronic transport in a large system which is driven at finite frequencies, for instance to calculate the optical conductivity.

In this section I derive a Kubo formula for the zero-frequency conductivity directly from the scattering approach. For simplicity I restrict myself to a quasi-one-

dimensional system, so that the scattering states in the leads are orthogonal. In this case the scattering amplitudes can be obtained by projecting the Green's function, describing the entire system including the leads, onto the scattering states, which form a basis. The general derivation is more complicated [117] but can be facilitated by means of generalized orthogonality relations [118]. In the following derivation I follow refs. [104, 119, 120].

Since the transverse motion of the electrons in the leads in a quasi-one-dimensional system is negligible, the scattering states $|\psi_m^{\pm}\rangle$ are eigenstates of the current operator $\hat{v}_x$,

$$\hat{v}_x|\psi_m^{\pm}\rangle = \pm v_m|\psi_m^{\pm}\rangle, \tag{3.64}$$

with the normalization according to

$$\langle\psi_n^+|\psi_m^+\rangle = \langle\psi_n^-|\psi_m^-\rangle = \frac{1}{v_m}\delta_{nm}. \tag{3.65}$$

The left-incident and right-incident scattering state is given by

$$|\psi_n^L\rangle = \begin{cases} e^{ip_n x}|\phi_n^+\rangle + \sum\limits_m r_{mn}e^{-ip_m x}|\phi_m^-\rangle, & \text{left lead,} \\ \sum\limits_m t_{mn}e^{ip_m x}|\phi_m^+\rangle, & \text{right lead.} \end{cases} \tag{3.66}$$

$$|\psi_n^R\rangle = \begin{cases} \sum\limits_m t'_{mn}e^{-ip_m x}|\phi_m^-\rangle, & \text{left lead,} \\ e^{-ip_n x}|\phi_n^-\rangle + \sum\limits_m r'_{mn}e^{ip_m x}|\phi_m^+\rangle, & \text{right lead.} \end{cases} \tag{3.67}$$

I start by expanding the retarded Green's function from the left lead to the right lead in left-incident scattering states as,

$$\hat{G}^R(x \in R, x' \in L) = \sum_n |\psi_n^L(x)\rangle\langle a_n(x')|. \tag{3.68}$$

In order to find the states $\langle a_n(x')|$, I move the point x to the left lead and substitute the scattering state (3.66),

$$\hat{G}^R(x' + 0, x' \in L) = \sum_n \left[e^{ip_n x'}|\phi_n^+\rangle + \sum_m r_{mn}e^{-ip_m x'}|\phi_m^-\rangle \right] \langle a_n(x')|. \tag{3.69}$$

The retarded Green's function obeys the following equation in the ideal leads,

$$(\varepsilon + i\eta + i\hat{v}_x\partial_x)\hat{G}^R(x, x') = \delta(x - x'), \qquad (\eta \to 0+), \tag{3.70}$$

where the dispersion is linear (as for 'heavily' doped mono- or few-layer graphene), and the transverse part of the Hamiltonian has been neglected. Integrating equa-

tion (3.70) from $x = x' - 0$ to $x = x' + 0$ yields

$$\hat{G}^R(x' - 0, x' \in L) = \hat{G}^R(x' + 0, x' \in L) + i\hat{v}_x^{-1}. \tag{3.71}$$

Using $\hat{v}_x^{-1} = \sum_m (|\phi_m^+\rangle\langle\phi_m^+| - |\phi_m^-\rangle\langle\phi_m^-|)$ one obtains

$$\hat{G}^R(x' - 0, x' \in L) = \sum_n \Big[|\phi_n^+\rangle \left(e^{ip_n x'} \langle a_n(x')| + i\langle\phi_n^+| \right) \\ -i|\phi_n^-\rangle\langle\phi_n^-| + \sum_m r_{mn} e^{-ip_m x'} |\phi_m^-\rangle\langle a_n(x')| \Big]. \tag{3.72}$$

The term $i\eta$ in equation (3.70) determines that the retarded solution contains only right- (left-) propagating modes in the right (left) lead. Thus, in equation (3.72) all terms proportional to $|\phi_n^+\rangle$ must vanish, which determines

$$\langle a_n(x')| = -ie^{-ip_n x'} \langle\phi_n^+|. \tag{3.73}$$

Therefore equation (3.72) becomes

$$\hat{G}^R(x - 0, x \in L) = -i \sum_{mn} |\phi_m^-\rangle \, e^{-ip_m x} \; r_{mn} \; e^{-ip_n x} \langle\phi_n^+| - i \sum_n |\phi_n^-\rangle\langle\phi_n^-|. \tag{3.74}$$

The reflection amplitudes can thus be written as

$$r_{mn} = iv_m v_n e^{i(p_m + p_n)x} \langle\phi_m^-|\hat{G}^R(x \in L, x \in L)|\phi_n^+\rangle. \tag{3.75}$$

Similarly, the retarded Green's function from left to right lead is given by

$$\hat{G}^R(x \in R, x' \in L) = -i \sum_{mn} |\phi_m^+\rangle \, e^{ip_m x} \; t_{mn} \; e^{-ip_n x'} \langle\phi_n^+|, \tag{3.76}$$

so that transmission amplitudes can be expressed as

$$t_{mn} = iv_m v_n e^{ip_n x' - ip_m x} \langle\phi_m^+|\hat{G}^R(x \in R, x \in L)|\phi_n^+\rangle. \tag{3.77}$$

The relations (3.75) and (3.77) between scattering amplitudes and Green's functions are referred to as Fisher-Lee relations.

The advanced Green's function from right to left lead is found as the Hermitian conjugate of equation (3.76),

$$\hat{G}^A(x' \in L, x \in R) = i \sum_{mn} |\phi_m^+\rangle \, e^{ip_m x'} \; t_{nm}^* \; e^{-ip_n x} \langle\phi_n^+|. \tag{3.78}$$

Using equations (3.76), (3.78) I can write the moments of transmission matrix

square in terms of correlators of current operators as

$$\mathrm{Tr}(t^\dagger t)^n = \mathrm{Tr}_y[\,\hat{v}_x\,\hat{G}^R(x\in R, x'\in L)\,\hat{v}_x\,\hat{G}^A(x'\in L, x\in R)\,]^n. \tag{3.79}$$

For $n=1$ this equation is equivalent to the Kubo formula for conductivity. In this work I simply refer to this equation as the Kubo formula. It is also known as Fisher-Lee formula. The trace Tr_y in equation (3.79) includes transverse coordinates, corresponding to the integration over both transverse coordinates y and y'. In fact, the choice of these two cross-sections is arbitrary. Due to current conservation the points x and x' can be placed anywhere in the leads or even in the sample. It is often convenient to place these points at the interfaces between the leads and the sample, so that

$$\mathrm{Tr}(t^\dagger t)^n = \int dy \int dy'\,\mathrm{Tr}[\,\hat{v}_x\,\hat{G}^R(x_R, x_L; y, y')\,\hat{v}_x\,\hat{G}^A(x_L, x_R; y', y)\,]^n. \tag{3.80}$$

The Kubo formula (3.80) provides any moment of the transmission distribution. In the next section I will use this formula to construct a cumulant generating function in terms of Green's functions.

3.7 Matrix Green's Function Formalism

Any moment of the transmission distribution is expressed in the Kubo formula (3.80) in terms of retarded and advanced Green's functions. In fact, it is also possible to facilitate a relation between the full counting statistics and the Green's functions. This idea was developed by Nazarov [104]. Here I follow [104, 120, 121] and notes by P. Ostrovsky.

The key idea of this concept is to introduce a multi-component Green's function $\mathcal{G}(\boldsymbol{r}, \boldsymbol{r}')$, which, in the absence of any source field, just corresponds to the diagonal matrix of retarded and advanced Green's functions. The new space is called the Keldysh or retarded-advanced (RA) space. The two component Green's functions are mixed at two positions by two fictitious source fields ζ_+ and ζ_-. It is most convenient to place the source field ζ_+ (ζ_-) at the left (right) sample-lead interface. More precisely, the matrix Green's function $\mathcal{G}(\boldsymbol{r}, \boldsymbol{r}')$ in the external source fields is defined by

$$\mathcal{G}^{-1}\mathcal{G}(\boldsymbol{r}, \boldsymbol{r}') = \delta(\boldsymbol{r}-\boldsymbol{r}'), \quad \mathcal{G}^{-1} = \begin{pmatrix} \hat{G}_R^{-1} & -\hat{v}_x\zeta_+\delta(x-x_L) \\ -\hat{v}_x\zeta_-\delta(x-x_R) & \hat{G}_A^{-1} \end{pmatrix}, \tag{3.81}$$

where $\hat{G}_{R,A}^{-1} = \varepsilon \pm i\eta - H$. Note that here and in the following the notation of a matrix inversion includes the spatial coordinates corresponding to a discretized

space. I now introduce the functional determinant

$$\mathcal{F} = \mathrm{Tr}_{\boldsymbol{r}} \ln \mathcal{G}^{-1} = \ln \det{}_{\boldsymbol{r}} \mathcal{G}^{-1}, \tag{3.82}$$

where the trace includes spatial coordinates. A relation to a cumulant generating function may be established via the following steps,

$$\det \mathcal{G}^{-1} \propto \det \begin{pmatrix} 1 & -\hat{v}_x \zeta_+ \delta_L \hat{G}^R \\ -\hat{v}_x \zeta_- \delta_R \hat{G}^A & 1 \end{pmatrix} \tag{3.83}$$

$$= \det \left(1 - \zeta_+ \zeta_- \hat{v}_x \delta_L \hat{G}^R \hat{v}_x \delta_R \hat{G}^A \right) \tag{3.84}$$

$$= \det \left(1 - \zeta_+ \zeta_- t^\dagger t \right), \tag{3.85}$$

where in the last step I have used the Kubo formula (3.79). Therefore the function $\mathcal{F}$ defined in equation (3.82) is a cumulant generating function equivalent to the one defined in equation (3.26), but with a different choice of counting fields, $\zeta_+\zeta_- = 1 - e^\chi$. The function $\mathcal{F}$ is only defined up to a constant. Its negative can be understood as the 'free energy' of the system in the external source fields [120], which has a minimum for $\zeta_+ = \zeta_- = 0$.

It is convenient to introduce another cumulant generating function of the transmission matrix square as

$$F(\zeta_+\zeta_-) = \mathrm{Tr} \left[\frac{t^\dagger t}{1 - \zeta_+ \zeta_- \, t^\dagger t} \right]. \tag{3.86}$$

The expansion of $F(z)$ in small values of z provides the moments of the transmission distribution,

$$F(z) = \sum_{n=0}^{\infty} z^n \, \mathrm{Tr}(t^\dagger t)^{n+1}. \tag{3.87}$$

The generating function (3.86) is just the derivative of $\mathcal{F}$ with respect to one source field,

$$F(\zeta_+\zeta_-) = -\frac{1}{\zeta_+} \frac{\partial \mathcal{F}}{\partial \zeta_-} = -\frac{1}{\zeta_-} \frac{\partial \mathcal{F}}{\partial \zeta_+}. \tag{3.88}$$

Substituting equations (3.81) and (3.82) one finds the following expressions for the cumulant generating function in terms of the matrix Green's function,

$$F(\zeta_+\zeta_-) = \frac{1}{\zeta_-} \, \mathrm{Tr}_y \left[\begin{pmatrix} 0 & \hat{v}_x \\ 0 & 0 \end{pmatrix} \mathcal{G}(x_L, x_L) \right] = \frac{1}{\zeta_+} \, \mathrm{Tr}_y \left[\begin{pmatrix} 0 & 0 \\ \hat{v}_x & 0 \end{pmatrix} \mathcal{G}(x_R, x_R) \right]. \tag{3.89}$$

Let us consider the conductance as an example. To first order in the source fields, the matrix Green's function defined by equation (3.81) is found as

$$\mathcal{G} \simeq \begin{pmatrix} \hat{G}^R & \hat{G}^R \hat{v}_x \zeta_+ \delta_L \hat{G}^A \\ \hat{G}^A \hat{v}_x \zeta_- \delta_R \hat{G}^R & \hat{G}^A \end{pmatrix} + \mathcal{O}(\zeta_+\zeta_-). \tag{3.90}$$

Substitution into equation (3.89) gives the 0th-order term of the expansion of $F(z)$,

$$F(\zeta_+\zeta_-) \simeq \mathrm{Tr}_y\, \hat{v}_x \hat{G}^R(x_R, x_L)\hat{v}_x \hat{G}^A(x_L, x_R) + \mathcal{O}(\zeta_+\zeta_-). \tag{3.91}$$

The right hand side is just the Kubo formula (3.79) for the conductance and therefore agrees with the 0th-order term $F(0)$ as defined by equation (3.86).

Equation (3.88) shows that the two source fields $\zeta_\pm$ are equivalent in $\mathcal{F}$. Therefore one can consider a special case of two equal source fields $\zeta_+ = \zeta_- = \zeta$, so that

$$F(\zeta^2) = -\frac{1}{2\zeta}\frac{\partial \mathcal{F}}{\partial \zeta}. \tag{3.92}$$

The conductance can also be obtained by differentiating twice with respect to the source field,

$$\mathrm{G} = \mathrm{g}_0 F(0) = -\frac{1}{2}\,\mathrm{g}_0 \left[\frac{1}{\zeta}\frac{\partial \mathcal{F}}{\partial \zeta}\right]_{\zeta=0} = -\frac{1}{2}\,\mathrm{g}_0 \left.\frac{\partial^2 \mathcal{F}}{\partial \zeta^2}\right|_{\zeta=0}. \tag{3.93}$$

The Fano factor is given by

$$\mathrm{F} = 1 - \frac{1}{2}\left.\frac{\partial^2 F/\partial\zeta^2}{F}\right|_{\zeta=0} = 1 - \frac{1}{6}\left.\frac{\partial^4 \mathcal{F}/\partial\zeta^4}{\partial^2 \mathcal{F}/\partial\zeta^2}\right|_{\zeta=0}. \tag{3.94}$$

Note that the conductance quantum g_0 includes any degeneracies that are not included in the cumulant generating function.

Chapter 4 – Ballistic Transport in Chiral Symmetric Few-Layer Graphene

Few-layer graphene should be considered not as a single material but as a whole class of materials due to the manifold stacking configurations [55]. Even for the two most regular stacking types ABA and ABC the band structure in the minimal tight-binding model strongly depends on the number and the stacking of layers. However, as discussed in section 2.2, the multilayers with natural stacking order have a common property, which is the chiral symmetry. It implies the symmetry of the band structure with respect to the energy of the degeneracy points, $\varepsilon = 0$. In this chapter I will explore the consequences of this symmetry on the ballistic transport properties of undoped graphene multilayers.

The model Hamiltonian and its properties are discussed in section 4.1. The leads are modeled as heavily doped regions in the same way as discussed in section 3.5. In this chapter I include additional terms, namely weak crystal strains and arbitrary magnetic field, which both preserve the chiral symmetry in the case of an undoped sample.

The methods described in section 4.2 correspond to those introduced in the previous chapter. Here I concentrate on the cumulant generating function discussed in section 3.4, which contains not only the conductance and the noise but all higher moments of charge transfer.

In section 4.3 I use the transfer matrix approach to study ballistic transport in undoped graphene multilayers. A non-unitary gauge transformation is shown to reduce the transport problem in undoped few-layer graphene to transport in isolated monolayers. In this way the transport properties are related to the symmetry of the band structure. For all considered models the Fermi surface at $\varepsilon = 0$ remains point-like and the transport is facilitated entirely by evanescent modes, which leads to the same pseudo-diffusive transport regime as in monolayer graphene. As long as the chiral symmetry is preserved, this universality persists up to an arbitrary number of layers as well as for arbitrary perturbations such as weak crystal strains, arbitrary magnetic field, and interlayer hopping disorder.

In section 4.4 the transport properties of doped few-layer graphene samples are evaluated, where the electrostatic potential is assumed to be identical in all layers, so that the band-structure is not affected. I find that the transport properties strongly depend on the stacking configuration and are less universal due to the sample-specific Fabri-Perot oscillations. These oscillations appear in the monolayer transport properties as well (see figure 3.4), but their amplitude in a monolayer is suppressed due to the perfect transmission of normally incident electrons. The energy-dependence of the transport properties will be further analyzed by averaging

over the Fabri-Perot oscillations. Above the highest band threshold the transport properties are found to have universal asymptotics independent of the stacking type.

4.1 Model

The model is based on the nearest-neighbour tight-binding approximation discussed in section 2.2. The chiral symmetry is preserved for the regular stacking types, Bernal (AB$\cdots$) and rhombohedral (ABC$\cdots$), and for all irregular ones excluding sequences of the type AA. The model Hamiltonian is given by the sum of four terms

$$H = H_0 + H_A + H_S + H_\perp, \tag{4.1}$$

where H_0 describes the system of M uncoupled monolayers, H_A and H_S account for magnetic field and weak internal strain, correspondingly, and $H_\perp$ takes into account the coupling between the layers.

In the effective mass approximation for the in-plane dynamics, the Hamiltonian of M isolated monolayers,

$$H_0 = (-\mathrm{i}\hbar v_\mathrm{F}\, \boldsymbol{\sigma}\cdot\boldsymbol{\nabla}) \otimes \tau_0 \otimes \mathbb{1}_M, \tag{4.2}$$

consists of M copies of the familiar 2D Dirac equation. The matrix τ_0 is the unit matrix in valley space. The Hamiltonian H_0 is also a unit matrix in spin space, which is omitted in the notation. Since the Zeeman splitting is neglected, the external magnetic field only couples to the orbital momentum and is described by the term

$$H_A = e v_\mathrm{F} \boldsymbol{\sigma}\cdot\hat{\boldsymbol{A}} \otimes \tau_0, \tag{4.3}$$

where $\hat{\boldsymbol{A}}(\boldsymbol{r}) = \mathrm{diag}(\boldsymbol{A}_1, \boldsymbol{A}_2, \ldots, \boldsymbol{A}_M)$ and $\boldsymbol{A}_m$ is the vector potential in the m-th layer. A weak crystal strain can be taken into account by a similar term [122]

$$H_S = \boldsymbol{\sigma}\cdot\hat{\boldsymbol{S}} \otimes \tau_z, \tag{4.4}$$

where $\hat{\boldsymbol{S}}(\boldsymbol{r}) = \mathrm{diag}(\boldsymbol{S}_1, \boldsymbol{S}_2, \ldots, \boldsymbol{S}_M)$ is the crystal strain, e.g. due to ripples, and τ_z stands for the Pauli matrix in the valley space. Intrinsic out-of-plane deformations are much weaker in multilayer than in monolayer graphene, but ripples can also be induced by substrate inhomogeneities.

The interlayer hopping is described by the term (using a different phase conven-

tion than in equation (2.49))

$$H_\perp = \frac{t_\perp}{2} \begin{pmatrix} 0 & s_1 & 0 & 0 & \vdots \\ s_1^\dagger & 0 & s_2 & 0 & \vdots \\ 0 & s_2^\dagger & 0 & s_3 & \vdots \\ 0 & 0 & s_3^\dagger & 0 & \vdots \\ \dots & \dots & \dots & \dots & \ddots \end{pmatrix}, \tag{4.5}$$

with $t_\perp = 0.3\text{-}0.4\,\mathrm{eV}$ and $s_n = \sigma^\pm = \sigma_x \pm \mathrm{i}\sigma_y$, where the choice of sign depends on the stacking order. The energetically most favourable configuration is the Bernal stacking (AB) characterised by $s_{2m} = \sigma_+$, $s_{2m+1} = \sigma_-$. The less favourable rhombohedral configuration (ABC) corresponds to $s_m = \sigma_+$ for $m = 1, 2, \dots M-1$. To simplify the notations I omit outer products and let $\hbar v_\mathrm{F} = 1$ in those expressions where it cannot cause confusion.

The central property of this model is the chiral symmetry

$$\sigma_z H \sigma_z = -H, \tag{4.6}$$

which holds for any spatial dependence of the vector potential $\boldsymbol{A}$, strain field $\boldsymbol{S}$, and the hopping parameter $t_\perp$. It follows from the chiral symmetry that the spectrum determined by the 'Dirac' equation, $H\Psi = \varepsilon\Psi$, is symmetric with respect to $\varepsilon = 0$. In particular, for every eigenstate Ψ at energy ε there is an eigenstate $\sigma_z\Psi$ at energy $-\varepsilon$ with the same wave vector.

Analytical expressions for the dispersion relation are available for regular multilayers with $H_A = H_S = 0$, see equations (2.52) and (2.54). The spectrum of the ABC-stacked multilayer is gapless and contains exactly two branches touching at $\varepsilon = 0$ [88],

$$\varepsilon_{\boldsymbol{k}} = \pm t_\perp (|\boldsymbol{k}|\ell_\perp)^M + t_\perp \mathcal{O}\left((|\boldsymbol{k}|\ell_\perp)^{M+1}\right), \tag{4.7}$$

where $\ell_\perp \equiv \hbar v_\mathrm{F}/t_\perp = 1.6\text{-}2.2\,\mathrm{nm}$ and $\boldsymbol{k}$ is the wave-vector. The other $2(M-1)$ branches are gapped. The spectrum of the AB-stacked multilayer is given by [86]

$$\varepsilon_{m,\boldsymbol{k}} = t_\perp c_m \pm t_\perp \sqrt{|\boldsymbol{k}|^2\ell_\perp^2 + c_m^2}, \quad c_m = \cos\frac{\pi m}{M+1}, \tag{4.8}$$

where $m = 1, 2, \dots, M$. The result (4.8) is due to the exact mapping [65] onto a system of $M/2$ bilayers (for even M) or onto a system of a single monolayer and $(M-1)/2$ bilayers (for odd M). For both models (4.7) and (4.8) the Fermi surface at $\varepsilon = 0$ becomes point-like. We shall see in section 4.3 that this property extends to a general model with arbitrary spatially dependent terms H_A, H_S and $H_\perp$.

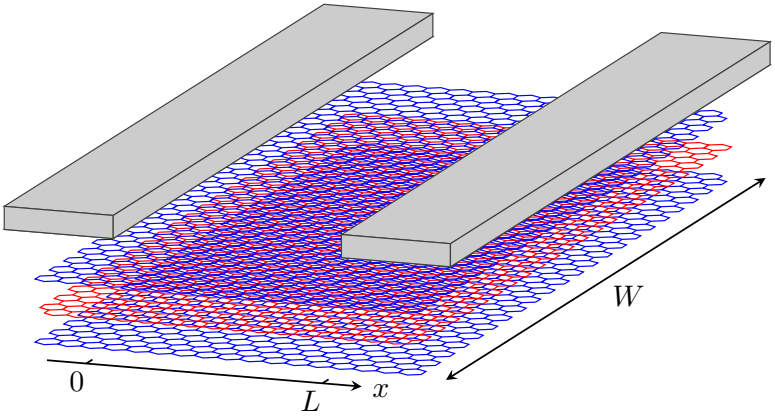

Figure 4.1: Schematic view of a rectangular trilayer graphene sample contacted by metallic leads.

4.2 Method

The transport properties are calculated from the Landauer-Büttiker scattering approach as outlined in chapter 3. Following the model introduced in section 3.5.1 I describe the leads in the two-terminal setup depicted in figure 4.1 as multilayer regions with a large chemical potential, thereby assuming sharp potential steps at the interfaces $x = 0$ and $x = L$. The potential steps are regarded as smooth on the scale of the lattice constant a, so that inter-valley scattering can be neglected. Since the sample itself is regarded as clean, the only scattering takes place at the sample-lead interfaces.

I focus on the limit $W \gg L$, where W is the width and L is the length of the rectangular sample. Without loss of generality I apply periodic boundary conditions in the transverse y direction, (a particular form of the boundary conditions is irrelevant for $W \gg L$), hence the momentum quantization in the leads is given by $q_n = 2\pi n/W$, where q stands for the projection of the momentum onto the y axis.

The full counting statistics for the charge transport at zero frequency and temperature is determined by the cumulant generating function [cf. equation (3.26)]

$$\mathcal{F}(\chi) = \ln \det \left[1 - \hat{t}\hat{t}^\dagger + \mathrm{e}^{\chi}\, \hat{t}\hat{t}^\dagger\right], \tag{4.9}$$

where χ is the counting field. The matrix of transmission amplitudes for the scattering states incident in the left (right) lead at a given energy ε are denoted by $\hat{t}$ ($\hat{t}'$). For $W \gg L$ the summation over transverse momentum q may be replaced by an integration, so that equation (4.9) can be written in terms of the q-dependent transmission eigenvalues (which are the eigenvalues of $\hat{t}\hat{t}^\dagger$) as

$$\mathcal{F}(\chi) = \frac{W}{2\pi} \int dq \sum_m \ln\left[1 + (e^{\chi} - 1)\, T_m(q)\right]. \tag{4.10}$$

In order to obtain the transport properties from the transfer matrix approach,

I use the Pichard relation [cf. equation (3.11)] between the transmission matrices and the transfer matrix $\mathcal{M}$,

$$\frac{\mathcal{M}\mathcal{M}^\dagger}{\left(1+\mathcal{M}\mathcal{M}^\dagger\right)^2} = \frac{1}{4}\begin{pmatrix} \hat{t}\hat{t}^\dagger & 0 \\ 0 & \hat{t}'\hat{t}'^\dagger \end{pmatrix}. \tag{4.11}$$

Due to the rigid boundary conditions the transmission eigenvalues can be equally characterized by the eigenvalues of $\mathcal{T}\mathcal{T}^\dagger$, where $\mathcal{T}$ is the evolution matrix. In particular, the cumulant generating function (4.9) can be written as [cf. equation (3.28)]

$$\mathcal{F} = \frac{1}{2}\ln\det\left[\left(1-\mathcal{T}\mathcal{T}^\dagger\right)^2 + 4\mathrm{e}^{\chi}\,\mathcal{T}\mathcal{T}^\dagger\right]. \tag{4.12}$$

The conductance and the Fano factor are given by the derivatives [cf. equations (3.27)]

$$\mathrm{G} = \mathrm{g}_0 \lim_{\chi\to 0}\frac{\partial\mathcal{F}}{\partial\chi}, \qquad \mathrm{F} = (\mathrm{g}_0/\mathrm{G})\lim_{\chi\to 0}\frac{\partial^2\mathcal{F}}{\partial\chi^2}, \tag{4.13}$$

where $\mathrm{g}_0 = 4e^2/h$ is the conductance quantum including the spin and valley degeneracies.

4.3 Transport in Undoped Few-layer Graphene

As discussed in section 3.5.5, the conductance of a ballistic monolayer setup is given by $\mathrm{G} = \sigma W/L$, where the two-terminal conductivity, σ, approaches the universal value $4e^2/\pi h$ at zero energy, while the Fano factor takes on the value $\mathrm{F} = 1/3$ as in a diffusive system. In [63] the case of bilayer graphene has been studied in an analogous model. The conductivity at $\varepsilon = 0$ is found to be twice as large as for a monolayer, while the Fano factor is given by the same value 1/3. In this section I extend these findings to a general model of few-layer graphene.

The chiral symmetry (4.6) suggests to make use of a local gauge transformation [123],

$$\Psi(\boldsymbol{r}) = \mathrm{e}^{\mathrm{i}\hat{\Omega}(\boldsymbol{r})}\Phi(\boldsymbol{r}), \tag{4.14}$$

where the matrix $\hat{\Omega}(\boldsymbol{r})$ yields the equation

$$-\boldsymbol{\sigma}\boldsymbol{\nabla}\hat{\Omega} = H_A + H_S + H_\perp. \tag{4.15}$$

The matrix $\hat{\Omega}(\boldsymbol{r})$ commutes with σ_z due to the chiral symmetry (4.6). Therefore the transformation (4.14) relates the zero-energy eigenstate, Ψ_0, of the full Hamiltonian, $H\Psi_0 = 0$, to the eigenstate, Φ_0, of the bare system, $H_0\Phi_0 = 0$. Since the spectrum of H_0 is gapless at $\varepsilon = 0$ and the Fermi surface is degenerate at $\varepsilon = 0$, the same properties apply to the full model, H. Below I show that at $\varepsilon = 0$ the transformation (4.14) also reduces the transport properties of the full model, H, to the transport

properties of monolayers described by H_0. Note that the transformation itself is applicable at any energy.

In general the matrix $\hat{\Omega}$ can be decomposed in sublattice space into a term proportional to σ_0 and a term proportional to σ_z. The σ_z-term is responsible for the spectra of H and H_0 to be different at $\varepsilon \neq 0$. Explicit expressions for $\hat{\Omega}$ are given below for a multilayer without magnetic and strain field, and for a monolayer with constant magnetic field in section 5.4.

The application of the transformation (4.14) to the transport problem in graphene multilayers is restricted to the vicinity of the degeneracy point, $|\varepsilon| \ll \{\hbar v_{\mathrm{F}}/L, t_\perp\}$, and relies on the model of the leads as strongly doped multilayer regions. Here I start from a simple case of ballistic multilayer in the absence of magnetic and strain fields, $H_A = H_S = 0$. In this case, the gauge transformation (4.14) reduces to $\Psi = \mathrm{e}^{\mathrm{i}\hat{\Sigma}x}\Phi$ with $\hat{\Sigma} = -\sigma_x H_\perp$. Due to the non-Hermiticity of $\hat{\Sigma}$ this transformation is non-unitary. Using the transfomation together with the evolution matrix for a monolayer at $\varepsilon = 0$ [cf. equation (3.57)], one obtains the evolution matrix as

$$\mathcal{T} = \mathrm{e}^{qL\sigma_z}\mathrm{e}^{\mathrm{i}\hat{\Sigma}L}, \qquad \mathcal{T}\mathcal{T}^\dagger = \begin{pmatrix} \mathrm{e}^{2qL}\hat{P} & 0 \\ 0 & \mathrm{e}^{-2qL}\hat{P}^{-1} \end{pmatrix}, \tag{4.16}$$

with $\mathrm{diag}(\hat{P}, \hat{P}^{-1}) = \mathrm{e}^{\mathrm{i}\hat{\Sigma}L}\mathrm{e}^{-\mathrm{i}\hat{\Sigma}^\dagger L}$. Here I used that the matrices σ_z and $\hat{\Sigma}$ commute. The eigenvalues of the matrix $\hat{P}$ are parameterised by $e^{-2\kappa_m L}$. Since the eigenvalues coincide with those of $\hat{P}^{-1}$, they appear in pairs with $\kappa_{m,m'} = \pm|\kappa_m|$. (The unpaired eigenvalue for odd M corresponds to $\kappa_m = 0$.) From equations (4.16), (4.11) one finds individual transmission probabilities as

$$T_m(q) = \left[\cosh^2(q - \kappa_m)L\right]^{-1}, \qquad m = 1, 2, \ldots M. \tag{4.17}$$

The wave numbers κ_m play the role of momentum shifts, which depend on the stacking configuration. In the limit $W \gg L$ the quantization of q is dense and therefore the values of these momentum shifts are irrelevant. Let us first evaluate the full counting statistics for this case. By writing the logarithmic function in equation (4.10) as a Taylor series and using the identity

$$\int_{-\infty}^{\infty} d\xi \cosh^{-2n}(\xi) = \frac{\sqrt{\pi}\Gamma(n)}{\Gamma(1/2 + n)}, \qquad \text{for } n > 0, \tag{4.18}$$

the zero-energy generating function is found as

$$\mathcal{F}(\chi) = -M\frac{W}{\pi L}\left[\arccos(e^{\chi/2})\right]^2, \qquad \text{for } W \gg L. \tag{4.19}$$

Thus the full counting statistics of charge transport is equivalent to that of M isolated layers of graphene in parallel.

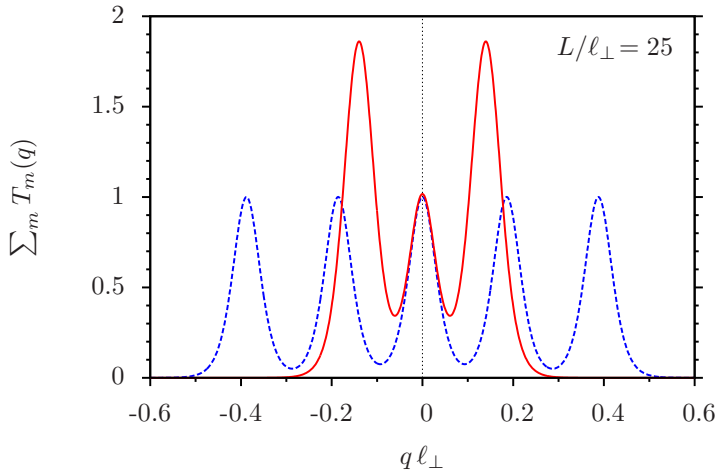

Figure 4.2: The sum of transmission probabilities, $\sum_{m=1}^{M} T_m(q)$, at $\varepsilon = 0$ as a function of the transversal momentum q in the case of few layer graphene ($M = 5$) with Bernal (solid line) and rhombohedral (dashed line) stacking and vanishing magnetic field.

The form (4.19) of the generating function coincides with that of a diffusive system [124] despite the ballistic nature of charge transport in this model.[1] This agreement is related to the uniform density of transmission eigenvalues as pointed out by Ryu *et al.* [110] for monolayer graphene. The direct consequence of this full counting statistics is the universal form of the conductivity, G, and the Fano factor, F, at zero energy

$$\mathrm{G} = M\frac{4e^2}{\pi h}\frac{W}{L}, \qquad \mathrm{F} = \frac{1}{3}, \qquad \text{for } W \gg L. \tag{4.20}$$

The full counting statistics (4.19) and the results (4.20) hold irrespective of the stacking order between the layers and are independent of the stacking specific momentum shifts κ_m. These results rely on the validity of the sharp boundary conditions with $\max \kappa_m \ll 2\pi/\lambda_\mathrm{F}$, where λ_F stands for the Fermi wave length in the leads.

The momentum dependence of the transmission probabilities is less universal which is illustrated in figure 4.2. For a multilayer with AB stacking one finds

$$\kappa_m = \frac{1}{L}\ln\left(c_m\frac{L}{\ell_\perp} + \sqrt{1+\left(c_m\frac{L}{\ell_\perp}\right)^2}\right), \tag{4.21}$$

where the coefficients c_m are defined in equation (4.8) and $m = 1, 2, \ldots, M$. This result is consistent with the mapping of the multilayer onto independent bilayers [65]. For $M = 2$, the result of equation (4.21) has been obtained by Snyman and Beenakker [63]. For multilayers with $M > 3$ in this stacking configuration, the

[1] This correspondence is highly nontrivial and related to the Zitterbewegung of Dirac fermions [75, 62].

spacing between the peaks with positive (or negative) shifts κ_m becomes constant for $\ell_\perp \ll L$, and is smaller than the peak width, so that these peaks add up to a single peak as can be seen in figure 4.2.

For the ABC stacking configuration one obtains the asymptotic expressions

$$\kappa_m = \frac{1}{L} \ln \left(\frac{(M-m)!}{(m-1)!} \left(\frac{L}{\ell_\perp} \right)^{2m-M-1} \right), \tag{4.22}$$

in the limit $\ell_\perp \ll L$. The transmission resonances shown in figure 4.2 are much better separated for the ABC multilayer than for the multilayer with the Bernal stacking. The momentum shifts κ_m in both cases depend logarithmically on the ratio $L/\ell_\perp$, so that the condition $\max \kappa_m \ll 2\pi/\lambda_\mathrm{F}$, is hard to violate. The validity of equation (4.17) is restricted to $|\varepsilon| \ll \varepsilon_0$, where $\varepsilon_0 = t_\perp/(2c_1)(\pi\ell_\perp/L)^2$ for AB and $\varepsilon_0 \approx t_\perp(\pi\ell_\perp/L)^M$ for ABC stacking. For ballistic graphene ribbons with $W \lesssim L$, the full counting statistics is sensitive to the shifts κ_m due to the transversal momentum quantization.

Remarkably, the results (4.19) and (4.20) remain valid even in the presence of arbitrary magnetic and strain fields.[2] To justify this statement it is convenient to consider the evolution operator $\mathcal{T}$ in the real space representation, such that $\Psi(L,y) = \mathcal{T}\Psi(0,y)$. Using the transformation (4.14) we find

$$\mathcal{T} = \mathrm{e}^{\mathrm{i}\hat{\Omega}(L,y)} \mathrm{e}^{-\mathrm{i}\sigma_z L\partial_y} \mathrm{e}^{-\mathrm{i}\hat{\Omega}(0,y)}, \tag{4.23}$$

where the magnetic and strain fields and inter-layer coupling are entering solely by means of the matrix phase $\hat{\Omega}$ taken at the graphene-metal boundaries. The gauge of the vector potential can be chosen such that the phase at the boundary is y-independent. Hence the matrix exponents in equation (4.23) commute and the evolution operator in the channel space takes the form of equation (4.16) with $\Sigma = (\hat{\Omega}(L) - \hat{\Omega}(0))/L$.

4.4 Gate-voltage Dependence of Transport Properties

In the vicinity of the Dirac point, for $|\varepsilon| \ll \hbar v_\mathrm{F}/L$, the transport is entirely due to the evanescent modes, which are responsible for the pseudo-diffusive form of the full counting statistics (4.19) at $\varepsilon = 0$. Away from the Dirac point, the transport is less universal and depends on a number of details. This section is limited to ballistic models with $H_A = H_S = 0$. Here I calculate the transmission probabilities $T_m(q)$ and perform the numerical integration over the transverse momentum q (assuming $2\pi/\lambda_\mathrm{F} \gg |\varepsilon|$) to find the conductance and the Fano factor in the limit $W \gg L$.

In the case of AB stacking the probabilities $T_m(q)$ can be found analytically

[2] I assume that the effect of the magnetic and strain field is negligible in the leads, which is the case for $eBL\lambda_\mathrm{F}/h \ll 1$.

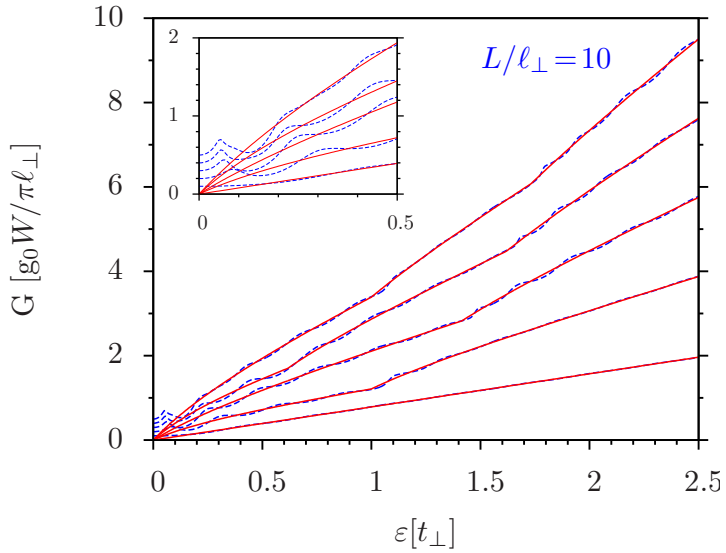

Figure 4.3: Quantum-mechanical (dashed lines) and averaged conductance of AB-stacked few-layer graphene as a function of the Fermi-energy. The layer number is one through five from bottom to top. The inset is a zoom into the low-energy region.

and the resulting energy dependence of the conductance is shown in figure 4.3 with dashed lines. The Fano factor for the trilayer with AB and ABC stacking is depicted with the dashed lines in figure 4.4 (inset) and figure 4.5, correspondingly. At $\varepsilon = 0$ the figures confirm the results of equation (4.20).

For energies exceeding the ballistic Thouless energy, $\hbar v_\mathrm{F}/L$, the transport is dominated by propagating modes, which give rise to the sample-specific Fabry-Pérot oscillations in conductance and noise. In order to get experimentally relevant results I perform the averaging over these oscillations treating the propagating phases as random quantities, which are uniformly distributed in the interval $(0, 2\pi)$ [125, 102]. This type of averaging corresponds to a quasiclassical approximation that respects the conservation of the transversal momentum, q, in the sample.

I introduce the individual scattering matrices for the left (L) and right (R) sample-lead interfaces

$$\hat{S}_{\mathrm{L/R}} = \begin{pmatrix} \hat{\rho}_{\mathrm{L/R}} & \hat{\tau}'_{\mathrm{L/R}} \\ \hat{\tau}_{\mathrm{L/R}} & \hat{\rho}'_{\mathrm{L/R}} \end{pmatrix}, \tag{4.24}$$

which relate the scattering state amplitudes in the leads with those in the sample. The number of open channels in the sample is given by $M_0 \leq M$ for a given energy, ε, and transversal momentum, q. In the planar geometry of figure 4.1 the S-matrices in equation (4.24) are readily calculated by matching the scattering states in the corresponding lead and in the sample.

As the result the total transmission matrix from the left to the right lead can

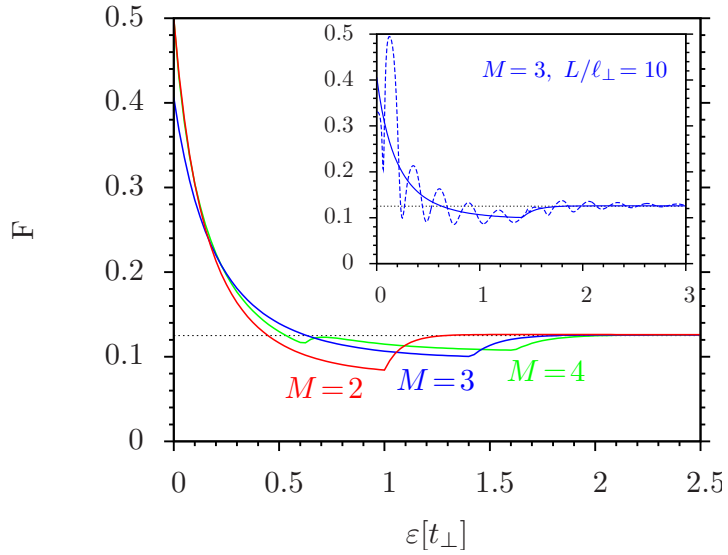

Figure 4.4: Averaged Fano factor in transport through AB-stacked few-layer graphene. The horizontal line corresponds to F = 1/8. The inset shows a comparison with the exact result (dashed curve) found from equations (4.11,4.12,4.13).

be written as a sum of Feynman paths

$$\hat{t} = \sum_{\nu} \hat{\tau}_{\rm R} \left(\hat{\tau}_0\ \hat{\rho}'_{\rm L}\ \hat{\tau}_0\ \hat{\rho}_{\rm R}\right)^{\nu}\ \hat{\tau}_0\ \hat{\tau}_{\rm L} \tag{4.25}$$

$$= \hat{\tau}_{\rm R} \left(\mathbb{1} - \hat{\tau}_0\ \hat{\rho}'_{\rm L}\ \hat{\tau}_0\ \hat{\rho}_{\rm R}\right)^{-1}\ \hat{\tau}_0\ \hat{\tau}_{\rm L}, \tag{4.26}$$

where $\hat{\tau}_0 = {\rm diag}({\rm e}^{{\rm i}\phi_1}, \ldots, {\rm e}^{{\rm i}\phi_{M_0}})$ is parameterised by the propagating phases $\phi_m = k_m L$ accumulated in the free propagation inside the sample. The number of propagating channels, M_0, is determined from the requirement ${\rm Im}(k_m) = 0$, where the longitudinal momentum k_m is found from the dispersion relation $\varepsilon = \varepsilon(k, q)$ for a given energy ε and transversal momentum q. Note that the sign of k_m is reversed (e.g. negative k_m for right-moving mode) if $d\varepsilon_m/dk_m < 0$.

An equivalent way to calculate the averaged conductance is formulated in terms of the classical transmission and reflection probabilities, ${\rm T}_{{\rm R(L)},nm} = |\tau_{{\rm R(L)},nm}|^2$, and ${\rm R}_{{\rm R(L)},nm} = |\rho_{{\rm R(L)},nm}|^2$, for the transport through the sample-graphene interfaces. The classical probabilities to pass through an entire sample are, then, organised in the matrix

$$\hat{\rm T} = \hat{\rm T}_{\rm R}(\mathbb{1} - \hat{\rm R}'_{\rm L}\hat{\rm R}_{\rm R})^{-1}\hat{\rm T}_{\rm L}, \tag{4.27}$$

for each value of q. The quantity, $\hat{\rm T}$, ignores the phase-coherence in the assumption that the transversal momentum is conserved inside the sample. The averaged conductance, $\overline{\rm G} = {\rm g}_0 \sum_q \sum_{nm} {\rm T}_{nm}$ coincides with $\overline{\rm G} = {\rm g}_0 \sum_q \langle {\rm Tr}\, \hat{t}\hat{t}^\dagger \rangle$, where the brackets stay for the averaging over the propagating phases ϕ_m in equation (4.26).

A special case of a single propagating channel, $M_0 = 1$, per transversal momentum, q, is naturally realised in a monolayer and multilayers with a single ungapped band for energies below the lowest band threshold. The example of the latter is

the ABC-stacked multilayer. If the two sample-lead junctions are equivalent, the cumulant generating function (4.9) can be expressed using equation (4.26) as

$$\mathcal{F}(\chi) = \sum_q \ln \frac{\bar{T}^2 \mathrm{e}^{\chi} + 4(1-\bar{T})\sin^2\phi}{\bar{T}^2 + 4(1-\bar{T})\sin^2\phi}, \tag{4.28}$$

where $\bar{T} = \hat{\tau}\hat{\tau}^\dagger$ is the q-dependent transmission probability of the sample-lead interface. The averaging over the propagating phase, ϕ, can be performed analytically with the result

$$\overline{\mathcal{F}}(\chi) = 2\sum_q \ln\left[\bar{T}\mathrm{e}^{\chi/2} + \sqrt{4(1-\bar{T}) + \bar{T}^2\mathrm{e}^{\chi}}\right]. \tag{4.29}$$

With the help of equation (4.13) I obtain for the averaged conductance and the Fano factor

$$\overline{\mathrm{G}} = \mathrm{g}_0 \sum_q \frac{\bar{T}}{2-\bar{T}}, \qquad \overline{\mathrm{F}} = \frac{\mathrm{g}_0}{\mathrm{G}} \sum_q \frac{2\bar{T}(1-\bar{T})}{(2-\bar{T})^3}. \tag{4.30}$$

Let us digest equations (4.29) and (4.30) in the case of monolayer graphene. If the leads in the setup of figure (3.2) are modeled by highly doped graphene one finds the interface transmission probability as $\bar{T}(q) = 1 - \tan^2\theta/2$, where $q = |\varepsilon|\sin\theta$ and $\theta \in (-\pi/2, \pi/2)$ is the angle of incidence. For $W \gg L$ I replace the summation in equations (4.30) with the integration over q in the interval $(-\varepsilon, \varepsilon)$ and reproduce the asymptotic results [62] $\overline{\mathrm{G}} = \mathrm{g}_0 W|\varepsilon|/4$ and $\overline{\mathrm{F}} = 1/8$.

Similarly, for the bilayer I find from equations (4.29,4.30) the averaged conductance below the band threshold,

$$\overline{\mathrm{G}} = \mathrm{g}_0 W\left(\frac{|\varepsilon|}{4} + t_\perp^2 \frac{\gamma - \sqrt{1+\gamma-\gamma^{-1}}}{8|\varepsilon|}\right), \qquad \text{for } |\varepsilon| < t_\perp, \tag{4.31}$$

where $\gamma = 1 + 2|\varepsilon|/t_\perp$. The result for the Fano factor in the bilayer setup takes the form

$$\overline{\mathrm{F}} = \frac{\mathrm{g}_0 W}{\overline{\mathrm{G}}}\left(\frac{|\varepsilon|}{32} + t_\perp^4 \frac{4c_1 + c_2\gamma^{-3}(1+\gamma-\gamma^{-1})^{-1/2}}{512|\varepsilon|^3}\right), \qquad \text{for } |\varepsilon| < t_\perp, \tag{4.32}$$

where $c_1 = 3 - 7\gamma(1+\gamma) - \gamma^3$ and $c_2 = 3 + \gamma(\gamma+2)(16\gamma^4 + 12\gamma^3 - 17\gamma^2 + 10\gamma - 6)$.

If several propagating channels per the value of q open up in the sample, the averaging procedure is complicated and has to be carried out numerically. Still, for AB-stacked multilayers the analysis is simplified by using Koshino-Ando mapping [65] to an effective bilayer-monolayer system. For energies below the first band threshold, the conductance and noise can be constructed from the available analytical results for mono- and bi-layer graphene using the effective bilayer coupling constants, $t_{\perp,m}^{\mathrm{eff}} = 2c_m t_\perp$, where $m = 1, 2, \ldots, \mathrm{Int}[M/2]$. For higher energies, one

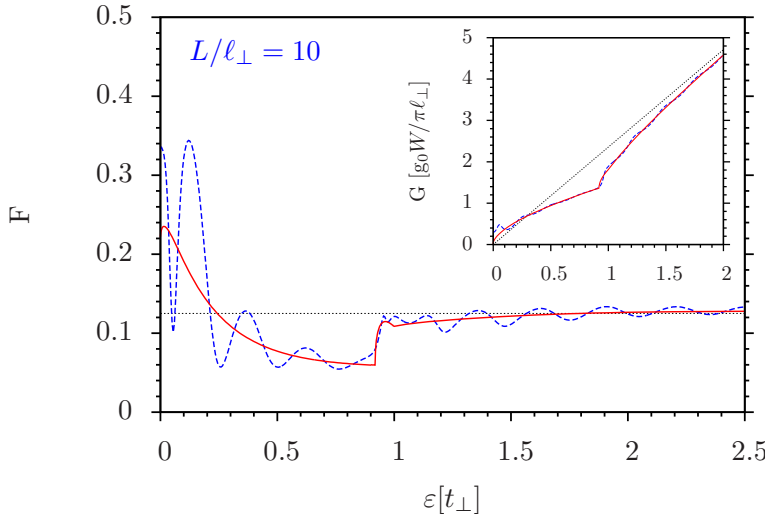

Figure 4.5: Exact (dashed line) and averaged (solid line) Fano factor for ABC-stacked trilayer graphene. The inset shows the transmission spectrum.

finds at most two propagating channels per q so that the numerical implementation of the averaging procedure is straightforward. The band thresholds are seen as kinks in the energy dependence (transmission spectra) of conductance and noise in figures 4.3 and 4.4. At $\varepsilon = 0$ I formally find $\overline{\mathrm{G}} = 0$ and (for AB-stacked multilayer) $\overline{\mathrm{F}} = 1/2$ for even M and $\overline{\mathrm{F}} = (6M-5)/(12M-4)$ for odd number of layers, M. These results ignore the contribution of evanescent modes.

The interlayer coupling becomes irrelevant for the transport at energies far above all band thresholds. Universal asymptotic results, $\mathrm{G} = M g_0 W|\varepsilon|/4$ and $\mathrm{F} = 1/8$, are obtained in this limit for any combination of AB and ABC stacking. This universality is due to the linear dispersion, $\varepsilon \approx c_m t_\perp \pm \hbar v_\mathrm{F}|\boldsymbol{k}|$, of all spectral branches in the effective few-layer model at high energies.

One can modify the decomposition (4.26) to account for evanescent modes, which correspond to imaginary values of the propagating phases, $\phi_m = k_m L$, and use an appropriate analytic continuation of the matrices $\hat{S}_{\mathrm{L/R}}$, which become non-unitary. I employ this approach to plot the exact conductance and Fano factor for ABC-stacked graphene in figure 4.5.

In ref. [126] the conductivity of Bernal-stacked graphene has been calculated using linear response theory as well as a quasiclassical approach based on the Boltzmann equation. This provides a good comparison since the same tight-binding model has been employed. The quasiclassical conductivity obtained in ref. [126] agrees with my approximation (i.e. the phase-averaged conductivity excluding evanescent modes), while the conductivity obtained from linear response theory in ref. [126] agrees with the phase-averaged conductance including evanescent modes. Note that the conductivity obtained from linear response theory corresponds to an infinite system and does not feature sample-specific Fabry-Perot oscillations.

4.5 Summary and Discussion

In this chapter a transfer matrix approach has been employed to study the full counting statistics of ballistic charge transport in few-layer graphene. The chiral symmetry of the simplistic tight-binding model allowed me to reduce the transport problem of undoped multilayer samples to transport in isolated monolayers. Therefore the full counting statistics in undoped few-layer graphene is described by the same characteristic function as in monolayer graphene, which corresponds to pseudo-diffusive transport despite the absence of disorder.

It should be emphasized that the results for the transport properties of undoped graphene rely on the symmetry of the band structure, which is reduced by the inclusion of other (inter-layer) hopping terms. More accurate tight-binding models predict a notable band overlap already for trilayer graphene [79], and even larger ones for thicker multilayers. Thus the analysis is reasonably accurate for bilayer graphene, which has a negligible band overlap, and still applicable to trilayers, but becomes strongly idealized for thicker multilayers. However, the finding of a non-unitary gauge invariance in the transport properties provides a concise description of electronic transport through undoped graphene multilayers. Similar gauge transformations will prove beneficial in the study of undoped monolayer graphene in chapter 5 and will be exploited in the study of magnetotransport in disordered graphene in chapter 8.

The transport properties of doped few-layer samples strongly depend on the stacking configuration. The band minima are clearly identifiable especially in the higher moments of charge transfer. In the absence of dephasing the quantum interference between multiple reflections causes sample-specific Fabri-Perot oscillations in the Landauer conductance and noise. I have derived quasiclassical results by averaging over the quantum phase acquired in the sample. The energy-dependence of the Landauer conductance shows good agreement with the linear response theory employed in ref. [126]. It also has been shown that, using the rigid boundary conditions for the lead model, the Koshino-Ando mapping [65] is applicable, hence the transport properties of a Bernal-stacked multilayer correspond to an effective system of isolated bilayers (and a monolayer).

A strong limitation of the model with respect to its experimental relevance is the description of the leads as strongly doped regions in combination with the abrupt metal-graphene transition at the interfaces. For more realistic boundary conditions (e.g. finite doping in the leads and/or smooth potential steps) the chiral symmetry is effectively broken and the transport properties become less universal. A more realistic model of the potential profile is introduced in chapter 6, and its effect on the ballistic transport through monolayer graphene is examined.

The neglection of edge effects also limits the validity of the results. For moderate aspect ratios W/L one has to replace the periodic boundary conditions in the

transverse direction by the microscopic boundary conditions, which depend on the crystallographic orientation of the lattice termination. Here the boundary conditions for the low-energy effective theory of graphene [73, 127] have to be applied to each layer of the multilayer system. These boundary conditions generally break the valley degeneracy of the Hamiltonian. Since the wave function in a ribbon can still be written as a superposition of plane waves in the transverse y direction, the effect of realistic edges is a change of the quantization of the transverse momentum q with respect to periodic boundary conditions. The existence of edge states along the transverse direction is not relevant for the charge transport, since they do not match with scattering states in the leads. In this chapter I considered the rectangular setup with periodic boundary conditions, corresponding to a carbon nanotube of a diameter much larger than the lattice constant. This cylinder geometry is topologically equivalent with the experimentally more feasible Corbino disk geometry, to which it can be conformally mapped as described in the following chapter.

This chapter has been published in large parts in ref. [128] and these parts have been originally written by M. Titov.

Chapter 5 – Generalized Transformations for Graphene Devices in Rectangular and Corbino Geometry

In chapter 4 I have discussed a non-unitary gauge invariance, which describes the insensitivity of the transport properties of undoped graphene in the short and wide rectangular geometry to an arbitrary magnetic flux. In the analysis I have assumed periodic boundary conditions in the transverse y direction, so that the rectangular geometry corresponds to a cylinder. Although the particular choice of boundary conditions is irrelevant in the clean sample with $W \gg L$, the situation can be different when disorder is present. In this case a strong external magnetic field can make the bulk insulating while the formation of edge states leads to a totally different transport mechanism. Since the physics of the edge states is not within the scope of this dissertation, it would be ideal to find an experimentally feasible setup to which I can apply my findings for the cylinder geometry. Such a setup is provided by the Corbino disk geometry shown schematically in figure 5.1. In this rotationally invariant geometry the bias voltage causes a radial current between the inner and the outer lead, while the simultaneous application of a perpendicular magnetic field generates a circular component of the current, which is unobstructed by any edges. It turns out that in the case of undoped graphene a conformal mapping [64] exists,[1] which directly relates the transport properties of the cylinder to those of the Corbino geometry.

In order to facilitate this mapping and a number of other generalized transformations, I employ the model of ideal graphene with the leads modeled as infinitely doped graphene and abrupt sample-lead interfaces. Since I assume that the potential steps at the interfaces are smooth on the scale of the lattice constant, the local crystallographic orientation of the interfaces (e.g. zigzag or armchair) is irrelevant. Transport properties are calculated for the case of undoped graphene samples, so that the Fermi energy lies exactly at the Dirac point in the entire sample.

Green's functions will be used extensively in the remainder of this thesis. In section 5.1 I discuss their general properties in the stationary regime and calculate the Green's functions for the clean undoped rectangular monolayer sample with heavily doped leads in the mixed channel-coordinate representation.

The case of undoped graphene with an isotropic potential is analyzed in section 5.2. I introduce the operator for the angular momentum and explicitly calculate the eigenstates in such a system. The Green's functions in the mixed channel-coordinate representation are calculated for the Corbino disk geometry with heavily doped leads.

In section 5.3 I show that the rectangular geometry with periodic boundary

[1] A transformation is called conformal if it preserves the angles.

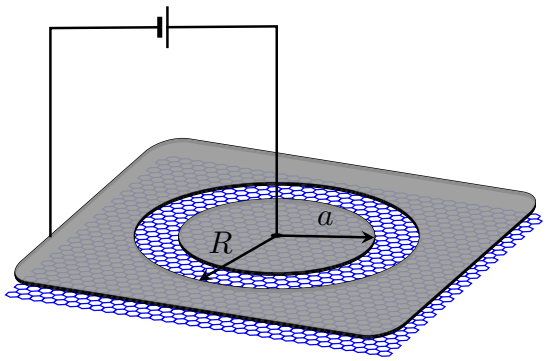

Figure 5.1: Schematic view of a graphene device in the Corbino transport geometry

conditions, which is in fact a cylinder, can be conformally mapped to the Corbino geometry [64]. This mapping consists of a non-unitary gauge transformation along with the proper re-definition of geometric length scales. It works in a similar form even for disordered graphene and thus allows for a comparison of the results in chapter 8 with the experiment.

A constant perpendicular magnetic field is treated by another non-unitary gauge transformation in section 5.4, corresponding to the one employed in chapter 4. The matrix phases are derived explicitly for the cylinder and Corbino geometries. The conformal mapping remains useful at zero energy even in the presence of an external magnetic field [129]. Both transformations are applied in section 5.5 to evaluate the ballistic transport properties of the Corbino geometry in the presence of a magnetic flux. The Kubo formulas for the two geometries are also equivalent due to the mapping.

In section 5.6 the Green's functions in real space are calculated for the two geometries in certain limits of the sample aspect ratio. These Green's functions are required for the study of disordered samples in chapter 8.

Section 5.7 extends the analysis to the Green's function in the external source fields, which, as discussed in section 3.7, is useful for evaluating the full counting statistics of charge transport. Here I also apply the conformal mapping and re-derive the transmission distribution of a short and wide rectangular device, which was already obtained from the transfer matrix approach in section 4.3.

In section 5.8 I use further transformations of the matrix Green's function to change the way how the external source fields acts. This leads to a decomposition which is very useful in the evaluation of the transport properties by means of the unfolded scattering approach in chapter 8.

In parts of this chapter I follow notes by M. Titov.

5.1 Bare Green's Function in Rectangular Geometry

Since I consider transport in a stationary regime, it is most convenient to use time-independent Green's functions. In the position basis the retarded and advanced

Green's functions describing the propagation of charge carriers in the graphene sheet are defined by the equation

$$\left(\varepsilon \pm i\eta - \bar{H}_{\boldsymbol{A}} - \bar{V}(x)\right) \bar{G}^{R,A}(\boldsymbol{r}, \boldsymbol{r}'; \varepsilon) = \delta(\boldsymbol{r} - \boldsymbol{r}'), \qquad \eta \to 0+, \tag{5.1}$$

where the term $i\eta$ determines the boundary conditions in the open system. The single-valley Hamiltonian including an arbitrary vector potential $\bar{\boldsymbol{A}}$ is given by

$$\bar{H}_{\boldsymbol{A}} = v_{\mathrm{F}} \boldsymbol{\sigma} \left(\bar{\boldsymbol{p}} + e\bar{\boldsymbol{A}}\right), \tag{5.2}$$

and the leads are described by the large potential V_0, such that

$$\bar{V}(x) = \begin{cases} 0, & \text{for } 0 < x < L, \\ -V_0, & \text{for } x < 0,\ x > L. \end{cases} \tag{5.3}$$

The bars are introduced in the notation to distinguish the rectangular geometry from the Corbino geometry considered below.

Before solving equation (5.1), I state some general properties of the Green's functions. Due to energy conservation, $\bar{H}_{\boldsymbol{A}} = \bar{H}_{\boldsymbol{A}}^{\dagger}$, the retarded and the advanced Green's functions are related as

$$\left[\bar{G}^{R}(\boldsymbol{r}, \boldsymbol{r}'; \varepsilon)\right]^{\dagger} = \bar{G}^{A}(\boldsymbol{r}', \boldsymbol{r}; \varepsilon). \tag{5.4}$$

It is thus sufficient to calculate the retarded Green's function only. Writing the Green's function in terms of the eigenstates of $\hat{H}$ which form a basis (spectral representation), one finds the operator for the density of states (number of states per energy) as [101]

$$\hat{\rho}(\varepsilon) = \frac{i}{2\pi} \lim_{\eta \to 0} \mathrm{Tr}[\bar{G}^{R}(\varepsilon) - \bar{G}^{A}(\varepsilon)] = -\frac{1}{\pi} \mathrm{Im}\, \mathrm{Tr}[\bar{G}^{R}(\varepsilon)]. \tag{5.5}$$

Here Green's functions are understood as operators. Evaluation in the position basis gives the local density of states,

$$\rho(\boldsymbol{r}; \varepsilon) = -\frac{4}{\pi} \mathrm{Im}\, \mathrm{Tr}\, \bar{G}^{R}(\boldsymbol{r}, \boldsymbol{r}; \varepsilon), \tag{5.6}$$

where the factor 4 includes the spin and valley degeneracies.

In this chapter I am mostly interested in the solution at the Dirac energy $\varepsilon = 0$. At this energy an arbitrary vector potential can be gauged away by means of a non-unitary transformation. Let us thus solve equation (5.1) for $\bar{\boldsymbol{A}} = 0$. The explicit form of the transformation gauging away a constant magnetic field in the rectangular setup is given in section 5.4.1. The retarded Green's function in the

sample fulfills

$$(i\eta + i\hbar v_{\mathrm{F}} \boldsymbol{\sigma} \boldsymbol{\nabla})\, \bar{G}^R(\boldsymbol{r}, \boldsymbol{r}'; 0) = \delta(\boldsymbol{r} - \boldsymbol{r}'), \qquad \eta \to 0+ . \tag{5.7}$$

Due to the translational invariance in the y direction the solution is most easily obtained in the mixed channel-coordinate representation defined by the Fourier transformation

$$\bar{G}^R(\boldsymbol{r}, \boldsymbol{r}'; 0) = \frac{1}{W} \sum_q e^{iq(y-y')} G_q^R(x, x'), \tag{5.8}$$

where the discrete values of the transversal momentum are given by $q_n = 2\pi n/W$ with integer index n, and the argument $\varepsilon = 0$ has been omitted. The quantization of q is only relevant for a moderate aspect ratio W/L. In this case the rectangular setup should be viewed as a cylinder geometry. If the cylinder is pierced by a magnetic flux, the index n is shifted by the number of flux quanta. This shift ensures that the Green's function $G_B^R(\boldsymbol{r}, \boldsymbol{r}')$ remains periodic in y and y'.

The term $i\eta$ in equation (5.1), together with the lead potential V_0, defines the boundary conditions at the interfaces $x = 0, L$. Infinitely doped leads correspond to 'metallic' boundary conditions, which are q-independent,

$$(1,1) G_q^R(0, x') = 0, \qquad\qquad (1,-1) G_q^R(L, x') = 0. \tag{5.9}$$

The boundary conditions thus have the same form for the real-space Green's function $\bar{G}^R(\boldsymbol{r}, \boldsymbol{r}')$. Corresponding boundary conditions are obtained at $x' = 0, L$ but not required to determine the Green's function.

The evolution of the channel space Green's function in the sample follows from equations (5.7),(5.8) as

$$\hbar v_{\mathrm{F}} (i\sigma_x \partial_x - m\sigma_y)\; G_q^R(x, x') = \delta(x - x'). \tag{5.10}$$

By integrating this equation around the point $x = x'$, one finds that the Green's function has a jump,

$$G_q^R(x' + 0, x') - G_q^R(x' - 0, x') = -i\sigma_x. \tag{5.11}$$

The conditions (5.9),(5.11), together with equation (5.10) at $x \neq x'$, fully determine the Green's function $G_q^R(x, x')$ in the mixed channel-coordinate representation, which is found as

$$G_q^R(x, x') = \frac{-i}{2\cosh(qL)} \begin{pmatrix} e^{-q(L-x-x')} & \zeta e^{-q(\zeta L - x + x')} \\ \zeta e^{q(\zeta L - x + x')} & e^{q(L-x-x')} \end{pmatrix}, \qquad \zeta = \begin{cases} +1, & \text{for } x > x', \\ -1, & \text{for } x < x'. \end{cases} \tag{5.12}$$

Advanced and retarded Green's functions in this representation are related by the

Hermitian, orthogonal, and chiral symmetries

$$G_q^A(x,x') = \left[G_q^R(x',x)\right]^\dagger, \tag{5.13}$$

$$G_q^A(x,x') = -\left[G_q^R(x',x)\right]^T, \tag{5.14}$$

$$G_q^A(x,x') = -\sigma_z G_q^R(x,x')\sigma_z. \tag{5.15}$$

The Hermitian and orthogonal symmetries hold at arbitrary energy, while the chiral symmetry is specific for $\varepsilon = 0$ and relies on the model of heavily doped leads and the abrupt interfaces as described by equation (5.3). I have used the preservation of the chiral symmetry by heavily doped leads in the study of ballistic transport in undoped graphene in chapter 4.

5.2 Eigenstates and Bare Green's Function in Isotropic Potential

This section is relevant for the Corbino transport geometry, in which the leads are described as doped regions, as well as for disk-shaped scalar impurities. In either case the intrinsic graphene is subjected to an isotropic scalar potential, which makes it convenient to use polar coordinates to describe the electronic motion. The single valley Dirac Hamiltonian is written in polar coordinates as (setting $\hbar v_\mathrm{F} = 1$)

$$H_0 = -i\boldsymbol{\sigma}\boldsymbol{\nabla} = -i\begin{pmatrix} 0 & e^{-i\theta}\left(\partial_r - \frac{i}{r}\partial_\theta\right) \\ e^{i\theta}\left(\partial_r + \frac{i}{r}\partial_\theta\right) & 0 \end{pmatrix}, \tag{5.16}$$

where $\boldsymbol{r} = (r\cos\theta, r\sin\theta)$. The vector potential describing a spatially constant magnetic field is most conveniently taken in the symmetric gauge, in which the components in polar coordinates are given by

$$A_r = 0, \tag{5.17}$$

$$A_\theta(r) = Br/2. \tag{5.18}$$

Thus the Hamiltonian in the presence of the magnetic field is

$$H_{\boldsymbol{A}} = H_0 + i\frac{e}{\hbar}\begin{pmatrix} 0 & -e^{-i\theta}A_\theta(r) \\ e^{i\theta}A_\theta(r) & 0 \end{pmatrix}. \tag{5.19}$$

The operator of the angular momentum is given by [130]

$$J = -i\partial_\theta + \tfrac{1}{2}\sigma_z. \tag{5.20}$$

This operator commutes with the Hamiltonian, $[H_{\boldsymbol{A}}, J] = 0$, so that the eigenfunctions can be labeled with two quantum numbers, m and ε, from the spectral

relations

$$J\Psi_{m,\varepsilon} = m\Psi_{m,\varepsilon}, \tag{5.21}$$

$$H_{\boldsymbol{A}}\Psi_{m,\varepsilon} = \varepsilon\Psi_{m,\varepsilon}. \tag{5.22}$$

The general expression for the eigenfunction of H_0, i.e. for absent scalar or vector potential, is

$$\Psi_{m,\varepsilon} = e^{i(m-\sigma_z/2)\theta}\,\Phi_{m,\varepsilon}(r), \quad \Phi_{m,\varepsilon}(r) = \sum_{s=1}^{2} \alpha_m^{(s)} \begin{pmatrix} H^{(s)}_{m-1/2}(\varepsilon r) \\ iH^{(s)}_{m+1/2}(\varepsilon r) \end{pmatrix}, \tag{5.23}$$

where $H_m^{(s)}$ are the Hankel functions of the first and second kind for $s = 1, 2$, respectively, i.e. combinations of the Bessel functions of the first and second kind, $H_m^{(1,2)}(z) = J_m(z) \pm iY_m(z)$. Due to the periodicity of $\Psi_{m,\varepsilon}$ in θ, the quantum number m for the angular momentum takes on half-integer values. Since $Y_m(z)$ is singular at $z = 0$, this term is only allowed if the center of the Corbino geometry is not included in the model, but the wavefunction is subjected to boundary conditions at a non-zero radius. The state $\Phi_{m,\varepsilon}(r)$ is an eigenstate of the operator

$$L_m \equiv -i \begin{pmatrix} 0 & \partial_r + \frac{m+1/2}{r} \\ \partial_r - \frac{m-1/2}{r} & 0 \end{pmatrix}, \tag{5.24}$$

which is Hermitian with respect to the proper scalar product since $\int r\,dr\,\Phi^\dagger L\Phi = \int r\,dr\,(L\Phi)^\dagger\Phi$ from the integration by parts.

5.2.1 Green's functions in Corbino geometry

In this subsection I derive the Green's functions for undoped graphene in Corbino geometry in the absence of a magnetic field. The leads are modeled as for the rectangular setup by a large chemical potential $V_0 > 0$. Using the assumption of abrupt interfaces, the radially symmetric potential $V(r)$ defining the sample and the leads is given by

$$V(r) = \begin{cases} 0, & \text{for } a < r < R, \\ -V_0, & \text{for } r < a,\ r > R. \end{cases} \tag{5.25}$$

The retarded bare Green's function is defined by the equation

$$(\varepsilon + i\eta - H_0 - V(r))\,G^R(\boldsymbol{r}, \boldsymbol{r}') = \delta(\boldsymbol{r} - \boldsymbol{r}'). \tag{5.26}$$

The advanced Green's function follows directly from the Hermitian symmetry (5.4).

Using the decomposition

$$G^R(\boldsymbol{r},\boldsymbol{r}') = \frac{1}{2\pi}\sum_m e^{i(m-\sigma_z/2)\theta}\, G^R_m(r,r') e^{-i(m-\sigma_z/2)\theta'}, \tag{5.27}$$

the equation on the retarded propagator $G^R_m(r,r')$ in the mixed channel-coordinate representation is found as,

$$(\varepsilon + i\eta - L_m - V(r))G^R_m(r,r') = \frac{1}{r}\delta(r-r'). \tag{5.28}$$

In this chapter I focus on zero energy, $\varepsilon = 0$, so that transport is facilitated only via evanescent modes near the Dirac point. The general solutions for the eigenfunction of H and L_m in the finite sample region $a < r < R$ are given by

$$\Psi_m = \begin{pmatrix} \alpha_m \left(re^{i\theta}\right)^{m-1/2} \\ \beta_m \left(re^{-i\theta}\right)^{-m-1/2} \end{pmatrix}, \qquad \text{and} \qquad \Phi_m = \begin{pmatrix} \alpha_m r^{m-1/2} \\ \beta_m r^{-m-1/2} \end{pmatrix}, \tag{5.29}$$

respectively. I also focus on the limit of high doping in the leads, $V_0 a \gg 1$ (and $V_0 R \gg 1$). This allows me to take advantage of the asymptotic relations

$$\Phi^{(1)}_m(r) = \begin{pmatrix} H^{(1)}_{m-1/2}(V_0 r) \\ iH^{(1)}_{m+1/2}(V_0 r) \end{pmatrix} \to \sqrt{\frac{2}{\pi V_0 r}} e^{i(V_0 r - \pi m/2)} \begin{pmatrix} 1 \\ 1 \end{pmatrix}, \tag{5.30}$$

$$\Phi^{(2)}_m(r) = \begin{pmatrix} H^{(2)}_{m-1/2}(V_0 r) \\ iH^{(2)}_{m+1/2}(V_0 r) \end{pmatrix} \to \sqrt{\frac{2}{\pi V_0 r}} e^{-i(V_0 r - \pi m/2)} \begin{pmatrix} 1 \\ -1 \end{pmatrix}, \tag{5.31}$$

which suggest the following boundary conditions for the retarded and advanced Green's functions at $r = a$ and $r = R$,

$$(1,1)G^R_m(a,r) = (1,-1)G^R_m(R,r) = 0, \quad G^R_m(r,a)\begin{pmatrix} 1 \\ -1 \end{pmatrix} = G^R_m(r,R)\begin{pmatrix} 1 \\ 1 \end{pmatrix} = 0, \tag{5.32}$$

$$(1,-1)G^A_m(a,r) = (1,1)G^A_m(R,r) = 0, \quad G^A_m(r,a)\begin{pmatrix} 1 \\ 1 \end{pmatrix} = G^A_m(r,R)\begin{pmatrix} 1 \\ -1 \end{pmatrix} = 0. \tag{5.33}$$

The construction of the Green's functions for a clean sample is analogous to the case of a rectangular sample. From equation (5.28) I obtain the normalization condition

$$G^R_m(r+0,r) - G^R_m(r-0,r) = -i\sigma_x \frac{1}{r}. \tag{5.34}$$

The bare retarded Green's function at $\varepsilon = 0$ is found as

$$G_m^R(r,r') = \frac{-i}{2\sqrt{rr'}\cosh(mL)} \begin{pmatrix} \left(\frac{rr'}{Ra}\right)^m & \zeta \left(\frac{R}{a}\right)^{-\zeta m} \left(\frac{r}{r'}\right)^m \\ \zeta \left(\frac{R}{a}\right)^{\zeta m} \left(\frac{r}{r'}\right)^{-m} & \left(\frac{rr'}{Ra}\right)^{-m} \end{pmatrix}, \tag{5.35}$$

$$\zeta = \begin{cases} +1, & r > r', \\ -1, & r < r'. \end{cases} \tag{5.36}$$

As in the rectangular setup, advanced and retarded Green's functions are related by the Hermitian, orthogonal, and chiral symmetries. In fact, apart from the prefactor $1/\sqrt{rr'}$, the Green's function (5.35) is equivalent to the Green's function (5.12) of the rectangular device if one redefines the variables according to the mapping derived in the following section.

5.3 Conformal Mapping Transformation

A conformal transformation between the rectangular and the Corbino geometries for undoped graphene has been described in ref. [64]. Here I present this mapping in the form of a non-unitary gauge transformation, which is applied to Green's functions. I start from the Corbino geometry of an undoped graphene disk in the presence of a constant perpendicular magnetic field B. An easier method to deal with the magnetic field is provided by the transformation gauging away the vector potential, as discussed in section 5.4.

The retarded bare Green's function at zero energy is defined by the equation

$$(i\eta - H_{\boldsymbol{A}} - V(r))\, G^R(\boldsymbol{r},\boldsymbol{r}') = \delta(\boldsymbol{r}-\boldsymbol{r}'), \tag{5.37}$$

with the single-valley Dirac Hamiltonian $H_{\boldsymbol{A}}$ given by equation (5.19) and the potential $V(r)$ defined in equation (5.25). The conformal mapping is facilitated by the following transformation,

$$G^R(\boldsymbol{r},\boldsymbol{r}') = \frac{1}{\sqrt{rr'}} e^{-i\sigma_z\theta/2} \bar{G}^R(\boldsymbol{r},\boldsymbol{r}') e^{i\sigma_z\theta'/2}. \tag{5.38}$$

Substitution into equation (5.37) yields an equation of the form (5.1),

$$\left(i\eta - \bar{H}_{\boldsymbol{A}} - \bar{V}(r)\right) \bar{G}^R(\boldsymbol{r},\boldsymbol{r}') = \delta(\boldsymbol{r}-\boldsymbol{r}'), \tag{5.39}$$

where the operators are given by

$$\bar{H}_{\boldsymbol{A}} = v_{\mathrm{F}}\boldsymbol{\sigma}\left(\bar{\boldsymbol{p}} + e\bar{\boldsymbol{A}}\right), \quad \bar{p}_x = -i\hbar r\frac{\partial}{\partial r}, \quad \bar{p}_y = -i\hbar\frac{\partial}{\partial\theta}, \tag{5.40}$$

and the vector potential (in x,y-coordinates) and scalar potential have the radial

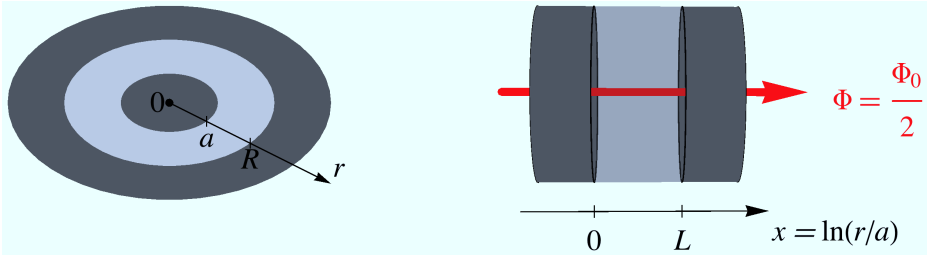

Figure 5.2: Schematic illustration of the conformal mapping between Corbino and cylinder geometries. Dark shaded areas represent heavily doped graphene leads. The red arrow represents a magnetic flux piercing the cylinder.

dependence

$$\bar{\boldsymbol{A}} = \begin{pmatrix} 0 \\ Br^2/2 \end{pmatrix}, \quad \bar{V}(r) = rV(r). \tag{5.41}$$

In terms of the dimensionless coordinates

$$x = \ln(r/a), \qquad y = \theta, \tag{5.42}$$

the momentum components take the form

$$\bar{p}_x = -i\hbar\frac{\partial}{\partial x}, \quad \bar{p}_y = -i\hbar\frac{\partial}{\partial y}, \tag{5.43}$$

hence the Hamiltonian $\bar{H}_{\boldsymbol{A}}$ just corresponds to a rectangular geometry of dimensionless length and width

$$L = \ln(R/a), \qquad W = 2\pi, \tag{5.44}$$

respectively. However, the spatially constant magnetic field and scalar lead potential are mapped to a spatially varying field and potential in the rectangular geometry.

The mapping is illustrated in figure 5.2. Here the inner (outer) lead of the Corbino disk corresponds to the left (right) lead of the rectangular setup, which is illustrated as a cylinder due to the periodic boundary conditions. A topological difference between the two geometries exists due to the properties of the graphene lattice. An electron encircling the inner lead of the Corbino disk acquires the phase π (Berry's phase), so that the wavefunction changes sign. This means that the periodic boundary conditions in the Corbino disk are mapped to antiperiodic boundary conditions for the rectangular geometry. This geometry can be interpreted as a cylinder which is pierced by half a magnetic flux quantum, $\Phi_0/2$, where $\Phi_0 = h/e$, as illustrated.

In the limit of strongly doped leads the spatial variation of the mapped potential $\bar{V}(x)$ in the leads is irrelevant and one can use the equivalent model (5.3). On the other hand, the constant magnetic field in the Corbino geometry is transformed

to an exponentially changing field in the cylinder. We will see, however, that the conformal mapping is still useful, because the effect on the ballistic transport properties is generally equivalent to a certain flux piercing the cylinder or threading the inner lead.

5.4 Non-Unitary Gauge Transformation of Vector Potential

In this section I consider a constant perpendicular magnetic field in either Corbino or rectangular geometry, which is generated by the vector potential as $\boldsymbol{B} = \boldsymbol{e}_z B = \boldsymbol{e}_z(\boldsymbol{\nabla} \times \boldsymbol{A})$. Here I give the explicit form of the non-unitary transformation, which has been introduced already in equation (4.14). Note that for a constant magnetic field the vector potential $\boldsymbol{A}$ is generally a linear function of the spatial coordinates [131]. At zero energy the eigenstates $\Psi(\boldsymbol{r})$ of $H_{\boldsymbol{A}}$ are related to those of H_0 by the transformation

$$\Psi(\boldsymbol{r}) = e^{i\Omega(\boldsymbol{r})}\Psi^{(0)}(\boldsymbol{r}), \quad \boldsymbol{\sigma}\boldsymbol{\nabla}\Omega(\boldsymbol{r}) = -\frac{e}{\hbar}\boldsymbol{\sigma}\boldsymbol{A}, \tag{5.45}$$

where the matrix phase Ω can be written in terms of scalar phases χ and φ as

$$i\Omega(\boldsymbol{r}) = \sigma_z\chi(\boldsymbol{r}) + i\varphi(\boldsymbol{r}). \tag{5.46}$$

These expressions hold for either geometry. The corresponding transformation of Green's functions is given by

$$G(\boldsymbol{r}, \boldsymbol{r}') = e^{\sigma_z\chi(\boldsymbol{r})+i\varphi(\boldsymbol{r})}G^{(0)}(\boldsymbol{r}, \boldsymbol{r}')e^{\sigma_z\chi(\boldsymbol{r}')-i\varphi(\boldsymbol{r}')}. \tag{5.47}$$

Note that such a non-unitary transformation can only be applied in finite systems, unless the phase χ is non-zero in a finite region only. Furthermore, the boundary conditions for the Green's function $G^{(0)}(\boldsymbol{r}, \boldsymbol{r}')$ are generally different from those for the Green's function in the absence of any magnetic field. This will be described in the following two subsections for the cylindrical and the Corbino geometry.

5.4.1 Rectangular geometry

Let us start with the rectangular geometry with periodic boundary conditions. (Here bars are omitted in the notation.) From equations (5.45) and (5.46) the relation between the scalar phases and the vector potential follows as

$$A_x = -\frac{\hbar}{e}\left(\frac{\partial\varphi}{\partial x} + \frac{\partial\chi}{\partial y}\right), \tag{5.48a}$$

$$A_y = -\frac{\hbar}{e}\left(\frac{\partial\varphi}{\partial y} - \frac{\partial\chi}{\partial x}\right). \tag{5.48b}$$

The phases can thus be expressed as the solutions of the following Poisson equations with appropriate boundary conditions,

$$\frac{\hbar}{e}\boldsymbol{\nabla}^2\varphi = \boldsymbol{\nabla}\boldsymbol{A}, \tag{5.49a}$$

$$-\frac{\hbar}{e}\boldsymbol{\nabla}^2\chi = \boldsymbol{\nabla}\times\boldsymbol{A} = B. \tag{5.49b}$$

In order to preserve the translational invariance in the y direction, it is most convenient to use the Landau gauge,

$$\boldsymbol{A}(\boldsymbol{r}) = B\begin{pmatrix} 0 \\ x-\bar{x}\end{pmatrix}. \tag{5.50}$$

At the position $x=\bar{x}$ the magnetic flux piercing the cylinder vanishes. The gauge freedom for the scalar phases can be used to choose the phase χ to be y-independent and vanishing at the boundaries of the sample. This choice determines the phases as

$$\chi(x) = -\frac{eB}{\hbar}\frac{x(L-x)}{2}, \tag{5.51}$$

$$\varphi(y) = \gamma y, \qquad \gamma = \frac{eB}{\hbar}\left(\bar{x}-\frac{L}{2}\right) = -\frac{2\pi}{W}\frac{\Phi_\mathrm{p}}{\Phi_0}, \tag{5.52}$$

where Φ_p is the magnetic flux piercing the cylinder cross section at $x=L/2$ and $\Phi_0 = h/e$ is the flux quantum. The boundary conditions for the Green's function $G^{(0)}(\boldsymbol{r},\boldsymbol{r}')$ are thus unchanged at $x=0$ and $x=L$, but the boundary conditions in y are generally different from periodic ones since the phase φ does not fulfill $\varphi(W)=\varphi(0)$.[2] However, since φ is linear in y the boundary conditions remain quasi-periodic. This means that the change is easily included as a shift of the mode index in the Fourier transformed wavefunction or Green's function. Such a shift is generally irrelevant in the limit $W \gg L$.

5.4.2 Corbino geometry

The relations between the scalar phases and the vector potential in polar coordinates are given by

$$A_r = \frac{\partial\varphi}{\partial r} + \frac{1}{r}\frac{\partial\chi}{\partial\theta}, \tag{5.53a}$$

$$A_\theta = \frac{1}{r}\frac{\partial\varphi}{\partial\theta} - \frac{\partial\chi}{\partial r}. \tag{5.53b}$$

In the Corbino geometry it is convenient to use the symmetric gauge, so that the radial component A_r vanishes. The magnetic field is generated by the angular

[2] The scalar phases are mathematical constructions and not subject to physical boundary conditions.

component A_θ as

$$B = \frac{1}{r}\frac{\partial}{\partial r} r A_\theta(r). \tag{5.54}$$

The solution in the sample, $a < r < R$, has the form

$$A_\theta(r) = \frac{Br}{2} + \frac{\delta\Phi_\mathrm{c}}{2\pi r}, \qquad \delta\Phi_\mathrm{c} = \Phi_\mathrm{c} - \pi a^2 B. \tag{5.55}$$

The additional term $\sim \delta\Phi_\mathrm{c}$ depends on the flux Φ_c through the central lead and vanishes if the magnetic field is homogeneous in the entire system, which will be assumed in the following. Again I keep the boundary conditions at the sample-lead interfaces the same as in the absence of magnetic field, which is achieved by setting $\chi(a) = \chi(R) = 0$. This choice determines the fields as

$$\chi(r) = -\frac{1}{4}\frac{eB}{\hbar}(r^2 - a^2) + \gamma \ln\frac{r}{a}, \tag{5.56}$$

$$\varphi(\theta) = \gamma\theta, \qquad \gamma = \frac{eB}{\hbar}\frac{R^2 - a^2}{4L} = \frac{\Phi_\mathrm{s}}{2L\Phi_0}, \tag{5.57}$$

where Φ_s is the flux through the sample. Analogous to the cylinder geometry, the boundary conditions in θ are changed by the transformation (5.47) from periodic ones for $G(\boldsymbol{r}, \boldsymbol{r}')$ to quasi-periodic ones for $G^{(0)}(\boldsymbol{r}, \boldsymbol{r}')$.

5.5 Applications of the Conformal Mapping

Due to the conformal mapping various electronic properties of undoped graphene can be established simultaneously for the cylinder and the Corbino geometry. As an example one obtains the relation between conductivity and conductance in the Corbino geometry directly from the corresponding relation in the rectangular setup,

$$\mathrm{G} = \frac{W}{L}\sigma = \frac{2\pi}{\ln(R/a)}\sigma. \tag{5.58}$$

The same relation is obtained from the ratio between the radial current density and the electric field generated by the bias voltage in the Corbino disk. This is possible because the transport mediated through evanescent modes obeys Ohm's Law.

In the following two subsections I evaluate the transport properties of the Corbino geometry. The spatial variables are used in this geometry as defined in equations (5.42) and (5.44).

5.5.1 Kubo formula in Corbino geometry

The Kubo formula was derived from the Landauer approach for the rectangular setup in section 3.6, cf. equation (3.79). An analogous Kubo formula can be derived

for the Corbino geometry. Since the operator for the radial current is given by

$$\hat{v}_r = \frac{\boldsymbol{\sigma}\,\boldsymbol{r}}{r} = \sigma_x e^{i\sigma_z\theta}, \tag{5.59}$$

the Kubo formula for the Corbino geometry reads ($\hbar v_{\rm F} = 1$)

$$\mathrm{Tr}(t^\dagger t)^n = \mathrm{Tr}\left\{\sigma_x e^{i\sigma_z\theta}\, G^R(R,a;\theta,\theta')\,\sigma_x e^{i\sigma_z\theta'}\,\left[G^R(R,a;\theta,\theta')\right]^\dagger\right\}^n, \tag{5.60}$$

where the integration over the two cross-sections $r = a$ and $r = R$ is implicit. The angle-dependence of the current density can be studied by integrating over one angle only. The Kubo formula (5.60) holds at arbitrary energy.

At zero energy the conformal mapping (5.38) transforms the Kubo formula (5.60) into the Kubo formula for the rectangular setup,

$$\mathrm{Tr}(t^\dagger t)^n = \mathrm{Tr}\left\{\,\sigma_x\,\bar{G}^R(L,0;y,y')\,\sigma_x\,\left[\bar{G}^R(L,0;y,y')\right]^\dagger\right\}^n. \tag{5.61}$$

Furthermore, at zero energy an external magnetic field can be included by applying the gauge transformation (5.47) for the vector potential, which just cancels in the Kubo formula. Therefore the effect of the external magnetic field on the transport properties is simply described by the appropriate shift of the mode index which ensures the periodic boundary conditions.

5.5.2 Ballistic conductance of Corbino device

In the case of a clean sample inter-mode scattering is absent. By Fourier transforming the Green's functions in the Kubo formula (5.61) according to equation (5.27), one obtains the transmission moments in individual channels,

$$T_m = \mathrm{Tr}\left\{\,\sigma_x\,G^R_m(R,a)\,\sigma_x\,\left[G^R_m(R,a)\right]^\dagger\right\}. \tag{5.62}$$

The zero-energy Green's function in channel space, equation (5.35), taken between the two heavily doped leads, has the simple form

$$G^R_m(R,a) = \frac{-i}{2\cosh(mL)}\begin{pmatrix}1 & 1\\ 1 & 1\end{pmatrix}. \tag{5.63}$$

Substitution into the Kubo formula (5.62) yields the well-known transmission moments

$$T_m = \frac{1}{\cosh^2(mL)}. \tag{5.64}$$

The result just corresponds to that in the rectangular geometry, which was derived in equation (3.61) from the evolution operator. The only difference is that the quantum number m for the angular momentum is generally quantized differently

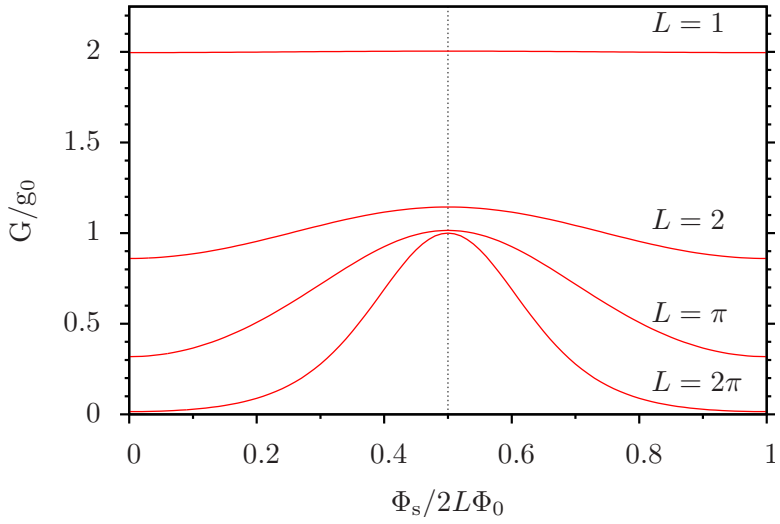

Figure 5.3: Conductance as a function of magnetic flux in Corbino geometry for different values of $L = \ln(R/a)$. The same curves for G/g_0 are obtained as a function of $\Phi_p/\Phi_0 - 1/2$ in the cylinder geometry. Note that $L = 2\pi$ corresponds to $W/L = 1$, hence the regime of single-mode transport (non-overlapping conductance peaks) is much easier reached in the cylinder geometry than in the Corbino disk, where $L = 2\pi$ corresponds to $R/a \approx 535$.

from the transverse momentum q in the rectangular geometry. In the following I study the conductance of the Corbino device in the presence of a constant magnetic field. For arbitrary ratio R/a the conductance is obtained as the sum over the transmission moments (5.64),

$$G = g_0 \sum_{n=-\infty}^{\infty} \frac{1}{\cosh^2(n + 1/2 - \gamma)L}, \tag{5.65}$$

where n is integer and the shift γ is given by $\Phi_s/2L\Phi_0$. In [132, 130] this result has been obtained directly from the wave function matching. The conductance is an oscillating function in the magnetic flux Φ_s with the unusual period $2L\Phi_0$. It is plotted in figure 5.3 for various values of L. The flux-averaged conductance is given by

$$G = g_0 \frac{2}{L}. \tag{5.66}$$

If the approximate condition $\ln(R/a) < 1$ is fulfilled, the summation in equation (5.65) can be replaced by the integration. In this case the oscillations in the magnetic flux dependence are negligible and equation (5.66) corresponds to the exact conductance. Furthermore, the conductivity, following from equation (5.58), is universal and identical with that of the short and wide rectangular setup, $\sigma = g_0/\pi$, valid roughly for aspect ratio $W/L > 2\pi$.

Note, however, that the ballistic conductivity at the Dirac point is generally geometry-dependent, i.e. not independent of the ratio R/a, because the charge transport is due to the tunneling between the two leads and not a local phenomenon.

For larger ratios R/a, such that $\ln(R/a) > 1$, all apart from a few modes are exponentially suppressed with transmission $T \ll 1$, and the approximation $\cosh(\xi) \to \exp(|\xi|)/2$ can be carried out for all those modes. In this case the infinite sum in equation (5.65) becomes a geometric series. If only the two strongest modes are taken exactly, the approximation is valid only for unrealistically large values of R/a. However, taking four modes exactly leads to a good approximation for roughly $R/a > 5$,

$$\frac{\mathrm{G}}{\mathrm{g}_0} = \sum_{m=-3/2}^{3/2} \frac{1}{\cosh^2(m-\bar{\gamma})L} + 8\frac{\cosh(2\bar{\gamma}L)}{(R/a)^5}, \qquad \bar{\gamma} = \gamma \mod 1. \tag{5.67}$$

In the unrealistic case $R \gg a$, such that $\ln(R/a) > 2\pi$, the conductance is due to one or two modes only. In the absence of magnetic field the two modes $m = \pm 1/2$ corresponding to s-waves lead to the negligibly small conductance

$$\mathrm{G} = \mathrm{g}_0 \frac{8a}{R}, \qquad \text{for } L > 2\pi. \tag{5.68}$$

This strong suppression of the conductance is related to the strong chemical potential in the leads.

Another useful approximation of the infinite sum (5.65) is possible in the regime $\ln(R/a) \ll \pi^2$ where the conductance is a simple oscillating function in the magnetic flux. This approximation is based on the Poisson summation, which yields the exact expression [132]

$$\mathrm{G} = \mathrm{g}_0 \frac{2}{L}\left(1 - \frac{2\pi^2}{L}\sum_{n=0}^{\infty} \frac{1+\cos(2\pi\gamma)\cosh(\pi^2(2n+1)/L)}{(\cos(2\pi\gamma)+\cosh(\pi^2(2n+1)/L))^2}\right). \tag{5.69}$$

For all experimentally relevant ratios R/a (corresponding to $L \ll \pi^2$) the first correction in equation (5.69) is sufficient, which leads to the following result [132],

$$\mathrm{G} = \mathrm{g}_0 \frac{2}{L}\left(1 - \frac{4\pi^2}{L} e^{-\pi^2/L}\cos(2\pi\gamma)\right), \qquad \text{for } L \ll \pi^2. \tag{5.70}$$

This formula provides a good approximation for $R/a < 20$ ($L < 3$).

5.6 Green's Functions in Real Space

Although the Green's function (5.12) in the mixed channel-coordinate representation is sufficient for evaluating the electronic properties of the clean sample, a compact expression for the real-space Green's function is required in order to efficiently deal with disordered systems. The approximations available for evaluating the infinite sum in the Fourier transform (5.8) correspond to those used for the ballistic conductance in subsection 5.5.2.

The real space Green's functions are also of interest, because they generally determine the local density of states (LDoS) as [cf. equation (5.6)]

$$\rho(\boldsymbol{r}) = -\frac{1}{\pi}\,\mathrm{Im}\,\mathrm{Tr}\,G^R(\boldsymbol{r},\boldsymbol{r}). \tag{5.71}$$

Note that since spin and valley degrees of freedom are not contained in the Green's function, the total LDoS is $4\rho(\boldsymbol{r})$.

In the rectangular setup with arbitrary aspect ratio W/L and constant magnetic field B, one finds from equations (5.8),(5.12) and the gauge transformation (5.47) the following expression for the LDoS,

$$\rho(x) = \frac{1}{\pi\hbar v_\mathrm{F} W}\sum_q \frac{\cosh\left(q(L-2x)-2\chi(x)\right)}{\cosh(qL)}. \tag{5.72}$$

The result hold analogously for the Corbino geometry, and the quantized values of q depend on the geometry and the magnetic flux as discussed above.

In the following I discuss the case of the short and wide rectangular setup and the case of the Corbino geometry with $R \gg a$, where compact expressions for the Green's functions are available.

5.6.1 Rectangular setup with large aspect ratio

Here I consider the case $W \gg L$ ($\ln(R/a) < 1$), which will be focused on in chapter 8 when studying transport in disordered graphene. Replacing the summation over the mode index q in the Fourier transform (5.8) by an integration, one obtains [133]

$$\bar{G}^R(\boldsymbol{r},\boldsymbol{r}') = \frac{-i}{4\hbar v_\mathrm{F} L}\begin{pmatrix} C_+(\boldsymbol{r},\boldsymbol{r}') & C_-(\boldsymbol{r},\boldsymbol{r}') \\ C_-^*(\boldsymbol{r},\boldsymbol{r}') & C_+^*(\boldsymbol{r},\boldsymbol{r}') \end{pmatrix}, \qquad \text{for } W \gg L, \tag{5.73}$$

$$C_\pm(\boldsymbol{r},\boldsymbol{r}') \equiv \left[\sin\left(\frac{\pi}{2L}(x \pm x' + i(y-y'))\right)\right]^{-1}. \tag{5.74}$$

Note that this Green's function is not periodic in the transverse coordinates anymore. The advanced Green's function is obtained from the Hermitian symmetry, equation (5.4), and the two Green's functions are also related by the chiral symmetry

$$\bar{G}^A(\boldsymbol{r},\boldsymbol{r}') = -\sigma_z \bar{G}^R(\boldsymbol{r},\boldsymbol{r}')\sigma_z. \tag{5.75}$$

The real space Green's function generally diverges for coinciding arguments. However, in the limit of coinciding arguments it can be decomposed into two parts,

$$\lim_{\boldsymbol{r}'\to\boldsymbol{r}}\left[\bar{G}^R(\boldsymbol{r},\boldsymbol{r}') - g_0(\boldsymbol{r},\boldsymbol{r}')\right] = \bar{G}_\mathrm{reg}(\boldsymbol{r}). \tag{5.76}$$

In general the non-diverging part $\bar{G}_\mathrm{reg}$ is diagonal, while the diverging part $g_0(\boldsymbol{r},\boldsymbol{r}')$

is off-diagonal, independent of the sample geometry,[3] and also independent of the magnetic field. It just corresponds to the free Green's function in an infinite graphene system without magnetic field. Here I omit the explicit derivation but extract this Green's function from the Green's function (5.73) for $W \gg L$,

$$g_0(\boldsymbol{r}, \boldsymbol{r'}) = -\frac{i}{2\pi\hbar v_\mathrm{F}} \frac{\boldsymbol{\sigma}(\boldsymbol{r} - \boldsymbol{r'})}{|\boldsymbol{r} - \boldsymbol{r'}|^2}. \tag{5.77}$$

Of particular importance in the study of disordered systems by means of the unfolded method (chapter 7) is the regularized Green's function $\bar{G}_\mathrm{reg}(\boldsymbol{r})$. It describes the effect of the leads and, in the absence of magnetic field, is proportional to the unit matrix in sublattice space. For any aspect ratio it can thus be expressed in terms of the LDoS $\rho_0(x)$ (per spin and valley) as

$$\bar{G}^R_\mathrm{reg}(\boldsymbol{r}) = -\frac{i\pi}{2}\rho_0(x). \tag{5.78}$$

In the case $W \gg L$ it is found from equations (5.73), (5.76) as

$$\bar{G}^R_\mathrm{reg}(\boldsymbol{r}) = \frac{-i}{4\hbar v L \sin(\pi x/L)}, \qquad \text{for } W \gg L, \tag{5.79}$$

and the LDoS follows as

$$\rho_0(x) = \frac{1}{2\pi\hbar v_\mathrm{F} L \sin(\pi x/L)}, \qquad \text{for } W \gg L. \tag{5.80}$$

The LDoS diverges at the interfaces due to the assumption of infinitely doped leads, and is minimal in the centre of the sample, $\rho_0(L/2) = 1/hv_\mathrm{F}L$. The $1/x$-power law decay near the interfaces is in contrast to the metal-induced LDoS in conventional semiconductors.

Using the gauge transformation (5.47), the LDoS in the presence of a magnetic field is readily found as

$$\rho(x) = \cosh\left(2\chi(x)\right)\rho_0(x). \tag{5.81}$$

It is unaffected by tat the interfaces but exponentially enhanced in the bulk of the sample due to the zero-energy Landau level.

5.6.2 Corbino geometry with small central lead

For completeness I also discuss the opposite limit $R \gg a$, in which the Corbino geometry corresponds to a long and narrow cylinder ($W \ll L$). In this case the sum over modes in equation (5.27) becomes a geometric series. Since a very large ratio $R \gg a$ is required in this approximation, it is experimentally less relevant.

[3]The conformal mapping transformation (5.38) leaves g_0 invariant in the limit $\boldsymbol{r'} \to \boldsymbol{r}$, which proves that the decomposition (5.76) holds analogously for the Green's function $G^R(\boldsymbol{r}, \boldsymbol{r'})$ in the Corbino geometry.

The real-space Green's function in this limit can be written as a sum of four terms,

$$G^R(\boldsymbol{r},\boldsymbol{r}') = g_0(\boldsymbol{r},\boldsymbol{r}') + \bar{g}_R(\boldsymbol{r},\boldsymbol{r}') - \bar{g}_a(\boldsymbol{r},\boldsymbol{r}') + g_\zeta(\boldsymbol{r},\boldsymbol{r}'), \qquad \text{for } R \gg a, \tag{5.82}$$

where $g_0(\boldsymbol{r},\boldsymbol{r}')$ is the Green's function (5.77) describing infinite graphene, which in polar coordinates reads

$$g_0(\boldsymbol{r}-\boldsymbol{r}') = -\frac{i}{2\pi}\begin{pmatrix} 0 & \left(r\,e^{i\theta} - r'\,e^{i\theta'}\right)^{-1} \\ \left(r\,e^{-i\theta} - r'\,e^{-i\theta'}\right)^{-1} & 0 \end{pmatrix}. \tag{5.83}$$

The terms $\bar{g}_R$ and $\bar{g}_a$ describe evanescent modes originating from the contacts,

$$\bar{g}_s(\boldsymbol{r},\boldsymbol{r}') = -\frac{i}{2\pi}\begin{pmatrix} \frac{s}{s^2 - rr'e^{i(\theta-\theta')}} & 0 \\ 0 & \frac{s}{s^2 - rr'e^{-i(\theta-\theta')}} \end{pmatrix}, \tag{5.84}$$

where $s = R, a$. The term g_ζ depends on the sign $\zeta = \mathrm{sign}(r - r')$ but vanishes in the limit $\boldsymbol{r} \to \boldsymbol{r}'$. For arguments where the condition $|\boldsymbol{r} - \boldsymbol{r}'| \ll R$ is not fulfilled, it can be written as

$$g_+(\boldsymbol{r},\boldsymbol{r}') = -\frac{i}{2\pi}\begin{pmatrix} 0 & \frac{a/R}{r'e^{i\theta'}} \\ \frac{a/R}{r'e^{-i\theta'}} & 0 \end{pmatrix}, \quad g_-(\boldsymbol{r},\boldsymbol{r}') = -\frac{i}{2\pi}\begin{pmatrix} 0 & \frac{a/R}{re^{i\theta}} \\ \frac{a/R}{re^{-i\theta}} & 0 \end{pmatrix}. \tag{5.85}$$

For $r \approx r'$ the term g_ζ is negligible compared to $g_0(\boldsymbol{r}-\boldsymbol{r}')$ and vanishes in the limit $\boldsymbol{r} \to \boldsymbol{r}'$, which is relevant for the regularized Green's function, since it implies that the off-diagonal elements are zero,

$$G^R_{\mathrm{reg}}(\boldsymbol{r}) = \bar{g}_R(\boldsymbol{r},\boldsymbol{r}) - \bar{g}_a(\boldsymbol{r},\boldsymbol{r}) = -\frac{i}{2\pi}\left(\frac{R}{R^2 - r^2} + \frac{a}{r^2 - a^2}\right), \quad \text{for } R \gg a. \tag{5.86}$$

Since the regularized Green's function is proportional to the unit matrix in sublattice space, the relation to the LDoS is given by equation (5.78).

5.7 Matrix Green's Function and Transmission Distribution

The matrix Green's function, which depends on the external source field, has been introduced in section 3.7 to express the full counting statistics of charge transport in terms of Green's functions. The approach is also particularly useful in the study of transport in disordered graphene as we will see in chapter 8. In this section, which is restricted to the case $\varepsilon = 0$ of undoped graphene, I apply the conformal mapping to the matrix Green's function, calculate the matrix Green's function for the rectangular setup and the Corbino disk, and evaluate the transmission distribution of a clean sample confirming the results obtained from the transfer matrix method in section 4.3.

5.7.1 Conformal mapping

The conformal mapping transformation for the matrix Green's function has exactly the same form as for the retarded Green's function, equation (5.38). In the Corbino geometry the Green's function $\mathcal{G}(\boldsymbol{r},\boldsymbol{r'})$ in the external source fields $\zeta_+,\ \zeta_-$ satisfies [cf. equation (3.81)]

$$\begin{pmatrix} i\eta - v_{\mathrm{F}}\boldsymbol{\sigma}\,\boldsymbol{p} - V(r) & -\hat{v}_r\,\zeta_+\,\delta(r-a) \\ -\hat{v}_r\,\zeta_-\,\delta(r-R) & -i\eta - v_{\mathrm{F}}\boldsymbol{\sigma}\,\boldsymbol{p} - V(r) \end{pmatrix} \mathcal{G}(\boldsymbol{r},\boldsymbol{r'}) = \delta(\boldsymbol{r}-\boldsymbol{r'}), \tag{5.87}$$

where the operator $\hat{v}_r$ for the radial current is given by (5.59), and the potential $V(r)$ is given by equation (5.25). As before I consider the case of strongly doped leads such that $V_0 a \gg 1$. Using the decomposition (5.38), equation (5.87) is reduced to the following one,

$$\begin{pmatrix} i\eta - v_{\mathrm{F}}\boldsymbol{\sigma}\,\boldsymbol{p} - \bar{V}(x) & -\sigma_x\,\zeta_+\,\delta(x) \\ -\sigma_x\,\zeta_-\,\delta(x-L) & -i\eta - v_{\mathrm{F}}\boldsymbol{\sigma}\,\boldsymbol{p} - \bar{V}(x) \end{pmatrix} \bar{\mathcal{G}}(\boldsymbol{r},\boldsymbol{r'}) = \delta(x-x')\delta(y-y'), \tag{5.88}$$

which is again equivalent to the rectangular setup with periodic boundary conditions in y-direction and a flux $\Phi_0/2$ piercing the cylinder.

In the following solution of equation (5.88) I follow ref. [48]. Since the source fields act only at the sample-lead interfaces, they can be incorporated into the boundary conditions along with the lead potential $V(x)$, leading to

$$\begin{pmatrix} 1 & 1 & i\zeta_+ & i\zeta_+ \\ 0 & 0 & 1 & -1 \end{pmatrix} \bar{\mathcal{G}}(0,x';y,y') = 0, \qquad \begin{pmatrix} 1 & -1 & 0 & 0 \\ -i\zeta_- & -i\zeta_- & 1 & 1 \end{pmatrix} \bar{\mathcal{G}}(L,x';y,y') = 0. \tag{5.89}$$

The matrix Green's function in the sample is then governed by the standard evolution

$$-\,v_{\mathrm{F}}\boldsymbol{\sigma}\boldsymbol{p}\,\bar{\mathcal{G}}(\boldsymbol{r},\boldsymbol{r'}) = \delta(x-x')\delta(y-y'). \tag{5.90}$$

Since the counting fields preserve the translational invariance in y direction, the solution to these equations can be found by a Fourier transform to the mixed channel-coordinate representation in the same way as it was done for the bare retarded Green's function in equation (5.8). This method used in ref. [48] is carried out in the following subsection. An alternative method to find the matrix Green's function is provided by the transformations presented in section 5.8.

5.7.2 Matrix Green's function without source field transformations

Applying the Fourier transform (5.8) correspondingly to $\bar{\mathcal{G}}(\boldsymbol{r},\boldsymbol{r'})$ in equation (5.90), one obtains the following equation for the Green's function in the mixed channel-

coordinate representation,

$$[i\sigma_x\partial_x - m\sigma_y]\,\bar{\mathcal{G}}_m(x,x') = \delta(x-x'). \tag{5.91}$$

Since the boundary conditions (5.89) are independent of m, they hold equally for each $\bar{\mathcal{G}}_m(x,x')$. Equation (5.91) may be solved by introducing yet another decomposition,

$$\bar{\mathcal{G}}_m(x,x') = e^{\sigma_z m(x-L/2)}\,M\,e^{\sigma_z m(x'-L/2)}, \qquad M = \begin{cases} M_<, & x<x', \\ M_>, & x>x'. \end{cases} \tag{5.92}$$

The normalization condition is obtained by integrating equation (5.91) from $x = x'-0$ to $x = x'+0$,

$$M_> - M_< = -i\,\sigma_x. \tag{5.93}$$

This condition, together with the boundary conditions (5.89), uniquely determines the matrices $M_{\lessgtr}$,

$$M_{\lessgtr} = \frac{-i}{2(\cosh^2(mL) - \zeta_+\zeta_-)}\Omega \pm \frac{i\sigma_x}{2}, \tag{5.94}$$

where

$$\Omega \equiv \begin{pmatrix} \cosh mL & \zeta_+\zeta_- - \frac{\sinh 2mL}{2} & i\zeta_+ e^{-mL} & i\zeta_+ \\ \zeta_+\zeta_- + \frac{\sinh 2mL}{2} & \cosh mL & i\zeta_+ & i\zeta_+ e^{mL} \\ i\zeta_- e^{mL} & i\zeta_- & -\cosh mL & -\zeta_+\zeta_- - \frac{\sinh 2mL}{2} \\ i\zeta_- & i\zeta_- e^{-mL} & -\zeta_+\zeta_- + \frac{\sinh 2mL}{2} & -\cosh mL \end{pmatrix}. \tag{5.95}$$

This completes the construction of the matrix Green's function in channel space, which determines the full counting statistics of charge transport in a clean sample.

In the following I carry out the Fourier transform to find compact expressions for the matrix Green's function in real space in the limit $W \gg L$. The infinite sum can also be carried out in the opposite limit $R \gg a$, using the same approximation as in section 5.6. The expressions for this limit are omitted as they are more lengthy and not used in the remainder of this work.

In the limit $W \gg L$ the Green's function can be Fourier transformed into real space by replacing the sum over m by an integral. Parametrizing the source fields as

$$\zeta_+ = \zeta_- = i\sinh(\phi/2), \tag{5.96}$$

the matrix Green's function is found as

$$\bar{\mathcal{G}} = \begin{pmatrix} \bar{\mathcal{G}}^R & \bar{\mathcal{G}}^+ \\ \bar{\mathcal{G}}^- & \bar{\mathcal{G}}^A \end{pmatrix}, \tag{5.97}$$

with the submatrices given by

$$\bar{\mathcal{G}}^{R,A}(x,x';y) = \frac{-i}{4L\,\cosh\frac{\phi}{2}} \begin{pmatrix} \pm\frac{\cosh\frac{\phi}{2L}(1-x-x'-iy)}{\sin\frac{\pi}{2L}(x+x'+iy)} & \frac{\cosh\frac{\phi}{2L}(\pm1-x+x'-iy)}{\sin\frac{\pi}{2L}(x-x'+iy)} \\ \frac{\cosh\frac{\phi}{2L}(\pm1-x+x'+iy)}{\sin\frac{\pi}{2L}(x-x'-iy)} & \pm\frac{\cosh\frac{\phi}{2L}(1-x-x'+iy)}{\sin\frac{\pi}{2L}(x+x'-iy)} \end{pmatrix}, \tag{5.98}$$

$$\bar{\mathcal{G}}^{\pm}(x,x';y) = \frac{i}{4L\,\cosh\frac{\phi}{2}} \begin{pmatrix} \pm\frac{\sinh\frac{\phi}{2L}(\pm1+1-x-x'-iy)}{\sin\frac{\pi}{2L}(x+x'+iy)} & \frac{\sinh\frac{\phi}{2L}(x-x'+iy)}{\sin\frac{\pi}{2L}(x-x'+iy)} \\ \frac{\sinh\frac{\phi}{2L}(x-x'-iy)}{\sin\frac{\pi}{2L}(x-x'-iy)} & \pm\frac{\sinh\frac{\phi}{2L}(\pm1+1-x-x'+iy)}{\sin\frac{\pi}{2L}(x+x'-iy)} \end{pmatrix}. \tag{5.99}$$

In ref. [48] it has been shown that this Green's function can be decomposed into simpler matrices in Keldysh and sublattice space. In section 5.8 I show that such a decomposition is possible quite generally.

5.7.3 Transmission distribution of short and wide rectangular device

I am now ready to evaluate the generating function of transmission distribution using the matrix Green's function. This function was defined in equation (3.86) and expressed in terms of the matrix Green's function in equation (3.89),

$$F(\zeta_+\zeta_-) = \frac{1}{\zeta_-}\,\mathrm{Tr}_y\left[\begin{pmatrix} 0 & \hat{v}_x \\ 0 & 0 \end{pmatrix}\mathcal{G}(0,0)\right] = \frac{1}{\zeta_+}\,\mathrm{Tr}_y\left[\begin{pmatrix} 0 & 0 \\ \hat{v}_x & 0 \end{pmatrix}\mathcal{G}(L,L)\right]. \tag{5.100}$$

This formula holds for the rectangular geometry, but it is easy to see that it holds equivalently in the Corbino geometry and at zero energy can be conformally mapped in the same way as the Kubo formula in section 5.5.1.

In the short and wide rectangular graphene sample it is particularly convenient to parameterize the source field by an angle ϕ as in equation (5.96). Substituting the matrix Green's function results (5.97), (5.99) into equation (5.100) one obtains

$$F(-\sinh^2\tfrac{\phi}{2}) = \frac{W}{iL\,\sinh\frac{\phi}{2}}\,\mathrm{Tr}\left[\sigma_x\,\bar{\mathcal{G}}^{-}(0,0;0)\right] = \frac{W}{\pi L}\frac{\phi}{\sinh\phi}, \qquad \text{for } W \gg L. \tag{5.101}$$

The negative of the ground-state energy, equation (3.82), is found as

$$\mathcal{F}(\phi) = \frac{W}{4\pi L}\phi^2, \qquad \text{for } W \gg L. \tag{5.102}$$

This result is in agreement with equation (4.19). Its simple form demonstrates the convenience of the source field parameterization (5.96). The charge transport in the clean sample responds linearly to the external field ϕ [120]. According to equation (3.93) the conductance is obtained as the following derivative of $\mathcal{F}$,

$$\mathrm{G} = 2\,\mathrm{g}_0\,\left.\frac{\partial^2\mathcal{F}}{\partial\phi^2}\right|_{\phi=0} = \mathrm{g}_0\frac{W}{\pi L}, \tag{5.103}$$

in agreement with equation (3.62).

5.8 Transformations of the Counting Field

In this Section I construct a decomposition of the matrix Green's function similar to the one given in ref. [48]. This decomposition is achieved by employing transformations changing the way in which the source field acts. Although I am still dealing with the Green's function of a clean sample, this decomposition will prove particularly useful in the evaluation of the transport properties of a disordered sample. The decomposition is achieved in two steps. The first transformation (section 5.8.1) acts in Keldysh space and transforms the source fields from the boundary conditions to the evolution of the Green's function as a spatially constant term. This transformation is applicable at arbitrary energy. The transformation itself contains the source fields, but drops out from any physical observable.

The second transformation (section 5.8.2) makes use of the chiral symmetry and is only applicable at zero energy. It is a transformation of a generalized type and does not generally drop from physical observables. This transformation turns the source field into a constant vector potential, corresponding to a flux through the cylinder (or inner lead). This flux can be treated in the same way as a magnetic flux by a non-unitary gauge transformation. Therefore the matrix Green's function is transformed into a bare retarded Green's function, with source field-dependent boundary conditions in the transverse y direction, which are irrelevant for $W \gg L$.

5.8.1 Transformation in Keldysh space

Starting from equation (5.90), with the lead potential and the source fields incorporated in the boundary condition (5.89), I apply the transformation

$$\bar{\mathcal{G}}(\boldsymbol{r},\boldsymbol{r'}) = V_\phi(x)\Lambda_K\tilde{\mathcal{G}}(\boldsymbol{r},\boldsymbol{r'})\Lambda_K^{-1}V_\phi^{-1}(x'), \tag{5.104}$$

where the source fields have been conveniently parameterized as in (5.96) and the matrices in Keldysh space are defined as

$$V_\phi(x) = \frac{1}{\sqrt{2\cosh\phi/2}}\begin{pmatrix} e^{\frac{\phi(L-x)}{2L}} & -e^{-\frac{\phi(L-x)}{2L}} \\ e^{-\frac{\phi x}{2L}} & e^{\frac{\phi x}{2L}} \end{pmatrix}, \qquad \Lambda_K = \frac{1}{\sqrt{2}}\begin{pmatrix} 1 & 1 \\ -1 & 1 \end{pmatrix}. \tag{5.105}$$

The evolution of the transformed Green's function contains the counting field ϕ,

$$\left(-v_{\mathrm{F}}\boldsymbol{\sigma p} - i\sigma_x\Sigma_x\frac{\phi}{2L}\right)\tilde{\mathcal{G}}(\boldsymbol{r},\boldsymbol{r'}) = \delta(\boldsymbol{r}-\boldsymbol{r'}). \tag{5.106}$$

The Pauli matrices in the Keldysh space are denoted by Σ_x, Σ_y, Σ_z. The purpose of the transformation (5.104) is that the boundary conditions (5.89) are transformed

to the standard ones,

$$\begin{pmatrix} 1 & 1 & 0 & 0 \\ 0 & 0 & 1 & -1 \end{pmatrix} \tilde{\mathcal{G}}(0,x';y,y') = 0, \qquad \begin{pmatrix} 1 & -1 & 0 & 0 \\ 0 & 0 & 1 & 1 \end{pmatrix} \tilde{\mathcal{G}}(L,x';y,y') = 0. \quad (5.107)$$

Even though the transformation (5.104) contains the counting field, the matrices V_ϕ and Λ_K drop out from any physical observable. This statement also holds in the presence of disorder, as we will see from the Dyson equation in chapter 8.

By applying the transformation (5.104) in the cumulant generating function (3.82), one finds the following representation of the Kubo formula,

$$\mathrm{Tr}(t^\dagger t)^n = \frac{1}{L^2} \int d^2\boldsymbol{r} \int d^2\boldsymbol{r}' \, \mathrm{Tr} \left[\hat{v}_x \, \hat{G}^R(\boldsymbol{r};\boldsymbol{r}') \, \hat{v}_x \, \hat{G}^A(\boldsymbol{r}';\boldsymbol{r}) \right]^n, \quad (5.108)$$

where the integration is over the sample area. This formula is in agreement with the Kubo formula (3.80), given that the choice of the two cross-sections is arbitrary due to current conservation.

5.8.2 Zero-energy transformations

The transformation (5.104) is general and holds at any energy. I now introduce another transformation which is useful only at zero energy. This is a transformation of a generalized kind and acts both in RA and sublattice space,

$$\tilde{\mathcal{G}}(\boldsymbol{r},\boldsymbol{r}') = \Lambda \, \mathcal{L} \, \overline{\mathcal{G}}(\boldsymbol{r},\boldsymbol{r}') \, \mathcal{L}^{-1} \, \Lambda, \qquad \mathcal{L} = \frac{1}{\sqrt{2}}(\Sigma_z + \Sigma_y), \qquad \Lambda = \begin{pmatrix} 1 & 0 \\ 0 & i\sigma_z \end{pmatrix}. \quad (5.109)$$

Using the chiral symmetry, the transformed evolution equation is found as

$$\left(-v_\mathrm{F} \boldsymbol{\sigma} \boldsymbol{p} + \Sigma_z \frac{\phi}{2L} \sigma_y \right) \overline{\mathcal{G}}(\boldsymbol{r},\boldsymbol{r}') = \delta(\boldsymbol{r} - \boldsymbol{r}'). \quad (5.110)$$

Thus, the counting field acts in the same way as a transverse vector potential, with an opposite sign in the retarded and advanced subspace. Moreover, the boundary conditions (5.107) acquire the simple form

$$\begin{pmatrix} 1 & 1 & 0 & 0 \\ 0 & 0 & 1 & 1 \end{pmatrix} \overline{\mathcal{G}}(0,x';y,y') = 0, \qquad \begin{pmatrix} 1 & -1 & 0 & 0 \\ 0 & 0 & 1 & -1 \end{pmatrix} \overline{\mathcal{G}}(L,x';y,y') = 0, \quad (5.111)$$

which correspond to retarded boundary conditions for both components in Keldysh space. It follows that the solution is diagonal in Keldysh space and can be written as

$$\overline{\mathcal{G}}(\boldsymbol{r},\boldsymbol{r}') = \begin{pmatrix} \overline{R}_+(\boldsymbol{r},\boldsymbol{r}') & 0 \\ 0 & \overline{R}_-(\boldsymbol{r},\boldsymbol{r}') \end{pmatrix}, \quad (5.112)$$

where the components are governed by the propagation

$$\left(-v_{\mathrm{F}}\boldsymbol{\sigma}\,\boldsymbol{p} \pm \frac{\phi}{2L}\sigma_y\right)\overline{R}_{\pm}(\boldsymbol{r},\boldsymbol{r'}) = \delta(\boldsymbol{r}-\boldsymbol{r'}), \tag{5.113}$$

along with the retarded boundary conditions

$$(1,1)\overline{R}_{\pm}(0,x';y,y') = 0, \qquad (1,-1)\overline{R}_{\pm}(L,x';y,y') = 0. \tag{5.114}$$

The transformed Green's function can thus be interpreted as the retarded Green's function of the system with a magnetic flux piercing the cylinder (or through the inner lead), which is proportional to the counting-field and opposite for retarded/advanced components. Indeed, an identical setup has been considered by Laughlin [134] in his proof of the quantization of the Hall conductivity. This proof is based on a gauge invariance, which implies that the addition of a flux quantum to the flux piercing the cylinder results in the excitation of the original system without any effect on the wave functions. In the case of a clean system the gauge invariance is related to the coherence of wave functions around the cylinder. Laughlin considered the case that the Fermi energy lies in a mobility gap between Landau levels. For this case he showed that the excitation caused by the change of flux corresponds to a net transfer of an integer number of electrons from one edge to the other, due to the location of the centers of the wave functions in the Landau gauge as $x_0 \to x_0 - \Delta A_y/B$, where ΔA_y is the vector potential increment and B is the perpendicular magnetic field in the sample. The proof holds in the same way in graphene, where the centers of the wave functions behave just in the same way. (For the $n = 0$-Landau level this follows from equation (3.41) and the gauge transformation (5.45).) In the absence of magnetic field there is still a net charge transfer due to the vector potential increment, although it is now not quantized. Note that since our sample is clean, it is irrelevant that we are sitting on a Landau level rather than in a mobility gap.

Equation (5.113) is solved in the usual way by the transformation

$$\overline{R}_{\pm}(\boldsymbol{r},\boldsymbol{r'}) = e^{\pm i(y-y')\phi/2L}R_{\pm}(\boldsymbol{r},\boldsymbol{r'}), \tag{5.115}$$

where $R_{\pm}$ fulfills the same equation as the bare retarded Green's function for absent magnetic field, equation (5.7). The Fourier transform is thus given by

$$R_{\pm}(\boldsymbol{r},\boldsymbol{r'}) = \frac{1}{W}\sum_m e^{im_{\pm}(y-y')}R_{m_{\pm}}(x,x'), \tag{5.116}$$

where $R_m(x,x')$ is the retarded Green's function in transverse channel space defined in equation (5.12), and the transformation (5.115) induces a shift of the mode index

with opposite signs for retarded and advanced components,

$$m_\pm = m \mp \frac{\phi}{2L}. \tag{5.117}$$

This shift ensures that $\bar{\mathcal{G}}$ obeys the periodic boundary conditions in y and y'.

Combining the transformations (5.104), (5.109), and (5.115) yields

$$\bar{\mathcal{G}}(\boldsymbol{r},\boldsymbol{r'}) = V_\phi(x)\Lambda_K\Lambda\,\mathcal{L}\,e^{i\Sigma_z(y-y')\phi/2L}\begin{pmatrix} R_+(\boldsymbol{r},\boldsymbol{r'}) & 0 \\ 0 & R_-(\boldsymbol{r},\boldsymbol{r'}) \end{pmatrix}\mathcal{L}^{-1}\,\Lambda\Lambda_K^{-1}V_\phi^{-1}(x'). \tag{5.118}$$

The transformation evidently commutes both with the conformal mapping transformation (5.38) and the magnetic field transformation (5.47). Therefore it is applicable in the same form in the Corbino geometry and in the presence of an arbitrary magnetic field.

In order to deal with point-like impurities I also need to decompose the regularized Green's function,

$$\bar{\mathcal{G}}_{\rm reg}(\boldsymbol{r}) = \lim_{\boldsymbol{r'}\to\boldsymbol{r}}\left[\bar{\mathcal{G}}(\boldsymbol{r},\boldsymbol{r'}) - g_0(\boldsymbol{r}-\boldsymbol{r'})\right] \tag{5.119}$$

$$= V_\phi(x)\Lambda_K\Lambda\,\mathcal{L}\,\overline{\mathcal{G}}_{\rm reg}(\boldsymbol{r})\,\mathcal{L}^{-1}\,\Lambda\Lambda_K^{-1}V_\phi^{-1}(x). \tag{5.120}$$

Since the divergent term $g_0(\boldsymbol{r}-\boldsymbol{r'})$ is left invariant by the transformation (5.118), the transformed regularized Green's function is given by

$$\overline{\mathcal{G}}_{\rm reg}(\boldsymbol{r}) = \lim_{\boldsymbol{r'}\to\boldsymbol{r}}\left[\overline{\mathcal{G}}(\boldsymbol{r},\boldsymbol{r'}) - g_0(\boldsymbol{r}-\boldsymbol{r'})\right] = \begin{pmatrix} \overline{R}_+^{\rm reg}(\boldsymbol{r}) & 0 \\ 0 & \overline{R}_-^{\rm reg}(\boldsymbol{r}) \end{pmatrix}, \tag{5.121}$$

with the regularized components defined in the usual way as

$$\overline{R}_\pm^{\rm reg}(\boldsymbol{r}) = \lim_{\boldsymbol{r'}\to\boldsymbol{r}}\left[\overline{R}_\pm(\boldsymbol{r},\boldsymbol{r'}) - g_0(\boldsymbol{r}-\boldsymbol{r'})\right]. \tag{5.122}$$

However, the transformation (5.115) does not become trivial in the limit $\boldsymbol{r'}\to\boldsymbol{r}$ as we will see below.

In the case $W \gg L$ the transverse momentum shift in equation (5.116) is irrelevant and the Green's functions $R_\pm$ coincides with the bare retarded Green's function $\bar{G}^R(\boldsymbol{r},\boldsymbol{r'})$, calculated in equation (5.73). Hence

$$\overline{\mathcal{G}}(\boldsymbol{r},\boldsymbol{r'}) = e^{i\Sigma_z(y-y')\phi/2L}\bar{G}^R(\boldsymbol{r},\boldsymbol{r'}), \qquad \text{for } W \gg L. \tag{5.123}$$

The counting field drops out for $y = y'$, but not in the limit $\boldsymbol{r'}\to\boldsymbol{r}$, where the regularized Green's function acquires an additive term linear in the counting field,

$$\overline{\mathcal{G}}_{\rm reg}(\boldsymbol{r}) = \bar{G}^R_{\rm reg}(\boldsymbol{r}) + \Sigma_z\sigma_y\frac{\phi}{4\pi L}, \qquad \text{for } W \gg L. \tag{5.124}$$

These results for the Green's function in the limit $W \gg L$ can be verified by the result (5.97) which was obtained via the Fourier transform to the matrix Green's function in the channel representation.

5.8.3 Summary

The standard representation of the matrix Green's function contains the retarded and advanced Green's functions, which are mixed by the source fields at the sample-lead interfaces. This virtual perturbation allows one to directly access all moments of the current response, giving the full counting statistics of charge transport. In this section I demonstrated alternative ways of introducing the source fields, allowing for an easier representation of the matrix Green's function. The first transformation, equation (5.104), holds at any energy and drops out from any physical observable. From the Kubo formula corresponding to the transformed matrix Green's function we have seen that this transformation is related to current conservation. The second transformation, equation (5.109), is only applicable in the clean undoped graphene sample. Its advantage is to transform the matrix Green's function into a retarded Green's function, where the source field enters only as a 'magnetic' flux piercing the cylinder, thereby changing the transverse boundary conditions. This transformation does not drop from all physical observables, but it is simple and does not contain the source fields. The fact that the current response may be obtained by adding a virtual flux piercing the cylinder instead of virtually injecting charge carriers at the sample-lead interfaces is closely related to Laughlin's proof of the quantized Hall conductivity.

The matrix Green's function of the clean sample describes the full counting statistics of ballistic charge transport. In chapter 7 an 'unfolded' scattering approach will be introduced to study transport in a sample with isolated impurities. The disorder correction to the full counting statistics can be expressed in terms of the matrix Green's function of the clean sample, taken between each two impurity sites, as well as the T-matrices of impurities, describing their individual scattering properties in an infinite system. When using this approach in chapter 8 to study magnetotransport in disordered graphene, the source field transformations of the matrix Green's functions will prove particularly helpful, as they strongly simplify the impurity correction to the full counting statistics. We will also see that the transformation describing the conformal mapping and the non-unitary gauge transformation for a vector potential are still applicable in the presence of impurities, if one takes into account the effect of each transformation on the individual impurity T-matrices.

Chapter 6 – Contact Potential and Effect on Ballistic Transport Properties

6.1 Introduction

Transport experiments with graphene require metallic electrodes for injecting a current and for measuring the voltage drop. The voltage probes can be designed in two different ways [135]. External probes are attached only to side arms of the main graphene sheet in a multi-terminal Hall-bar structure, meaning that their impact is minimized and the intrinsic transport properties of graphene can be accessed. However, the sample geometry becomes less universal and evanescent modes might not play any role for the transport. Invasive probes, on the other hand, cover the whole width of the graphene sheet, so that the influence on the transport becomes evident. These are either placed between the source and drain electrodes (four-terminal device) or identical with these electrodes (two-terminal device). The latter design, which is shown in figure 6.1, might be desired in the miniaturization of graphene-based electronic devices. In either case, the influence of invasive electrodes on the electric transport needs to be understood in order to interpret the measurement data.

Since the metallic contacts placed on top define an effective electron cavity in the graphene sheet, they determine the transport properties when the channel length of the graphene transistor is decreased to sub-micron length scales. The contact effects ultimately dominate in the regime where the transport is quasi-ballistic and phase coherent [136]. This regime has been approached recently both in suspended graphene [30, 15] and graphene on SiO_2 substrate [137, 115].

The simplistic theory of ballistic transport [24, 138] studied in the previous chapters models the sample-lead interfaces as a scalar step-function potential in the Dirac equation. However, the experiments in the quasi-ballistic regime have common features such as the electron-hole asymmetry in the gate-voltage dependence of the conductance and much more prominent conductance oscillations at positive doping than at negative doping. In this chapter I attribute these experimental observations to the effect of charge transfer in a vicinity of metal electrodes and to a weak screening in graphene at low doping.

I suggest a minimal model that includes the contact-induced doping in a self-consistent manner and reproduces the large electron-hole asymmetry observed in experiments. The model leads to a very good description of experimental data by Du *et al.* [15] on charge transport in suspended graphene. The gate-voltage dependence of transport properties predicted by the model also agree qualitatively with those observed by Heersche *et al.* [137] for graphene on SiO_2 substrate. Qualita-

tively similar results have also been obtained in the theoretical study in ref. [139], where the interface is modeled by an exponentially decaying potential. These models, however, are not self-consistent and cannot describe the large electron-hole asymmetry observed in experiments.

In general, two mechanisms have been discussed to explain the often observed electron-hole asymmetry in the graphene transport properties, namely the presence of charged impurity scatterers and contact effects. In refs. [140, 135, 31] the influence of the potential steps near the metallic contacts on the conductance of a graphene strip has first been studied quantitatively. The odd part of the gate-voltage dependent resistance has been clearly identified as a contact resistance in ref. [135], and the electrostatic potential landscape has been imaged by means of scanning photocurrent microscopy [140, 141] to demonstrate the long-range decay of the contact-induced potential (about 1 μm). The contact resistance for both mono- and few-layer graphene samples has been analyzed and explained by the charge transfer at the graphene/metal interface in ref. [142].

Most experiments suggest that the charge density in graphene covered by a metal is pinned, i.e. not affected by the gate voltage. The pinning is much weaker if the graphene sheet is oxidized and the metal-graphene contact is resistive. In this case the second minimum in the gate voltage dependence of conductance can emerge which corresponds to the charge density minimum in the metal-covered graphene. In ref. [143] this mechanism is claimed to be responsible for the electron-hole asymmetry observed in the studies in refs. [144, 30]. I argue, however, that the asymmetry seen in refs. [30, 15, 145] is entirely due to the contact-induced potential in the free-standing graphene. I also regard the observed saturation of the conductance for large negative gate voltages as the signature of the charge density pinning in the metal-covered graphene. The same mechanism of the electron-hole asymmetry has been put forward recently in ref. [146].

The adsorption of graphene on metal substrates has been studied by means of density functional theory (DFT) in refs. [147, 148]. In agreement with the experiments, these studies suggest that for the commonly used elements Al, Ag, Cu, Au, and Pt the main effect of the metal deposition can be modeled by a shift of the Fermi level, i.e. by the chemical doping. This shift can be of any sign. Its precise value, μ_l, is comparatively large due to the small density of states of intrinsic graphene, and depends on the workfunctions of graphene and the metal as well as on the direct chemical interaction. The most recent analysis [148] predicts, e.g. $\mu_l = -0.51\,\mathrm{eV}$ for Al, $-0.40\,\mathrm{eV}$ for Ag, $-0.43\,\mathrm{eV}$ for Cu, and $0.21\,\mathrm{eV}$ for Au. Other metals (Co, Ni, Pd, and Ti) bind more strongly with graphene, so that the Dirac-like behaviour of quasiparticles is usually destroyed.

Microscopic DFT-modeling has been employed in ref. [149] to investigate the contact-induced potential in short ($L < 14\mathrm{nm}$) graphene samples, and its effect

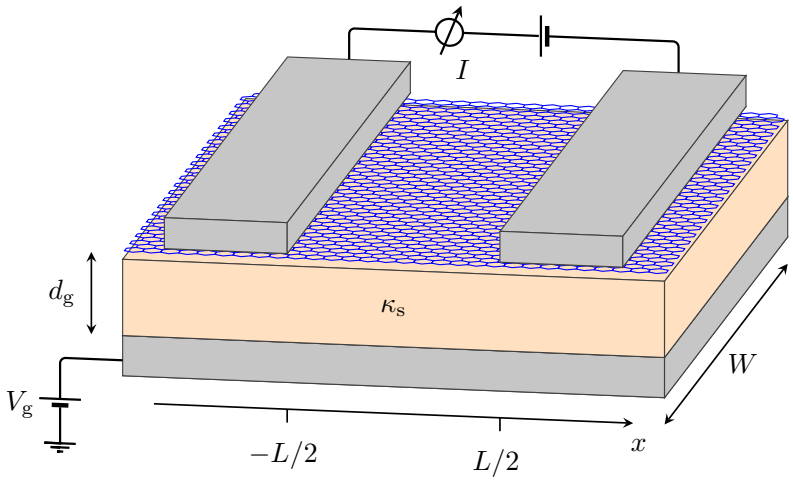

Figure 6.1: Schematics of a two-terminal graphene device with a global back gate electrode.

on the two-terminal conductance. In this study a gate electrode is absent and the conductance is studied as a function of Fermi energy using electrostatic potential for undoped graphene. The reported electron-hole asymmetry is, therefore, of a different type than the one occurring with pinned charge density in the leads. It is also hard to scale the results of ref. [149] to realistic system sizes ($L > 100\,\mathrm{nm}$).

In this chapter I propose an effective model taking into account the charge density pinning in the leads as well as the band bending in the graphene sheet. The model allows me to calculate the contact potential in the graphene sheet self-consistently, and therefore to quantitatively investigate the effect of the band bending on the transport properties. As in the previous chapters I focus on the two-terminal geometry and neglect the resistance of the metal-graphene interfaces. I employ the effective Dirac Hamiltonian and take into account the large density of states in a metal, which enhances the screening capacities of the leads. The gate electrode is incorporated implicitly into the model, since I use the externally induced charge densities in the sample and the leads (while disconnected) as external parameters for the self-consistent calculation. The actual interaction problem is thus restricted to the two-dimensional plane of the graphene sheet, and the system size poses no serious restriction in this effective model. The presence or absence of a substrate is taken into account by an appropriate choice of the permittivity constant.

The self-consistent potential in graphene is calculated using two different approximations, namely the self-consistent Hartree (SCH) and the Thomas-Fermi (TF) approximation. Subsequently, the two-terminal conductance and noise as a function of gate voltage are obtained from the Kubo formula. The different approximations result in a qualitatively similar form of the effective potential. The potential penetrates deeply into the sample and reveals a power-law decay with the exponent varying from -1 to -0.5 depending on the electron concentration. This

behavior agrees with the TF analysis of a single metal-graphene contact in ref. [150]. I demonstrate that the slow decay of the potential is responsible for the asymmetric gate-voltage dependence of conductance and noise, increasing in intensity with the lead doping $|\mu_l|$. For small positive gate voltages the Dirac point crosses the chemical potential twice inside the sample so that two n-p interfaces are formed. The slow potential decay ensures that the transmission through the interfaces is strongly selective with respect to the momentum direction ref. [113]. The electron scattering at the n-p interfaces is the reason for the enhanced Fabry-Pérot oscillations of the conductance as a function of electron concentration at moderate positive doping. When describing gate-voltage asymmetries I refer to negatively doped leads, $\mu_l < 0$. For positively doped leads the polarity of the effect is reversed. One can further argue that Fabry-Pérot oscillations are easily distorted by disorder. The presence and shape of the Fabry-Pérot oscillations can, therefore, be used as a direct indicator of the sample quality.

6.2 Charge and Potential Profiles

6.2.1 Model

The charge carriers in the graphene sheet (defining the xy-plane) are described by the single-valley Dirac Hamiltonian

$$H = H_0 + V(x), \qquad H_0 = -i\hbar v_{\mathrm{F}} \boldsymbol{\sigma} \cdot \boldsymbol{\nabla}, \tag{6.1}$$

where $\boldsymbol{\sigma}$ is a vector of Pauli matrices and $V(x)$ is the spatially dependent effective potential. In equation (6.1) I neglect any effects arising from the finite band width and assume translational invariance in y.

Doping of the graphene sheet is caused by the contact with the metal electrodes and by applying a voltage to the global back gate. The externally compensated charge density $\bar{n}(x)$ in the graphene sheet is used as an input parameter for a self-consistent calculation. I consider the two-terminal setup for which the metal-covered and free-standing parts of the graphene sheet correspond to $|x| > L/2$ (leads) and $|x| \leq L/2$ (sample), respectively (see figure 6.1). Accordingly, the compensated charge density has the spatial dependence

$$\bar{n}(x) = \begin{cases} \bar{n}_s, & \text{for } |x| < L/2, \\ \bar{n}_l, & \text{for } |x| > L/2, \end{cases} \tag{6.2}$$

where $\bar{n}_s$ is proportional to the gate voltage, since the distance d_{g} to the gate electrode is typically such that the quantum corrections to capacitance can be neglected. I assume that the charge density in the lead, $\bar{n}_l$, is pinned [143], i.e. not influenced by the gate-voltage. The screening inside the gate electrode can be neglected for

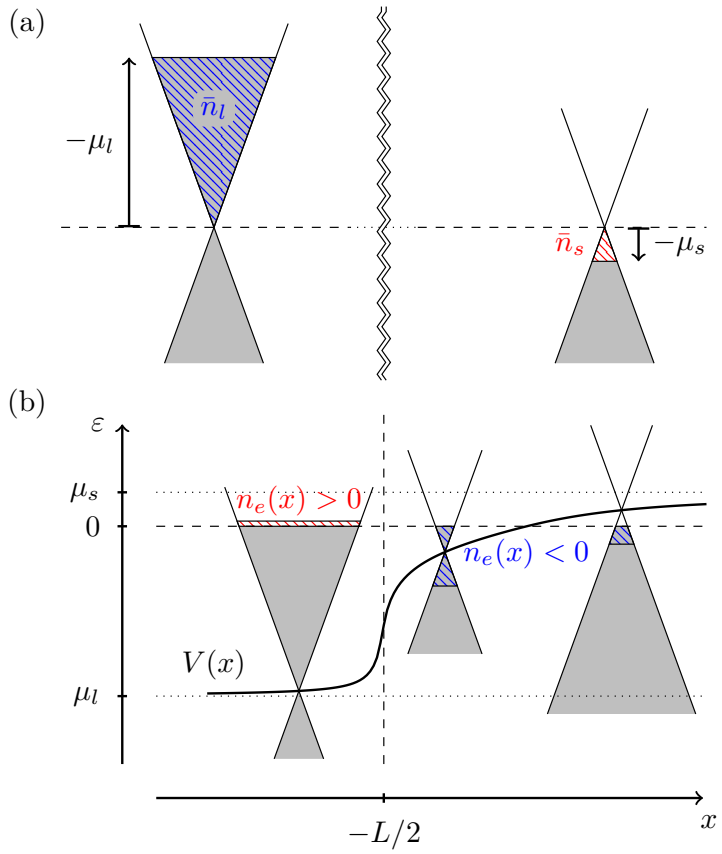

Figure 6.2: Schematic illustration of the doping in the left lead (metal-covered graphene) and the sample (ballistic graphene) if they (a) are not and (b) are in electrical contact with each other. The indicated excess charge density $n_e(x)$ in (b) (hashed regions) corresponds to the semiclassical (local) approximation. Quantum mechanical (non-local) corrections to $n_e(x)$ exist in the gray-shaded regions (Friedel oscillations) and in regions where the transverse momentum is outside the Dirac cone (evanescent modes).

$L \lesssim \kappa_\mathrm{s}\, d_\mathrm{g}$, with κ_s the relative permittivity of the gate dielectric. Finally, the inter-valley coupling at the metal-contact/graphene interface is also disregarded.

The band bending near the interfaces is most easily understood by first considering the artificial situation with disconnected sample and leads as shown in figure 6.2(a). The relation between the charge densities $\bar{n}_s$ and $\bar{n}_l$ and their respective chemical potentials $-\mu_s$ and $-\mu_l$ is given by

$$\bar{n}_{s,l} = \int d\varepsilon\ \rho_0(\varepsilon)\left\{(1-\theta_\varepsilon)(1-f_{\varepsilon+\mu_{s,l}}) - \theta_\varepsilon f_{\varepsilon+\mu_{s,l}}\right\}, \tag{6.3}$$

where f_ε is the Fermi distribution function, θ_ε is the Heaviside step function, and

$$\rho_0(\varepsilon) = \frac{2|\varepsilon|}{\pi\hbar^2 v_\mathrm{F}^2} \tag{6.4}$$

is the density of states (DoS) in infinitely extended ballistic graphene described by Hamiltonian H_0 from equation (6.1) including the spin and valley degeneracy. At

zero-temperature equation (6.3) becomes

$$\bar{n}_{s,l} = \frac{\mu_{s,l}|\mu_{s,l}|}{\pi\hbar^2 v_{\mathrm{F}}^2}. \tag{6.5}$$

The density profile $\bar{n}(x)$ corresponds to a charge-neutral setup with disconnected leads. Bringing the sample into electric contact with the leads causes the charge redistribution and the band bending shown in figure 6.2(b). The excess charge density $n_e(x)$ in the entire device is defined as

$$n_e(x) = n(x) + n_{\mathrm{m}}(x) - \bar{n}(x), \tag{6.6}$$

where $n(x)$ is the total charge density in the graphene sheet relative to intrinsic graphene, and

$$n_{\mathrm{m}}(x) = (V(x) - \mu_l)\ \rho_{\mathrm{m}}\, \theta_{|x|-L/2} \tag{6.7}$$

is the additional charge density induced in the metal surface deposited on the graphene sheet. The DoS in the metal is assumed to be much larger than the DoS in the contacted graphene sheet, $\rho_{\mathrm{m}} \gg \rho_0(\mu_l)$, and can be taken energy independent. The transport properties do not depend on the value of ρ_{m} under these conditions. Due to this addition to my model, the screening in the leads is strongly enhanced by the metal electrodes, which ensures the charge-density pinning.

The potential profile $V(x)$ and the total charge density $n(x)$ have to be determined self-consistently. In this study I ignore the exchange interaction and restrict myself to the scalar Hartree potential

$$V(x) = \mu_l + V_{\mathrm{H}}(x), \tag{6.8}$$

where

$$V_H(x) = \alpha\hbar v_{\mathrm{F}} \int_{-\infty}^{\infty} dx'\, n_e(x') \int_{-W/2}^{W/2} dy\ \frac{e^{-r(x-x',y)/a_0}}{r(x-x',y)}. \tag{6.9}$$

The coupling constant is given by $\alpha = \alpha_0/\kappa_{\mathrm{bg}}$, where $\alpha_0 = e^2/4\pi\epsilon_0\hbar v_{\mathrm{F}} \approx (c/v) \times (1/137) \approx 2.2$ is the fine structure constant in ballistic graphene, and κ_{bg} is the effective background dielectric constant in the graphene plane ($\kappa_{\mathrm{bg}} = 1$ for suspended graphene and $\kappa_{\mathrm{bg}} \approx 2.0$ for graphene on SiO_2 with the other side exposed to air/vacuum). The distance $r(x, y)$ depends on the 'geometry' of the graphene sheet. In a planar geometry, $r = \sqrt{x^2 + y^2}$, one has to regularize the interaction term by choosing a finite screening length $a_0 \gg L$. In this case on has to restrict the interaction problem to an x-range smaller than a_0 in order to fulfill the charge neutrality condition.[1] Alternatively one can let $a_0 \to \infty$ by considering a graphene sheet in the form of a cylinder with circumference $W \gg L$. This choice yields the

[1] This is allowed if the excess charge density $n_e(x)$ outside this x-range is negligible.

same results for $V(x)$ with a computational advantage.

The self-consistent scheme is closed by relating the total charge density $n(x)$ to the potential profile $V(x)$. This is done in two different approximations, which are discussed in the following two subsections.

6.2.2 Self-consistent Hartree approximation

The quantum-mechanical expression for $n(x)$ in the self-consistent Hartree (SCH) approximation reads

$$n_{\mathrm{SCH}}(x) = \int d\varepsilon\, f_{\varepsilon - V(x)}\, \rho_0(\varepsilon - V(x)) - f_\varepsilon \rho(x;\varepsilon). \tag{6.10}$$

The LDoS $\rho(x;\varepsilon)$ is most easily obtained using Green's functions as discussed in the previous chapter. I consider transport in a stationary regime, hence it is most convenient to use time-independent Green's functions. In the position basis the retarded and advanced Green's functions in the energy domain are defined by the equations

$$(\varepsilon \pm i\eta - H) G^{R,A}(\boldsymbol{r}, \boldsymbol{r}';\varepsilon) = \delta(\boldsymbol{r} - \boldsymbol{r}') \qquad (\eta \to 0+), \tag{6.11}$$

where η is a decoherence term. The retarded Green's function determines the LDoS (including the spin and valley degeneracies) as [cf. equation (5.6)]

$$\rho(x;\varepsilon) = -\frac{4}{\pi} \operatorname{Im} \operatorname{Tr} G^R(\boldsymbol{r}, \boldsymbol{r};\varepsilon), \tag{6.12}$$

which is only x-dependent due to the translational invariance in the y direction. The dependence of the LDoS on the effective potential is non-local. In order to solve the equation (6.11) for the retarded Green's function I again take advantage of the translational invariance in y by introducing the Fourier transform

$$G^R(\boldsymbol{r}, \boldsymbol{r}';\varepsilon) = \frac{1}{W} \sum_q \exp[iq\,(y - y')]\; G^R_q(x, x';\varepsilon), \tag{6.13}$$

where the summation runs over the discrete values of conserved transverse momentum, $q_n = 2\pi n/W$, with n integer (periodic boundary conditions in y direction). The Green's function $G^R_q(x, x';\varepsilon)$ in the channel representation thus fulfills

$$(\varepsilon + i\eta - V(x) + \hbar v_{\mathrm{F}}(i\sigma_x \partial_x - \sigma_y q))\; G^R_q(x, x') = \delta(x - x'). \tag{6.14}$$

The boundary conditions in x are obtained from the exact analytical solution in the asymptotic regions $|x| > \xi$ and $|x'| < \xi$, where $\xi > L/2$ is such that $V(|\xi|) \simeq \mu_l$. Selecting the decaying solution ($G^R_q(x, x';\varepsilon) \to 0$ for $x \to \pm\infty$) I take the limit $\eta \to 0$. Still, since the spectrum is partially discrete (some modes are confined in the sample), it is necessary to keep η finite to maintain the computational stability

of the scheme. I consider the limit $\hbar v_{\mathrm{F}}/W \ll \eta \ll \hbar v_{\mathrm{F}}/L$ such that coherence is preserved on the scale $\hbar v_{\mathrm{F}}/\eta \gg L$.

The numerical computation of the Green's function $G_q^R(x,x;\varepsilon)$ for $|x| < \xi$ is demanding since a large energy range has to be considered. For $\mu_l < \mu_s$ the lower energy bound at which the integrand in equation (6.10) becomes negligible is roughly $\mu_l - 2\times(\mu_s - \mu_l)$. To ensure the charge conservation one has to keep the parameters W and η in equation (6.10) identical for both $\rho(x;\varepsilon)$ and $\rho_0(\varepsilon)$, so that

$$\rho_0(\varepsilon) = \frac{4}{\hbar v_{\mathrm{F}} \pi W} \sum_q \mathrm{Im}\left(\frac{\varepsilon + i\eta}{\sqrt{-(\varepsilon+i\eta)^2 + (\hbar v_{\mathrm{F}}\, q)^2}}\right), \tag{6.15}$$

instead of equation (6.4). The expression (6.15) converges to equation (6.4) in the limit $W \to \infty$, $\eta \to 0$.

6.2.3 Thomas-Fermi approximation

The relation between charge density and effective potential is local in the TF approximation, which dramatically improves the computational efficiency. Replacing $\rho(x;\varepsilon)$ in equation (6.10) by $\rho_0(\varepsilon - V(x))$, setting the temperature to zero, and using the ideal DoS (6.4) leads to the semiclassical expression for $n(x)$,

$$n_{\mathrm{TF}}(x) = \frac{V(x)|V(x)|}{\pi\hbar^2 v_{\mathrm{F}}^2}, \tag{6.16}$$

which I regard as the charge density in the TF approximation.

6.2.4 Self-consistent solutions

The set of equations (6.8),(6.6), along with equation (6.10) for SCH and equation (6.16) for TF approximations, is solved by means of an iterative algorithm. It is run until $V(x)$ reaches a self-consistency with accuracy of 10^{-3} relative to $|\mu_l|$. For strong interactions ($\alpha \sim 1$) and large potential steps the procedure requires the use of strong damping in each iteration to ensure convergence (the weight of a new iteration is roughly of the order of 10^{-3}).

Potential profiles $V(x)$ for different values of μ_s but fixed μ_l, calculated at zero temperature, are shown in figure 6.3. The dimensionless potential $\alpha V(x)L/\hbar v_{\mathrm{F}}$ in the TF approximation depends on the two parameters $\alpha\mu_s L/\hbar v_{\mathrm{F}}$ and $\alpha\mu_l L/\hbar v_{\mathrm{F}}$. Such scaling is only approximate for the SCH potential. I also note that the TF potential transforms exactly as $V(x) \to -V(x)$ under the global transformation $\bar{n}(x) \to -\bar{n}(x)$, which is not the case for the SCH potential.

My results apply to large system sizes which are not accessible by the DFT models. For instance, for Al contacts ($\mu_l = -0.51\,\mathrm{eV}$) and $L = 250\,\mathrm{nm}$ one finds $\mu_l L/\hbar v_{\mathrm{F}} \approx -200$. The sample width is of minor influence as far as $W > L$. Al-

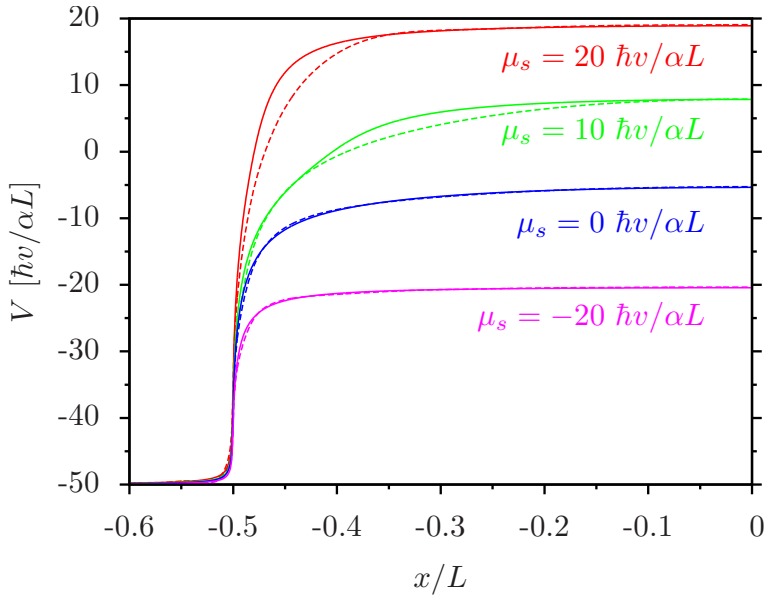

Figure 6.3: Contact potentials, $V(x)$, (symmetric with respect to $x = 0$) are calculated in the TF approximation (solid lines) and SCH approximation (dashed lines, $\alpha = 1$) for different values of the sample doping, μ_s, and fixed $\mu_l = -50\,\hbar v_\mathrm{F}/\alpha L$ ($\alpha\rho_\mathrm{m}\hbar v_\mathrm{F} L = 100$, $W/L = 200$).

though the parameter ρ_m determines the potential decay in the leads (but not the charge profile), it has no significant effect on transport properties as long as $|\mu_s| < |\mu_l|$.

The validity of the TF approximation is governed by the semi-classical criterion $|d\lambda(x)/dx|/2\pi \ll 1$, where $\lambda(x)$ is the de Broglie wavelength. This is equivalent to the condition $|dV(x)/dx| \ll V^2(x)/\hbar v_\mathrm{F}$ [150], which is violated for the upper curve in figure 6.3 ($\alpha\mu_s L/\hbar v_\mathrm{F} = 20$). The notable difference between the TF and SCH potential in this case indicates the importance of non-local quantum effects: evanescent modes and Friedel oscillations. Evanescent modes strongly increase the charge density in a vicinity of the sample-lead interface for energies close to the Dirac point [133]. This effect, however, is partially compensated in the considered geometry by the Friedel oscillations. The latter suppress the LDoS near the interface for energies far from the Dirac point. To illustrate the compensation I show in figure 6.4 the quantum correction $n_\mathrm{SCH}(x) - n_\mathrm{TF}(x)$ for energies $|\varepsilon - V(x)| < 10\,\hbar v_\mathrm{F}/L$ (dominated by the evanescent modes) and $|\varepsilon - V(x)| > 10\,\hbar v_\mathrm{F}/L$ (dominated by the Friedel oscillations). The partial compensation of the non-local quantum corrections makes the TF approximation reliable even outside its applicability range. Still the mentioned discrepancy between the TF and SCH potentials shows the limitations of local density approximations such as TF in positively doped samples[2].

To make a direct comparison of my self-consistent calculation with the TF anal-

[2]Strictly speaking, there exists a purely technical reason for the difference between TF and SCH potentials since the latter is calculated for a finite broadening η. This effect is, however, negligible in figure 6.3.

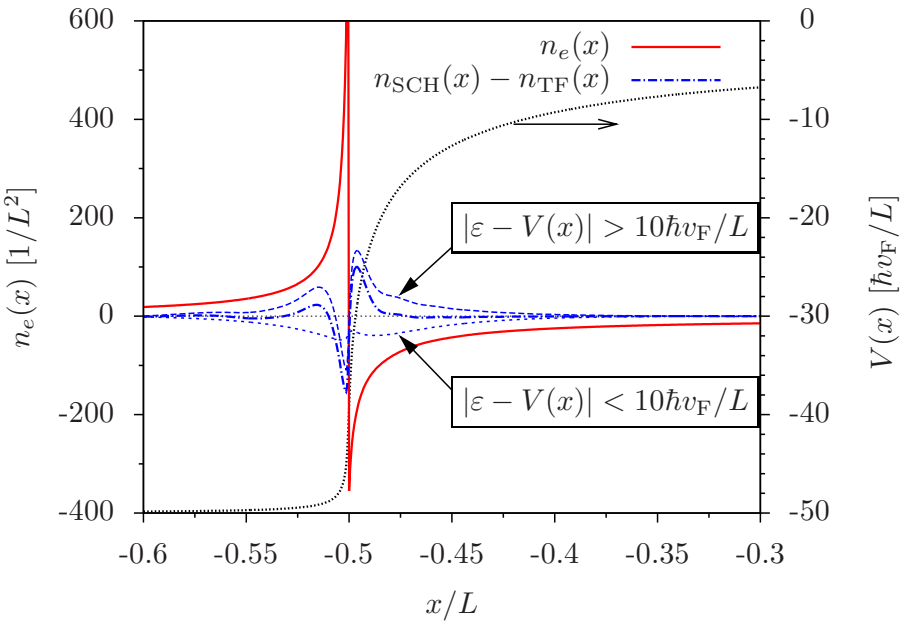

Figure 6.4: The dotted curve (right axis) shows the self-consistent TF potential, $V(x)$, for $\mu_s = 0$ and $\mu_l = -50\,\hbar v_F/L$ ($\alpha = 1$, $\rho_m \hbar v_F L = 100$, $W/L = 200$). The corresponding TF excess charge density $n_e(x)$ is plotted with a solid line. The dash-dotted curve is the quantum correction to the charge density, obtained from the SCH method. This correction is split into contributions from energies close and further away from the Dirac point as shown by dashed lines.

ysis of ref. [150], I calculate the TF potential for a single sample-lead interface at $x = 0$ ($\bar{n}(x) = \bar{n}_l$ for $x < 0$ and $\bar{n}(x) = \bar{n}_s$ for $x > 0$). I find that the TF potential decays for $x > 0$ as x^{-p}. The exponent p is given by $p = 1/2$ for $|V(x)/\mu_l| \ll 1$ and $p = 1$ otherwise (which means that p can vary with position). A similar behavior is found in ref. [150] when the doping inside the sample, μ_s, is due to the charged impurities. My results for gated graphene are different since no charge density pinning in the leads is assumed in ref. [150].

In order to compare my results with the full DFT treatment of ref. [149], I plot in figure 6.5 the self-consistent TF potentials calculated from my model for the same set of parameters $\mu_l = -0.6\,\text{eV}$, $\mu_s = 0$, $\alpha = 2.2$, and $L = 3.4$, 6.8, and 13.6 nm. Despite the simplicity of my model (notably, the absence of exchange interactions) the potentials agree well with those calculated in ref. [149].

6.3 Transport Properties

For a given potential profile I calculate the zero-temperature conductance from the Landauer formula [cf. equation (3.14)]

$$G = \frac{4e^2}{h} \sum_q T_q, \tag{6.17}$$

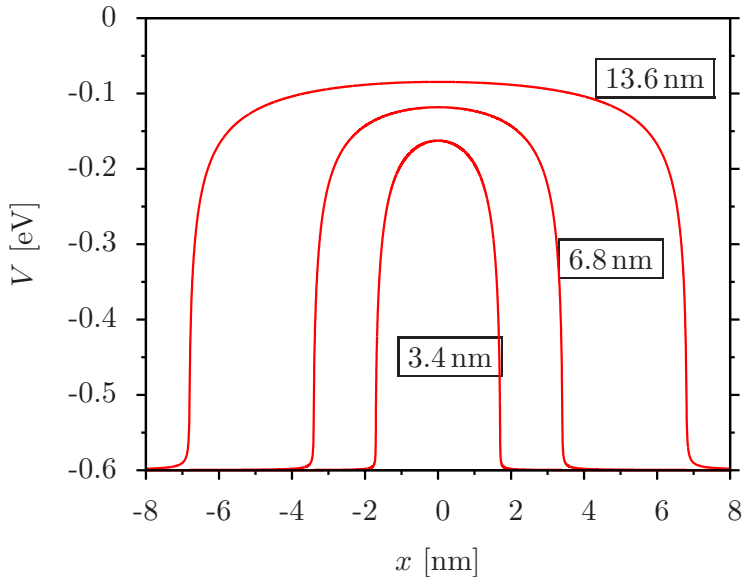

Figure 6.5: Potential profiles $V(x)$ for $\mu_l = -0.6\,\mathrm{eV}$, $\mu_s = 0$, $\alpha = 2.2$, and three different sample lengths $L = 3.4$, 6.8, and 13.6 nm chosen as in ref. [149].

where the sum extends over the transverse momenta $q = 2\pi n/W$. The shot noise is quantified by the Fano factor [cf. equation (3.18)]

$$\mathrm{F} = \frac{\sum_q T_q(1-T_q)}{\sum_q T_q}. \tag{6.18}$$

The transmission probability $T_q = T_q(\varepsilon = 0)$ for a given channel at the Fermi energy is related to the Green's function by the Kubo formula [cf. equation (3.80)] [151]

$$T_q(\varepsilon) = (\hbar v_\mathrm{F})^2\,\mathrm{Tr}\left[\sigma_x G_q^R(\xi,-\xi;\varepsilon)\sigma_x G_q^{R\dagger}(\xi,-\xi;\varepsilon)\right], \tag{6.19}$$

where ξ is an optional cross-section. I choose ξ such that $V(x) \simeq \mu_l$ for $|x| > \xi$.

The conductance in the TF approximation is shown in figure 6.6 as a function of the charge density in the sample, $\bar{n}_s$, for different values of μ_l (using the SCH approximation gives very similar results). I note that the conductance scales approximately with the parameter $\mu_l L/\alpha\hbar v_\mathrm{F}$ for $|\mu_l|L/\alpha\hbar v_\mathrm{F} \gg 1$. A similar plot of the Fano factor is given in figure 6.7.

The most evident consequence of the charge transfer between the sample and the leads is an electron-hole asymmetry in the dependence of the conductance and noise on the charge density $\bar{n}_s$ (or the gate voltage). To illustrate the key role of the slow potential decay I plot in figs. 6.6,6.7, for comparison, the results obtained from the step-function model ($V(x) = \mu_s$ for $|x| < L/2$ and $V(x) = \mu_l$ for $|x| > L/2$) with thin solid lines. The step-function model also leads to an asymmetry, which is, however, negligible in the experimentally relevant regime $|\mu_l|L/\hbar v_\mathrm{F} \gg 1$, $|\mu_s| \ll |\mu_l|$.

The conductance is enhanced for negative doping since $|V(x)| > |\mu_s|$ in the entire sample and suppressed for sufficiently large positive doping since $|V(x)| < |\mu_s|$ in

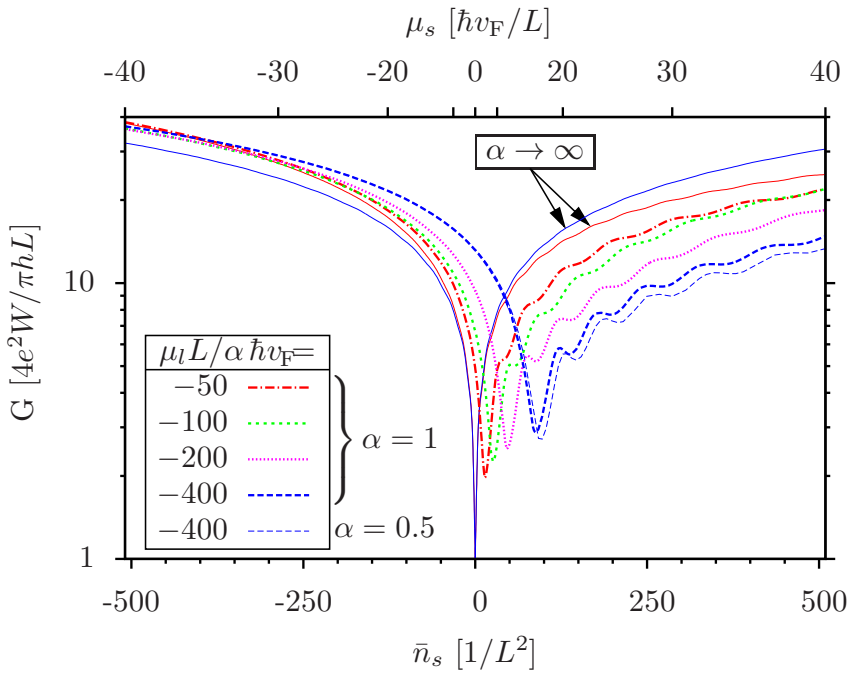

Figure 6.6: Zero-temperature conductance as a function of external doping $\bar{n}_s$. The TF potential profiles are used. The thin solid lines marked with '$\alpha \to \infty$' correspond to step-like potentials, $V(x) = \mu_l$ for $|x| > L/2$ and $V(x) = \mu_s$ for $|x| < L/2$, with $\mu_l L/\hbar v_F$ given by -50 and -400 for the red (light) and blue (dark) line, respectively.

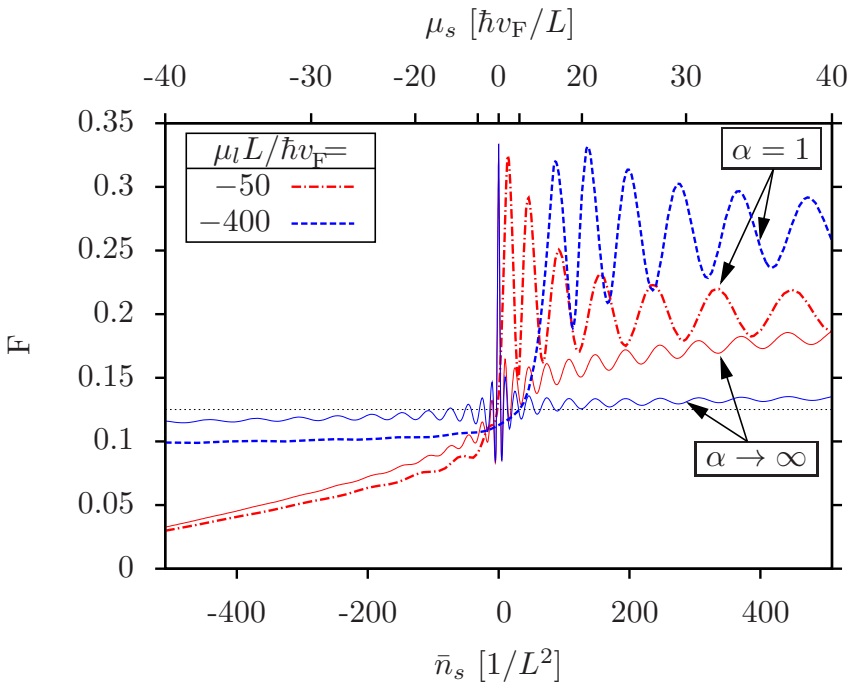

Figure 6.7: Zero-temperature Fano factor as a function of external doping $\bar{n}_s$. As in figure 6.6, the TF potential profiles are used (for the thick lines) and the thin solid lines correspond to the corresponding step-like potentials. The horizontal dotted line indicates the asymptotics $F = 1/8$ for a step-like potential with $\mu_l \to \pm\infty$ [24].

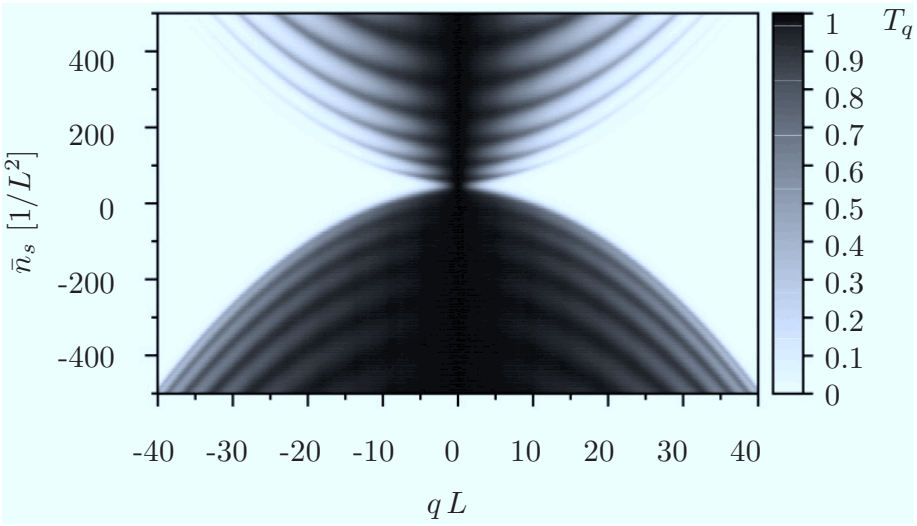

Figure 6.8: Zero-temperature transmission probability T_q as a function of transverse momentum q and doping $\bar{n}_s$ ($\alpha = 1$, $\mu_l L/\hbar v_\mathrm{F} = -200$).

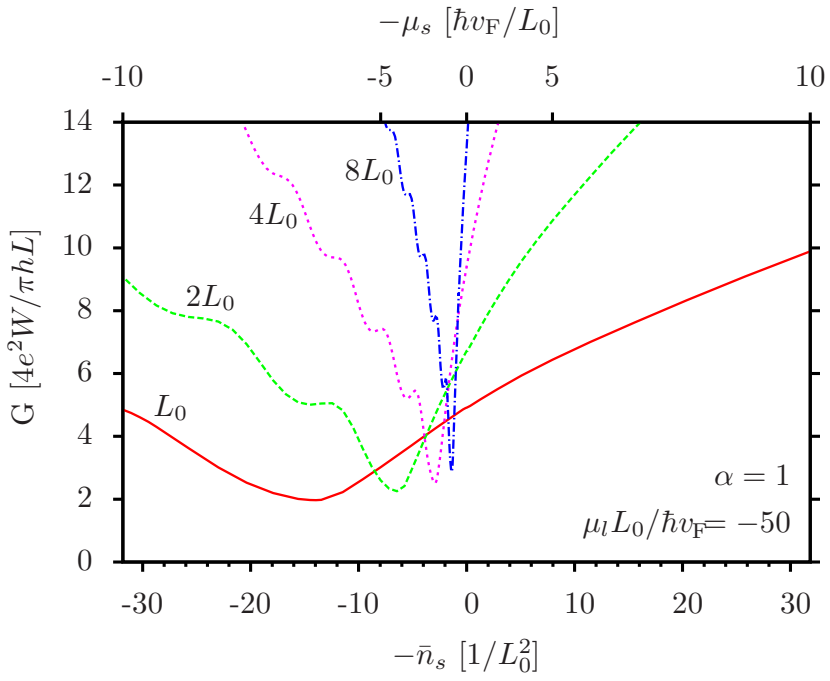

Figure 6.9: Same conductance data as in figure 6.6 plotted with fixed μ_l and varying L, which is indicated in multiples of the sample length $L = L_0$ for the solid curve. Note that the horizontal axis is inverted.

this case. The minimal conductance is gradually increasing for large $\mu_l L$, while the position of the conductivity minimum is shifted towards the positive doping.

Another consequence of the slow potential decay is the specific form of the Fabry-Pérot oscillations, which are only visible on one side of the conductance minimum (in the Fano factor one can also observe weak oscillations for negative doping). As demonstrated by thin solid lines in figure 6.7, a small asymmetry already exists in the step-function model with finite doping of the leads. However, the oscillation amplitude is strongly enhanced (reduced) for positive (negative) doping as a conse-

quence of the slow potential decay. The enhancement is strongest when the position of the Dirac point, $V(x)$, coincides with the chemical potential in a spatially extended region, which (as illustrated in figure 6.8) leads to selective transmission of charge carries with low transverse momenta at the n-p interfaces [113].

In a particular set of experiments it is the sample length, L, rather than the lead doping, that is varied. In figure 6.9 I rearrange the data to show the dependence of conductance on the sample doping for different sample lengths. As expected the contact-induced electron-hole asymmetry is more pronounced for shorter samples. The shift of the conductance minimum qualitatively agrees with recent measurements reported in ref. [146].

6.4 Conclusions

In conclusion I have modeled two-terminal electron transport through ballistic graphene samples taking into account the effects of charge transfer at the metal-contact/graphene interfaces. My analysis explains the electron-hole asymmetry in the conductance and the Fabry-Pérot conductance oscillations at positive doping, which have been observed in many experiments [137, 30, 15, 145]. These phenomena are most clearly resolved in ref. [15] (figure 2 b,c therein) for two different sample lengths. The period $\delta\mu_s$ of the oscillations, found by transforming the positions of the peaks into μ_s, corresponds to $\delta\mu_s L/\hbar v_{\mathrm{F}} \approx \pi$, which unambiguously confirms that the oscillations are of the Fabry-Pérot type. The amplitude of the oscillations in this experiment is somewhat stronger than in figure 6.6, which is likely due to a modification of graphene by the metal leads that has resulted in an increased reflectivity of the sample-lead interfaces.

The contents of this chapter have been published in ref. [152]. Parts have been written by M. Titov and M. Jonson.

Chapter 7 – Unfolded Scattering Approach for Point-like Impurities

In disordered systems quantum transport is generally far more difficult to investigate than in clean systems. Solving the transport problem exactly is usually a hopeless task. Only for weak disorder, a perturbative expansion in the impurity potential can provide a good estimation of transport properties. The transport properties of the disordered sample are determined by the full Green's function taking into account the impurities, which can be expressed in terms of bare Green's functions and the disorder potential in the infinite Dyson series. Recently an unfolded scattering approach has been developed [48, 50] that provides an exact solution to the Dyson equation. It does not require weak impurities but instead assumes the limit of point-like impurities, so that the characteristic size of impurities is much smaller than their mean distance, the Fermi wavelength, and the sample dimensions. The approach is particularly well suited for undoped graphene, since the Fermi wavelength diverges at the Dirac point. Here I introduce the approach in order to apply it to magnetotransport in graphene with scalar impurities in the following chapter.

In section 7.1 I solve the Dyson equation by introducing T-matrix operators. The full Green's function is then expressed in terms of bare Green's functions between impurity sites. The scattering properties of impurities enter through their T-matrices, which can be derived from scattering theory. The closed expression for the full Green's function becomes particularly simple in the s-wave approximation, in which electrons do not 'see' the spatial structure of impurities. This section is not specific to graphene but applies to any 2DEG.

The T-matrix of scalar impurities in undoped graphene is discussed in section 7.2. I omit the explicit derivation of the T-matrix, which requires an extrapolation of finite energy calculations, but show that the scattering length diverges if the scalar impurity supports a bound state at the Dirac energy $\varepsilon = 0$.

One way to obtain the transport properties of the disordered sample is to substitute the full Green's function into the Kubo formula. Another method is provided by the matrix Green's function and the corresponding cumulant generating function, which was introduced in section 3.7. This method turns out to be very practical in conjunction with the unfolded scattering approach as discussed in section 7.3.

7.1 Solution of the Dyson Equation

In this section I follow unpublished notes by M. Titov. I denote Green's functions by symbols $\mathcal{G}$, but the entire discussion applies equally to retarded, advanced, or matrix Green's function.

The full Green's function in the presence of impurities fulfills the standard operator equation

$$\left(\mathcal{G}_0^{-1} - V(\boldsymbol{r})\right)\mathcal{G}(\boldsymbol{r},\boldsymbol{r}') = \delta(\boldsymbol{r}-\boldsymbol{r}'), \tag{7.1}$$

where $\mathcal{G}_0$ is the Green's function for the clean sample and V describes the impurity potential, $V = \sum_{n=1}^{N} V_n(\boldsymbol{r}-\boldsymbol{r}_n)$. The number of impurities is N and each impurity has a characteristic size a. The inversion of the Green's function $\mathcal{G}_0$ includes spatial coordinates so that $\mathcal{G}_0^{-1}\mathcal{G}_0 = \delta(\boldsymbol{r}-\boldsymbol{r}')$.

The Dyson equation is obtained from equation (7.1) in the form

$$\begin{aligned}\mathcal{G}(\boldsymbol{r},\boldsymbol{r}') = \mathcal{G}_0(\boldsymbol{r},\boldsymbol{r}') + \sum_{n=1}^{N}\mathcal{G}_0(\boldsymbol{r},\boldsymbol{r}'')V_n(\boldsymbol{r}''-\boldsymbol{r}_n)\mathcal{G}_0(\boldsymbol{r}'',\boldsymbol{r}')+ \\ \sum_{n=1}^{N}\sum_{m=1}^{N}\mathcal{G}_0(\boldsymbol{r},\boldsymbol{r}'')V_n(\boldsymbol{r}''-\boldsymbol{r}_n)\mathcal{G}(\boldsymbol{r}'',\boldsymbol{r}''')V_m(\boldsymbol{r}'''-\boldsymbol{r}_m)\mathcal{G}_0(\boldsymbol{r}''',\boldsymbol{r}'),\end{aligned} \tag{7.2}$$

where the integration over $\boldsymbol{r}'', \boldsymbol{r}'''$ in the corresponding terms is implicit. Naively one might expect that in the limit of point-like impurities ($a \to 0$) this equation becomes

$$\mathcal{G}(\boldsymbol{r},\boldsymbol{r}') = \mathcal{G}_0(\boldsymbol{r},\boldsymbol{r}') + \sum_{n=1}^{N}\sum_{m=1}^{N}\mathcal{G}_0(\boldsymbol{r},\boldsymbol{r}_n)\mathbb{T}_{nm}\mathcal{G}_0(\boldsymbol{r}_m,\boldsymbol{r}'), \tag{7.3}$$

$$\mathbb{T}_{nm} = \delta_{nm}V_n + V_n\mathcal{G}(\boldsymbol{r}_n,\boldsymbol{r}_m)V_m, \qquad V_n = \int d^2\boldsymbol{r}\; V_n(\boldsymbol{r}-\boldsymbol{r}_n). \tag{7.4}$$

However, the Green's function diverges at coinciding arguments and therefore the matrices $\mathbb{T}_{nn}$ are not well-defined. In order to circumvent this problem one has to work in a folded space of impurity space ($N \times N$) and spatial coordinates. In particular, I introduce the matrices $\hat{\mathcal{G}}, \hat{\mathcal{G}}_0$ in the impurity space (with identical elements $\hat{\mathcal{G}}_{nm} = \mathcal{G}(\boldsymbol{r},\boldsymbol{r}')$), as well as the diagonal matrix of impurity potentials, $\hat{V} = \mathrm{diag}\{V_1(\boldsymbol{r}-\boldsymbol{r}_1),\ldots,V_N(\boldsymbol{r}-\boldsymbol{r}_N)\}$. I can now write the Dyson equation (7.2) in the compact form

$$\hat{\mathcal{G}} = \hat{\mathcal{G}}_0 + \hat{\mathcal{G}}_0\hat{V}\hat{\mathcal{G}}_0 + \hat{\mathcal{G}}_0\hat{V}\hat{\mathcal{G}}\hat{V}\hat{\mathcal{G}}_0. \tag{7.5}$$

where all matrix products are understood as integral convolutions. In analogy to equation (7.3) I can write equation (7.5) in the form

$$\hat{\mathcal{G}} = \hat{\mathcal{G}}_0 + \hat{\mathcal{G}}_0\hat{\mathbb{T}}\hat{\mathcal{G}}_0, \tag{7.6}$$

$$\hat{\mathbb{T}} = (1+\hat{V}\hat{\mathcal{G}})\hat{V} = \frac{1}{1-\hat{V}\hat{\mathcal{G}}_0}\hat{V}. \tag{7.7}$$

In this form the Dyson equation is valid for arbitrary impurity potentials. My goal is to take the limit of point-like impurities, hence I have to deal with the divergence of the Green's function $\mathcal{G}_0(\boldsymbol{r},\boldsymbol{r}')$ at coinciding arguments. As discussed in the case

of undoped graphene in section 5.6.1, the divergent part just corresponds to the bare Green's function g of an infinite system. In the case that the impurities are well separated, the divergences are irrelevant in all off-diagonal elements of $\hat{\mathcal{G}}_0$, and I can write the full T-matrix (7.7) as

$$\hat{\mathbb{T}} = \frac{1}{1 - \hat{T}(\hat{\mathcal{G}}_0 - \hat{g})}\hat{T}, \tag{7.8}$$

where $\hat{g} = \mathrm{diag}(g, g, \ldots, g)$, and the diagonal matrix of single-impurity T-matrices is given by

$$\hat{T} = \hat{V} + \hat{V}\hat{g}\hat{V} + \hat{V}\hat{g}\hat{V}\hat{g}\hat{V} + \ldots = \frac{1}{1 - \hat{V}\hat{g}}\hat{V} = \mathrm{diag}(T_1, \ldots, T_N). \tag{7.9}$$

Note that the operator products still include spatial coordinates. In the last step I again used that the impurities are non-overlapping. Thus, for individual T-matrices we have

$$T = V + VgV + VgVgV + \ldots = \frac{1}{1 - Vg}V, \tag{7.10}$$

an expression well-known from scattering theory (see e.g. [153]). The first term in the expansion of T is the potential scattering term, while the higher terms describe multiple-scattering processes. A diagrammatic representation of the T-matrix equation (7.10) is shown in figure 7.1.

The T-matrix (7.10) is an operator depending on two spatial coordinates. However, in the limit of point-like impurities one may assume that the Green's function $\mathcal{G}_{\mathrm{reg}}$ varies slowly over the spatial region of the impurity potential, requiring that the characteristic impurity size is much smaller than their mean distance, the sample dimensions, and the Fermi wavelength. In this limit only s-wave scattering is relevant as the electrons do not 'see' any spatial structure of the impurity potential. The implicit spatial integrations in equations (7.6) and (7.8) thus transform the T-matrix operator of an impurity with potential $V_n(\boldsymbol{r})$ into the integrated T-matrix

$$\begin{aligned} T_n = &\int d^2\boldsymbol{r}\; V_n(\boldsymbol{r}) + \int d^2\boldsymbol{r}\; d^2\boldsymbol{r}'\; V_n(\boldsymbol{r}) g(\boldsymbol{r} - \boldsymbol{r}') V_n(\boldsymbol{r}') \\ &+ \int d^2\boldsymbol{r}\; d^2\boldsymbol{r}'\; d^2\boldsymbol{r}''\; V_n(\boldsymbol{r}) g(\boldsymbol{r} - \boldsymbol{r}') V_n(\boldsymbol{r}') g(\boldsymbol{r}' - \boldsymbol{r}'') V_n(\boldsymbol{r}'') + \ldots, \end{aligned} \tag{7.11}$$

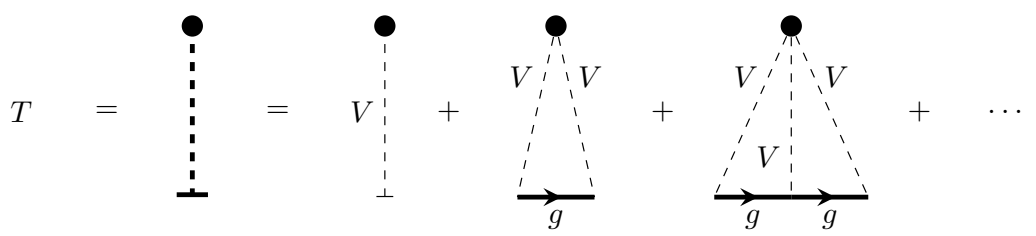

Figure 7.1: Diagrammatic representation of the T-matrix equation (7.10).

while the matrix $\hat{\mathcal{G}}_0 - \hat{g}$ is replaced by a matrix $\hat{\mathcal{G}}_{\mathrm{reg}}$ with the elements,

$$(\mathcal{G}_{\mathrm{reg}})_{nm} = \begin{cases} \mathcal{G}_0(\boldsymbol{r}_n, \boldsymbol{r}_m), & m \neq n, \\ \mathcal{G}_{\mathrm{reg}}(\boldsymbol{r}_n), & m = n, \end{cases} \tag{7.12}$$

where

$$\mathcal{G}_{\mathrm{reg}}(\boldsymbol{r}) = \lim_{\boldsymbol{r}' \to \boldsymbol{r}} [\mathcal{G}_0(\boldsymbol{r}, \boldsymbol{r}') - g(\boldsymbol{r} - \boldsymbol{r}')] \tag{7.13}$$

is the regularized bare Green's function. As the result I have obtained a solution of the Dyson equation which does not involve any spatial convolutions but is expressed in terms of a finite set of Green's functions between the impurity sites, as well as the impurity T-matrices in the s-wave approximation:

$$\mathcal{G}(\boldsymbol{r}, \boldsymbol{r}') = \mathcal{G}_0(\boldsymbol{r}, \boldsymbol{r}') + \sum_{n=1}^{N} \sum_{m=1}^{N} \mathcal{G}_0(\boldsymbol{r}, \boldsymbol{r}_n) \left[\frac{1}{1 - \hat{T}\hat{\mathcal{G}}_{\mathrm{reg}}} \hat{T} \right]_{nm} \mathcal{G}_0(\boldsymbol{r}_m, \boldsymbol{r}'), \tag{7.14}$$

where $\hat{T} = \mathrm{diag}\{T_n\}$ is the diagonal matrix of the integrated T-matrices (7.11) and all products are simple products.

If an impurity supports a bound state, its T-matrix is not perturbative in V, which means that the Born approximation fails. However, equation (7.14) can be used even if the scattering lengths diverges. In the next section I study the T-matrix of scalar impurities in graphene, since their effect on magnetotransport will be the subject of the following chapter. The unfolded method can be applied to other impurity types as well. For any impurity potential varying over the scale of the lattice constant, the T-matrix obtains a structure in valley space. As vacancies are infinitely strong on-site potentials, their T-matrix is a projector to one sublattice in each valley [50].

7.2 T-Matrix of Scalar Impurities in Undoped Graphene

The zero-energy Green's function $g(\boldsymbol{r} - \boldsymbol{r}')$ corresponding to the single-valley Dirac Hamiltonian of infinite graphene is given by equation (5.77). The divergent part of the Green's function $\mathcal{G}_0(\boldsymbol{r}, \boldsymbol{r}')$ at coinciding arguments is independent of the sample geometry and corresponds to $g(\boldsymbol{r} - \boldsymbol{r}')$ even in the presence of a magnetic field. Therefore the impurity T-matrices can be generally calculated at zero magnetic field. Furthermore, since $g(\boldsymbol{r} - \boldsymbol{r}')$ has identical retarded and advanced components, the impurity T-matrices (7.11) are proportional to the unit matrix in Keldysh space.

For rotationally invariant impurities the T-matrix is given by the scattering length ℓ_s in the s-channel [48],

$$T = 2\pi\hbar v_{\mathrm{F}} \ell_s. \tag{7.15}$$

Since there are no normalizable solutions in infinite graphene at zero energy, the scattering length ℓ_s must be derived from the solution at a low energy [154, 155, 156]. For the disk-shaped impurity potential $V(r) = V_0\theta(r-a)$ one finds

$$\frac{\ell_s}{a} = \frac{J_1(V_0 a)}{J_0(V_0 a)} \tag{7.16}$$

Here I omit the derivation of this scattering length but make it plausible by looking at the eigenstates inside and outside the impurity potential. The general solution of the Dirac equation in a rotationally symmetric potential is discussed in section 5.2. The allowed states for $r < a$ are

$$\Psi_m = e^{i(m-\sigma_z/2)\theta}\,\Phi_m(r), \qquad \Phi_m = \begin{pmatrix} J_{m-1/2}(V_0 r) \\ iJ_{m+1/2}(V_0 r) \end{pmatrix}, \tag{7.17}$$

where J_n denotes the Bessel function. Note that these solutions are less general than the solutions (5.23) used in the Corbino geometry, due to the additional requirement that the solutions are regular at $r = 0$. Restricting myself to the s-wave channels $m = \pm 1/2$, I find the following solutions at zero energy,

$$\Phi_m(r)|_{r<a} = \begin{cases} \begin{pmatrix} J_0(V_0 r) \\ iJ_1(V_0 r) \end{pmatrix}, & m = \frac{1}{2}, \\ \begin{pmatrix} -J_1(V_0 r) \\ iJ_0(V_0 r) \end{pmatrix}, & m = -\frac{1}{2}, \end{cases} \qquad \Phi_m(r)|_{r>a} = \begin{cases} \begin{pmatrix} 0 \\ r^{-1} \end{pmatrix}, & m = \frac{1}{2}, \\ \begin{pmatrix} r^{-1} \\ 0 \end{pmatrix}, & m = -\frac{1}{2}. \end{cases} \tag{7.18}$$

Thus the scattering length ℓ_s given in equation (7.16) diverges for resonant scattering, i.e. when the impurity supports a bound state at zero energy. This bound state decays outside the disk-shaped potential as $1/r$ and is entirely located on one sublattice (depending on the sign of m).

Using the approximations of the Bessel functions $J_n(z)$ with integer n at $z = 0$,

$$\lim_{z\to 0} J_n(z) = \begin{cases} 1, & n = 0, \\ z/2, & n \neq 0, \end{cases} \tag{7.19}$$

one can see that for $V_0 a \ll 1$ the T-matrix just corresponds to the potential-scattering term in the expansion (7.11), $T = V_0 \pi a^2$. On the other hand, in the quasiclassical limit $V_0 a \gg 1$ one finds [48]

$$\ell_s = a\tan(V_0 a - \pi/4). \tag{7.20}$$

Note that in both cases the scattering length ℓ_s can have any sign.

7.3 Impurity Correction to the Cumulant Generating Function

The unfolded method used in section 7.1 for point-like impurities can also be applied to directly calculate the impurity correction to the cumulant generating function. This yields an even more efficient approach to evaluate the conductance of a disordered sample, which I make use of in chapter 8.

The cumulant generating function is given by $\mathcal{F} = \operatorname{Tr} \ln \mathcal{G}^{-1}$, where $\mathcal{G}$ is the full Green's function in the source field and the trace includes spatial coordinates [cf. equation (3.82)]. According to equation (7.1) I can split $\mathcal{F}$ into the ballistic part $\mathcal{F}_0 = \operatorname{Tr} \ln \mathcal{G}_0^{-1}$ and the impurity correction

$$\delta\mathcal{F} = \operatorname{Tr} \ln(1 - V\mathcal{G}_0) = -\sum_{p=1}^{\infty} \frac{1}{p} \operatorname{Tr}(V\mathcal{G}_0)^p. \tag{7.21}$$

The second equality is the definition of the matrix logarithm as a Taylor series and all matrix products are understood as integral convolutions. From this expansion it is easy to see that

$$\delta\mathcal{F} = \operatorname{Tr} \ln(1 - \hat{V}\hat{\mathcal{G}}_0), \tag{7.22}$$

where the structure of $\hat{V}$ and $\hat{\mathcal{G}}_0$ in impurity space is defined as in the Dyson equation (7.5), and I again extract the regular part by writing

$$\delta\mathcal{F} = \operatorname{Tr} \ln(1 - \hat{T}(\hat{\mathcal{G}}_0 - \hat{g})) + \operatorname{Tr} \ln(1 - \hat{V}\hat{g}). \tag{7.23}$$

The last term does not depend on the counting field and can be omitted. In the limit of point-like impurities the T-matrices in $\hat{T}$ are reduced to the s-wave approximation (7.11) and one obtains

$$\delta\mathcal{F} = \operatorname{Tr} \ln(1 - \hat{T}\hat{\mathcal{G}}_{\mathrm{reg}}), \tag{7.24}$$

where no spatial integrations are left, which is the main advantage of this method over the Kubo formula. The elements of $\hat{\mathcal{G}}_{\mathrm{reg}}$ are defined in equation (7.12). Therefore the correction to the cumulant generating function is expressed in terms of a finite set of Green's functions of the clean system, taken between the impurity sites, as well as the impurity T-matrices.

In the case of an undoped graphene sample the matrix Green's function decomposition from section 5.8 may be used in the corresponding model to simplify the dependence of $\delta\mathcal{F}$ on the source field as shown in section 8.2.1. The resulting conductance correction contains a finite set of retarded Green's functions only. This is shown for the case of scalar impurities in section 8.2.2.

Chapter 8 – Magnetoconductance of Undoped Graphene with Point-like Impurities

The charge transport through an undoped graphene sample is facilitated by evanescent rather than propagating modes. This is a consequence of the vanishing DoS at the Dirac point and leads to highly unusual transport characteristics corresponding to that in a diffusive metal. The Dirac nature of the quasiparticles also leads to unusual effects of impurities on transport properties. For example, in the ballistic regime the conductance of undoped graphene increases when impurities are added, an effect known as impurity-assisted tunneling [33]. Another peculiar property is the absence of localization, which means that the observed minimal conductivity of the order of e^2/h is largely temperature independent.

The theory of electron transport in a vicinity of the Dirac point is strongly complicated by the small electron concentration, the vanishing mass, the weak screening properties, and the diverging wavelength of Dirac quasiparticles. The quasiclassical approximation generally breaks down even in the diffusive regime. Instead, the nature of disorder is crucially important for the localization properties [151]. The absence of localization is attributed to two types of disorder, namely chiral impurities, which preserve the chiral symmetry of clean graphene, and scalar impurities, which are smooth on the atomic scale and do not mix the two valleys [151].

A well suited method to study transport in graphene with isolated impurities is the unfolded scattering approach [48, 50] introduced in chapter 7, because it is essentially exact and therefore holds even in the strong-coupling regime with conductivity $\sigma \sim e^2/h$. It has been successfully tested for different impurity types. For resonant scalar impurities, the conductivity as a function of impurity concentration has been shown to be in good agreement with that obtained from the renormalization group of the corresponding σ model [50]. In ref. [51] the approach has been applied in the ballistic regime to graphene with ad-atoms or vacancies and compared with numerical simulations using the recursive Green's function technique. In this chapter I use this formalism together with the transformations developed in chapter 5 to study the Dirac-point conduction of graphene with randomly positioned point-like impurities in a perpendicular magnetic field. I start with general considerations and then focus on the case of scalar impurities of arbitrary scattering length.

In section 8.1 I apply the conformal mapping transformation (5.38) and the vector potential transformation (5.47) to the Green's function in the presence of N_{imp} impurities, which is written in terms of bare Green's functions and impurity T-matrices by means of the unfolded method introduced in chapter 7. The T-matrix describes the scattering properties of an isolated impurity in an infinite

graphene sheet. Here I focus on scalar impurities, which preserve the sublattice and valley symmetry and correspond to a scalar potential in the Dirac equation. I do not explicitly derive the T-matrix but consider the case of rotationally invariant impurities for which the T-matrix is given by the scattering length ℓ_s in the s-wave channel [48] (see section 7.2).

In section 8.2 I evaluate the impurity correction to the full counting statistics expressed in terms of the matrix Green's function. The unfolded method leads to a particularly simple expression for the impurity correction to the cumulant generating function (see section 7.3). The evaluation is facilitated by means of the matrix Green's function decomposition derived in section 5.8. I subsequently obtain the conductance correction for the case of scalar impurities, which are the subject of the remaining sections. The evaluation of this formula for a given impurity configuration amounts to an inversion of a single matrix of size $2N_{\mathrm{imp}} \times 2N_{\mathrm{imp}}$.

The conductance of a short and wide rectangular graphene sample with one and two impurities is analyzed in section 8.3. I study the effects of the magnetic field on both the conductance and the LDoS corrections for varying scattering lengths. The understanding of the behaviour of resonant and non-resonant impurities helps me to interprete the numerically obtained mean conductivity of a sample with many scalar impurities, which is evaluated in section 8.4. For the case of absent magnetic field I study the crossover from the ballistic to the diffusive transport regime for increasing impurity concentration. Then I turn to the dependence of the conductivity on the external magnetic field. I discuss the QH regime, in which the conductivity is suppressed to zero or of the order of 0.5 e^2/h (per spin and valley), depending on the distribution of impurity scattering lengths. For even stronger magnetic fields another crossover is revealed, beyond which the conductivity assumes the ballistic value and the sample-to-sample fluctuations are vanishing. A possible interpretation of this crossover based on the so-called level condensation of the Landau level at $\varepsilon = 0$ is given.

The main findings of this chapter are summarized in section 8.5 and compared with the case of vacancies. Possible extensions of this project are discussed. I also summarize the current understanding of the experimentally observed QH plateau at filling factor $\nu = 0$.

8.1 Transformation of Full Green's Function

The unfolded method discussed in the previous chapter provides a compact solution to the Dyson equation, expressed in terms of bare Green's functions and impurity T-matrices. The key advantage of this method is that the integral convolutions inherent in the original Dyson series are reduced to standard matrix products. For 'point-like' impurities the T-matrix operators are integrated out and the T-matrix

of an impurity becomes

$$T_n = \frac{1}{1 - V_n g_n} V_n, \tag{8.1}$$

where the spatial integrations are implicit [cf. equation (7.11)]. This approximation requires that the structure of an individual impurity is irrelevant to the electronic motion, so that the characteristic impurity size has to be small compared with the Fermi wavelength and the sample size.

It should be remarked that the Green's function g and thus the T-matrix are generally defined for absent magnetic field (in the infinite system), since the divergent part of the Green's function in a finite sample is independent of the magnetic field, and g is used for the regularization only. Due to the Landau quantization the Green's function of infinitely extended graphene in a constant magnetic field would not be suitable for the regularization.

For point-like and well separated impurities the full Green's function, i.e. the Green's function in the presence of impurities, may be written as [cf. equation (7.14)]

$$G^R_{\text{full}}(\boldsymbol{r}, \boldsymbol{r}') = G^R(\boldsymbol{r}, \boldsymbol{r}') + \sum_{\mu\nu} G^R(\boldsymbol{r}, \boldsymbol{r}_\mu) \left[\frac{1}{1 - \hat{T}\hat{G}_{\text{reg}}} \hat{T} \right]_{\mu\nu} G^R(\boldsymbol{r}_\nu, \boldsymbol{r}'), \tag{8.2}$$

where the sums run over impurity indices and the matrix $\hat{T} = \operatorname{diag}\{T_n\}$ contains the integrated impurity T-matrices (8.1) in the s-wave approximation, in which the impurity potential may be written as $V_n(\boldsymbol{r}) = V_n \delta(\boldsymbol{r} - \boldsymbol{r}_n)$. The elements of the matrix $\hat{G}_{\text{reg}}$ are given by

$$(G_{\text{reg}})_{nm} = \begin{cases} G^R(\boldsymbol{r}_n, \boldsymbol{r}_m), & \text{for } m \neq n, \\ G^R_{\text{reg}}(\boldsymbol{r}_n), & \text{for } m = n. \end{cases} \tag{8.3}$$

Note that the solution (8.2) and the following transformations have the same form for the advanced or the matrix Green's function.

It is easy to see that the conformal mapping transformation (5.38) as well as the transformation (5.47) for an external magnetic field can be applied to the full Green's function in the same way as to the bare Green's function, if the impurity T-matrices are transformed accordingly. Using the same notations as in chapter 5, the transformations are given by

$$G^R_B(\boldsymbol{r}, \boldsymbol{r}') = e^{\sigma_z \chi(r) + i\varphi(\theta)} G'^R(\boldsymbol{r}, \boldsymbol{r}') e^{\sigma_z \chi(r') - i\varphi(\theta')}, \qquad \hat{T}' = e^{\sigma_z \chi(\hat{r})} \hat{T} e^{\sigma_z \chi(\hat{r})}, \tag{8.4}$$

$$G^R(\boldsymbol{r}, \boldsymbol{r}') = \frac{1}{\sqrt{rr'}} e^{-i\sigma_z \theta/2} \bar{G}^R(\boldsymbol{r}, \boldsymbol{r}') e^{i\sigma_z \theta'/2}, \qquad \hat{\bar{T}} = \frac{1}{\hat{r}} e^{i\sigma_z \hat{\theta}/2} \hat{T} e^{-i\sigma_z \hat{\theta}/2}. \tag{8.5}$$

For example, the full Green's function G'^R fulfills equation (8.2) with the replacements $G^R \to G'^R$ and $T \to T'$.

General statements about the electronic transport properties of the disordered

sample can be made if the impurities possess certain symmetries. For chiral impurities the T-matrices obey

$$\hat{T} = -\sigma_z \hat{T} \sigma_z, \tag{8.6}$$

hence these impurities preserve the chiral symmetry provided it is present in the clean system [cf. equation (5.75)]. Furthermore, the transformation (8.4) leaves the T-matrices of chiral impurity unaffected, hence the transport properties remain independent of the magnetic flux (for $W \gg L$) as in the clean sample.

Two other impurity types, namely scalar and mass impurities, have the property

$$\hat{T} = \sigma_z \hat{T} \sigma_z, \tag{8.7}$$

and the chiral symmetry is generally broken. Specific properties of resonant scalar impurities are discussed in subsection 8.2.2.

8.2 Full Counting Statistics of Charge Transport

The cumulant generating function describing charge transport through the disordered system can be decomposed into ballistic and impurity parts,

$$\mathcal{F}(\phi) = \mathcal{F}_0(\phi) + \delta\mathcal{F}(\phi). \tag{8.8}$$

As before I parameterize the source fields by $\zeta_+ = \zeta_- = i \sinh(\phi/2)$, so that the cumulant generating function of the clean sample with $W \gg L$ reads [cf. equation (5.102)]

$$\mathcal{F}_0(\phi) = \mathrm{Tr}_{\boldsymbol{r}} \ln \mathcal{G}_0^{-1} = \frac{W}{4\pi L}\phi^2, \quad \text{for } W \gg L. \tag{8.9}$$

The spin and valley degrees of freedom are excluded from the Green's function and included as a factor to the conductance quantum, $\mathrm{g}_0 = 4e^2/h$. The ballistic conductance of a short and wide sample is given by [cf. equation (5.103)]

$$\mathrm{G}_0 = 2\mathrm{g}_0 \left.\frac{\partial^2 \mathcal{F}_0}{\partial \phi^2}\right|_{\phi=0} = \mathrm{g}_0 \frac{W}{\pi L}, \quad \text{for } W \gg L, \tag{8.10}$$

corresponding to the universal conductivity $\sigma = \mathrm{g}_0/\pi$. The same expression applies to the Corbino geometry, where $W = 2\pi$ and $L = \ln(R/a)$.

In the following subsection the disorder correction $\delta\mathcal{F}(\phi)$ is simplified by means of the matrix Green's function decomposition from section 5.8. Restricting myself to scalar impurities, I evaluate the conductance correction in subsection 8.2.2, thereby also discussing the effect of a perpendicular magnetic field.

8.2.1 Disorder correction through unfolded scattering approach

The function $\delta\mathcal{F}(\phi)$ encodes the impurity correction to the entire transmission distribution. Using the unfolded scattering approach it can be written as

$$\delta\mathcal{F}(\phi) = \mathrm{Tr}\ln(1 - \hat{T}\hat{\mathcal{G}}_{\mathrm{reg}}), \tag{8.11}$$

where the matrix $\hat{\mathcal{G}}_{\mathrm{reg}}$ is defined by the following elements in the impurity space,

$$\left(\mathcal{G}_{\mathrm{reg}}\right)_{nm} = \begin{cases} \mathcal{G}(\boldsymbol{r}_n, \boldsymbol{r}_m), & \text{for } m \neq n, \\ \mathcal{G}_{\mathrm{reg}}(\boldsymbol{r}_n), & \text{for } m = n. \end{cases} \tag{8.12}$$

The decompositions of the Green's functions $\mathcal{G}$ and $\mathcal{G}_{\mathrm{reg}}$ are given in equations (5.118) and (5.120), respectively, so that the elements of $\hat{\mathcal{G}}_{\mathrm{reg}}$ are decomposed as

$$\left(\mathcal{G}_{\mathrm{reg}}\right)_{nm} = V_\phi(x_n)\Lambda_K\Lambda\,\mathcal{L}\,\left(\overline{\mathcal{G}}_{\mathrm{reg}}\right)_{nm}\,\mathcal{L}^{-1}\,\Lambda\Lambda_K^{-1}V_\phi^{-1}(x_m), \tag{8.13}$$

where

$$V_\phi(x) = \frac{1}{\sqrt{2\cosh(\phi/2)}}\begin{pmatrix} e^{\frac{\phi(L-x)}{2L}} & -e^{-\frac{\phi(L-x)}{2L}} \\ e^{-\frac{\phi x}{2L}} & e^{\frac{\phi x}{2L}} \end{pmatrix}, \qquad \Lambda_K = \frac{1}{\sqrt{2}}\begin{pmatrix} 1 & 1 \\ -1 & 1 \end{pmatrix} \tag{8.14}$$

$$\mathcal{L} = \frac{1}{\sqrt{2}}(\Sigma_z + \Sigma_y), \qquad \Lambda = \begin{pmatrix} 1 & 0 \\ 0 & i\sigma_z \end{pmatrix}, \tag{8.15}$$

and, according to equation (5.115),

$$\hat{\overline{\mathcal{G}}}_{\mathrm{reg}} = \begin{pmatrix} \hat{\overline{R}}_\phi^{\mathrm{reg}} & 0 \\ 0 & \hat{\overline{R}}_{-\phi}^{\mathrm{reg}} \end{pmatrix}, \qquad \hat{\overline{R}}_\phi^{\mathrm{reg}} = e^{i\hat{Y}\phi/2}\hat{R}_\phi^{\mathrm{reg}}e^{-i\hat{Y}\phi/2}, \quad \hat{Y} = \frac{1}{L}\,\mathrm{diag}\{y_n\}. \tag{8.16}$$

The elements in impurity space of the matrices $\hat{\overline{\mathcal{G}}}_{\mathrm{reg}}$, $\hat{\overline{R}}_\phi^{\mathrm{reg}}$, and $\hat{R}_\phi^{\mathrm{reg}}$ are defined analogously to equation (8.12).

The unitarity constraint on the T-matrix ensures that the retarded and advanced components of the T-matrix are equal.[1] It follows immediately that the matrices V_ϕ and Λ_K drop out from the full counting statistics and equation (8.11) becomes

$$\delta\mathcal{F} = \mathrm{Tr}\ln\left[1 - \mathcal{L}\begin{pmatrix} \hat{T} & 0 \\ 0 & -\sigma_z\hat{T}\sigma_z \end{pmatrix}\mathcal{L}\begin{pmatrix} \hat{\overline{R}}_\phi^{\mathrm{reg}} & 0 \\ 0 & \hat{\overline{R}}_{-\phi}^{\mathrm{reg}} \end{pmatrix}\right]. \tag{8.17}$$

If the impurities obey one of the symmetries (8.6) and (8.7), the trace can be carried

[1] At zero energy this can be seen immediately from the definition (7.11), since the zero-energy Green's function $g(\boldsymbol{r} - \boldsymbol{r}')$ is a unit matrix in RA space.

out in Keldysh space. For chiral impurities, $\hat{T} = -\sigma_z \hat{T} \sigma_z$, one obtains

$$\delta\mathcal{F} = K(\phi) + K(-\phi), \qquad K(\phi) = \mathrm{Tr}\ln\left(1 - \hat{T}\hat{\overline{R}}_{\phi}^{\mathrm{reg}}\right). \tag{8.18}$$

For scalar or mass impurities, the symmetry $\hat{T} = \sigma_z \hat{T} \sigma_z$ implies

$$\delta\mathcal{F} = \mathrm{Tr}\ln\left(1 - \hat{T}\hat{\overline{R}}_{\phi}^{\mathrm{reg}}\hat{T}\hat{\overline{R}}_{-\phi}^{\mathrm{reg}}\right). \tag{8.19}$$

In the following subsection I evaluate the conductance correction due to scalar impurities from this formula.

8.2.2 Transport properties for scalar impurities in a magnetic field

The T-matrix of a scalar impurity is proportional to the unit matrix in both valley and sublattice space and parameterized by a scattering length ℓ_s as

$$T = 2\pi\hbar v_{\mathrm{F}} \ell_s. \tag{8.20}$$

Here I omitted the impurity index as I will mostly refer to the case of identical impurities.

It can be seen that the chiral symmetry is preserved in the resonance case $|\ell_s| \to \infty$, since the T-matrices effectively drop out from the full Green's function (8.2) (after neglecting the unit matrix in the denominator). However, in a sufficiently strong magnetic field the chiral symmetry is broken for impurities of any finite scattering length as discussed below.

Before evaluating the conductance, let me include a perpendicular magnetic field by means of the transformation

$$\hat{R}_{\phi,B}^{\mathrm{reg}} = e^{\sigma_z \hat{\chi}} \hat{R}_{\phi}^{\mathrm{reg}} e^{\sigma_z \hat{\chi}}, \qquad \hat{\chi} = \mathrm{diag}\{\chi(x_n)\}, \tag{8.21}$$

where the phases $\varphi(y_n)$ have been omitted since they drop out in $\delta\mathcal{F}$. Equation (8.19) is now written as

$$\delta\mathcal{F} = \mathrm{Tr}\ln\left[1 - \hat{\mathcal{M}}(\phi)\hat{\mathcal{M}}(-\phi)\right], \tag{8.22}$$

$$\hat{\mathcal{M}}(\phi) = \hat{T} e^{i\hat{Y}\phi/2} e^{\sigma_z \hat{\chi}} \hat{R}_{\phi}^{\mathrm{reg}} e^{\sigma_z \hat{\chi}} e^{-i\hat{Y}\phi/2}. \tag{8.23}$$

For resonant impurities, $|\ell_s| \to \infty$, the unit matrix in equation (8.22) may be neglected, which leads to $\delta\mathcal{F} = \mathrm{Tr}\ln\left(e^{i\hat{Y}\phi}\hat{R}_{\phi}^{\mathrm{reg}} e^{-i\hat{Y}\phi}\hat{R}_{-\phi}^{\mathrm{reg}}\right)$. Thus the transport properties become independent of the magnetic field. However, this approximation requires $|\ell_s/L| \gg \exp(L/\ell_{\mathrm{B}})^2$ and is therefore not applicable in the presence of a strong magnetic field.[2] If the scattering lengths ℓ_s of impurities are finite, so that

[2]The transport properties for $|\ell_s| \to \infty$ and $\ell_B \to 0$ depend on the order of taking the limits.

this condition is violated, the chiral symmetry is broken and the correction $\delta\mathcal{F}$ vanishes in a sufficiently strong magnetic field. In this case all transport properties are again field-independent but given by the same universal values as that of a ballistic sample. As discussed in section 8.4 this strong-field regime beyond the QH regime is reached when the number of flux quanta exceeds the number of impurities.

In order to evaluate the conductance correction due to scalar impurities, I redefine the matrix $\hat{\mathcal{M}}(\phi)$ in equation (8.22) as

$$\hat{\mathcal{M}}(\phi) = \hat{T} e^{i\hat{Y}\phi} \hat{R}^{\mathrm{reg}}_{\phi,B}, \tag{8.24}$$

which is allowed under the trace. Differentiating equation (8.22) twice with respect to the counting field leads to the conductance correction

$$\delta \mathrm{G} = 2\mathrm{g}_0 \left.\frac{\partial^2 \delta\mathcal{F}}{\partial\phi^2}\right|_{\phi=0} = 4\mathrm{g}_0 \,\mathrm{Tr}\left(\frac{1}{1+\hat{\mathcal{M}}}\hat{\mathcal{M}}'\frac{1}{1-\hat{\mathcal{M}}}\hat{\mathcal{M}}' - \frac{\hat{\mathcal{M}}}{1-\hat{\mathcal{M}}^2}\hat{\mathcal{M}}''\right), \tag{8.25}$$

where $\hat{\mathcal{M}}$, $\hat{\mathcal{M}}'$, and $\hat{\mathcal{M}}''$ denote the zeroth, first, and second derivatives of $\hat{\mathcal{M}}(\phi)$ at $\phi = 0$, respectively.

The expressions given so far hold for any aspect ratio W/L. In the limit $W/L \gg 1$, which I consider in the following, the matrix $\hat{R}^{\mathrm{reg}}_{\phi}$ is given by

$$\hat{R}^{\mathrm{reg}}_{\phi} = \hat{R}^{\mathrm{reg}}_{0} + \alpha\sigma_y\phi, \qquad \alpha = \frac{1}{4\pi L}, \qquad (R^{\mathrm{reg}}_0)_{nm} = \begin{cases} G^R(\boldsymbol{r}_n, \boldsymbol{r}_m), & \text{for } n \neq m, \\ G^R_{\mathrm{reg}}(\boldsymbol{r}_n), & \text{for } n = m. \end{cases} \tag{8.26}$$

The counting field ϕ enters only in the diagonal elements in impurity space. As before, G^R is the retarded Green's function. For simplicity I drop the distinction ($\bar{G}^R$, G^R) between the cylinder and the Corbino geometry. The matrix $\hat{\mathcal{M}}(\phi)$ and its derivatives at $\phi = 0$ are given by

$$\hat{\mathcal{M}} = \hat{T}\hat{R}^{\mathrm{reg}}_{0,B}, \tag{8.27}$$

$$\hat{\mathcal{M}}' = i\hat{T}\hat{Y}\hat{R}^{\mathrm{reg}}_{0,B} + \alpha\hat{T}\sigma_y, \tag{8.28}$$

$$\hat{\mathcal{M}}'' = \hat{T}\hat{Y}\left(-\hat{Y}\hat{R}^{\mathrm{reg}}_{0,B} + 2i\alpha\sigma_y\right). \tag{8.29}$$

By substituting into equation (8.25) and applying some matrix algebra one can cast the conductance correction in the form

$$\delta \mathrm{G} = 4\mathrm{g}_0 \,\mathrm{Tr}\left(M_- Y_s M_+ Y_s^\dagger - M_- M_+ \hat{Y}^2\right), \tag{8.30}$$

$$M_\pm = \frac{1}{1 \pm \hat{T}\hat{R}^{\mathrm{reg}}_{0,B}}, \qquad Y_s = \hat{Y} + i\alpha\hat{T}\sigma_y. \tag{8.31}$$

If the chiral symmetry is preserved by the boundary conditions in the clean sample,

as in the model of infinitely doped leads, the matrix $\hat{R}_0^{\mathrm{reg}}$ has the property

$$\hat{R}_0^{\mathrm{reg}\,\dagger} = -\sigma_z \hat{R}_0^{\mathrm{reg}} \sigma_z, \tag{8.32}$$

which implies a simple relation between M_+ and M_-. This can be used to write the conductance correction as

$$\delta \mathrm{G} = 4\mathrm{g}_0 \,\mathrm{Tr}\left(M_- Y_s \sigma_z \hat{T} M_-^\dagger \hat{T}^{-1} Y_s \sigma_z - \hat{Y}^2 M_- \sigma_z \hat{T} M_-^\dagger \hat{T}^{-1} \sigma_z \right). \tag{8.33}$$

Thus the evaluation of the conductance for a given impurity configuration amounts to an inversion of a single matrix of size $2N_{\mathrm{imp}} \times 2N_{\mathrm{imp}}$. From equation (8.33) it is obvious that the resulting conductance correction $\delta \mathrm{G}/\mathrm{g}_0$ is a real number. If all impurities have the same scattering length ℓ_s, one may use that $\hat{T} M_-^\dagger \hat{T}^{-1} = M_-^\dagger$.

The evaluation of equation (8.33) is the subject of the following two sections. I will consider both the quasi-ballistic transport regime (few impurities) and the diffusive transport regimes. In the case of many impurities and strong magnetic field the matrix M_-^{-1} is badly defined and its inversion requires a significant computational effort.

In the limit of resonant impurities with diverging scattering length, the conductance is found from equation (8.30) as

$$\frac{\delta \mathrm{G}}{\mathrm{g}_0} = -4\alpha^2 \,\mathrm{Tr}\left[\left(\hat{R}_0^{\mathrm{reg}} \right)^{-1} \sigma_y \left(\hat{R}_0^{\mathrm{reg}} \right)^{-1} \sigma_y \right], \qquad \text{for } |\ell_s/L| \to \infty, \tag{8.34}$$

so that the vector potential drops out as seen above from the full counting statistics. This formula has been derived in ref. [50]. In the absence of magnetic field it is accurate for $|\ell_s/L| \gg 1$. However, in the presence of a magnetic field the condition is $|\ell_s/L| \gg \exp(L/\ell_{\mathrm{B}})^2$. Thus, for any finite scattering length a sufficiently strong magnetic field does have an effect on the conductance.

8.3 Conductance and LDoS of a Sample with One and Two Impurities

In this section I consider the short and wide rectangular geometry in the presence of a spatially constant perpendicular magnetic field B. The conductance and the LDoS are analyzed for a single scalar impurity in section 8.3.1 and for two scalar impurities in section 8.3.2. The conductivity of a sample with many scalar impurities is the subject of section 8.4. Due to the large aspect ratio W/L the periodic boundary conditions may be applied in the transverse y direction, hence only transport properties of the bulk are studied. In a strong magnetic field edge states emerge in a rectangular Hall bar device, leading to a different transport mechanism. Therefore the results given here are more relevant for experimental devices in the Corbino geometry, to which the cylinder geometry is related by the conformal transforma-

tion from section 5.3. Since a spatially constant magnetic field in one geometry is mapped to an exponentially varying field in the other, an exact mapping of the results from this section to the Corbino geometry is more difficult and has not been attempted.

The conductance is evaluated using equation (8.33), while the LDoS is obtained directly from the full retarded Green's function, which is transformed by the vector potential according to equation (8.4). The only input in the evaluation is the retarded Green's function of the clean sample, as well as the impurity positions and their scattering lengths. In the model of infinitely doped leads and abrupt sample-lead interfaces the bare Green's function is given by [see equation (5.73)]

$$G^R(\boldsymbol{r},\boldsymbol{r}') = \frac{-i}{4\hbar v_\mathrm{F} L}\begin{pmatrix} C_+(\boldsymbol{r},\boldsymbol{r}') & C_-(\boldsymbol{r},\boldsymbol{r}') \\ C_-^*(\boldsymbol{r},\boldsymbol{r}') & C_+^*(\boldsymbol{r},\boldsymbol{r}') \end{pmatrix}, \tag{8.35}$$

$$C_\pm(\boldsymbol{r},\boldsymbol{r}') = \frac{1}{\sin\left(\frac{\pi}{2L}(x \pm x' + i(y-y'))\right)}. \tag{8.36}$$

The off-diagonal elements of the matrix $\hat{R}_0^\mathrm{reg}$ are given by this Green's function taken between two impurity sites, while the diagonal elements are regularized Green's functions, hence

$$(R_0^\mathrm{reg})_{nm} = \frac{-i}{4\hbar v_\mathrm{F} L}\begin{pmatrix} \frac{1}{\sin(z_n+z_m^*)} & \frac{1-\delta_{nm}}{\sin(z_n-z_m)} \\ \frac{1-\delta_{nm}}{\sin(z_n^*-z_m^*)} & \frac{1}{\sin(z_n^*+z_m)} \end{pmatrix}, \qquad z_m = \frac{\pi}{2L}(x_m + iy_m), \tag{8.37}$$

where δ_{nm} denotes the Kronecker delta. The matrix $\hat{R}_0^\mathrm{reg}$ fulfills the chiral symmetry (8.32). For simplicity I set $\hbar v_\mathrm{F} = 1$ in the following expressions.

In the presence of a magnetic field the Green's functions and T-matrices are transformed as shown above. For $W \gg L$ the transformations are determined by the scalar phase [cf. equation (5.51)]

$$\chi(x) = -\mathrm{sgn}(eB\ell_B^2/h)\frac{x(L-x)}{2\ell_B^2}, \tag{8.38}$$

where the strength of the magnetic field is characterized by the magnetic length ℓ_B.

The conductance correction for the short and wide geometry, $W \gg L$, does not contain the aspect ratio W/L. Thus it enters only implicitly via the impurity positions. For a single impurity the conductance correction δG is therefore independent of the aspect ratio. On the other hand, for a uniform impurity distribution with $y_n \in [-W/2, W/2]$ and fixed density $n_\mathrm{imp} = N_\mathrm{imp}/WL \gg 1/L^2$ the conductivity is independent of the aspect ratio. In the following two subsections I study the cases of a single and two impurities, $N_\mathrm{imp} = 1$ and $N_\mathrm{imp} = 2$, before turning to the uniform impurity distribution in section 8.4.

8.3.1 Single scalar impurity

In the case of a single scalar impurity, $N_{\text{imp}} = 1$, one finds compact formulas for the conductance and the LDoS. According to equations (5.80),(5.81) the LDoS in the clean sample ($N_{\text{imp}} = 0$) is given by

$$\rho(x) = \frac{\cosh\left[x(L-x)/\ell_B^2\right]}{2\pi L \sin(\pi x/L)}. \tag{8.39}$$

The LDoS diverges at the interfaces $x = 0, L$ due to the assumption of infinitely doped leads. In a weak magnetic field ($\ell_B > 0.423L$) the LDoS has a minimum at $x = L/2$, while in a strong magnetic field it has a maximum at $x = L/2$, and one minimum near each interface, in a distance ℓ_B^2/L.

The correction to the LDoS caused by a single scalar impurity at the site $\boldsymbol{r}_1$ is given by

$$\delta\rho(\boldsymbol{r}) = -\frac{1}{\pi}\operatorname{Im}\operatorname{Tr} e^{2\sigma_z\chi(\boldsymbol{r})}G^R(\boldsymbol{r},\boldsymbol{r}_1)\frac{1}{e^{-2\sigma_z\chi(\boldsymbol{r}_1)}+F(x_1)}TG^R(\boldsymbol{r}_1,\boldsymbol{r}) \tag{8.40}$$

$$= \frac{TF(x_1)}{16\pi L^2}\left[\Gamma_\chi(\boldsymbol{r},\boldsymbol{r}_1)+\Gamma_{-\chi}(\boldsymbol{r},\boldsymbol{r}_1)\right], \tag{8.41}$$

$$\Gamma_\chi(\boldsymbol{r},\boldsymbol{r}_1) = e^{2\chi(\boldsymbol{r})}\left(\frac{|C_-(\boldsymbol{r},\boldsymbol{r}_1)|^2}{e^{4\chi(\boldsymbol{r}_1)}+F^2(x_1)} - \frac{|C_+(\boldsymbol{r},\boldsymbol{r}_1)|^2}{e^{-4\chi(\boldsymbol{r}_1)}+F^2(x_1)}\right), \tag{8.42}$$

where the function $F(x)$ is proportional to the T-matrix and the LDoS for absent magnetic field,

$$F(x) = \frac{\ell_s}{L}\frac{\pi}{2\sin(\pi x/L)}. \tag{8.43}$$

The impurity correction may be written as $\delta\rho(\boldsymbol{r}) = \delta\rho_-(\boldsymbol{r}) - \delta\rho_+(\boldsymbol{r})$, where each term $\delta\rho_\pm$ is positive and proportional to $|C_\pm(\boldsymbol{r},\boldsymbol{r}_1)|^2$. The term $\delta\rho_-(\boldsymbol{r})$ diverges as $\sim 1/|\boldsymbol{r}-\boldsymbol{r}_1|^2$ at the impurity site. This agrees with the existence of a quasi-bound state at the resonance energy of the impurity [in agreement with equation (7.18)]. For any finite scattering length this quasi-bound state exists at zero energy due to the finite size of the sample, which causes a broadening of the bound states at the resonance energies. The term $\delta\rho_+(\boldsymbol{r})$ is non-diverging and corresponds to a superposition of eigenstates in the clean sample.

In the following I further analyze the LDoS in the cases of weak and strong magnetic field. I do not consider the case that the impurity is in the close vicinity of the contacts, where the LDoS is dominated by the metal-induced states and the effect of the impurity becomes small. I will generally use the symbols $\delta\rho_\pm(\boldsymbol{r})$ in the same way as above.

For roughly $\ell_B > L$ the magnetic field is generally negligible and equation (8.41) becomes

$$\delta\rho(\boldsymbol{r}) = \frac{TF(x_1)}{8\pi L^2}\frac{|C_-(\boldsymbol{r},\boldsymbol{r}_1)|^2 - |C_+(\boldsymbol{r},\boldsymbol{r}_1)|^2}{1+F^2(x_1)}, \qquad \text{for } \ell_B > L. \tag{8.44}$$

The correction, and, in fact, both terms $\delta\rho_+(\boldsymbol{r})$ and $\delta\rho_-(\boldsymbol{r})$, are negligible for distances $|\boldsymbol{r}-\boldsymbol{r}_1| > \min\{\ell_s, L\}$, as compared with the LDoS of the clean sample, $\rho_0(\boldsymbol{r})$. In the limit of resonant scattering, $\ell_s \gg L$, the LDoS becomes independent of ℓ_s. At the impurity site the term $\delta\rho_+$ equals $\rho_0(\boldsymbol{r}_1)$ in this case, so that the LDoS in the vicinity of the impurity consists of the diverging term $\delta\rho_-$ only. This reflects the fact that a resonant impurity supports a bound state but completely suppresses the LDoS formed by eigenstates of the clean sample.

On the other hand, the strong-field regime corresponds to $e^{2|\chi(\boldsymbol{r}_1)|} \gg |\ell_s/L| \gg e^{-2|\chi(\boldsymbol{r}_1)|}$. In this case the two terms of the LDoS correction are approximated as follows,

$$\delta\rho_-(\boldsymbol{r}) = \left[\frac{\sin(\pi x_1/L)}{\pi} e^{-2|\chi(\boldsymbol{r})|} + \frac{\pi(\ell_s/L)^2}{4\sin(\pi x_1/L)} e^{2|\chi(\boldsymbol{r})|-4|\chi(\boldsymbol{r}_1)|}\right] \frac{|C_-(\boldsymbol{r},\boldsymbol{r}_1)|^2}{4L}, \quad (8.45)$$

$$\delta\rho_+(\boldsymbol{r}) = \frac{\sin(\pi x_1/L)}{4\pi L} e^{2|\chi(\boldsymbol{r})|} |C_+(\boldsymbol{r},\boldsymbol{r}_1)|^2. \quad (8.46)$$

Although the term $\delta\rho_-(\boldsymbol{r})$ still diverges as $\sim 1/|\boldsymbol{r}-\boldsymbol{r}_1|^2$ at the impurity site, it is exponentially suppressed, so that it exceeds the LDoS $\rho_0(\boldsymbol{r})$ only for distances

$$|\boldsymbol{r}-\boldsymbol{r}_1| < \begin{cases} 2\sqrt{2}\sin(\pi x_1/L) e^{-2|\chi(\boldsymbol{r}_1)|}, & \text{for } \ell_s \ll L, \\ \sqrt{2}\pi\ell_s e^{-2|\chi(\boldsymbol{r}_1)|}, & \text{for } \ell_s \gtrsim L. \end{cases} \quad (8.47)$$

The spatial width (8.47) of this bound state at $\varepsilon = 0$ strongly depends on ℓ_B, but becomes independent of ℓ_s for $\ell_s \ll L$ (provided $|\ell_s/L| \gg e^{-2|\chi(\boldsymbol{r}_1)|}$).

By contrast, the term $\delta\rho_+(\boldsymbol{r})$, equation (8.46), is negligible only for distances larger than L. It is completely independent of the scattering length ℓ_s (provided $|\ell_s/L| \gg e^{-2|\chi(\boldsymbol{r}_1)|}$). At the impurity site $\delta\rho_+(\boldsymbol{r}_1) = \rho_0(\boldsymbol{r}_1)$, so that impurities of any scattering length require the LDoS formed by the solutions in the clean sample to vanish at the impurity site, which is a consequence of the sublattice polarization of the Landau states. This observation will become relevant in the interpretation of the conductance in the case of many impurities and strong magnetic field.

Let me analyze the conductance correction due to a single scalar impurity. Remember that the conductance of the clean sample is given by equation (8.10) for any strength of the magnetic field. The conductance correction for arbitrary scattering length and magnetic field is found as

$$\delta\mathrm{G} = 2\mathrm{g}_0 \left(\frac{\ell_s}{L}\right)^2 \frac{1+F^2(x_1)}{1+2\cosh[4\chi(\boldsymbol{r}_1)]F^2(x_1)+F^4(x_1)}. \quad (8.48)$$

Due to the translational invariance in the y-direction the conductance correction is independent of the y-coordinate of the impurity. It is maximal if the impurity is in the centre of the sample, $x_1 = L/2$, and vanishes if it is at the interfaces with the leads. The position-averaged conductance correction $\langle\delta\mathrm{G}\rangle$ is plotted in figure 8.1

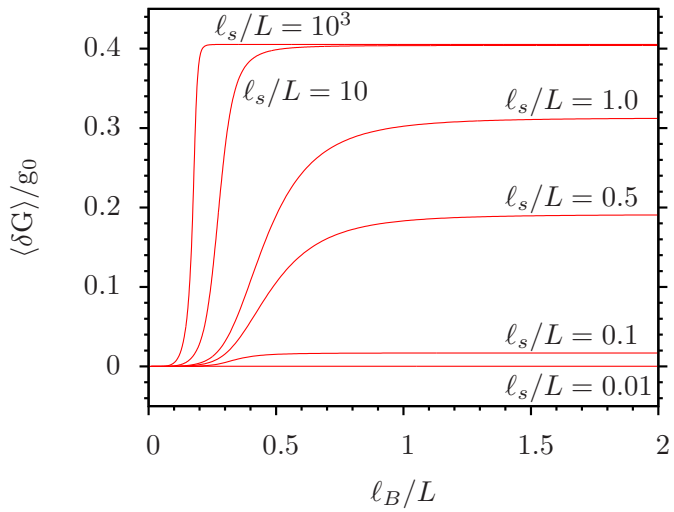

Figure 8.1: Conductance correction due to a single impurity, numerically averaged over its position, as a function of magnetic length for varying scattering length.

as a function of the magnetic length. In a strong magnetic field the conductance correction δG vanishes regardless of the impurity strength and position. This is in contrast to the LDoS, which is strongly affected in this regime.

For absent magnetic field the conductance correction becomes

$$\delta \mathrm{G} = 2\mathrm{g}_0 \left(\frac{\ell_s}{L}\right)^2 \frac{1}{1+F^2(x_1)}, \qquad \text{for } \ell_B \gtrsim L. \tag{8.49}$$

In this case the position average is found analytically as

$$\langle \delta \mathrm{G} \rangle = 2\mathrm{g}_0 \left(\frac{\ell_s}{L}\right)^2 \left(1 - \frac{\pi \ell_s/L}{\sqrt{4+(\pi \ell_s/L)^2}}\right), \qquad \text{for } \ell_B \gtrsim L. \tag{8.50}$$

This correction becomes independent of ℓ_s for $|\ell_s/L| \gg 1$. On the other hand, for a strong magnetic field the resonance condition corresponds roughly to $|\ell_s/L| \gg \exp[2\chi(\boldsymbol{r}_1)] \sim \exp(L/2\ell_B)^2$. The conductance correction of a resonant impurity is given by

$$\delta \mathrm{G} = \mathrm{g}_0 \frac{8}{\pi^2} \sin^2(\pi x_1/L), \tag{8.51}$$

which is valid for any field strength as long as the resonance condition is fulfilled. The average follows as $\langle \delta \mathrm{G} \rangle / \mathrm{g}_0 = 4/\pi^2 \approx 0.405$ in agreement with ref. [48]. This positive correction is comparable with the ballistic conductance (unless for very large aspect ratio). The conductance enhancement, rather than diminution, by the impurity is due to the fact that the transport takes place via evanescent modes. The effect is known as 'impurity-assisted tunneling' [33]. We will see in the following subsection that the effect is generally reduced if another impurity is placed in the vicinity $\sim L$ of the first one. In this case the conductance correction does become negative for certain impurity configurations. For dense impurities the conductivity

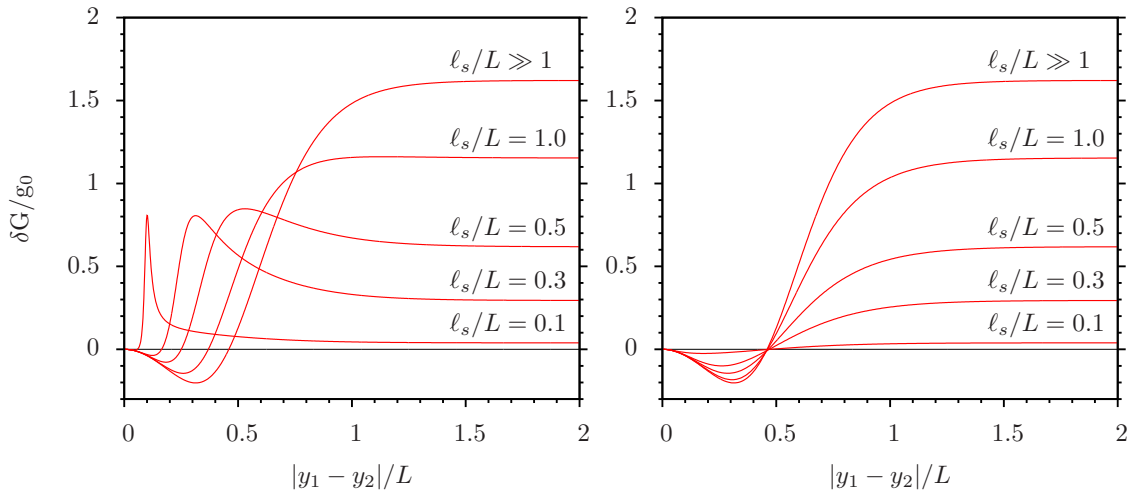

Figure 8.2: Conductance correction due to two impurities at $x_1 = x_2 = L/2$ as a function of their distance for absent magnetic field. Left panel: same scattering length ℓ_s for both impurities; Right panel: opposite scattering lengths ℓ_s and $-\ell_s$.

increases logarithmically with the impurity concentration if the magnetic field is absent (see section 8.4).

8.3.2 Two scalar impurities

I start with the conductance correction for absent magnetic field. For simplicity I place both impurities at the center of the sample, $x_1 = x_2 = L/2$. In this case one obtains a relatively simple expression, which is plotted as a function of the distance in figure 8.2. The two impurities are assumed to have the same strength. However, the signs of the two scattering lengths are chosen as identical and as opposite in the left and right panel, respectively.

As expected, for distances larger than the sample length L the correction is just twice the value (8.49) of a single impurity. The two impurities hybridize for distances smaller than L. For strong impurities this means that their effect becomes smaller until the conductance correction becomes negative, with the minimum $\delta G/g_0 = -2/\pi^2$ at $|y_1 - y_2|/L = \operatorname{arccosh}(\sqrt{7/3})/\pi \approx 1/\pi$. For weak impurities $\ell_s \ll L$ and identical signs of ℓ_s the correction increases towards a maximum $\delta G/g_0 = 8/\pi^2$ at $|y_1 - y_2| = \ell_s$. In fact, the maximal value just corresponds to the conductance correction (8.51) of a single resonant impurity at $x = L/2$. The LDoS for this configuration corresponds to that of a single resonant impurity (8.44) as well, which shows that the two impurities support a bound state at zero energy (even in an infinite system). Numerically one finds that this resonance effect does not rely on $x_1 = x_2 = L/2$. As shown in the right panel of figure 8.2, the resonance effect does not occur if the two impurities have opposite signs of the scattering length.

If the distance between the two impurities is much smaller than both ℓ_s and L, the LDoS is only affected in a region of the order of this distance, hence the

conductance correction vanishes regardless of the scattering length.

The effect of the magnetic field is generally similar to that in the case of a single impurity. This means that a sufficiently strong magnetic field suppresses the correction δG to zero. For strong impurities, $\ell_s \gg L$, the transition is at $\ell_B/L = 1/2\sqrt{\ln(|\ell_s/L|)}$, while for weak impurities this happens at $\ell_B/L \ll 1$. The resonance peak at the distance $|y_1 - y_2| = \ell_s$ for weak impurities becomes narrower and vanishes for $\ell_B \ll L$ as well.

8.4 Conductivity for Many Scalar Impurities in Magnetic Field

In the regime studied in this section, the mean impurity spacing $\ell_{\text{imp}} \equiv \sqrt{N_{\text{imp}}/WL}$ is much smaller than the sample length L. As a reminder, the impurities are assumed to be non-overlapping, so that their characteristic size is still much smaller than ℓ_{imp}. For typical impurity scattering lengths the electronic transport in this regime is diffusive, meaning that the mean free path of electrons is much shorter than the sample length L. Only if the scattering length ℓ_s of impurities is much smaller than their mean spacing ℓ_{imp}, transport may be considered as quasi-ballistic. We will see that these statements do not generally hold in the presence of a magnetic field – the transport is either diffusive or absent in the QH regime, while the transport generally becomes ballistic again in the regime of even higher field strength.

In disordered metals the transport in the diffusive regime is often described by the semiclassical approximation. However, this picture is inadequate in graphene at the Dirac point, due to the diverging Fermi wavelength and conductivity of the order of the conductance quantum. In graphene, quantum interference effects play an important role and can manifest in various ways depending on the symmetry of the disordered system. For a review on the classification of disordered systems into symmetry classes, see ref. [99]. In disordered graphene, the following quantum interference effects have been discussed (see ref. [120]):

(i) For random potential disorder the time reversal symmetry $H = -\sigma_y H^T \sigma_y$ is preserved and the sample belongs to the symplectic symmetry class AII [157]. Due to weak antilocalization the quantum corrections to the conductivity are positive. The system is metallic at large scales [120].

(ii) If the disorder can be described as an assembly of resonant scatterers, the potential disorder preserves not only time reversal symmetry but also the particle-hole symmetry of the unperturbed Hamiltonian. The Hamiltonian falls into the Bogoliubov-de Gennes symmetry class DIII. [3]

(iii) In the case of a random vector potential, the chiral symmetry $H = -\sigma_z H \sigma_z$ is preserved [62] as discussed in chapter 4. The system belongs to the chiral unitary symmetry class AIII. Since an arbitrary vector potential can be gauged away at the

[3] Another model in this symmetry class is that of massless Dirac electrons with random velocity [39].

Dirac point, the system is effectively ballistic at any scale.

These types of disorder are smooth on the atomic scale. Other types of disorder include randomly distributed vacancies (symmetry class BDI) [50] and a random mass term (symmetry class D) [120]. If more than one of the above-mentioned disorder types are present and all symmetries are broken, the system belongs to the standard A symmetry class (unitary[4]).

In the following I study the conductivity of graphene with many non-resonant scalar impurities as a function of the external magnetic field B, which is spatially constant. I thus study a crossover from the AII symmetry class for $B = 0$ to the A symmetry class for increasing B. The latter corresponds to the QH regime. I reveal another transition to the chiral unitary class AIII at even stronger fields, where transport becomes effectively ballistic again.

Again I consider the limit $W \gg L$, in which the transport properties are independent of the aspect ratio. In the plots in this section I have usually set $W/L = 2\pi$, which is approximately the lower bound for this regime. The impurities are placed at random positions and the distance between each two impurities is calculated as in a rectangular setup without periodicity, so that the maximal difference in the y-coordinates is W. The conductivity is found numerically from equation (8.33). At strong magnetic fields ($\ell_B \ll L$), a precision greater than that of double-precision numbers is required. To this end the *MPFR* library [158], a C library for multiple-precision floating-point computations, has been employed. Unfortunately the use of this library greatly increases the computation time, so that it is difficult to obtain results for several thousand impurities.[5] The results in this section were partially obtained by means of a matrix inversion algorithm, based on Gauss-Jordan elimination, written by S. Gattenlöhner.

8.4.1 Overview of results

For completeness I start with the case of absent magnetic field, which has been studied previously [120, 50]. Figure 8.3 shows the conductivity of graphene with resonant ($\ell_s/L = 1000$) and non-resonant ($\ell_s/L = 0.01$) scalar impurities as a function of the impurity density. In either case the conductivity increases logarithmically with the density if the transport is diffusive. This reflects the antilocalization properties of quasiparticles [120]. For weak impurities and low densities ($n_{\mathrm{imp}}L^2 < 50$) the transport is in the ballistic regime, so that a perturbative theory in the impurity potential holds, which implies $\langle\sigma\rangle \sim n_{\mathrm{imp}}^2$. The disordered sample belongs to the symmetry class AII if scatterers are non-resonant [157] and to the symmetry class DIII if they are resonant.

[4]This refers to the invariance of the Hamiltonian with respect to rotations by unitary matrices.

[5]For $N_{\mathrm{imp}} = 500$ impurities the calculation of the conductivity on a typical machine with sufficient physical memory takes about 2 hours. The calculation time roughly increases as $\sim N_{\mathrm{imp}}^3$.

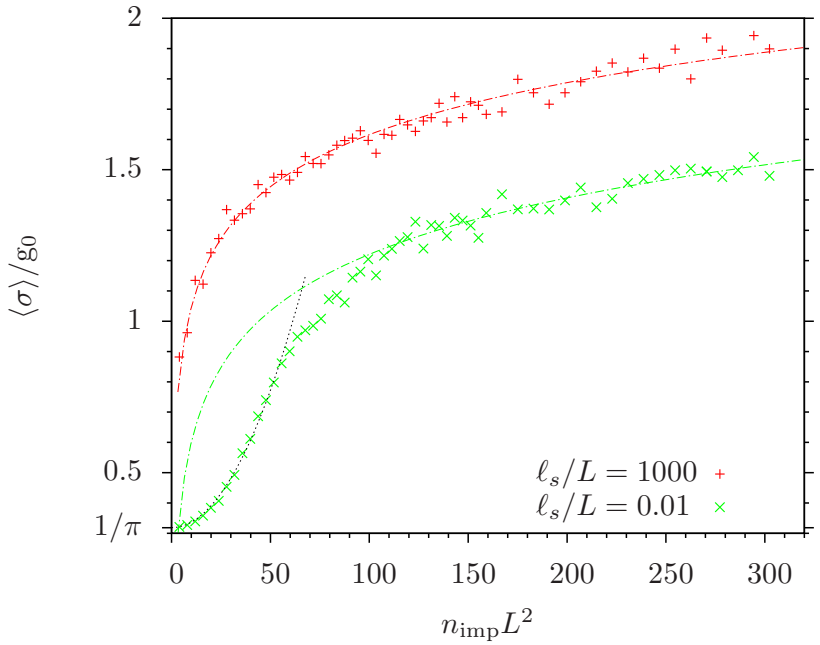

Figure 8.3: The sample-averaged conductivity of a short and wide rectangular graphene sample with resonant ($\ell_s/L = 1000$) and non-resonant ($\ell_s/L = 1/100$) scalar impurities is shown as a function of impurity density for absent magnetic field. Each data point is an average from several disorder realizations. The dotted line is a parabolic fit in the quasi-ballistic regime. The dash-dotted lines are logarithmic fits in the diffusive regimes.

The results for absent magnetic field are approximately valid for $\ell_B > L$. Plots of the conductivity as a function of the magnetic length ℓ_B are shown in figure 8.4. In these plots all scalar impurities have the same scattering length ℓ_s, which is varied for different curves. One notices that the conductivity drops to very small (positive) values in the QH regime, for $\ell_B \lesssim 0.1L$. This transition depends only weakly on the scattering length ℓ_s.

Before I discuss the QH regime, I take a closer look at the transition regime at moderate magnetic fields, $\ell_B \lesssim L$. In this regime one notices a rather strong dependence of the conductivity on the scattering length ℓ_s. This dependence is shown explicitly in figure 8.5. It seems that a resonance effect takes place with the peak approximately at $\ell_s = \ell_{\text{imp}}/\pi$. This applies to all curves with different ℓ_{imp}/L and ℓ_B/L, so that the position of the resonance peak is independent of both L and ℓ_B. It seems that the resonance effect has a similar origin as that discussed for two impurities in the absence of magnetic field. However, this resonance effect disappears for weaker magnetic fields. Another observation is that the transition to the QH regime becomes sharper if the impurities are stronger.

A reduction of the conductivity by the magnetic field has already been discussed for one and two impurities in the previous section. The result of zero conductivity in the QH regime is remarkable insofar as it means that the conductivity correction, equation (8.33), is $-g_0/\pi$ independently of the impurity configuration. It is also

interesting to evaluate the LDoS in this regime (not shown). One finds that the LDoS in the central region of the sample ($x \approx L/2$) is suppressed to nearly zero. The LDoS diverges at the impurity sites, but the localized states are exponentially suppressed and their spatial width is negligible as discussed for the case of a single impurity. At the low-field end of the QH regime the spatial width of the localized states starts to increase and to be governed by ℓ_s, so that a percolation transition takes place and the conductivity increases. Since it is the LDoS correction that is calculated from the unfolded method, and the LDoS in the clean sample increases exponentially with the magnetic field (for example, $\rho(L/2)L \sim 10^{10}$ for $\ell_B/L = 0.1$), the suppressed LDoS in the QH regime partially explains that a very high precision is required in the numerical computation. It will be discussed in section 8.4.2 that generally different results are obtained for the conductivity in the QH regime, if the distribution of scattering length values among impurities is chosen differently, and in particular if the ℓ_s-values are distributed equally around zero.

The QH regime extends between $\ell_B \sim 0.1L$ and another transition at strong magnetic fields, which depends on the ratio $\ell_B/\ell_{\rm imp}$ only. This strong-field transition takes the conductivity back to the ballistic value. It is well resolved in the plot of σ versus the field strength B shown in figure 8.6 for impurities of identical scattering lengths. The transition happens between $N_\phi = N_{\rm imp}/2$ (approximately) and $N_\phi = 2N_{\rm imp}$, with both ends being independent of ℓ_s. The conductivity data obtained so far is not sufficient to precisely determine the lower end of the transition. In the transition region, the conductivity is particularly strong if ℓ_s is of the order of the magnetic length ($\ell_B/L \sim 0.05$ for $N_{\rm imp} = 500$, cf. figure 8.4), but otherwise is almost independent of ℓ_s. The sample-to-sample fluctuations of the conductivity are exponentially suppressed in the regime above this transition, i.e. for $N_\phi > 2N_{\rm imp}$, where $\sigma/{\rm g}_0 = 1/\pi$. This transition implies that a sufficient amount of disorder is necessary for the observation of the QH effect. Its origin is the level condensation discussed in section 8.4.3.

8.4.2 Interpretation of the Quantum Hall regime

Since the Dirac energy $\varepsilon = 0$ corresponds to the Landau level $n = 0$, I need to recall the physics of the QH phase transition (section 2.3.2) in order to interpret the longitudinal conductivity in the QH regime. Due to the disorder the zero-energy Landau level is broadened in energy into a Landau band. In the QH regime the energy width of the band is still small compared with the Landau level spacing. Therefore I do not need to take into account higher Landau levels. The longitudinal conductivity at zero energy depends on whether extended states are available at this energy. In the present model each scalar impurity is described by a scattering length ℓ_s. The distribution of ℓ_s-values seems to determine the DoS within the Landau band. The DoS in a non-relativistic 2DEG in the presence of a strong magnetic

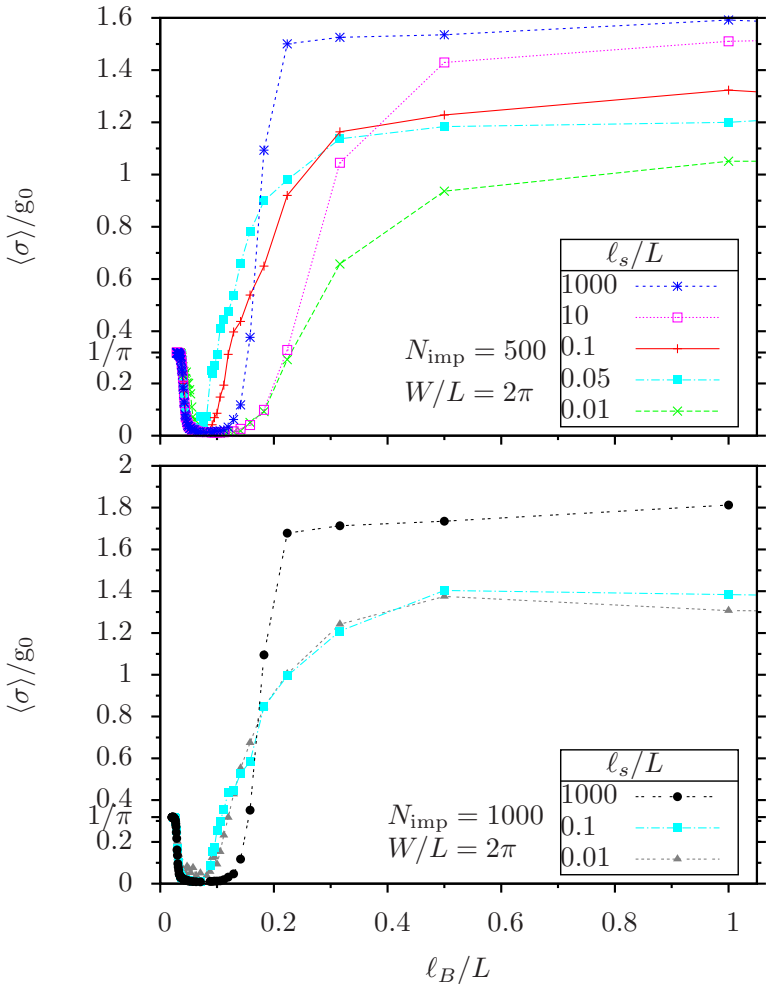

Figure 8.4: Conductivity of a rectangular sample as a function of magnetic length. The sample contains 500 (top panel) and 1000 (bottom panel) scalar impurities with the same scattering length, which is varied for different curves. The conductivity is suppressed to nearly zero in the QH regime and returns to g_0/π at stronger fields. (Straight lines between data points are to guide the eye.)

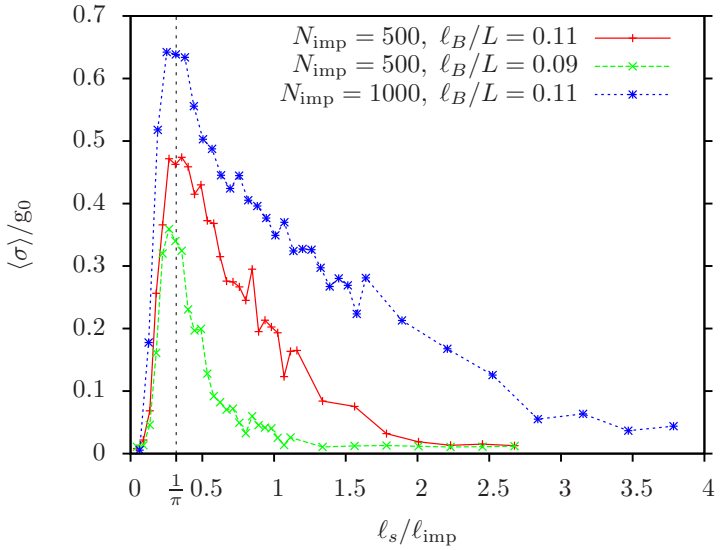

Figure 8.5: Conductivity as a function of scattering length, at field strength just below the transition to the QH regime, cf. figure 8.4. The conductivity shows a resonance with the maximum at $\ell_s/\ell_{\rm imp} \sim 1/\pi$, independently of L and ℓ_B.

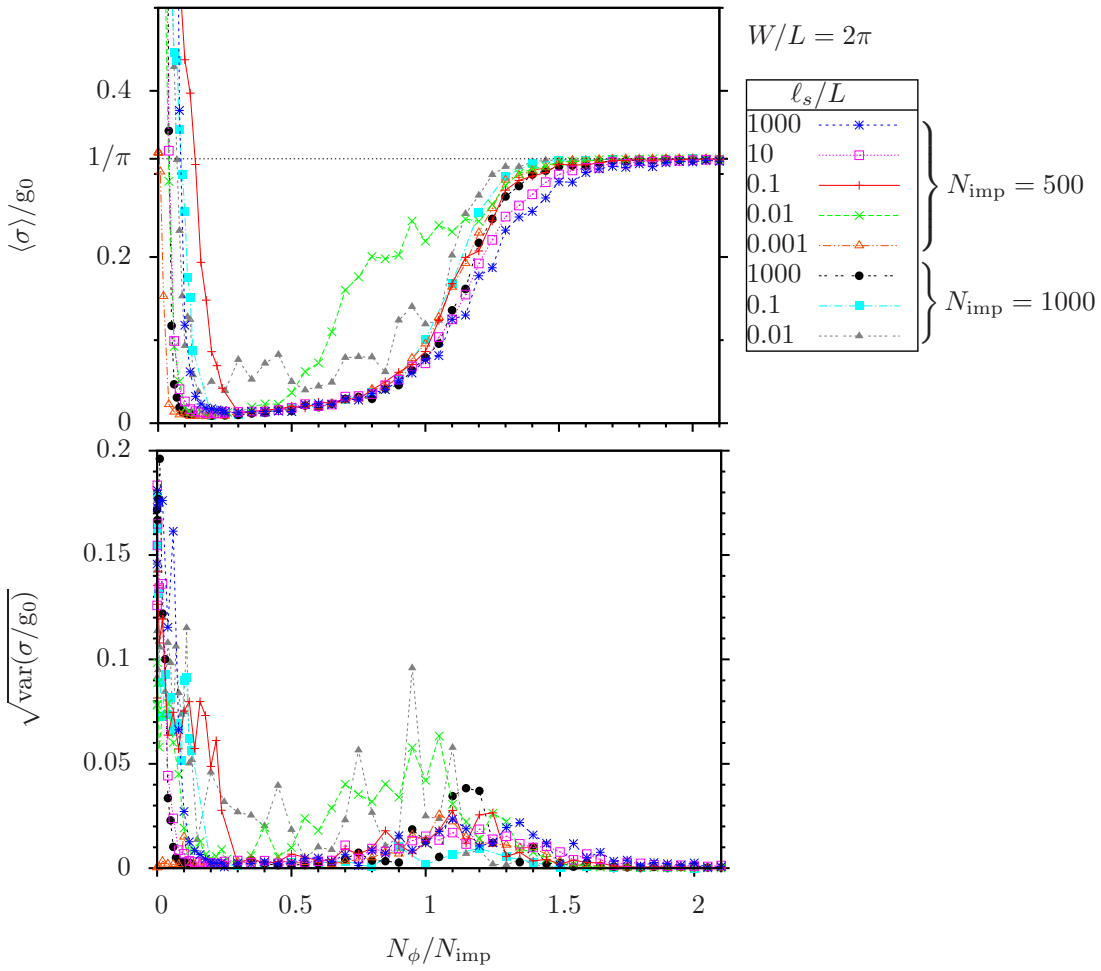

Figure 8.6: Averaged conductivity (top panel) and standard deviation of the sample-to-sample fluctuations (bottom panel) as a function of field strength. (Same data as in figure 8.4.)

field has been studied long time ago for a white noise distribution of impurties [159] as well as for other distributions of scatterers [160]. The critical energy, at which extended states exist and the QH transition happens, is typically located at the center of the Landau band.[6]

If all ℓ_s-values are the same (or have the same sign), the center of the $n = 0$-Landau band is shifted to a finite energy and only strongly localized states remain at zero energy. Therefore the longitudinal conductivity is expected to vanish, while the Hall conductivity is in the plateau region, i.e. half-integer. On the other hand, if the distribution of the scattering lengths ℓ_s is such that the mean value $\langle\ell_s\rangle$ is small compared to the variance, the conductivity in the QH regime is finite due to the availability of states with wavefunctions extended throughout the sample.

It seems that if the mean value of ℓ_s-values is zero, one can study the longitudinal conductivity exactly at the QH phase transition. In the plot in figure 8.7 $|\ell_s|$ is the same for all impurities and the sign of ℓ_s is positive/negative for each one half of the

[6]Note that in the case of a potential with only repulsive scatterers the critical energy is not simply related to features in the density of states [97, 161].

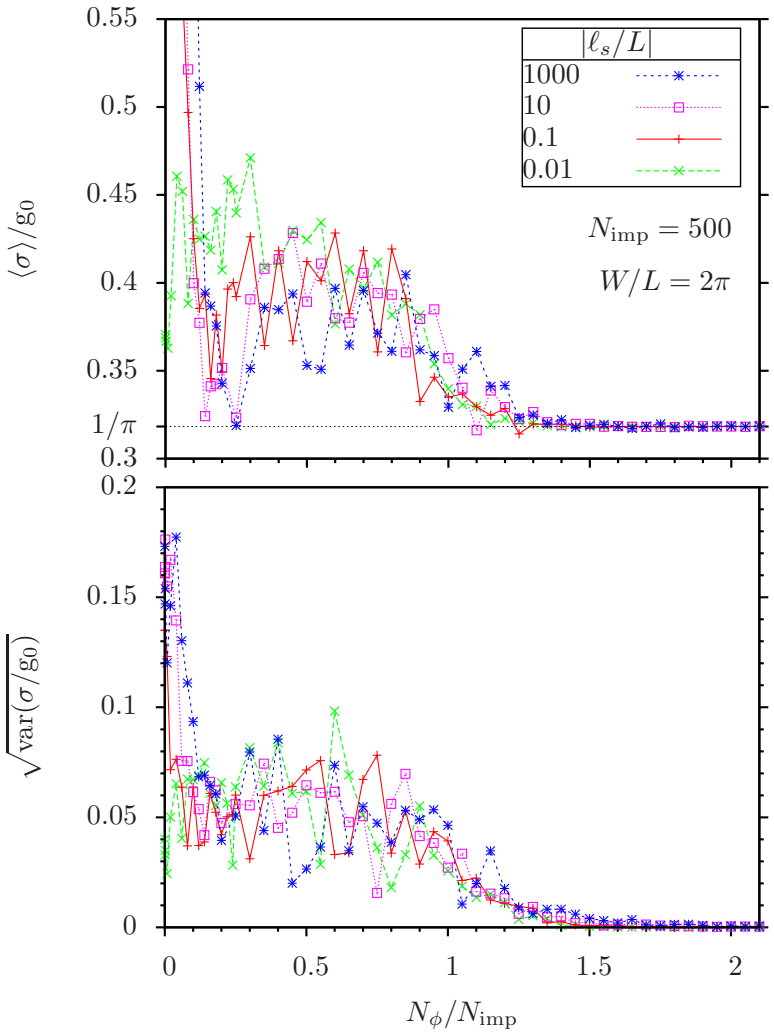

Figure 8.7: The average (top panel) and the sample-to-sample fluctuations (bottom panel) of the conductivity are shown as a function of the field strength. By contrast to figure 8.6 the scalar impurities have opposite scattering lengths $\pm|\ell_s|$ (ratio 1:1). The conductivity is again constant in the QH regime. (The rapid fluctuations are due to an insufficient number of samples used for averaging.)

impurities.[7] The mean conductivity in the QH regime is constant and of the order of $0.4\mathrm{g}_0$, in rough agreement with the numerical models mentioned in section 2.3.2. More data needs to be collected in order to precisely determine the longitudinal conductivity in the limit of large system scales and to confirm that the Pruisken scaling flow diagram applies to the present model.

8.4.3 Interpretation of the level condensation regime

In the strong field regime, $N_\phi > 2N_{\mathrm{imp}}$, the conductivity returns to the ballistic value g_0/π independently of the distribution of scattering lengths ℓ_s. This phenomenon may be understood from the so-called level condensation [162] as outlined below. The only difference to the non-relativistic 2DEG discussed in ref. [162] is given by

[7] Similar results are obtained for random sign of ℓ_s for each impurity.

the sublattice degree of freedom.

The key point is that apart from the localized states, which are irrelevant for the carrier transport, all other solutions in the sample with point-like impurities vanish at the impurity sites. Therefore these solutions may be written as superpositions of the eigenstates in the clean sample, which are in the Landau gauge given by equation (3.41).

The number of states in the sample, i.e. the degeneracy of the $n = 0$-Landau level, is given by the number of flux quanta N_ϕ. However, since the two sublattice components are independent of each other at zero energy,[8] there are $2N_\phi$ independent coefficients in any superposition of these states. The requirement that both sublattice components vanish at all impurity sites gives $2N_{\mathrm{imp}}$ homogeneous equations for the coefficients. It thus follows that such a superposition exists for $N_\phi > N_{\mathrm{imp}}$. In this regime, the transmission eigenvalues may still be affected by the impurities, since I have assumed that the two sublattice components are independent of each other. Another condition is obtained, if one requires that the transmission eigenvalues are not affected by the impurities, but correspond to that of the clean sample,

$$T_q = \frac{1}{\cosh^2\left[qL - L(\bar{x} - L/2)/\ell_B^2\right]}, \tag{8.52}$$

where $\bar{x}$ is the position at which the magnetic flux piercing the cylinder vanishes and $eB\ell_B^2/h$ is chosen positive. This requirement fixes the ratio between the sublattice components, leading to N_ϕ independent coefficients. For $N_\phi > 2N_{\mathrm{imp}}$ one can thus find a superposition of eigenstates in the clean sample with unaffected transmission eigenvalues. In other words, one can choose the amplitudes of incoming scattering states such that the transport remains quasi-one-dimensional, since the solution in the sample does not 'feel' the impurities. It seems that the transmission amplitudes are changed and transverse momentum is not conserved if the amplitudes of incoming scattering states are fixed (e.g. normalized to the unit current), but the transmission eigenvalues must not depend on the occupation of the incoming scattering states and therefore are given by equation (8.52) as long as $N_\phi - 2N_{\mathrm{imp}}$ is positive. This implies that the full counting statistics of charge transport in this regime is the same as that in a clean sample. Deviations from this ideal description are due to the fact that the states in the Landau gauge with center outside the sample as well as the localized states may contribute to the transport as well.

The transport in the regime $N_{\mathrm{imp}} < N_\Phi/2$ is not diffusive but ballistic. This can be seen directly from equation (8.33). Since in this regime the tunneling from one impurity to another impurity is irrelevant, one may set all off-diagonal elements of the matrix $\hat{R}_0^{\mathrm{reg}}$ in impurity space to zero, so that only the regularized Green's

[8] The solutions on one of the two sublattices only exist in a finite system and may be viewed as a mixture between Landau states and evanescent modes.

functions remain on the diagonal. In this approximation the conductance correction is given by the sum over impurities of the conductance correction (8.48) due to a single impurity. If the scattering length ℓ_s is the same for all impurities, each term under the sum depends only on the impurity x-coordinate. Since I consider $N_{\rm imp} \gg 1$, I may replace this sum by an integration over x, so that the conductivity correction becomes

$$\delta\sigma = 2\mathrm{g}_0 \left(\frac{\ell_s}{\ell_{\rm imp}}\right)^2 \frac{1}{L}\int_0^L dx \frac{1+F^2(x)}{1+2F^2(x)\cosh[4\chi(x)]+F^4(x)}. \tag{8.53}$$

Numerically one finds that this correction is generally small (as compared to the ballistic conductivity g_0/π for $\ell_B \to 0$) for $\ell_B/\ell_{\rm imp} < 1/\sqrt{4\pi}$ and $\ell_{\rm imp}/L \ll 1$ (for any realistic value of ℓ_s/L).

In the approximation discussed above the matrix $\hat{\mathcal{M}}(\phi)$ defined in equation (8.23) commutes with σ_z, which might determine the symmetry class of the transport in this regime, which is expected to be AIII (chiral unitary).

8.5 Summary and Discussion

The interplay between point-like disorder and an external magnetic field in the bulk transport of undoped graphene has been the subject of this chapter. In the evaluation I focused on scalar impurities, which may be realized by an electrostatic potential that is smooth on the scale of the lattice constant. I have identified three different regimes in the magnetic field dependence. These are the regime of negligible field strength ($\ell_B > L$), the QH regime ($\ell_B \ll L$ and $\ell_B > \ell_{\rm imp}/\sqrt{\pi}$), and the strong field regime ($\ell_B < \ell_{\rm imp}/2\sqrt{\pi}$).

In the case of zero magnetic field, I find that the conductivity grows logarithmically with the impurity density for both resonant (DIII symmetry class) [50] and non-resonant (AII symmetry class) scalar impurities. The conductivity in the QH regime depends on the distribution of the impurity scattering lengths. For even higher magnetic field strength the conductivity generally assumes the ballistic value g_0/π, with exponentially suppressed fluctuations, if the number of flux quanta exceeds twice the number of impurities. This is due to the level condensation, which has been first discussed for point-like impurities in refs. [162, 160]. In this regime there are still linear combinations of wavefunctions which do not 'know' about the impurities, since the superpositions vanish at the impurity sites. These solutions are still degenerate at the energy of the unperturbed Landau level. For scalar impurities the degeneracy of the unperturbed Landau level is $N_\phi - 2N_{\rm imp}$, where the factor 2 originates in the sublattice degree of freedom.

It is interesting to compare these results with other impurity types in undoped graphene. The case of vacancies has been studied by means of the unfolded scattering approach in the absence of magnetic field in ref. [50], with very different results

as compared to scalar impurities. The mean conductivity is found to be constant in the limit $n_{\mathrm{imp}}L^2 \gg 1$, and the limiting value depends on how the vacancies are distributed on the lattice. For randomly distributed vacancies, this value is equal to g_0/π, while it takes on various higher values if vacancies are randomly placed on the sites which belong to a superlattice [50, 51]. Graphene with vacancies belongs to the BDI symmetry class. By turning on the magnetic field one can induce a crossover to the AIII symmetry class with $\sigma = \mathrm{g}_0/\pi$ as for scalar impurities [163]. The transition to this regime may be explained in the same way as for scalar impurities, i.e. by the level condensation at $\varepsilon = 0$. However, for vacancies the number of available states is $N_\phi - N_{\mathrm{imp}}$, because they require only one sublattice component to vanish in each valley at the impurity site. Therefore the conductivity deviates from g_0/π at $\ell_B/\ell_{\mathrm{imp}} > 1/\sqrt{2\pi}$.

There are several options to extend this study of magnetotransport in graphene with scalar impurities. For a more precise analysis of the QH regime, it would be desirable to collect more data for higher impurity densities, such that the QH regime extends from a small value of N_ϕ/N_{imp}-values to the value 1. In the limit of infinite density of point-like scatterers, their potential approaches the white-noise potential, so that the distribution has a Gaussian dependence on the potential [164, 161]. It would be also interesting to further analyze the conductance fluctuations occurring at the QH phase transition. Such fluctuations are reminiscent of the universal conductance fluctuations in metals (see ref. [165] and references therein). Much insight on the QH phase transition could be gained by extending the calculation to finite doping. Unfortunately this might be difficult since the transformations employed here are specific to the Dirac energy and because there is no closed expression for the real-space Green's function at finite energy. Another relevant quantity to study is the Hall conductivity σ_{xy}, which has a transition at $\varepsilon = 0$ from the plateau at $-\mathrm{g}_0/2$ to the one at $\mathrm{g}_0/2$. According to the interpretation of my results, σ_{xy} is expected to vanish in the case of a scattering length distribution with vanishing mean value, while it should be finite for an asymmetric distribution ($\langle \ell_s \rangle \neq 0$).

The interpretation of the transition to the level condensation regime could be supported by calculating the transmission eigenvalues directly from the wavefunction matching technique. To this end one could neglect the states which are localized at the impurity sites, since these are irrelevant in this and the QH regime, if ℓ_s has the same value for all impurities. Thus the general solution in the sample would be given by a superposition of eigenstates in the clean sample, which is subjected to the scattering boundary conditions at the interfaces and required to vanish at the impurity sites.

Experimentally, a steeply divergent longitudinal resistance has indeed been measured at the Dirac point in strong magnetic fields, along with a plateau in the Hall conductivity at filling factor $\nu = 0$ [166, 167]. The nature of this insulating state

is not fully understood yet, but probably involves a lifting of the four-fold spin and valley degeneracy of the Landau level. The mechanism is therefore not related to the results of this chapter, which does not take into account any interactions. In fact, the physics of this QH state might be outside of the Dirac equation continuum model [55]. Recent experiments did not confirm that spin polarization plays a role as it was initially suspected [168]. Since the insulating state has been observed recently in a Corbino disk geometry measurement [169], one may expect that this metal-insulator transition is an intrinsic bulk property and not an edge phenomenon [170]. On a phenomenological basis, it has been argued that the $\nu = 0$ QH state is only observable at very strong magnetic fields due to the presence of electron-hole puddles [170]. Due to the weak screening properties of quasiparticles at the Dirac point, such puddles exist in the absence of magnetic field (and the presence of charged impurities), but have also been observed in the presence of magnetic field [44]. In fields below the critical strength there may be domains with different filling factors, in this case bulk transport may be facilitated by a percolation network of edge currents propagating along the domain walls. Since the energy spacing between the spin and valley degeneracy-lifted Landau levels increase with the magnetic field, the puddles are suppressed above the critical field strength (much higher than that required to lift the Landau level degeneracy), so that the $\nu = 0$ QH effect becomes observable. The insulating phase at $\nu = 0$ has also been suggested as the reason, why it is difficult to observe the fractional QH effect (at $\nu = \pm 1/3$) in graphene [145], despite the large energy scale of the Coulomb interactions.

Chapter 9 Summary

The electronic properties of graphene systems described by the nearest-neighbour tight-binding Hamiltonian in the effective mass approximation have been investigated using the scattering approach. The emphasis of this work has been on the use of non-unitary gauge transformations, mostly acting in the two-fold sublattice space. Such transformations have provided significant insight into the quantum transport through undoped samples, in particular its dependence on the external magnetic field and the number of layers in stacked graphene. To this end a relatively simple model has been employed, assuming ideal leads and the limits of zero temperature and zero bias voltage. Transport properties have been generally calculated excluding interaction effects. Other parts of the thesis have been concerned with graphene samples, in which the chiral symmetry is broken, either due to doping, contact effects, or the presence of non-resonant point-like scalar impurities. In the latter case I have studied magnetotransport and in particular the quantum Hall regime of the longitudinal conductivity.

The elementary electronic properties of graphene mono- and multi-layers have been reviewed in chapter 2. I have also discussed the quantum Hall phase transition as a delocalization transition. The scattering approach has served as a framework for all transport calculations in this work. It has been introduced along with its extension to full counting statistics in chapter 3. The same concepts have been reformulated in terms of Green's functions, which are easier to calculate for a disordered system than the transfer matrix. The transmission moments can be directly expressed in terms of retarded and advanced Green's functions in a Kubo formula, while the cumulant generating function requires the introduction of a multicomponent Green's function depending on a counting field. The scattering approach has been applied to a clean monolayer graphene device in the two-terminal geometry. A general relation between the transfer matrix and the evolution operator in graphene has been derived. In the following three chapters I have used analogous approaches to study ballistic transport in other graphene devices.

Chiral symmetric few-layer graphene has been studied in a simplistic model in chapter 4. In undoped samples the chiral symmetry has suggested a non-unitary gauge transformation, which has allowed me to prove that the transport through a multilayer is equivalent with that through uncoupled monolayers. For samples without large aspect ratio this correspondence implies that the periodic boundary conditions are altered, and the change can be interpreted as a flux through the cylinder. The same transformation is valid in the presence of arbitrary magnetic and strain fields, which can be gauged away (or gauged to a flux piercing the cylinder) by similar transformations. In the second part of this chapter I have studied the energy

dependence of the conductance, noise, and higher moments of charge transfer. In order to average over sample-specific Fabry-Perot oscillations I have developed a double-contact scheme, which has allowed me to average the cumulant generating function and thus any moment of the transmission distribution. In this way I have obtained analytical results for conductance and noise in the case that only one channel per transverse momentum is open for propagating modes. Numerical results have been presented for any other energy. Since this scheme is numerically more stable than the transfer matrix method, it has been extended to account for evanescent modes, and employed to calculate non-averaged conductance and noise as well.

Returning to the case of monolayer graphene, I have derived a number of gauge transformations simplifying the transport studies for undoped graphene in chapter 5. Here I used the simplistic model of the two-terminal setup with heavily doped leads in either Corbino or rectangular geometry. A conformal mapping transformation has been found that relates the two geometries. The transformations to gauge away a vector potential describing a constant magnetic field in these geometries have been given. Green's functions have been derived for either geometry. The matrix Green's functions have been obtained by means of generalized transformations acting in sublattice and Keldysh space, changing the way how the counting field acts and providing a useful decomposition of the Green's function. These transformations have been employed in the study of magnetotransport in graphene with point-like disorder in chapter 8. In this case the transformations are useful even though the chiral symmetry is broken by the disorder.

In chapter 6 I investigated the effect of charge transfer at the metal-graphene boundaries in a two-terminal monolayer graphene device. I have proposed a model which allows one to self-consistently calculate the potential and charge profile in such a device. The scheme has been evaluated both in the self-consistent Hartree approximation and the Thomas-Fermi approximation. Despite the importance of evanescent modes near the Dirac point, the two approximations have been shown to be in good agreement. A slowly decaying potential has been found for typical parameters of the dielectric constant. The self-consistent potential profiles have been used to calculate transport properties and to explain the experimentally observed electron-hole asymmetries. This includes the asymmetric magnitude of conductance and noise and the asymmetric appearance of Fabry-Perot oscillations, which are typically observed in the ballistic transport regime.

An unfolded scattering approach to deal with point-like disorder has been introduced in chapter 7. The recently developed approach is most suitable for the case that the impurities are non-overlapping and their size is much smaller than the Fermi-wave length and sample size L, so that the s-wave approximation is sufficient. It provides a closed expression for the full Green's function, which does not

involve any spatial integrations like in the original Dyson equation. The key of this method is to move the spatial integrations to the individual impurity T-matrices, where they can be carried out in the s-wave approximation. The T-matrix of a scalar impurity has been discussed by analyzing the bound states at a disk-shaped impurity.

In chapter 8 the gauge transformations derived in chapter 5 have been applied to the full Green's function (in the presence of point-like disorder) expressed by means of the unfolded scattering approach. The impurity correction to the full counting statistics of an undoped sample has been evaluated for impurities of different symmetries. I have derived a relatively compact expression for the conductance correction due to scalar impurities, which has served as a basis for extensive analytical and numerical evaluations for a rectangular sample with large aspect ratio. For a single impurity the impurity-assisted tunneling enhances the conductance of the undoped sample. In strong magnetic fields, the correction has been shown to vanish. For two impurities a resonance effect has been discussed, which occurs if the distance between the impurities equals their scattering length ℓ_s. Further, the strong dependence on the relative sign of scattering lengths in a magnetic field has been discussed. For many impurities with mean distance $\ell_{\mathrm{imp}} \ll L$ the magnetotransport becomes relatively complicated. I have identified the three regimes: (i) negligible field strength, (ii) QH regime, and (iii) strong-field regime. In all three regimes the conductivity is independent of the magnetic length ℓ_B. The transition between (i) and (ii) depends on ℓ_B/L and only weakly on ℓ_s/L. The transition between (ii) and (iii) depends only on $\ell_B/\ell_{\mathrm{imp}}$. In both transition regions resonance effects give rise to an ℓ_s-dependence of the conductivity. The transition to (iii) has been explained by the level condensation of the $n = 0$ Landau level at the charge neutrality point. The conductivity in the QH regime has been shown to depend on the distribution of ℓ_s-values, which determine the energy shift of Landau levels. A possible connection with the QH phase transition has been discussed. Finally, I have mentioned possible extensions of this project and briefly discussed the experimentally observed QH plateau at filling factor $\nu = 0$, which is probably due to interaction-induced lifting of the spin and/or valley degeneracy.

Since the field of graphene research is rapidly developing, any future attempt to extend the findings presented here must be oriented at the current state of the knowledge. The ballistic regime of electron transport in graphene seems to be largely understood, but can always be considered in different models or using different assumptions than in the established studies. Also, it might be interesting to study topological quantum numbers such as winding numbers in the Corbino geometry, which can be obtained from scattering properties [165]. By analyzing such numbers in a graphene device with few impurities as a function of the external magnetic field or gate voltage, one might gain a better understanding of the

quantum Hall transition. Of course, it would also be highly desirable to extend the results on transport in graphene with a large amount of disorder. For example, higher moments of the transmission distribution might be relatively easy to obtain in the model considered in this thesis. Other properties such as the gate voltage dependence of transport properties might also be interesting, but probably demand the development of new approaches, which are suitable for a numerical evaluation.

References

[1] P. R. Wallace, *The Band Theory of Graphite*, Phys. Rev., **71**, 622–634 (1947)

[2] J. W. McClure, *Band Structure of Graphite and de Haas-van Alphen Effect*, Phys. Rev., **108**, 612–618 (1957)

[3] J. C. Slonczewski and P. R. Weiss, *Band Structure of Graphite*, Phys. Rev., **109**, 272–279 (1958)

[4] D. P. DiVincenzo and E. J. Mele, *Self-consistent effective-mass theory for intralayer screening in graphite intercalation compounds*, Phys. Rev. B, **29**, 1685–1694 (1984)

[5] G. W. Semenoff, *Condensed-Matter Simulation of a Three-Dimensional Anomaly*, Phys. Rev. Lett., **53**, 2449–2452 (1984)

[6] Y. Zhang, Y.-W. Tan, H. L. Stormer, and P. Kim, *Experimental observation of the quantum Hall effect and Berry's phase in graphene*, Nature, **438**, 201–204 (2005)

[7] H. P. Boehm, A. Clauss, G. O. Fischer, and U. Hofmann, *Das Adsorptionsverhalten sehr dünner Kohlenstoff-Folien*, Zeitschrift für anorganische und allgemeine Chemie, **316**, 119–127 (1962)

[8] H. P. Boehm, R. Setton, and E. Stumpp, *Nomenclature and Terminology of Graphite Intercalation Compounds*, Pure & Appl. Chem., **66**, 1893 (1994)

[9] M. S. Dresselhaus and G. Dresselhaus, *Intercalation compounds of graphite*, Advances in Physics, **51**, 1–186 (2002)

[10] K. S. Novoselov, A. K. Geim, S. V. Morozov, D. Jiang, Y. Zhang, S. V. Dubonos, I. V. Grigorieva, and A. A. Firsov, *Electric Field Effect in Atomically Thin Carbon Films*, Science, **306**, 666–669 (2004)

[11] K. S. Novoselov, A. K. Geim, S. V. Morozov, D. Jiang, M. I. Katsnelson, I. V. Grigorieva, S. V. Dubonos, and A. A. Firsov, *Two-dimensional gas of massless Dirac fermions in graphene*, Nature, **438**, 197–200 (2005)

[12] C. Berger, Z. Song, T. Li, X. Li, A. Y. Ogbazghi, R. Feng, Z. Dai, A. N. Marchenkov, E. H. Conrad, P. N. First, and W. A. de Heer, *Ultrathin Epitaxial Graphite: 2D Electron Gas Properties and a Route toward Graphene-based Nanoelectronics*, The Journal of Physical Chemistry B, **108**, 19912–19916 (2004)

[13] S. V. Morozov, K. S. Novoselov, M. I. Katsnelson, F. Schedin, L. A. Ponomarenko, D. Jiang, and A. K. Geim, *Strong Suppression of Weak Localization in Graphene*, Phys. Rev. Lett., **97**, 016801 (2006)

[14] K. Bolotin, K. Sikes, Z. Jiang, M. Klima, G. Fudenberg, J. Hone, P. Kim, and H. Stormer, *Ultrahigh electron mobility in suspended graphene*, Solid State Communications, **146**, 351 – 355 (2008)

[15] X. Du, I. Skachko, A. Barker, and E. Y. Andrei, *Approaching ballistic transport in suspended graphene*, Nat Nano, **3**, 491–495 (2008)

[16] A. S. Mayorov, R. V. Gorbachev, S. V. Morozov, L. Britnell, R. Jalil, L. A. Ponomarenko, P. Blake, K. S. Novoselov, K. Watanabe, T. Taniguchi, and A. K. Geim, *Micrometer-Scale Ballistic Transport in Encapsulated Graphene at Room Temperature*, Nano Letters, **11**, 2396–2399 (2011)

[17] M. I. Katsnelson, K. S. Novoselov, and A. K. Geim, *Chiral tunnelling and the Klein paradox in graphene*, Nat Phys, **2**, 620–625 (2006)

[18] T. Ando, T. Nakanishi, and R. Saito, *Berry's Phase and Absence of Back Scattering in Carbon Nanotubes*, Journal of the Physical Society of Japan, **67**, 2857–2862 (1998)

[19] T. Ando and T. Nakanishi, *Impurity Scattering in Carbon Nanotubes – Absence of Back Scattering –*, Journal of the Physical Society of Japan, **67**, 1704–1713 (1998)

[20] C. W. J. Beenakker, *Colloquium : Andreev reflection and Klein tunneling in graphene*, Rev. Mod. Phys., **80**, 1337–1354 (2008)

[21] T. Ando, *Theory of Electronic States and Transport in Carbon Nanotubes*, Journal of the Physical Society of Japan, **74**, 777–817 (2005)

[22] T. Ando, Y. Zheng, and H. Suzuura, *Dynamical Conductivity and Zero-Mode Anomaly in Honeycomb Lattices*, Journal of the Physical Society of Japan, **71**, 1318–1324 (2002)

[23] M. I. Katsnelson, *Zitterbewegung, chirality, and minimal conductivity in graphene*, The European Physical Journal B - Condensed Matter and Complex Systems, **51**, 157–160 (2006)

[24] J. Tworzydlo, B. Trauzettel, M. Titov, A. Rycerz, and C. W. J. Beenakker, *Sub-Poissonian Shot Noise in Graphene*, Phys. Rev. Lett., **96**, 246802 (2006)

[25] N. H. Shon and T. Ando, *Quantum Transport in Two-Dimensional Graphite System*, Journal of the Physical Society of Japan, **67**, 2421–2429 (1998)

[26] N. M. R. Peres, F. Guinea, and A. H. Castro Neto, *Electronic properties of disordered two-dimensional carbon*, Phys. Rev. B, **73**, 125411 (2006)

[27] V. P. Gusynin and S. G. Sharapov, *Unconventional Integer Quantum Hall Effect in Graphene*, Phys. Rev. Lett., **95**, 146801 (2005)

[28] F. Miao, S. Wijeratne, Y. Zhang, U. C. Coskun, W. Bao, and C. N. Lau, *Phase-Coherent Transport in Graphene Quantum Billiards*, Science, **317**, 1530–1533 (2007)

[29] R. Danneau, F. Wu, M. Craciun, S. Russo, M. Tomi, J. Salmilehto, A. Morpurgo, and P. Hakonen, *Evanescent Wave Transport and Shot Noise in Graphene: Ballistic Regime and Effect of Disorder*, Journal of Low Temperature Physics, **153**, 374 (2008)

[30] X. Du, I. Skachko, and E. Y. Andrei, *Towards Ballistic Transport in Graphene*, International Journal of Modern Physics B, **22**, 4579 (2008)

[31] P. Blake, R. Yang, S. Morozov, F. Schedin, L. Ponomarenko, A. Zhukov, R. Nair, I. Grigorieva, K. Novoselov, and A. Geim, *Influence of metal contacts and charge inhomogeneity on transport properties of graphene near the neutrality point*, Solid State Communications, **149**, 1068 – 1071 (2009)

[32] S. Das Sarma, S. Adam, E. H. Hwang, and E. Rossi, *Electronic transport in two-dimensional graphene*, Rev. Mod. Phys., **83**, 407–470 (2011)

[33] M. Titov, *Impurity-assisted tunneling in graphene*, EPL (Europhysics Letters), **79**, 17004 (2007)

[34] A. Rycerz, J. Tworzydlo, and C. W. J. Beenakker, *Valley filter and valley valve in graphene*, Nat Phys, **3**, 172–175 (2007)

[35] V. V. Cheianov, V. I. Fal'ko, B. L. Altshuler, and I. L. Aleiner, *Random Resistor Network Model of Minimal Conductivity in Graphene*, Phys. Rev. Lett., **99**, 176801 (2007)

[36] T. Ando, *Screening Effect and Impurity Scattering in Monolayer Graphene*, Journal of the Physical Society of Japan, **75**, 074716 (2006)

[37] M. I. Katsnelson, *Nonlinear screening of charge impurities in graphene*, Phys. Rev. B, **74**, 201401 (2006)

[38] E. McCann, K. Kechedzhi, V. I. Fal'ko, H. Suzuura, T. Ando, and B. L. Altshuler, *Weak-Localization Magnetoresistance and Valley Symmetry in Graphene*, Phys. Rev. Lett., **97**, 146805 (2006)

[39] P. M. Ostrovsky, I. V. Gornyi, and A. D. Mirlin, *Electron transport in disordered graphene*, Phys. Rev. B, **74**, 235443 (2006)

[40] E. H. Hwang, S. Adam, and S. Das Sarma, *Carrier Transport in Two-Dimensional Graphene Layers*, Phys. Rev. Lett., **98**, 186806 (2007)

[41] J. C. Meyer, A. K. Geim, M. I. Katsnelson, K. S. Novoselov, T. J. Booth, and S. Roth, *The structure of suspended graphene sheets*, Nature, **446**, 60–63 (2007)

[42] M. Katsnelson and A. Geim, *Electron scattering on microscopic corrugations in graphene*, Philosophical Transactions of the Royal Society A: Mathematical, Physical and Engineering Sciences, **366**, 195–204 (2008)

[43] K. Nomura and A. H. MacDonald, *Quantum Hall Ferromagnetism in Graphene*, Phys. Rev. Lett., **96**, 256602 (2006)

[44] J. Martin, N. Akerman, G. Ulbricht, T. Lohmann, J. H. Smet, K. von Klitzing, and A. Yacoby, *Observation of electron-hole puddles in graphene using a scanning single-electron transistor*, Nat Phys, **4**, 144–148 (2008)

[45] Z. H. Ni, L. A. Ponomarenko, R. R. Nair, R. Yang, S. Anissimova, I. V. Grigorieva, F. Schedin, P. Blake, Z. X. Shen, E. H. Hill, K. S. Novoselov, and A. K. Geim, *On Resonant Scatterers As a Factor Limiting Carrier Mobility in Graphene*, Nano Letters, **10**, 3868–3872 (2010)

[46] T. O. Wehling, M. I. Katsnelson, and A. I. Lichtenstein, *Impurities on graphene: Midgap states and migration barriers*, Phys. Rev. B, **80**, 085428 (2009)

[47] J. P. Robinson, H. Schomerus, L. Oroszlány, and V. I. Fal'ko, *Adsorbate-Limited Conductivity of Graphene*, Phys. Rev. Lett., **101**, 196803 (2008)

[48] M. Titov, P. M. Ostrovsky, I. V. Gornyi, A. Schuessler, and A. D. Mirlin, *Charge Transport in Graphene with Resonant Scatterers*, Phys. Rev. Lett., **104**, 076802 (2010)

[49] T. O. Wehling, S. Yuan, A. I. Lichtenstein, A. K. Geim, and M. I. Katsnelson, *Resonant Scattering by Realistic Impurities in Graphene*, Phys. Rev. Lett., **105**, 056802 (2010)

[50] P. M. Ostrovsky, M. Titov, S. Bera, I. V. Gornyi, and A. D. Mirlin, *Diffusion and Criticality in Undoped Graphene with Resonant Scatterers*, Phys. Rev. Lett., **105**, 266803 (2010)

[51] J. Schelter, P. M. Ostrovsky, I. V. Gornyi, B. Trauzettel, and M. Titov, *Color-Dependent Conductance of Graphene with Adatoms*, Phys. Rev. Lett., **106**, 166806 (2011)

[52] L. A. Ponomarenko, A. K. Geim, A. A. Zhukov, R. Jalil, S. V. Morozov, K. S. Novoselov, I. V. Grigorieva, E. H. Hill, V. V. Cheianov, V. I. Fal'ko, K. Watanabe, T. Taniguchi, and R. V. Gorbachev, *Tunable metal-insulator transition in double-layer graphene heterostructures*, Nat Phys, **7**, 958–961 (2011)

[53] Y.-W. Tan, Y. Zhang, H. L. Stormer, and P. Kim, *Temperature dependent electron transport in graphene*, The European Physical Journal Special Topics, **148**, 15–18 (2007)

[54] H. Suzuura and T. Ando, *Crossover from Symplectic to Orthogonal Class in a Two-Dimensional Honeycomb Lattice*, Phys. Rev. Lett., **89**, 266603 (2002)

[55] Y. Barlas, K. Yang, and A. H. MacDonald, *Quantum Hall effects in graphene-based two-dimensional electron systems*, Nanotechnology, **23**, 052001 (2012)

[56] K. S. Novoselov, E. McCann, S. V. Morozov, V. I. Fal'ko, M. I. Katsnelson, U. Zeitler, D. Jiang, F. Schedin, and A. K. Geim, *Unconventional quantum Hall effect and Berry's phase of 2π in bilayer graphene*, Nat Phys, **2**, 177–180 (2006)

[57] D. S. L. Abergel and T. Chakraborty, *Generation of valley polarized current in bilayer graphene*, Applied Physics Letters, **95**, 062107 (2009)

[58] E. McCann, *Asymmetry gap in the electronic band structure of bilayer graphene*, Phys. Rev. B, **74**, 161403 (2006)

[59] J. B. Oostinga, H. B. Heersche, X. Liu, A. F. Morpurgo, and L. M. K. Vandersypen, *Gate-induced insulating state in bilayer graphene devices*, Nat Mater, **7**, 151–157 (2008)

[60] R. Landauer, *Spatial Variation of Currents and Fields Due to Localized Scatterers in Metallic Conduction*, IBM Journal of Research and Development, **1**, 223 –231 (1957)

[61] M. Büttiker, *Scattering theory of thermal and excess noise in open conductors*, Phys. Rev. Lett., **65**, 2901–2904 (1990)

[62] A. Schuessler, P. M. Ostrovsky, I. V. Gornyi, and A. D. Mirlin, *Analytic theory of ballistic transport in disordered graphene*, Phys. Rev. B, **79**, 075405 (2009)

[63] I. Snyman and C. W. J. Beenakker, *Ballistic transmission through a graphene bilayer*, Phys. Rev. B, **75**, 045322 (2007)

[64] A. Rycerz, P. Recher, and M. Wimmer, *Conformal mapping and shot noise in graphene*, Phys. Rev. B, **80**, 125417 (2009)

[65] M. Koshino and T. Ando, *Orbital diamagnetism in multilayer graphenes: Systematic study with the effective mass approximation*, Phys. Rev. B, **76**, 085425 (2007)

[66] A. H. Castro Neto, F. Guinea, N. M. R. Peres, K. S. Novoselov, and A. K. Geim, *The electronic properties of graphene*, Rev. Mod. Phys., **81**, 109–162 (2009)

[67] P. Allain and J. Fuchs, *Klein tunneling in graphene: optics with massless electrons*, The European Physical Journal B - Condensed Matter and Complex Systems, **83**, 301–317 (2011)

[68] F. D. M. Haldane, *Model for a Quantum Hall Effect without Landau Levels: Condensed-Matter Realization of the "Parity Anomaly"*, Phys. Rev. Lett., **61**, 2015–2018 (1988)

[69] H. Min, J. E. Hill, N. A. Sinitsyn, B. R. Sahu, L. Kleinman, and A. H. MacDonald, *Intrinsic and Rashba spin-orbit interactions in graphene sheets*, Phys. Rev. B, **74**, 165310 (2006)

[70] T. Ando, *Spin-Orbit Interaction in Carbon Nanotubes*, Journal of the Physical Society of Japan, **69**, 1757–1763 (2000)

[71] H. Nielsen and M. Ninomiya, *Absence of neutrinos on a lattice: (I). Proof by homotopy theory*, Nuclear Physics B, **185**, 20 – 40 (1981)

[72] H. Nielsen and M. Ninomiya, *Absence of neutrinos on a lattice: (II). Intuitive topological proof*, Nuclear Physics B, **193**, 173 – 194 (1981)

[73] E. McCann and V. I. Fal'ko, *Symmetry of boundary conditions of the Dirac equation for electrons in carbon nanotubes*, Journal of Physics: Condensed Matter, **16**, 2371 (2004)

[74] M. Mecklenburg and B. C. Regan, *Spin and the Honeycomb Lattice: Lessons from Graphene*, Phys. Rev. Lett., **106**, 116803 (2011)

[75] J. Cserti and G. Dávid, *Unified description of Zitterbewegung for spintronic, graphene, and superconducting systems*, Phys. Rev. B, **74**, 172305 (2006)

[76] M. O. Goerbig, *Quantum Hall Effects*, arXiv:0909.1998v2 (2009)

[77] J. W. McClure, *Diamagnetism of Graphite*, Phys. Rev., **104**, 666–671 (1956)

[78] S. V. Morozov, K. S. Novoselov, F. Schedin, D. Jiang, A. A. Firsov, and A. K. Geim, *Two-dimensional electron and hole gases at the surface of graphite*, Phys. Rev. B, **72**, 201401 (2005)

[79] B. Partoens and F. M. Peeters, *From graphene to graphite: Electronic structure around the K point*, Phys. Rev. B, **74**, 075404 (2006)

[80] A. Grüneis, C. Attaccalite, L. Wirtz, H. Shiozawa, R. Saito, T. Pichler, and A. Rubio, *Tight-binding description of the quasiparticle dispersion of graphite and few-layer graphene*, Phys. Rev. B, **78**, 205425 (2008)

[81] S. Latil and L. Henrard, *Charge Carriers in Few-Layer Graphene Films*, Phys. Rev. Lett., **97**, 036803 (2006)

[82] M. Aoki and H. Amawashi, *Dependence of band structures on stacking and field in layered graphene*, Solid State Communications, **142**, 123 – 127 (2007)

[83] J. L. Manes, F. Guinea, and M. A. H. Vozmediano, *Existence and topological stability of Fermi points in multilayered graphene*, Phys. Rev. B, **75**, 155424 (2007)

[84] J.-C. Charlier, J.-P. Michenaud, and X. Gonze, *First-principles study of the electronic properties of simple hexagonal graphite*, Phys. Rev. B, **46**, 4531–4539 (1992)

[85] E. McCann and V. I. Fal'ko, *Landau-Level Degeneracy and Quantum Hall Effect in a Graphite Bilayer*, Phys. Rev. Lett., **96**, 086805 (2006)

[86] F. Guinea, A. H. Castro Neto, and N. M. R. Peres, *Electronic states and Landau levels in graphene stacks*, Phys. Rev. B, **73**, 245426 (2006)

[87] J. Nilsson, A. H. Castro Neto, F. Guinea, and N. M. R. Peres, *Electronic properties of bilayer and multilayer graphene*, Phys. Rev. B, **78**, 045405 (2008)

[88] H. Min and A. H. MacDonald, *Chiral decomposition in the electronic structure of graphene multilayers*, Phys. Rev. B, **77**, 155416 (2008)

[89] K. S. Novoselov, Z. Jiang, Y. Zhang, S. V. Morozov, H. L. Stormer, U. Zeitler, J. C. Maan, G. S. Boebinger, P. Kim, and A. K. Geim, *Room-Temperature Quantum Hall Effect in Graphene*, Science, **315**, 1379 (2007)

[90] J. T. Chalker, *The integer quantum Hall effect and Anderson localization*, In T. J. A. Comtet and S. Ouvry, editors, *Ecole des Houches: Topological Aspects of Low Dimensional Systems*. EDP Sciences, Les Ulis (1999)

[91] B. Kramer, T. Ohtsuki, and S. Kettemann, *Random network models and quantum phase transitions in two dimensions*, Physics Reports, **417**, 211 – 342 (2005)

[92] E. Abrahams, P. W. Anderson, D. C. Licciardello, and T. V. Ramakrishnan, *Scaling Theory of Localization: Absence of Quantum Diffusion in Two Dimensions*, Phys. Rev. Lett., **42**, 673–676 (1979)

[93] A. M. M. Pruisken, *The Quantum Hall Effect*, Springer Berlin (1987)

[94] A. M. M. Pruisken, *Universal Singularities in the Integral Quantum Hall Effect*, Phys. Rev. Lett., **61**, 1297–1300 (1988)

[95] P. M. Ostrovsky, I. V. Gornyi, and A. D. Mirlin, *Theory of anomalous quantum Hall effects in graphene*, Phys. Rev. B, **77**, 195430 (2008)

[96] J. T. Chalker and P. D. Coddington, *Percolation, quantum tunnelling and the integer Hall effect*, Journal of Physics C: Solid State Physics, **21**, 2665 (1988)

[97] Y. Huo, R. E. Hetzel, and R. N. Bhatt, *Universal conductance in the lowest Landau level*, Phys. Rev. Lett., **70**, 481–484 (1993)

[98] L. Schweitzer and P. Markoš, *Universal Conductance and Conductivity at Critical Points in Integer Quantum Hall Systems*, Phys. Rev. Lett., **95**, 256805 (2005)

[99] F. Evers and A. D. Mirlin, *Anderson transitions*, Rev. Mod. Phys., **80**, 1355–1417 (2008)

[100] C. W. J. Beenakker, *Random-matrix theory of quantum transport*, Rev. Mod. Phys., **69**, 731–808 (1997)

[101] M. Di Ventra, *Transport in Nanoscale Systems*, Cambridge University Press (2008)

[102] Y. Blanter and M. Büttiker, *Shot noise in mesoscopic conductors*, Physics Reports, **336**, 1 – 166 (2000)

[103] D. S. Fisher and P. A. Lee, *Relation between conductivity and transmission matrix*, Phys. Rev. B, **23**, 6851–6854 (1981)

[104] Y. V. Nazarov, *Limits of universality in disordered conductors*, Phys. Rev. Lett., **73**, 134–137 (1994)

[105] J.-L. Pichard, *(title not found)*, Ph.D. thesis, University of Paris at Orsay (1984)

[106] W.-R. Hannes, *Detection of Spin Entanglement in Semiconductor Heterostructures*, Diploma thesis, Universität Konstanz (2008)

[107] W. Schottky, *Über spontane Stromschwankungen in verschiedenen Elektrizitätsleitern*, Annalen der Physik, **362**, 541–567 (1918)

[108] L. S. Levitov and G. B. Lesovik, *Charge distribution in quantum shot noise*, JETP Lett., **58**, 230 (1993)

[109] H. Schomerus, *Effective contact model for transport through weakly-doped graphene*, Phys. Rev. B, **76**, 045433 (2007)

[110] S. Ryu, C. Mudry, A. Furusaki, and A. W. W. Ludwig, *Landauer conductance and twisted boundary conditions for Dirac fermions in two space dimensions*, Phys. Rev. B, **75**, 205344 (2007)

[111] Y. M. Blanter and I. Martin, *Transport through normal-metal–graphene contacts*, Phys. Rev. B, **76**, 155433 (2007)

[112] J. P. Robinson and H. Schomerus, *Electronic transport in normal-conductor/graphene/normal-conductor junctions and conditions for insulating behavior at a finite charge-carrier density*, Phys. Rev. B, **76**, 115430 (2007)

[113] V. V. Cheianov and V. I. Fal'ko, *Selective transmission of Dirac electrons and ballistic magnetoresistance of n-p junctions in graphene*, Phys. Rev. B, **74**, 041403 (2006)

[114] P. San-Jose, E. Prada, and D. S. Golubev, *Universal scaling of current fluctuations in disordered graphene*, Phys. Rev. B, **76**, 195445 (2007)

[115] R. Danneau, F. Wu, M. F. Craciun, S. Russo, M. Y. Tomi, J. Salmilehto, A. F. Morpurgo, and P. J. Hakonen, *Shot Noise in Ballistic Graphene*, Phys. Rev. Lett., **100**, 196802 (2008)

[116] L. DiCarlo, J. R. Williams, Y. Zhang, D. T. McClure, and C. M. Marcus, *Shot Noise in Graphene*, Phys. Rev. Lett., **100**, 156801 (2008)

[117] S. Datta, *Electronic Transport in Mesoscopic Systems*, Cambridge University Press (1997)

[118] M. Wimmer, *Quantum transport in nanostructures: From computational concepts to spintronics in graphene and magnetic tunnel junctions*, Ph.D. thesis, Universität Regensburg (2008)

[119] P. M. Ostrovsky, *Transmisson distribution beyond RG*, unpublished notes (2009)

[120] A. Schuessler, P. M. Ostrovsky, I. V. Gornyi, and A. D. Mirlin, *Full counting statistics in disordered graphene at the Dirac point: From ballistics to diffusion*, Phys. Rev. B, **82**, 085419 (2010)

[121] A. Lamacraft, B. D. Simons, and M. R. Zirnbauer, *Localization from σ-model geodesics*, Phys. Rev. B, **70**, 075412 (2004)

[122] V. M. Pereira and A. H. Castro Neto, *Strain Engineering of Graphene's Electronic Structure*, Phys. Rev. Lett., **103**, 046801 (2009)

[123] Y. Aharonov and A. Casher, *Ground state of a spin-1/2 charged particle in a two-dimensional magnetic field*, Phys. Rev. A, **19**, 2461–2462 (1979)

[124] O. N. Dorokhov, *Transmission coefficient and the localization length of an electron in an N bound disordered chain*, ZETP, **36**, 259 (1982)

[125] M. Büttiker, *Coherent and sequential tunneling in series barriers*, IBM J. Res. Dev., **32**, 63–75 (1988)

[126] M. Nakamura and L. Hirasawa, *Electric transport and magnetic properties in multilayer graphene*, Phys. Rev. B, **77**, 045429 (2008)

[127] A. R. Akhmerov and C. W. J. Beenakker, *Boundary conditions for Dirac fermions on a terminated honeycomb lattice*, Phys. Rev. B, **77**, 085423 (2008)

[128] W.-R. Hannes and M. Titov, *Ballistic charge transport in chiral-symmetric few-layer graphene*, EPL (Europhysics Letters), **89**, 47007 (2010)

[129] M. Katsnelson, *Quantum Transport via Evanescent Waves in Undoped Graphene*, Journal of Computational and Theoretical Nanoscience, **8**, 912–918 (2011)

[130] A. Rycerz, *Magnetoconductance of the Corbino disk in graphene*, Phys. Rev. B, **81**, 121404 (2010)

[131] A. H. MacDonald, *Introduction to the Physics of the Quantum Hall Regime*, arXiv:cond-mat/9410047 (1994)

[132] M. I. Katsnelson, *Aharonov-Bohm effect in undoped graphene: Magnetotransport via evanescent waves*, EPL (Europhysics Letters), **89**, 17001 (2010)

[133] M. Titov, P. M. Ostrovsky, and I. V. Gornyi, *Metallic proximity effect in ballistic graphene with resonant scatterers*, Semiconductor Science and Technology, **25**, 034007 (2010)

[134] R. B. Laughlin, *Quantized Hall conductivity in two dimensions*, Phys. Rev. B, **23**, 5632–5633 (1981)

[135] B. Huard, N. Stander, J. Sulpizio, and D. Goldhaber-Gordon, *Evidence of the role of contacts on the observed electron-hole asymmetry in graphene*, Phys. Rev. B, **78**, 121402 (2008)

[136] Y. Wu, V. Perebeinos, Y.-m. Lin, T. Low, F. Xia, and P. Avouris, *Quantum Behavior of Graphene Transistors near the Scaling Limit*, Nano Letters, **12**, 1417–1423 (2012)

[137] H. B. Heersche, P. Jarillo-Herrero, J. B. Oostinga, L. M. K. Vandersypen, and A. F. Morpurgo, *Bipolar supercurrent in graphene*, Nature, **446**, 56–59 (2007)

[138] M. Titov and C. W. J. Beenakker, *Josephson effect in ballistic graphene*, Phys. Rev. B, **74**, 041401 (2006)

[139] J. Cayssol, B. Huard, and D. Goldhaber-Gordon, *Contact resistance and shot noise in graphene transistors*, Phys. Rev. B, **79**, 075428 (2009)

[140] E. Lee, K. Balasubramanian, R. Weitz, M. Burghard, and K. Kern, *Contact and edge effects in graphene devices*, Nature nanotechnology, **3**, 486–490 (2008)

[141] T. Mueller, F. Xia, M. Freitag, J. Tsang, and P. Avouris, *Role of contacts in graphene transistors: A scanning photocurrent study*, Phys. Rev. B, **79**, 245430 (2009)

[142] S. Russo, M. Craciun, M. Yamamoto, A. Morpurgo, and S. Tarucha, *Contact resistance in graphene-based devices*, Physica E: Low-dimensional Systems and Nanostructures, **42**, 677 – 679 (2010), <ce:title>18th International Conference on Electron Properties of Two-Dimensional Systems</ce:title>

[143] R. Nouchi and K. Tanigaki, *Charge-density depinning at metal contacts of graphene field-effect transistors*, Appl. Phys. Lett., **96**, 253503 (2010)

[144] R. Nouchi, M. Shiraishi, and Y. Suzuki, *Transfer characteristics in graphene field-effect transistors with Co contacts*, Applied Physics Letters, **93**, 152104 (2008)

[145] X. Du, I. Skachko, F. Duerr, A. Luican, and E. Y. Andrei, *Fractional quantum Hall effect and insulating phase of Dirac electrons in graphene*, Nature, **462**, 192–195 (2009)

[146] R. Nouchi, T. Saito, and K. Tanigaki, *Determination of Carrier Type Doped from Metal Contacts to Graphene by Channel-Length-Dependent Shift of Charge Neutrality Points*, Appl. Phys. Express, **4**, 035101 (2011)

[147] P. A. Khomyakov, G. Giovannetti, P. C. Rusu, G. Brocks, J. V. D. Brink, and P. J. Kelly, *First-principles study of the interaction and charge transfer between graphene and metals*, Phys. Rev. B, **79**, 195425 (2009)

[148] M. Vanin, J. J. Mortensen, A. K. Kelkkanen, J. M. Garcia-Lastra, K. S. Thygesen, and K. W. Jacobsen, *Graphene on metals: A van der Waals density functional study*, Phys. Rev. B, **81**, 081408 (2010)

[149] S. Barraza-Lopez, M. Vanević, M. Kindermann, and M. Y. Chou, *Effects of Metallic Contacts on Electron Transport through Graphene*, Phys. Rev. Lett., **104**, 076807 (2010)

[150] P. A. Khomyakov, A. A. Starikov, G. Brocks, and P. J. Kelly, *Nonlinear screening of charges induced in graphene by metal contacts*, Phys. Rev. B, **82**, 115437 (2010)

[151] P. M. Ostrovsky, I. V. Gornyi, and A. D. Mirlin, *Conductivity of disordered graphene at half filling*, The European Physical Journal - Special Topics, **148**, 63–72 (2007), 10.1140/epjst/e2007-00226-4

[152] W.-R. Hannes, M. Jonson, and M. Titov, *Electron-hole asymmetry in two-terminal graphene devices*, Phys. Rev. B, **84**, 045414 (2011)

[153] E. Mueller, *Scattering Tutorial*, people.ccmr.cornell.edu/∼emueller/scatter.pdf (2002)

[154] M. Hentschel and F. Guinea, *Orthogonality catastrophe and Kondo effect in graphene*, Phys. Rev. B, **76**, 115407 (2007)

[155] D. S. Novikov, *Elastic scattering theory and transport in graphene*, Phys. Rev. B, **76**, 245435 (2007)

[156] D. M. Basko, *Resonant low-energy electron scattering on short-range impurities in graphene*, Phys. Rev. B, **78**, 115432 (2008)

[157] P. M. Ostrovsky, I. V. Gornyi, and A. D. Mirlin, *Quantum Criticality and Minimal Conductivity in Graphene with Long-Range Disorder*, Phys. Rev. Lett., **98**, 256801 (2007)

[158] L. Fousse, G. Hanrot, V. Lefèvre, P. Pélissier, and P. Zimmermann, *MPFR: A Multiple-Precision Binary Floating-Point Library with Correct Rounding*, ACM Transactions on Mathematical Software, **33**, 13:1–13:15 (2007)

[159] F. Wegner, *Exact density of states for lowest Landau level in white noise potential superfield representation for interacting systems*, Zeitschrift für Physik B Condensed Matter, **51**, 279 (1983)

[160] E. Brezin, D. J. Gross, and C. Itzykson, *Density of states in the presence of a strong magnetic field and random impurities*, Nuclear Physics B, **235**, 24 – 44 (1984)

[161] B. Huckestein, *Scaling theory of the integer quantum Hall effect*, Rev. Mod. Phys., **67**, 357–396 (1995)

[162] É. M. Baskin, L. N. Magarill, and M. V. Éntin, *Two-dimensional electron-impurity system in a strong magnetic field*, Soviet Journal of Experimental and Theoretical Physics, **48**, 365 (1978)

[163] S. Gattenlöhner, W.-R. Hannes, P. M. Ostrovsky, I. V. Gornyi, A. D. Mirlin, and M. Titov, *Transport at the zeroth Landau level in graphene with point-like impurities*, in preparation (2013)

[164] T. Ando and H. Aoki, *Finite-Size Scaling Study of Localization in Landau Levels*, Journal of the Physical Society of Japan, **54**, 2238–2249 (1985)

[165] I. C. Fulga, F. Hassler, A. R. Akhmerov, and C. W. J. Beenakker, *Topological quantum number and critical exponent from conductance fluctuations at the quantum Hall plateau transition*, Phys. Rev. B, **84**, 245447 (2011)

[166] J. G. Checkelsky, L. Li, and N. P. Ong, *Zero-Energy State in Graphene in a High Magnetic Field*, Phys. Rev. Lett., **100**, 206801 (2008)

[167] J. G. Checkelsky, L. Li, and N. P. Ong, *Divergent resistance at the Dirac point in graphene: Evidence for a transition in a high magnetic field*, Phys. Rev. B, **79**, 115434 (2009)

[168] D. A. Abanin, K. S. Novoselov, U. Zeitler, P. A. Lee, A. K. Geim, and L. S. Levitov, *Dissipative Quantum Hall Effect in Graphene near the Dirac Point*, Phys. Rev. Lett., **98**, 196806 (2007)

[169] Y. Zhao, P. Cadden-Zimansky, F. Ghahari, and P. Kim, *Magnetoresistance measurements of Graphene at the Charge Neutrality Point* (2012), ArXiv:1201.4434 [cond-mat.mes-hall]

[170] S. D. Sarma and K. Yang, *The enigma of the quantum Hall effect in graphene*, Solid State Communications, **149**, 1502 – 1506 (2009)